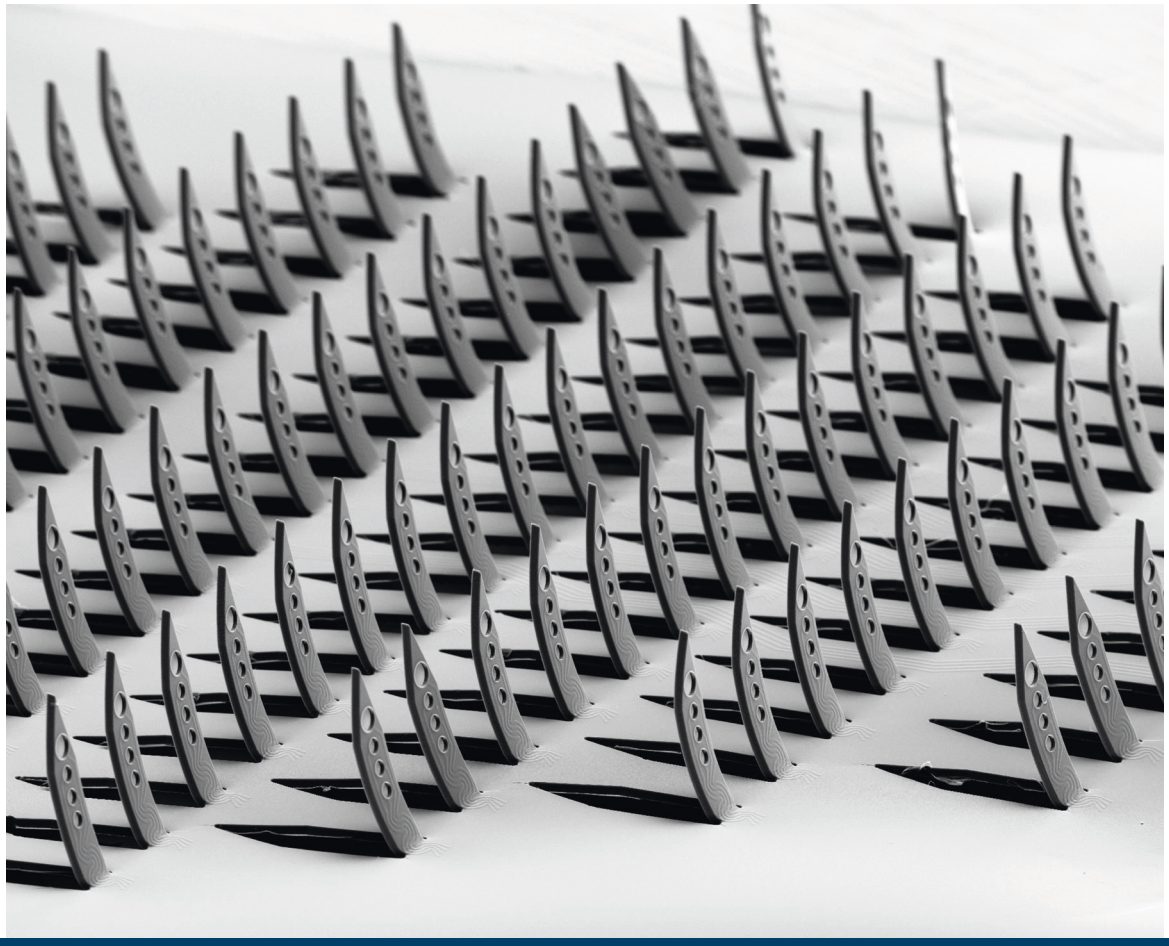

3D neural implants for in *vivo applications*

Marie Jung

Schlüsseltechnologien / Key Technologies
Band / Volume 300
ISBN 978-3-95806-852-0

Mitglied der Helmholtz-Gemeinschaft

JÜLICH
Forschungszentrum

Schriften des Forschungszentrums Jülich
Reihe Schlüsseltechnologien / Key Technologies Band / Volume 300

Forschungszentrum Jülich GmbH
Institut für Biologische Informationsprozesse (IBI)
Bioelektronik (IBI-3)

3D neural implants for in vivo *applications*

Marie Jung

Schriften des Forschungszentrums Jülich
Reihe Schlüsseltechnologien / Key Technologies Band / Volume 300

ISSN 1866-1807 ISBN 978-3-95806-852-0

Bibliografische Information der Deutschen Nationalbibliothek.
Die Deutsche Nationalbibliothek verzeichnet diese Publikation in der
Deutschen Nationalbibliografie; detaillierte Bibliografische Daten
sind im Internet über http://dnb.d-nb.de abrufbar.

Herausgeber und Vertrieb:	Forschungszentrum Jülich GmbH Zentralbibliothek, Verlag 52425 Jülich Tel.: +49 2461 61-5368 Fax: +49 2461 61-6103 zb-publikation@fz-juelich.de www.fz-juelich.de/zb
Umschlaggestaltung:	Grafische Medien, Forschungszentrum Jülich GmbH
Titelbild:	Taken from Marie Jung et al., Flexible 3D Kirigami Probes for In Vitro and In Vivo Neural Applications; Advanced Materials, Volume 37, Issue 24, 2025.
Druck:	Grafische Medien, Forschungszentrum Jülich GmbH
Copyright:	Forschungszentrum Jülich 2025

Schriften des Forschungszentrums Jülich
Reihe Schlüsseltechnologien / Key Technologies, Band / Volume 300

D 82 (Diss. RWTH Aachen University, 2025)

ISSN 1866-1807
ISBN 978-3-95806-852-0

Vollständig frei verfügbar über das Publikationsportal des Forschungszentrums Jülich (JuSER)
unter www.fz-juelich.de/zb/openaccess.

Declaration of Authorship

I, *Marie Jung*
declare that this thesis and the work presented in it are my own and has been generated by me as the result of my own original research. I do solemnely swear that:

1. This work was done wholly or mainly while in candidature for the doctoral degree at this faculty and university;
2. Where any part of this thesis has previously been submitted for a degree or any other qualification at this university or any other institution, this has been clearly stated;
3. Where I have consulted the published work of others or myself, this is always clearly attributed;
4. Where I have quoted from the work of others or myself, the source is always given. This thesis is entirely my own work, with the exception of such quotations;
5. I have acknowledged all major sources of assistance;
6. Where the thesis is based on work done by myself jointly with others, I have made clear exactly what was done by others and what I have contributed myself;
7. Parts of this work have been published before as:

- **M. Jung**, J. Abu Shihada, S. Decke, L. Koschinski, P. S. Graff, S. Maruri Pazmino, A. Höllig, H. Koch, S. Musall, A. Offenhäusser, V. Rincón Montes. "Flexible 3D Kirigami Probes for in Vitro and in Vivo Neural Applications". 14 April 2025. A dv. Mater. 2418524 (2025) doi:10.1002/adma.202418524.
- **M. Jung**, A. Willuweit, & V. Rincón Montes “Intraretinal Electrophysiology and Resistivity Profiles of WT and RCS Rat Retina.” *Sensors*, *25*(12), 2025, https://doi.org/10.3390/s25123765
- Patent application: Rincón Montes, V., **Jung, M**., Shihada, J.A., Offenhäusser, A., Koschin- ski, L. “Herstellung dreidimensional strukturierten Elektrodenlagen, insbesondere im Kirigami- Prinzip”. DE 102023102257.1; PCT/EP2024/051829, January 30, 2023.
- Patent application: Shihada, J.A., Offenhäusser, A., **Jung, M.**, Rincón Montes, V., Koschinski, L. “Herstellung dreidimensionaler Elektroden mittels schablonengestützter elektrochemis- cher Abscheidung ”. DE 102023102460.4; PCT/EP2024/052176, February 1, 2023.
- J. Abu Shihada* and **M. Jung***, S. Decke, L. Koschinski, S. Musall, V. Rincón Montes, A. Of- fenhäusser. "Highly Customizable 3D Microelectrode Arrays for In Vitro and In Vivo Neuronal Tissue Recordings". Advanced Science 2024, 11, 2305944, ISSN: 2198-3844, 2198-3844. DOI: 10.1002/advs.202305944. (*Equal contribution)
- N. Nruthyathi, **M. Jung**, J. Wang, V. Rincón Montes, A. Offenhäusser, A. Willuweit, M. Müller. "Late emergence of pathological oscillatory activity in the retina of the Retinitis pigmentosa model RCS (Royal College of Surgeons) rats". 27 May 2025, PLoS One 20(5): e0324345. https://doi.org/10.1371/journal.pone.0324345
- **M. Jung**, M. Kasavetov, N. Nruthyathi, J. Abu Shihada, S. Decke, L. Koschinski, F. Balcewicz, T. Lohmann, P. Walter, A. Offenhäusser, V. Rincón Montes. “Towards the in vivo validation of 3D retinal implants: an in vitro and cadaveric validation” *in Preparation*

Marie Jung, 05.09.25

Zusammenfassung

3D-Elektroden-Arrays (3D-MEA) haben im Bereich der Biomedizin zunehmend an Bedeutung gewonnen, insbesondere bei der Untersuchung von elektrophysiologischer Aktivitäten. Die Interaktion zwischen diesen Arrays und dem neuronalen Gewebe sind durch die elektrochemischen, mechanischen und geometrischen Eigenschaften der Elektroden beeinflusst. Während 2D-MEA nur begrenzt in der Lage sind, die Komplexität neuronaler Zellnetzwerke zu erfassen, müssen herkömmliche 3D-MEA in Bezug auf Auflösung und Gewebeintegration weiter verbessert werden. Ziel dieses Projekts war es daher, die Anzahl der Schäfte eines 3D-MEA zu erhöhen und damit die Anzahl der Elektroden zu vergrößern. Flexible Polymere wurden als primäres Material gewählt, um Schäden bei der Implantierung und Reaktionen des Gewebes zu minimieren.
Bei der Herstellung wurden zwei Ansätze verfolgt, um aus einem 2D-Design eine 3D-Struktur zu erzeugen: Die Elektroden wurden entweder auf ein flexibles Substrat gedruckt (PiRi) oder ausgeschnitten und gefaltet, um Kirigami-Strukturen zu erhalten (KiRi). Der erste Ansatz nutzt ein präzises 3D-Druckverfahren in Kombination mit einer schablonengestützten Elektroabscheidung, um bis zu 400 µm hohe 3D-Mikroelektroden auf einem flexiblen Substrat herzustellen. Der zweite Ansatz verwendet ein mechanisches Formgebungsverfahren, das die Herstellung von bis zu 512 Elektroden, verteilt auf 128 Schäfte, in einem einzigen, flexiblen Implantat ermöglicht. Dabei kann die Höhe der Schäfte bis zu 1 mm betragen.
Um die Implantate in *in vivo*-Anwendungen zu testen, müssen die Eigenschaften des Designs und die chirurgischen Methoden berücksichtigt werden. Ziel war es daher, die Machbarkeit der Implantation, die Biokompatibilität, die Langzeitstabilität und die Sicherheit der hergestellten Implantate nachzuweisen, indem eine Reihe von elektrischen und mechanischen Charakterisierungen der Elektroden durchgeführt wurden.
Die Vorteile beider Ansätze zeigen sich in der Flexibilität des Designs zum Beispiel bei der Anzahl und Konfiguration der Elektroden. Die Implantate können daher für verschiedene neuronale Anwendungen, wie der Netzhaut oder dem Kortex, eingesetzt werden. Gesunde und degenerierte Netzhäute von Ratten wurden verwendet, um die Implantate zu validieren und zu zeigen, wie sich die elektrophysiologische Aktivität im gesamten 3D-Raum der Netzhaut unterscheidet. Bei degenerierten Netzhäuten wurde eine charakteristische pathologische Aktivität in Form von Oszillationen untersucht. Die Auswirkung der Insertion in Bezug auf verletztes Gewebe, was sich bei beiden Implantaten als gering erwies, wurden mithilfe von Zellfärbungen evaluiert. Zur Vorbereitung akuter *in vivo* Versuche wurden chirurgische Ansätze für 3D-Netzhautimplantate mit Kadavern durchgeführt, einschließlich der "Open-Sky" Operation und der *pars-plana* Implantation. Außerdem wurden die KiRis und PiRis für den Einsatz in kortikalen Anwendungen optimiert. In menschlichen Hirnschnitten wurden epileptische Anfälle durch Behandlung mit modifiziertem aCSF (artificial cerebrospinal fluid) ausgelöst. 3D-Messungen zeigten anfallsartige Aktivität in verschiedenen lokalen Netzwerken zu unterschiedlichen Zeitpunkten. Darüber hinaus wurden KiRis und PiRis in den Kortex lebender Mäuse in akuten und kurzzeitigen chronischen Anwendungen implantiert. Dies ermöglichte die Erfassung von Spiking-Aktivität und typischen lokalen Feldpotentialen (LFPs) bei verschiedenen somatosensorischen und visuellen Reizen.
Zusammenfassend untersucht die vorliegende Studie die Entwicklung, Charakterisierung und Validierung von zwei neuartigen Ansätzen zur Herstellung von flexiblen 3D-Neuroimplantaten, PiRi und KiRi. Wie in den *in vitro* und *in vivo* Studien bewiesen wurde, bieten diese Messplattformen verbesserte Möglichkeiten für die Analyse von neuronalen Störungen, bei denen eine hohe räumliche Auflösung erforderlich ist.

Abstract

3D microelectrode arrays (MEAs) have become increasingly prominent in the field of brain-machine interfaces (BMI), particularly in the context of studying electrophysiological activity. The interaction between these arrays and neural tissue is influenced not only by the electrochemical characteristics of the electrodes, but also by the mechanical and spatial characteristics of the recording platform. While 2D MEA are constrained in their capacity to capture the complexity of neural cell networks, conventional 3D platforms continue to necessitate enhancement with regard to resolution and tissue integration. Thus, the objective of this project was to increase the number of penetrating shanks on a 3D MEA thereby increasing the number of electrodes. Flexible polymers were selected as the primary material in order to minimize insertion damage and foreign body reactions (FBR).

Two approaches to create a 3D structure out of a 2D design were followed: The electrodes were either printed on a flexible substrate (PiRi) or cut out to obtain kirigami structures (KiRi). The first approach utilizes a highly customizable 3D printing process in combination with template-assisted electrodeposition to fabricate up to 400 µm high 3D microelectrodes on a flexible substrate. The latter approach employs a matched-die forming process, enabling the fabrication of up to 512 electrodes distributed across 128 shanks within a single, flexible device, with shank heights reaching up to 1 mm.

In order to test the implants in *in vivo* applications, it is necessary to take into consideration the characteristics of the design and the surgical methods to be employed. Thus, the objective of the research was to demonstrate the implantation feasibility, biocompatibility, long-term stability, and safety of the fabricated implants by performing a number of electrical and mechanical characterizations of the probes.

The advantages inherent in both approaches are evident in the extent and flexibility of customization. This extends to the electrode count and configuration, allowing for the employment of the approaches in a number of different neural applications, such as the retina or the cortex. Healthy and degenerated retinas of rats were used to validate 3D-printed and kirigami electrodes demonstrating how electrophysiological activity differs throughout the 3D space of the retina. In Royal College of Surgeons (RCS) rats, characteristic pathological activity in the form of oscillations was identified and investigated. Following intraretinal insertions, cell stainings were conducted to evaluate the insertion impact, which was found to be low for both implants. Furthermore, in preparation for acute *in vivo* retinal applications, surgical approaches for 3D retinal implants were conducted in a cadaveric setting, including open-sky surgery as well as *pars-plana* implantation. Moreover, the KiRis and PiRis were optimized for use in cortical applications. In human brain slices, epileptic seizures were induced by treating them with modified artificial cerebrospinal fluid (aCSF) (high potassium and low magnesium). 3D recordings revealed seizure-like activity in distinct local networks at different time points. Furthermore, kirigami intraneural implants (KiRi)s and 3D printed intraneural implants (PiRi)s were implanted in the cortex of living mice in acute and short-term chronic settings, allowing the capture of spiking activity in the somatosensory cortex upon whisker stimulation and foot-pinches, and of typical local field potentials (LFP)s in the visual cortex upon visual stimuli, respectively.

In summary, the present study examines the development, characterization and validation of two novel approaches to the fabrication of 3D flexible penetrating neural implants, PiRi and KiRi. As proven with the *in vitro* and *in vivo* studies, these tools offer enhanced capabilities for analyzing neural disorders and disease models where high spatial resolution is required.

Contents

Abbreviations

aCSF	artificial cerebrospinal fluid
AFM	atomic force microscopy
Ag/AgCl	silver/silver chloride
AMD	age-related macular degeneration
AP	action potential
Ar	argon
Au	gold
BBB	blood-brain barrier
BCI	brain computer interface
BiMEA	bidirectional microelectrode array
BMI	brain-machine interface
CAD	computer-aided design
Cal	calretinin
Ca^{2+}	calcium ion
CDB	critical dimension bias
CE	counter electrode
Cl^{-}	chloride ion
CIC	charge injection capacity
CMOS	complementary metal-oxide semiconductor
CNS	central nervous system
CPE	constant phase element
CSC	charge storage capacity
CSF	cerebrospinal fluid
CV	cyclic voltammetry
CVD	chemical vapor deposition
DAPI	4'-6-diamidino-2-phenylindole
DAQ	data acquisition system
DBS	deep brain stimulation
DNA	deoxyribonucleic acid
E	Young's modulus
ECoG	electrocorticogram
EDL	electric double layer
EDOT	3,4-ethylenedioxythiophene
EDS	energy-dispersive X-ray spectroscopy
EEG	electroencephalography
EIS	electrochemical impedance spectroscopy
$\mathbf{E}_{ma}$	maximum anodic potential limit
$\mathbf{E}_{mc}$	maximum cathodic potential limit
EOG	electrooculographic

ERG electroretinography

EthD-1 ethidium homodimer-1

FBR foreign body reactions

FEM finite element method

FFT fast Fourier transformation

fMRI functional magnetic resonance imaging

FIB focused ion beam

FR firing rate

GABA gamma-aminobutyric acid

GCL ganglion cell layer

GFAP glial fibrillary acidic protein

GFP green fluorescent protein

GSA geometric surface area

I second moment of inertia

ICP inductively coupled plasma

ID ictal discharge

IFB interface board

IHL inner Helmholtz layer

INL inner nuclear layer

IPA isopropanol

IPL inner plexiform layer

ipRGC intrinsically photosensitive retinal ganglion cells

Ir iridium

IrOx iridium oxide

ITA insertion trauma area

K bending stiffness

K^+ potassium ion

KiRi kirigami intraneural implants

KiRiCor kirigami intraneural implants for the cortex

KiRiRet kirigami intraneural implants for the retina

HFO high-frequency oscillation

Iba-1 ionized calcium-binding adaptor molecule 1

LED light-emitting diode

LFP local field potentials

LGN lateral geniculate nucleus

MA mask aligner

MCS multi channel system

MEA microelectrode array

Mg^{2+} magnesium ion

MLA mask-less aligner

MUA multi-unit activity

Na^+ sodium ion

NeuN neuron-specific nuclear protein

NFL nerve fiber layer

OHL outer Helmholtz layer

ONL outer nuclear layer

OPA one-photon absorption

OPL outer plexiform layer

PaC parylene-C

PB phosphate buffer

PBS phosphate buffered solution

PCB printed circuit board

P_{cb} critical buckling load

PDMS polydimethylsiloxane

PEA peanut agglutinin biotin

PEB post exposure bake

PEDOT poly(3,4-ethylenedioxythiophene

PEDOT:PSS poly(3,4-ethylenedioxythiophene): poly(4-styrenesulfonate)

PEG polyethylene glycol

PFA paraformaldehyde

PI polyimide

PiRi 3D printed intraneural implants

PNS peripheral nervous system

PL photoreceptor layer

PPX polyparaxylylene

PSS poly(4-styrenesulfonate)

Pt platinum

RA rapidly adapting

RCS Royal College of Surgeons

RD retinal degeneration

rd1 retinal degeneration 1

rd10 retinal degeneration 10

RE reference electrode

RF radio frequency

RGC retinal ganglion cells

RIE reactive ion etching

RMS root mean square

RNA ribonucleid acid

ROI region of interest

RP retinitis pigmentosa

RPE retinal pigment epithelium

PET positron-emission tomography

PRF peak resistance frequency

PSS poly(sodium 4-styrenesulfonate)

SA slowly adapting

SCU signal collector unit

SE standard error (of the mean)

sEEG stereoelectroencephalography

SEM scanning electron microscope

Si silicon

SiO2 silicon dioxide

SIROF sputtered iridium oxide film

SLE seizure-like event

SNR signal-to-noise ratio

SUA single-unit activity

S1 primary somatosensory cortex

Ti titanium

UV ultraviolet

TPA two-photon absorption

$\mathbf{T}_{ph}$ stimulation pulse width

VEP visual evoked potential

VEGF vascular endothelial growth factor

$\mathbf{v}_{in}$ insertion speed

V_m membrane potential

V_{eq} resting potential

V1 primary visual cortex

WE working electrode

WT wild-type

XPS X-ray photoelectron spectroscopy

2PP 2-photon-polymerization

1. Introduction

Neurological disorders affect more than one out of three people worldwide [1]. In general, the term "neurological disorders" is used to describe a subgroup of human disorders characterized by complications affecting the human brain and nervous system, which are considered the most complex organs in the human body. Among the most prevalent neurological disorders are Alzheimer's disease and other forms of dementia, epilepsy, Parkinson's disease, stroke, and migraine. While some neurological conditions are inherent and chronic, others manifest as a result of neurological degeneration, which is a significant concern in today's aging population, or as a consequence of accidents leading to sensory impairment or loss. These neurological conditions can result in brain, cognitive, and, behavioral disorders that impair the patient's ability to perform fundamental activities, such as walking, speaking, learning, and moving. While awareness of these diseases has contributed to a reduction in mortality rates, some chronic neurological disorders can result in permanent and partial disability, as well as an enduring state of suffering [1][2]. While conventional pharmaceutical treatments and surgical procedures [3][4] may reduce the burden of disease, they are accompanied by serious risk of side effects. These include the necessity for repeated treatment and a heightened risk of infection from surgical procedures, which may be perceived as a potential limitation in certain circumstances. Currently, neurological diseases represent a significant global health concern, particularly in the context of a rising life expectancy worldwide [1]. Moreover, despite recent advancements in neuroimaging techniques and the utilization of deep learning models for the processing of large data sets, our comprehension of brain functionality still remains incomplete [2]. Furthermore, for certain neurological conditions and disorders, effective treatments remain unavailable. Therefore, as the most prevalent cause of global disease burden with rising global rates, there is a pressing need for effective prevention, diagnose, treatment, and rehabilitation for disorders affecting the nervous system [1].
Consequently, a substantial number of attempts have been made to provide alternatives to conventional treatments. These include non-pharmaceutical treatments, such as therapeutic music therapy for Alzheimer's and autism [5], gene [6] and stem cell therapies [7][8]. Furthermore, there are ongoing investigations into using nanomaterials, such as quantum dots, metallic or polymeric nanoparticles, or carbon nanotubes, for drug delivery and for bioimaging [9]. Moreover, neurotechnology research has yielded evidence that direct brain interfacing is a viable approach for measuring or modulating nervous system activity. Among neural interfaces, it is important to differentiate between various types. Non-invasive brain recordings (brain computer interface (BCI)), such as electroencephalography (EEG), are distinct from neural implants or prostheses, which are considered implantable and invasive (brain-machine interface (BMI)) [10]. In addition to the widely utilized cochlear implants, which have been implanted in over one million patients [11], and deep brain stimulation (DBS), which has emerged as a highly accepted therapeutic approach for neurological disorders in recent years [12], there are numerous other neural implants. These are currently employed not only in neuroscientific investigations but also in pre-clinical and clinical settings, thereby improving the quality of life for patients. The applications of neural interfaces span a range of neuroscientific investigations, including the neural mechanisms underlying memory and behavior, as well as the study of abnormal brain signals, such as epileptic seizures [13] or using neural stimulators in patients with Parkinson [14]. Additionally, BMIs were employed for the functional restoration of sensory abilities, e.g. to restore motor function following spinal cord injury through the implantation of paddle electrodes within the spinal cord [15] and to partially restore vision in patients with retinal degeneration through the use of retinal implants [16]. Consequently,

during the last decades, neural interface technologies were capable of discerning details regarding the functionality or dysfunction of the brain through the analysis of recorded neural activity. Thereafter, these information were employed for therapeutic purposes enhancing the quality of life for numerous patients with neurological disorders in ways that were not feasible with traditional treatments [17].

In addition to an electronic interface and signal processing unit, MEAs represent a crucial element of neural interfaces. Microelectrodes, developed through the process of "microfabrication", facilitate the transmission of electrical pulses to stimulate neural tissue and enable the detection of changes in current, impedance, and potential as the nervous system responds. Consequently, MEAs are a valuable instrument for acquiring a fundamental understanding of the brain's functionality through high-resolution recording and stimulation. The flexibility or rigidity of MEAs is contingent upon their substrate material, enabling adaptation to diverse experimental configurations [18][19]. MEAs can be arranged in a grid configuration, thereby covering the surface of neural tissue. For example, they have been employed to examine epileptic activity through the use of electrocorticogram (ECoG) [20], or to provide sensory input through electrical stimulation of the epiretinal surface in patients with retinal degenerative diseases [21]. Nevertheless, further investigation is required to ascertain the defining characteristics of the underlying pathological dysfunctions. For instance, there is a lack of understanding with regard to the mechanisms of seizure spread and onset in deeper layers of epileptic patients [22] and the remodeling of retinal layers following photoreceptor loss [23]. The cortex and retina are sophisticated 3D neural spaces, the further study of which would facilitate enhanced diagnostic capabilities and the development of more efficacious treatments for the aforementioned neurological disorders and degeneration. It would therefore be advantageous to gain access to the 3D space of nervous tissues, which encompasses not only the surface but also the laminar or multilayered structured nervous tissues. This can be achieved via the implementation of a spatial arrangement of penetrating or protruding microelectrodes or shanks containing multiple electrodes, which hereafter will be referred to as 3D MEAs.

Over the past five decades, a variety of 3D neural implants have been developed with the objective of penetrating neural tissue to reach deeper neural layers. These implants can be classified into two main categories: silicon (Si)-based and thin-film polymer-based. "Utah" and "Michigan-like" arrays are the gold standard in the field of invasive neural implants, belonging to the former category of probes. Utah arrays are composed of Si needles with metal-based or conductive polymer tips and a biocompatible polymer encapsulation, forming a grid of needles with equal or oblique heights and depths [24]. Standard 2D Michigan arrays, comprising multiple gold (Au) electrodes on Si-based shanks [25], permit the formation of 3D neural implants through the stacking and overlaying of 2D arrays with predefined spacers [26][27][28]. While Utah and stacked Michigan-like arrays can penetrate tissue to reach deeper neurons, they typically elicit a strong FBR during chronic implantation due to the mechanical mismatch between the stiff Si MEAs and the soft neural tissue [29][30].

Significant advances have been made in recent years with regard to the development of softer and more flexible materials and micro-scale electrodes that can be used in a 3D fashion, thereby reducing the occurrence of FBR in comparison to rigid 3D microelectrodes. Among these techniques, penetrating threads or shanks are implanted individually to cover the 3D neural space [31][32]. This approach can result in prolonged implantation and surgical procedures, as each thread must be addressed individually, with difficulties in tracking the position of individual threads. In order to overcome this challenge, various research groups have proposed the use of flexible Michigan-style arrays [33] and kirigami-based methodologies as a means of achieving 3D flexible neural implants. The term "kirigami" is derived from the Japanese art of cutting and folding paper. The cut-and-fold principle is then applied to micromachining, whereby a 2D flexible MEA is initially processed and subsequently a 3D structure is generated from the 2D MEA through either i) mag-

netic fields [34][35], ii) mechanical [36][37], or iii) electrostatic actuation [38]. While existing 3D flexible kirigami-based MEA approaches have successfully enabled 3D neural sampling - from *in vitro* 3D neuronal cultures [36] to simultaneous cortical and intracortical monitoring *in vivo* [37] - these methods either involve the use of hazardous materials and strong magnetic fields or are manual, time-consuming processes that do not allow for the folding of a large number of shanks simultaneously.
In light of the aforementioned challenges, this study addresses the development of flexible 3D neural microelectrodes with the objective of utilizing them in *in vivo* applications, with the ultimate goal of interacting with the 3D space of neural tissue. This study focuses on two specific applications: the cortex and the retina. From the perspective of fabrication, two approaches are employed to create a 3D structure from a 2D design (Figure 1.1):

- A: flexible kirigami structures
- B: 3D printed electrodes on flexible substrates using 2PP

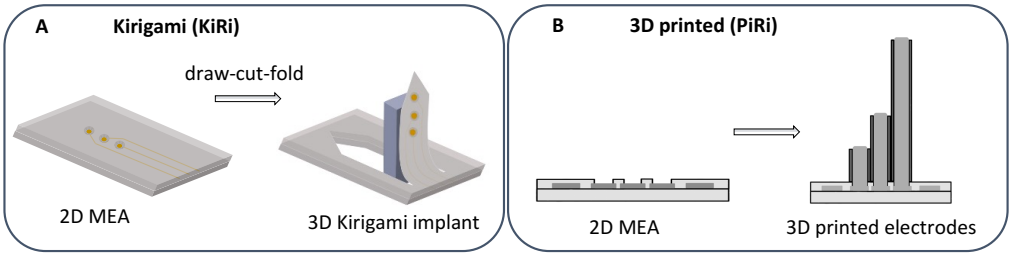

Figure 1.1.: Approaches to develop 3D neural implants: A) Kirigami and B) 3D printed electrodes.

In order to overcome the spatial sampling and manufacturing limitations of the presented kirigami methods, a key-lock principle was employed during a matched-die forming process to develop a flexible, biocompatible and high-resolution kirigami MEA (Method A). This approach enabled the fabrication of customizable and scalable 3D flexible MEAs with up to 128 shanks with a length of up to 1000 µm, offering a rapid and reproducible method. In the case of method B, 2PP was employed, which is widely regarded as one of the most adaptable and precise processes for the manufacturing of micro and nano 3D objects. The resolution achievable with this process is approximately 100 nm, which is appropriate for neural applications, as it enables the reliable production of structures of arbitrary geometry on the scale of individual cells or even structures below the cellular level. In addition to the high resolution and the possibility of high aspect ratio achieved by the printing process, commercially available photoresins have a Young's modulus in the gigapascal range. Furthermore, there are biocompatible and non-cytotoxic resins available [39][40][41]. In this study, 2PP printing is combined with thin film technology and template-assisted electrodeposition to achieve a 3D flexible MEA with pillar electrodes reaching a height of 400 µm and a diameter of only 12 µm.
To test the novel implants *in vivo*, it is essential to consider several factors, including the characteristics of the implant design and the surgical techniques to be employed. Moreover, the objective is to demonstrate the biocompatibility, long-term stability, and safety of the manufactured implants through the execution of multiple electrical and mechanical characterizations of the probes, in addition to *in vitro* and cadaveric validations.
This thesis provides an overview of the fundamental concepts of neuroscience and an examination of neural interfaces, including an analysis of the various types, applications, and requirements (Chapter 2). After describing the applied materials and methods (Chapter 3), the fabrication of kirigami and 3D-printed implants, which were developed throughout the course of this project, will

be presented in Chapter 4. Following this, the electrical, mechanical, and long-term performance of the devices is addressed (Chapter 5). Then, the findings of studies conducted in the context of retinal applications are presented. These studies encompass a range of methodologies, from cadaveric surgical trials to *in vitro* validations utilizing explanted wild-type (WT) and diseased rodent retinas (Chapter 6). Chapter 7 presents the findings of experiments conducted on cortical applications with cultured and acute human brain slices and *in vivo* cortex of rodents. The final section of this work offers a synthesis of the analysis of the performance and applications of the 3D devices, an evaluation of their current research impact, and a discussion of prospects for their future development (Chapter 8).

2. Theoretical background

2.1. Fundamentals of neuroscience

In order to gain a deeper understanding of the most complex human organ, the brain, scientists often employ a reduction approach breaking down the complexity into elementary parts. Molecular neuroscience, therefore, describes the most elementary functionalities that are crucial for understanding cellular neuroscience. This field of study focuses on how the molecules work together to create functional units, the neurons, and how they interact with one another. Subsequently, the neurons form networks to perform complex tasks such as vision or movement. These systems, such as the "visual system" or the "motor system," have specific neural circuits within the brain that analyze and process sensory information and act accordingly. The next levels of complexity are understanding behavior or even cognitive mechanisms like self-awareness, which is arguably the greatest challenge [42].
The following sections present an overview of the fundamental principles of molecular and cellular neuroscience, as well as the architecture of the nervous system and human brain. The visual and somatosensory systems, which were the primary focus of the conducted electrophysiological experiments, are explained in more detail. Additionally, a brief overview of the neurological disorders, that were in the focus of this study, is provided.

2.1.1. Principles of molecular and cellular neuroscience

There are two main types of cells at an approximately equal number in the nervous systems: Neurons and glia, which both are subdivided into many different types. While neurons sense, communicate and command, glia cells support and nourish them [42].

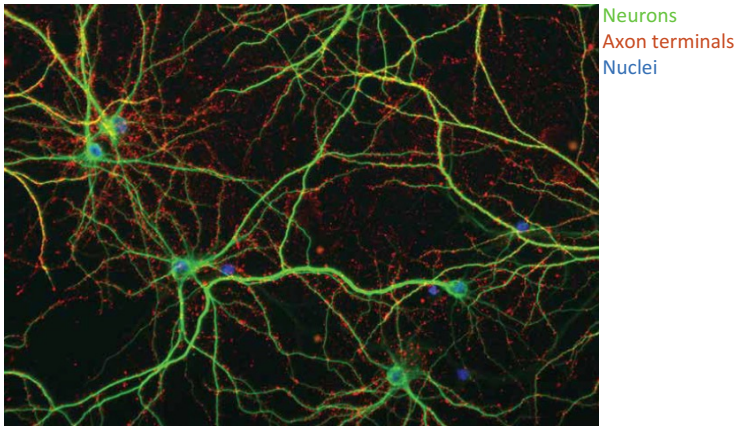

Figure 2.1.: Fluorescent image of stained neurons (green), nuclei (blue) and synapses (red-orange) shows that the dendrites of neurons contain a high number of synapses [42].

The neuron is composed of a soma and extensive branching structures, the axons and dendrites, which enable communication with other neurons (Figure 2.1 and Figure 2.2A). The soma

contains cell-typical organelles. The nucleus, which is 5-10 µm thick, contains chromosomes with deoxyribonucleic acid (DNA). The endoplasmic reticulum and golgi apparatus are primarily responsible for protein synthesis and storage. Mitochondria generate energy to power the cells. The neuronal membrane serves to separate the neuron from the external environment, and contains protein pumps and pores that facilitate the exchange of substances between the two environments. Nevertheless, it is the axon, a distinctive and highly specialized neuronal structure, that distinguishes the neuron from other cells. Axons branch to facilitate communication with other cells and can extend to lengths exceeding 1 m. Their starts are called axon hillock, where an action potential (AP) is generated, and their ends are the axon terminals where a synapse connects to the subsequent cell [42].

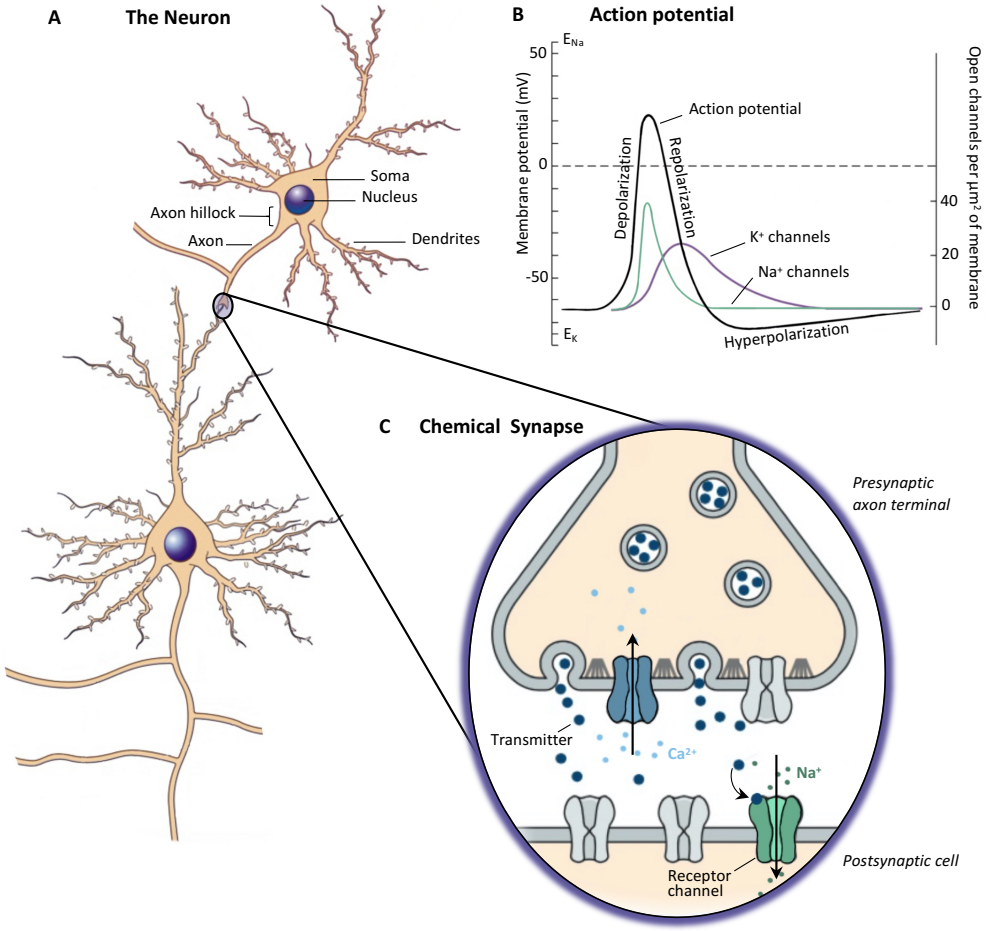

Figure 2.2.: The neuron (A), action potential (B) and chemical synapse (C) (adapted from [42][43]).

Action potentials are initiated when a sufficient stimulus causes membrane potential (V_m) of an electrically excitable cell to reach a specific threshold value, typically –55 mV (see Figure 2.2B). Once the threshold is exceeded, an AP will occur in accordance with the "all or none" law. During the process of depolarization, the opening of sodium ion (Na^+) channels occurs rapidly, resulting

in an influx of Na^+. This influx subsequently triggers the opening of additional sodium voltage-gated channels. Consequently, V_m is driven above zero until the equilibrium potential of Na^+ is reached, resulting in an overshoot. Similarly, potassium ion (K^+) channels are stimulated by depolarization, but open approximately 1 ms later, in conjunction with the closing of Na^+ channels. During the following repolarization phase, K^+ flow out of the cell driving V_m towards the equilibrium potential of potassium at -90 mV, resulting in an undershoot. Subsequently, K^+ channels close, Na^+ channels reset, and the membrane returns to resting value of resting potential (V_{eq}) = -70 mV. The refractory period restricts the upper limit of the firing frequency. During the absolute refractory period, when the Na^+ channels are inactive, a subsequent AP is not possible. During the relative refractory period, when $V_m < V_{eq}$, larger stimuli are needed to depolarize the membrane [44]. The exact threshold, amplitude and time course of an AP are influenced not only by the ion channels and concentrations, but also by the capacitance, resistance and geometry of the cell. Thus, the shape of an AP, or often also referred to as spike, is highly dependent on the cell-type [45]. In neurons, the AP travels along the length of an axon to transmit the stimuli to the subsequent cell [45].

The synapse is defined as a contact structure utilized for the transmission of a chemical or electrical signal from one neuron to another (interneuronal synapses) or to another target cell. Here, the presynaptic side contacts the postsynaptic side of another neuron's dendrite or soma. In chemical synapses (Figure 2.2C), transfer of information (synaptic transmission) between the two sides (synaptic cleft) occurs through the conversion of electrical impulses into chemical signals. More specifically, the voltage-gated calcium ion (Ca^{2+}) channel open when an AP reaches the axon terminal. Ca^{2+} causes the release of neurotransmitters from synaptic vesicles. The neurotransmitters then bind to specific protein receptors at the postsynaptic membrane which results in an inhibitory or excitatory postsynaptic potential. In electrical synapses, the direct transfer of ionic current is permitted via gap junctions which bridge the cytoplasm of two cells. Electrical synapses are predominantly located in brain regions where a high level of synchronization between neurons is observed [42].

2.1.2. The architecture of the nervous system

The nervous system is comprised of neurons that function and communicate in order to enable a range of essential human processes, including perception, audition, sensation, movement, memory, and dreaming. It consists of two distinct parts: the central nervous system (CNS), which encompasses the brain and spinal cord, and the peripheral nervous system (PNS). The latter refers to the remainder of the nervous system, including the nerves that are under voluntary control (somatic PNS), such as the somatic motor axons responsible for muscle contraction, and the autonomic nervous system (visceral PNS), which includes neurons that innervate organs or blood vessels. The CNS is not in direct contact with the bones, but circumvented by the meninges, a membrane system that consists of the dura mater, arachnoid membrane and the pia mater. Between the thin pia mater and the arachnoid, there is the cerebrospinal fluid (CSF) which is a salty liquid that provides nourishment and protects the brain from mechanical injury [42].

The brain is organized into functionally specific areas, within which the number and types of neurons vary. The specific interconnection of neurons in each area is responsible for the resulting functional organization. The brain is composed of four primary sections: the brain stem, which is connected to the spinal cord and plays a crucial role in processing sensory information and reflexes; the cerebellum, which primarily modulates muscle movement; the diencephalon, which contains the thalamus and the hypothalamus; and the cerebrum, which comprises two cerebral hemispheres and is the largest part of the brain. The thalamus is responsible for processing the

majority of information reaching the cerebral cortex from the CNS. In contrast, the hypothalamus regulates autonomic, endocrine, and visceral functions [43].

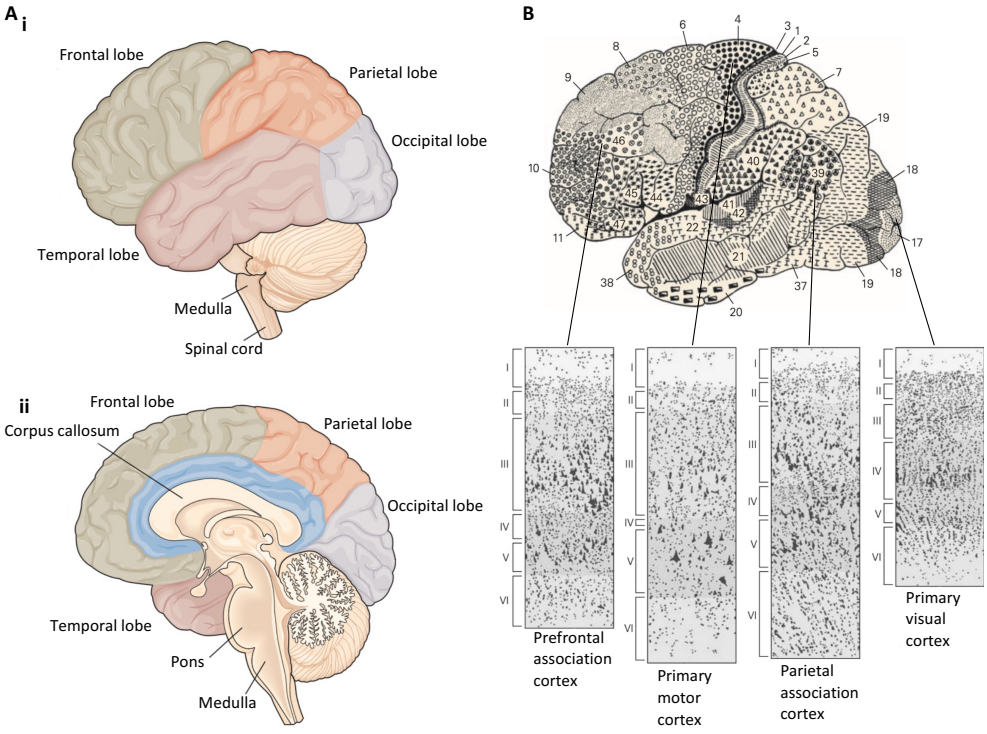

Figure 2.3.: The major lobes (A) and Brodmann's areas of the cortex (B). A) Lateral (i) and medial (ii) view of the major lobes of the cortex. B) Brodmann's division of the human cerebral cortex into 52 discrete functional areas, Nissl stainings of certain areas are shown (adapted from [43]).

The cerebral cortex is the outer layer of the cerebral hemisphere and is subdivided into four lobes - frontal, parietal, temporal, and occipital -, which encompass discrete functional subregions responsible for perception, motor and cognitive functions, memory, and emotion (Figure 2.3A). While the cerebral cortex on both sides of the brain exhibits general similarities, distinct functional characteristics are observed in specific regions of the cortex on each side. The neocortex is the region of the cerebral cortex that is in closest proximity to the surface. The neocortex receives the majority of its input from the thalamus, as well as from other cortical regions in both hemispheres. Meanwhile, it primarily transmits output to other regions of the neocortex, the thalamus, and the spinal cord. The input-output relationships in the neocortex are organized through the neural structure in layers and columns, which increases computational efficiency. The majority of the neocortex contains six layers, with clearly defined input and output paths. These layers are numbered from I to VI, commencing at the outer surface (pia mater) of the cortex and continuing towards the white matter. Layer I (molecular layer) is primary composed of dentrites and axons. The majority of cells in layer II (external granule layer) and III (external pyramidal layer) are small pyramidal cells which primary communicate intracortically. In contrast, the small spherical neurons of layer IV (internal granule layer) receive the majority of sensory information from the thalamus. The pyramidal cells of layer V (internal pyramidal layer) contain large pyramidal cells which mainly output to other cortical layers and subcortical structures. Layer VI (multiform layer) contains mostly

axons to and from cortical areas. While the layers are distinguished by their specific cell types and densities, their dendrites extend to neighboring layers, influencing the inputs received from these regions. The thicknesses of individual layers and the specifics of their structural organization demonstrate variability throughout the cortex. Figure 2.3B illustrates Nissl stainings that elucidate the variations in the layered structure of the cortex across different cortical areas. A number of regions delineated by Brodmann have been identified as regulators of discrete cerebral functions (Figure 2.3B). This framework remains a prominent topic in contemporary neuroscience and is subject to ongoing refinement [42][43].

Neural systems are composed of multiple anatomical structures distributed throughout the brain, which operate in a cooperative manner. The CNS is comprised of multiple neural systems, including those responsible for sensory perception, motor control, and language processing, which operate independently. Neural systems are hierarchically organized, with primary sensory areas conveying information to higher-order areas. Neurons in these areas selectively encode specific information, thereby representing complex information. The arrangement of the hierarchy is topographical, whereby inputs from neighboring peripheral receptive surfaces are projected to the cortex. Typically, sensory information crosses to the contralateral side of the body on its way to the cerebral cortex. Consequently, each hemisphere is primarily concerned with sensory and motor processes from the contralateral side of the body. The following sections will provide a detailed description of two neural systems: the visual and somatosensory system [42].

2.1.3. The visual system

Sight is one of the most crucial senses for humans and animals alike, enabling to navigate the surroundings. The visual system is comprised of two primary components: the optical part of the eye (Figure 2.4A), which picks up light, focuses an image and is often compared to a camera, and the neurological segment, which commences at the retina (Figure 2.4B), where photoreceptor cells transform light into electrochemical signals and pass the preprocessed information on following the visual pathway (Figure 2.4C) to the visual cortex of the brain via the optic nerve [45].

The eyeball

The eyeball (Figure 2.4A) is located in the bony orbit and is moved by six external eye muscles, e. g. the lateral and medical rectus. The cooperative task of the cornea, iris, and lens is to focus on an image. More specifically, light is refracted by the lens and cornea to a focal point (fovea centralis in the middle of the macula lutea) on the back of the eye, the retinal surface. Zonular fibers tense and ciliary muscles relax to flatten the lens which sharpens the vision for far vision while the opposite muscle behavior rounds the shape of the lens for near vision. Additionally, the aperture is constrained by intraocular muscles of the iris narrowing and enlarging the pupil, which regulates the light intensity. The light then passes unobstructed through the aqueous humor in the anterior chamber and the vitreous body in the posterior chamber eventually arriving at the target destination within the retina: the light-sensitive photoreceptor cells where light is converted into electrochemical signals [46]. The aqueous humor, which is secreted by the ciliary epithelium in the ciliary body and drained in the canal of Schlemm, helps to keep the eye's pressure. A disruption of the drainage system can result in elevated intraocular pressure, which can subsequently lead to the development of glaucoma. This condition can cause damage to the axons of the ganglion cells and the optic nerve [45]. The optic disc is the blind spot of the eye where the optic nerve and the central retinal artery, which runs inferior the optic nerve, exit the eyeball [46].

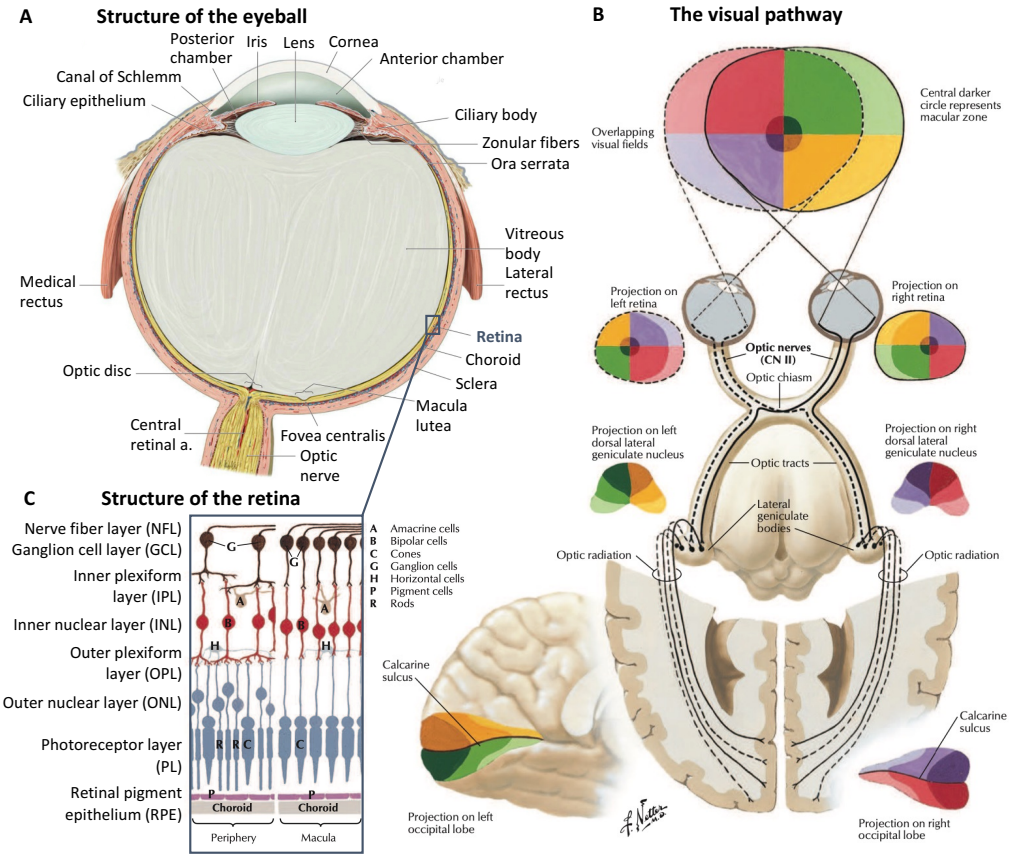

Figure 2.4.: Schematic of the visual system. A) Structure of the eyeball (adapted from [46]). B) The visual pathway [47]. C) Structure of the retina (adapted from [47]).

The retina

The retina (Figure 2.4C), an around 200 µm thick layered neural structure, acts as the first neurological segment in the visual pathway and is thereby a component of the central nervous system (CNS) which preprocesses visual information. It is composed of five main cell types: photoreceptors for converting light into electrochemical signals and four other types of neurons to process the information (ganglion, bipolar, horizontal and amacrine cells). The human eye contains about 100 x 10^6 photoreceptors while there are only 1 x 10^6 ganglion cells, which generate the output of the retina with their axons that combine to form the optic nerve. This implies that a high level of convergence of information must be handled. This is primarily accomplished by bipolar cells in the inner nuclear layer (INL) through direct radial connections between photoreceptors and ganglion cells, as well as horizontal and amacrine cells, which spread mainly in a horizontal direction. More specifically, horizontal cells establish connections between photoreceptors and bipolar cells within the outer plexiform layer (OPL), while amacrine cells facilitate connections between bipolar and ganglion cells within the inner plexiform layer (IPL).The thin and dense nature of the retina results in short distances between neurons, with potentials propagating through a cascade of chemical and electrical events. When the signal reaches the ganglion cells, a AP is formed when a threshold is reached to fasten the visual information spread along their axons to the thalamus. In fact,

the retina is far more complex than this description suggests. For instance, each of the four neurons can be differentiated into 10 to 20 subtypes with different physiological and morphological characteristics [45].

The photoreceptors are located at the outer surface of the retina in the photoreceptor layer (PL) which is in close proximity to the retinal pigment epithelium (RPE) (see Figure 2.4C). Thus, light must first pass through all retinal layers before reaching the photoreceptors that are responsible for the phototransduction process, which comprises a sequence of chemical and electrical processes to create a response to light. There are two main types of photoreceptors: the rods and cones, which have a ratio of approximately 16:1. The human retina contains one type of rod for monochromatic dark-adapted vision, while there are three types of cones for color-sensitive vision in bright conditions (for long (red), middle (green), and short (blue) wavelengths). Additionally, in the mammalian retina, there is a third type of light-sensitive cells, the intrinsically photosensitive retinal ganglion cells (ipRGC) which also express a photopigment. In the fovea, the photoreceptor - ganglion cell ratio is relatively low, indicating that the majority of the photoreceptors synapse with a single bipolar cell, which in turn synapses with a single ganglion cell (small receptive field). Conversely, in the periphery, the ratio is high, resulting in a large receptive field (see Figure 2.4B). A large receptive field is associated with low resolution but high sensitivity, while a small receptive field is associated with the opposite characteristics. In the fovea, there are only cones while there are few toward the periphery where the density of rods increases. Rods and cones are elongated cells composed of a synaptic terminal, an inner and an outer segment. The inner segment regulates the metabolism and the membrane potential, which is passed on by the synaptic terminal to postsynaptic neurons via the release of neurotransmitters (here: glutamate). The outer segment of the rods is the light-sensitive region and holds approximately 1,000 disks, which are invaginations of the membrane that increase the surface area. Similar membrane folds are present within the cones. The membrane folds contain rhodopsin in rods and related molecules in cones which are the photopigments that are activated by photons hitting the retina. Similar to other sensory receptors, photoreceptors use electrical events (receptor potentials) to carry a signal from the outer segment to their synapse because chemical messengers are too slow. When photons are absorbed, cation channels in the outer segment close decreasing the conductance of the cell membrane. Concurrently, K^+ channel in the inner segment remain open allowing the outward flow of K^+. This leads to hyperpolarization of the cell (membrane potential (V_m) < resting potential (V_{eq})) which scales with light intensity. Thus, a flash of light causes a decrease in glutamate release from the synapse to the postsynaptic neuron. On the contrary, photoreceptors depolarize and release more glutamate in dark conditions [42][45].

The ON and OFF pathway is an example for parallel information processing, a critical component of visual reception, as it facilitates fast and efficient processing of information from multiple environmental features. Information is divided into pathways such as the ON/OFF pathway, which originates at the ON/OFF bipolar cells that synapse with the photoreceptors. The OFF bipolar cells contain ionotropic glutamate receptors which depolarize when glutamate is released during dark condition. On the contrary, the ON bipolar cells hyperpolarize following glutamate binding via their metabotropic glutamate receptors [48]. The bipolar cells then directly synapse with the ganglion cells. Here, the ON and OFF reactions are transferred to 15 - 20 types of ganglion cells. The exact number depends on the means of classification and is discussed controversially [49]. However, retinal ganglion cells (RGC)s can mainly be divided into ON, OFF and ON-OFF cells, which are activated similarly to the bipolar cells with light increase, decrease or both, respectively [48][50]. Within those types there are sustained responses with regular spiking activity as well as transient responses with spiking activity at the ON and OFF set of the stimuli (Figure 2.5A). The RGC outputs are the result of integrated excitatory input from bipolar cells as well as inhibitory

input from amacrine and horizontal cells [50]. Many of the RGCs have center-surround receptive fields, which can be simulated by two overlaying Gaussian functions with opposite effects (Figure 2.5B$_i$). The small center originates from the bipolar cell input, while the larger surround properties are defined by the horizontal and amacrine cells. The resulting receptive field then depends on the size and location of the stimulus [50]. An example is shown in Figure 2.5B$_{ii}$, where a ganglion cell with ON center and OFF surround reacts with an increase in spiking activity when the center is hit by the stimulus. On the contrary, the spiking frequency decreases when the stimulus hits the OFF surround. The ON and OFF signals then start to combine in the brain following the visual pathway (Figure 2.4B) [42][48][51].

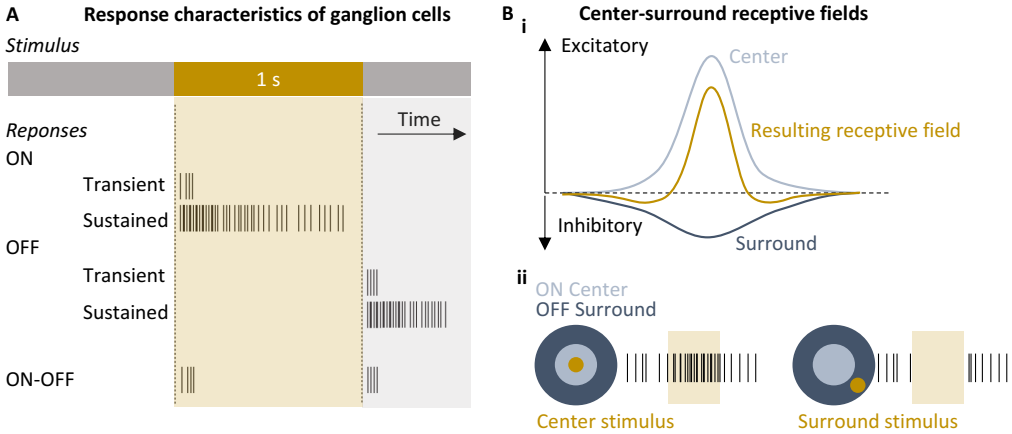

Figure 2.5.: Characteristics of ganglion cell responses. A) Response characteristics from ON, OFF and ON-OFF sustained and transient ganglion cells (adapted from [50]). B) Center surround receptive fields. The resulting receptive field results from an excitatory and an inhibitory response (i, adapted from [50]) depending on the center and surround characteristics (ii, adapted from [51]).

The central visual system

A total of 1.5 million axons of the RGCs collectively form the optic nerve, which exits the retina at the blind spot. In comparison to the 120 million photoreceptors, the information has undergone a significant convergence. At the optic chiasm, the two optic nerves from both eyes intermingle and are sorted into two optic tracts. Approximately 50% of the axons cross to the contralateral hemisphere. Consequently, the optic tracts contain information from the contralateral visual field (Figure 2.4B). In the optic nerve, the topography is retained, with a retinotrophic map projected to the lateral geniculate nucleus (LGN) of the thalamus, where the majority of axons terminate [42][51].

The LGN is divided into six layers, labeled from 1 to 6 in a ventral to dorsal sequence. In layer 1 and 2 (magnocellular layers), which are populated by large neurons, large RGC terminate corresponding to large receptive fields, that are sensitive to contrasts and movements. In contrast, layer 3 and 6 (parvocellular layers) contain small cells, which respond to small receptive fields with low contrast sensitivity. The axons from the contralateral eye terminate in layers 1, 4, and 6, while those from the ipsilateral eye terminate in layers 2, 3, and 5. The retinotropic structure is again maintained through the projection of the LGN to the primary visual cortex (V1) via the optic radiation. Additionally, the LGN receives input from the other parts of the thalamus and the brain stem as well as feedback from the V1 [42][51].

The primary visual cortex is located in the occipital lobe and it is the first cortical area where visual information is converged. V1 contains a wide variety of cells, mainly pyramidal and spiny stellate cells, which are organized in layers I to VI (dorsal to ventral) like other cortical areas (Figure 2.3B). However, layer IV is typically subdivided into IVA, IVB, IVCα and IVCβ due to its complexity and high population of neurons. Spiny stellate cells, which generally connect locally within V1, are primarily contained in IVC, whereas outside of IVC there are mostly pyramidal cells, which output to other parts of the brain. Within the V1, the retinotopic organization is preserved by the organization of neurons into columns, whereby neighboring cells in V1 exhibit receptive fields that correspond to adjacent portions of the visual field. Columns depend on the ocular dominance as well as on the orientation preference of the cells. The inputs of ocular-dominance-columns arise from different layers of the LGN. The projections from LGN to V1 are illustrated in Figure 2.6A. Magnocellular LGN neurons project primarily to layer IVCα, and parvocellular LGN neurons project to layer IVCβ. Additionally, alternating layers of LGN receive input from retinal ganglion cells located in either the ipsilateral or contralateral retina, which is conserved in the inputs from LGN to V1. From IVC stellate cells project axons radial to layers IVB and III. Due to the alternating input of the ipsilateral and contralateral eye in IVC from the respective layers and the radial projection, the neurons are organized into alternating bands either dominated by the left or the right eye. A computational model of V1 is illustrated in Figure 2.6B. It shows that neurons with orientation selectivity are additionally grouped into columns. Here, the neurons of V1 of the same column respond to elongated bars of light where the orientation of that bar is crucial. The orientation and ocular dominance columns are arranged in a criss-cross pattern across the cortical surface. Alongside the columns are blobs, which are associated with color-selective neurons and contain fewer orientation-selective cells. Thus, blobs convey information from surfaces rather than edges. The columnar organization of V1 increases the speed of information processing due to the short distance between neurons of similar function, where they can share inputs. Thereby, the absolute number of neurons needed to extract certain features from the visual information is minimal [42][43][51].

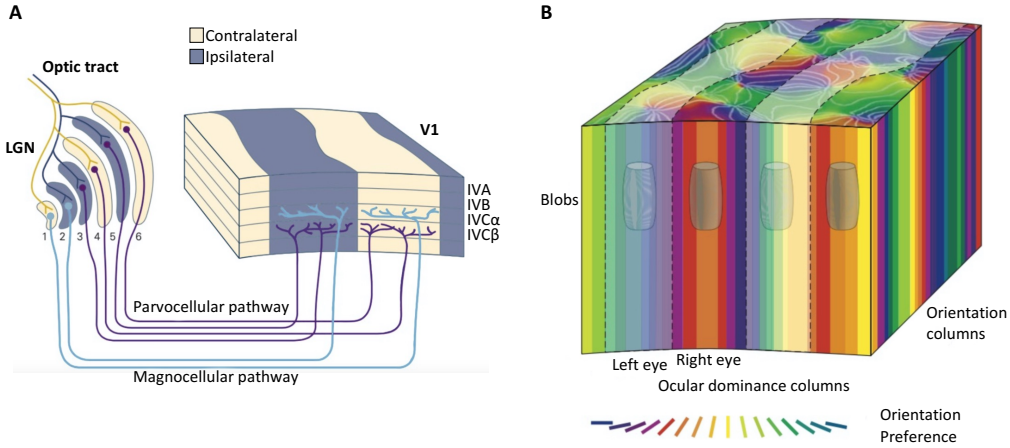

Figure 2.6.: Projections from the LGN to V1 (A) and a computational model of V1 (B). A) The LGN is a laminated structure comprising four parvocellular layers (layers 3 to 6) and two magnocellular layers (layers 1 and 2). The contralateral eye projects to layers 1, 4, and 6, whereas the ipsilateral eye sends input to layers 2, 3, and 5. The parvocellular and magnocellular inputs to the primary visual cortex are received in discrete sublayers. The parvocellular layers project to layer IVCβ, while the magnocellular layers project to layer IVCα. Moreover, the afferents from the ipsilateral and contralateral layers of the LGN are segregated into alternating columns of ocular dominance. B) This cortical computational module represents a piece of cortical tissue, 1 mm in diameter. It contains an orientation hypercolumn, a cycle of left- and right-eye ocular-dominance columns, and blobs with interblobs. This module is repeated hundreds of times to cover the visual field (adapted from [43]).

Beyond V1 distinct cortical regions engage in parallel processing of selective visual attributes. The specific contribution of these areas to visual processing remains unclear. Nevertheless, two principal large-scale cortical pathways of information processing have been identified: The dorsal and the ventral stream. The first pathway extends dorsally to the parietal lobe and is primarily engaged in motion processing, whereas the latter pathway extends to the temporal lobe and is predominantly involved in recognition and perception. Subsequently, the processed information, manifested as cortical activity associated with orientation, movement, color, and object location, must be synthesized. High-level visual processing entails the integration of information, incorporating emotional and memory-related factors, to identify meaningful attributes, thereby facilitating a unified perception of the environment. Consequently, the complex task of object perception is a combination of vision and cognition [43].

2.1.4. The somatosensory system

The somatosensory system enables the human body to perceive a range of internal and external stimuli, including touch, pain, temperature, and pressure. In contrast to other sensory systems, the receptors are distributed throughout the body, rather than concentrated at specialized locations such as the retina or the cochlea. Moreover, the somatosensory system is capable of responding to a multitude of stimuli, which can be further classified into a greater number of categories. Among these, pain is the sensation that is triggered by nociceptors when stimuli reach a threshold level that can damage the tissue. Furthermore, itch shares certain characteristics with pain caused by histamine receptors. Thermal sensation is the result of a discrepancy between the external temperature and the temperature registered by thermal receptors, which are sensitive to cold, cool, warm, and hot temperatures. Mechanoreceptors in muscles and joints provide information about the body's posture and movements, which is crucial for motor control. Visceral receptors regulate essential survival behaviors, such as breathing, hunger, and thirst, by sensing the status of internal organs. The following sections will examine the sensation of touch in greater detail as an exemplary process within the somatosensory system [42][43].

Mechanoreceptors and the sense of touch

Mechanoreceptors are capable of detecting physical deformation of the tissue in which they are located. The receptor protein is deformed by mechanical stimulation, which results in lipid tension and consequently in the opening of stretch-sensitive ion channels. Consequently, an increase in the flow of Na^+ and Ca^{2+} then results in the depolarization of the receptor neuron. In other types of mechanoreceptors, channels are activated by structural proteins that are linked to the channels themselves, or by proteins that link to a second messenger and thereby act as force sensors in the tissue membrane. In total, human skin hosts eight types of mechanoreceptors, four of which are found in the hands and feet. The combined synthesized information from these receptors contributes to the perception of touch. The specific manner in which each individual receptor responds is distinctive and determined by a number of factors, including its morphology, the pattern of innervation to which it is sensitive, and its depth within the skin. Accordingly, they can be innervated by either slowly adapting (SA) or rapidly adapting (RA) fibers. The former is responsible for detecting skin deformation and pressure, while the latter is involved in the perception of motion and vibration. Individual mechanoreceptor fibers transmit data from a restricted portion of the skin known as the receptive field. Furthermore, the mechanoreceptors are distinguished by the characteristics of their receptive fields. The rapidly (RA1, Meisser corpuscles) and slowly (SA1, Merkel cells) adapting fibers of type 1 have small receptive fields with high sensitivity and are located in the superficial layers of the skin (Figure 2.7A$_i$). In contrast, the type 2 fibers - RA2 (Pascinian corpuscle) and SA2 (Ruffini ending) - correspond to large receptive fields and are

found in deeper layers (Figure 2.7A$_{ii}$) [42][43].

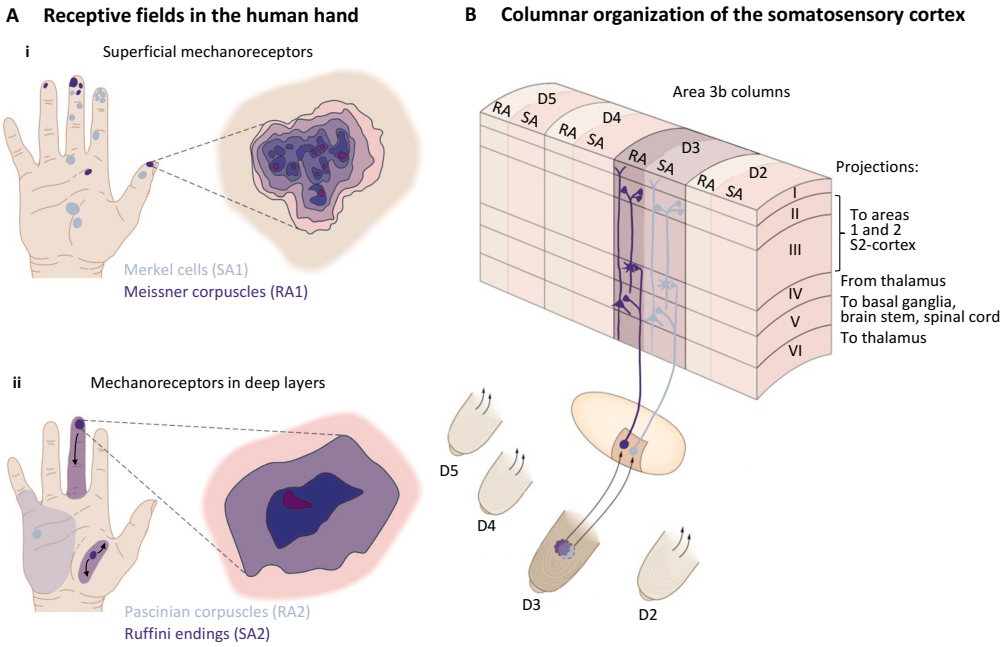

Figure 2.7.: A) Receptive fields in the human hand are colored indicating the receptive fields of respective mechanoreceptors. The receptive fields in the superficial layers (i) are small patches, while the ones of mechanoreceptors in deeper layers (ii) emcompass wider regions (light patches) with strongest responses directly over the receptors (dark patches). SA2 fibers are activated by stretching the skin, which is indicated by arrows. The pressure sensitivity of the receptive fields depends on the underlying receptor. The receptive field of an RA1 fibers (i) has a high amount of high sensitivity areas (dark spots), which indicate the positions of the small Meissner corpuscles. On the contrary, the receptive field of RA2 (ii) has a single high sensitive region close to the position of the large Pascinian corpuscle. SA1 and SA2 fibers possess similar receptive fields according to RA1 and RA2 (adapted from [43]). **B) Columnar organization of the somatosensory cortex**, where each column receives input from the respective part of the body (here from slowly and rapidly adapting fibers in the fingers D2 - D5). The projections of the layers of the somatosensory cortex are indicated, where each layer sends or receives information to or from other areas of the brain (adapted from [43]).

The central touch system

The central touch system is composed of the dorsal column tracts which belong to the spinal cord, as well as parts of the brain stem, thalamus and cerebral cortex. Thus, when tactile information reaches the primary somatosensory cortex (S1), the information delivered by the neurons was already synthesized by the preceding stages.

The primary somatosensory cortex (S1) stretches out through four Brodmann's areas (1, 2, 3a and 3b), which are interconnected to enable serial and parallel processing of somatosensory information. In S1, the cortical neurons have larger receptive fields in comparison to the mechanoreceptive fibers. To illustrate, the type 1 fibers in the fingertips are tiny regions, whereas the cortical neurons in S1 that receive those inputs each encompass areas exceeding that of an entire fingertip. Thus, the overall organization of S1 areas reflects the functional significance of different body regions in the perception of touch. Furthermore, the receptive fields in S1 are characteristically composed of excitatory zones circumscribed by inhibitory zones, which guarantee that only meaningful information is conveyed by suppressing irrelevant stimuli. Similar to V1, S1 is organized in

vertical columns, each of which encompasses all six cortical layers (Figure 2.7B). The neurons in a column typically engage in the processing of a singular subtype of sensory information, such as pressure or vibration, depending on the pathway that originated from the respective mechanoreceptive fibers. Like that, a complete somatotopic representation of the body is contained in the column structure in each of the four areas of S1. The most apparent indication of the columns is observed in the stellate cells of layer IV, which project vertically towards other layers. Similarly, as with other cortical areas, layers II and III connect neurons in neighboring columns to facilitate the transfer of information. Layer V projects to subcortical structures, while layer VI neurons provide input to the thalamus. Moreover, the feedback pathway in layer I of each column is involved in the selection of sensory information for cognitive processing and memory. Following the initial processing of somatosensory information in S1, this information is then forwarded in parallel from the four aforementioned areas to higher levels within the cortex, including the somatosensory cortex (S2), the posterior parietal cortex, and the primary motor cortex [42][43].

2.1.5. Neurological disorders

The nervous system is susceptible to a range of conditions that can affect its functionality throughout the lifespan. These include disruptions in brain growth, damage to the brain, spinal cord, or peripheral nerves, and impairment of various functions, including cognition, sensory perception, socioemotional processes, and motor abilities and behaviors. It is estimated that globally, over one-third of the population is affected by neurological conditions, which represent the leading cause of illness and disability [1]. The present study analyzed retinal degeneration and provoked epileptic-like activity. The following section will provide an explanation of these conditions.

Retinal degenerative diseases

Retinal degenerative diseases, such as retinitis pigmentosa (RP) and age-related macular degeneration (AMD), result in blindness and affect millions of individuals globally. The aforementioned diseases result in not only the loss of photoreceptors but also a remodeling process of the retinal structures due to the absence of signal inputs. In late stages, phenomena include glial hypertrophy, neuronal translocations, loss of neurons, and alteration of retinal circuits with the formation of new synaptically active neuronal connections. These effects present a significant challenge for the successful development of retinal prostheses, as the disease alters normal visual information processing [52].

Age-related macular degeneration (AMD) primarily affects the elderly and is the third leading cause of blindness worldwide. The following factors have been identified as potential contributors to the development of AMD: smoking, cardiovascular disorders, genetics, and certain nutritional deficiencies. Diagnosis is accomplished through a combination of clinical examination and imaging techniques, including retinal photography, angiography, and optical coherence tomography. AMD impairs central vision by causing pathological alterations to the macula. The disease can be classified into two distinct categories. Dry AMD is distinguished by a deficiency of serum or blood leakage, which results in blurred vision and, in severe cases, the formation of a disciform scar. Dry AMD may evolve into wet AMD, a condition marked by the expansion of abnormal blood vessels that can trigger bleeding and thereby significant vision loss [53]. Currently, there is a lack of evidence-based treatments for dry AMD, whereas for wet AMD, repeated injections of anti-vascular endothelial growth factor (VEGF) agents are employed [54].

Retinitis pigmentosa (RP) represents the primary cause of visual impairment and blindness among patients under the age of 60. Typically, RP commences with a loss of night vision, which

is then followed by a decline in peripheral vision and, in more advanced stages, a complete loss of central vision. The loss of night vision is attributed to the injury or death of rods. This may be a consequence of gene mutations, which can result in the destabilization of the rod outer segment or an increased vulnerability to oxygen toxicity. Rod degeneration then affects the death of cones. Subsequently, degeneration of the rods results in the death of the cones. This can be attributed to a number of factors, including a reduction in cell density and an elevated level of oxygen, which can result in oxidative stress. Another potential cause is the formation of microglia due to rod death, which can trigger a pro-inflammatory response and consequently lead to the degradation of cones. This sequence of cell death culminates in the loss of central and color vision in later stages. Currently, RP is regarded as an incurable disease, with therapeutic interventions primarily aimed at managing complications and addressing the psychosocial impact of the condition [55].

Epilepsy

Epilepsy is one of the most prevalent neurological disorders globally, affecting an estimated 50 million individuals of all ages [56]. The pathological condition is defined by the spontaneous occurrence of seizures, which are caused by abnormal electrical activity and result in a range of neurobiological, cognitive, psychological, and social consequences [22]. This increases the likelihood of disability, social isolation, psychiatric comorbidities, and premature mortality in individuals with epilepsy. Despite ongoing advances in anti-seizure medications, approximately one-third of patients continue to experience drug-resistant epilepsy [57]. As an alternative, patients may undergo surgical intervention to remove the portion of the brain responsible for the seizures. The seizure may originate in a single hemisphere of the brain, in both hemispheres, or remain unidentified [22]. Consequently, not all patients are suitable candidates for surgical intervention if the seizure onset is poorly localized or in regions with a high risk of neurological deficits. Another alternative is neurostimulation, such as DBS, which is considered a safe and effective therapy for the treatment of drug-resistant epilepsy [57]. Nevertheless, the spatial and temporal scales that delineate the fundamental pathological process remain insufficiently defined [58].

2.2. Neural interfaces

The application of MEAs allows for interfacing with the neural system, thereby performing as a neural prosthesis - an artificial device which aims to partly replace or repair function of a damaged neural system [59]. A neural prosthesis comprises a substrate with embedded microelectrodes and associated hardware, including amplifiers, filters, a digitizer, data transmission, and a stimulator [60]. The presence of a conductive extracellular volume enables the formation of an electric field induced by the neural signal origins, thus enabling the recording and stimulation processes [60]. The following sections provide an overview of the different types of neural implants and their applications. Subsequently, the fundamental principles of electrophysiological recordings and stimulation with neural implants, as well as the key considerations and requirements for implantable MEAs, are presented. Additionally, an in-depth analysis of the state of the art in 3D BMIs and retinal implants in clinical trials is provided.

2.2.1. Types and applications overview of neural interfaces

In recent years, neural prostheses have emerged as a promising technology for diagnosing and treating a range of diseases, including neurological disorders, degenerative conditions, and sensory and motor injuries [61]. The scope of potential applications is vast (see Figure 2.8A), encompassing implants in the PNS, such as those used for the vagal nerve or peripheral nerves, as

well as implants for sensory loss, such as retina or cochlear implants. Additionally, there are implants in the CNS, including penetrating and surface implants for the brain, as well as spinal cord implants. Consequently, in addition to the growth in neuroscientific research, there has been a corresponding increase in the number of clinical studies and commercially available devices. Among the most commercially available implants are the widely utilized cochlear implants, which have been implanted in over one million patients, and DBS, which has emerged as a highly accepted therapeutic approach for neurological disorders in recent years. Moreover, retinal implants are currently being tested by a number of companies [62] (Further discussion in section 2.2.6). In addition, several start-ups, including Neurosoft Bioelectronics, CorTec, and InBrain, are developing soft brain implants for the surface of the cortex to record electrocorticograms with high resolution (ECoG electrodes). Another target are peripheral nerve electrodes, which can either be cuffs or penetrating devices. The commercialization of these devices has also commenced, with CorTec for the former and Sensars for the latter.

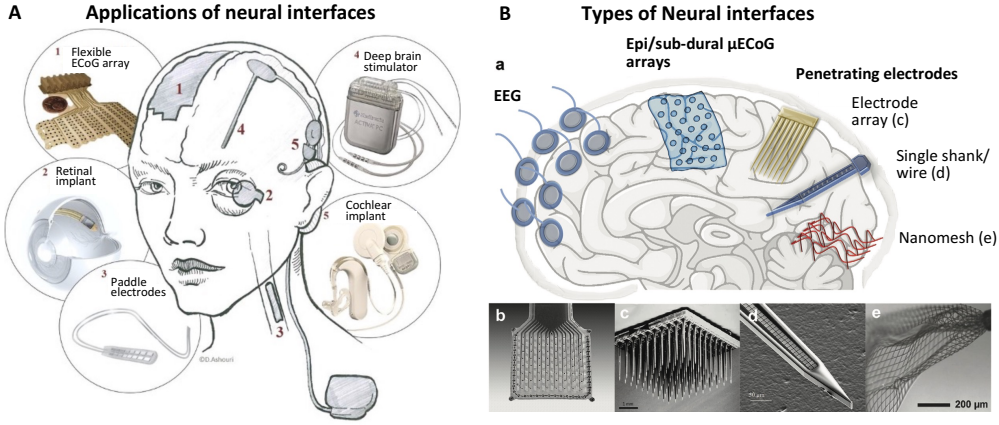

Figure 2.8.: Applications (A) and types (B) of neural interfaces A) The application of neural interfaces reaches from flexible ECoG arrays paddle electrodes and retinal implants to widely used cochlear implants and devices for DBS (modified from [63]). B) Neural implants differ by their level of invasiveness. Here, EEG electrodes are used directly on the skin (non-invasive), while µECoGs are placed directly on the surface of the brain (image a). Another category is penetrating electrodes, such as needle-like electrode arrays (b), single shank devices (c) or meshes (d) (modified from [64]).

Similarly, the range of different types of neural implants is vast (see Figure 2.8B). MEAs represent a fundamental component of neural interfaces, in addition to an electronic interface and signal processing unit. MEAs facilitate the transmission of electrical pulses to stimulate the targeted neural tissue, and enable the detection of changes in current, impedance, and potential as a result of the nervous system's physiological response. The flexibility and rigidity of MEAs are dependent on the material used as their substrate. The selection of materials for microelectrodes is a critical determinant of their electrochemical performance and durability [18][19]. Most commonly noble metal, such as Au, platinum (Pt) and iridium (Ir), along with alloys including PtIr and iridium oxide (IrOx), or conductive polymers, such as poly(3,4-ethylenedioxythiophene): poly(4-styrenesulfonate) (PEDOT:PSS), are used as electrode material or coating [65]. The microelectrodes can be arranged in a grid configuration, thereby covering the surface of neural tissue. Notable examples include electrocorticography (ECoG) arrays for the cortex [20][58][66][67] and paddle electrodes implanted into the spinal cord [15]. In the case of peripheral nerves, soft cuff devices are employed as a means of circumventing them [68][69][70]. It should be noted, however, that these examples are limited to the surface of neural tissue. To gain further insight into the defining characteristics of the underlying pathological dysfunctions, it may be necessary to conduct studies at deeper neural layer levels. For example, there is a lack of knowledge regarding

the mechanisms of seizure spread and onset in deeper layers of epileptic patients [22] and the remodeling of retinal layers following photoreceptor loss [23]. Consequently, penetrating electrodes are employed, which can stimulate and record from deeper neural layers, thus facilitating the acquisition of data at the single-neuron level and enhancing the comprehension of neural networks. These devices encompass a range of designs, including stiff and flexible single-shank devices with multiple electrodes and meshes of electrodes, as well as fully 3D devices that simultaneously cover the surface and the layered neural structure. As the development of flexible 3D neural interfaces is the objective of this study, the state-of-the-art of such devices is discussed in section 2.2.5.
It is evident that an increase in the invasiveness of the implants or the level of difficulty in accessing the surgical site will inevitably lead to a higher probability of complications. This, in turn, presents a significant challenge in translating the technology from scientific investigations conducted using animal models to human trials. Consequently, for numerous applications, there is a need for reliable surgical techniques and long-term stable solutions for functional BMIs [71]. It is crucial to consider biocompatibility and long-term stability for the next generation of neural implants with the choice of material and electronic design being one of the most important factors [72].

2.2.2. Electrophysiological recordings and stimulation with neural interfaces

The simplest setup consists of a working electrode (WE), which is the electrode of interest, and a counter electrode (CE) to complete the electric circuit and force electric current to pass between them. For electrical potential measurements, a third reference electrode (RE) is useful to define a reference potential [73].

Electrode-electrolyte interface

When a metallic electrode gets in contact with electrolyte, an interfacial region - the electric double layer (EDL) - is formed. At the metal side, the charge carriers are electrons, while in the electrolyte, such as extracellular fluid, there are ions (K^+, Na^+, and chloride ion (Cl^-)) close to the electrode surface. The EDL affects electrochemical measurements and its properties depend on several parameters, such as the electrolyte's and electrode's material properties and the temperature. The concept was initially introduced by Helmholtz in 1879, wherein he proposed the existence of a compact layer of ions in direct contact with a charged metal surface. Gouy and Chapman built upon the initial description of the EDL by proposing that the accumulation of ions reaches a certain extent from the solid surface, a phenomenon attributed to the Boltzmann distribution. Stern then proposed that the EDL comprises a rigid Helmholtz layer and a diffuse one as proposed by Gouy and Chapman. Subsequent developments by Graham regarding the adsorption of particular ions on the metal surface and the characteristics of the solvent described by Parsons and Bockris serve to illustrate the complexity of the EDL [73][74][75]. In a simplified model (Figure 2.9A$_i$), adsorbed water molecules on the electrode surface orient themselves towards the negative-charged metal surface and thereby form a hydration layer. However, some ions penetrate the hydration layer and adhere to the electrode, which thereby form the (inner Helmholtz layer (IHL)). Outside of that layer, ions in the electrolyte form a charged layer parallel to the electrode's surface outer Helmholtz layer (OHL). In an increasing distance from the surface, their distribution is diffuse and called the Gouy-Champman layer. The charge distribution at the EDL may thereby be summarized by series of three capacitors (Figure 2.9A$_{ii}$), each describing the charge distribution of the three layers. Additionally, there is a charge transfer resistor R$_e$ (Figure 2.9A$_{iii}$), which is connected in parallel [74][76].

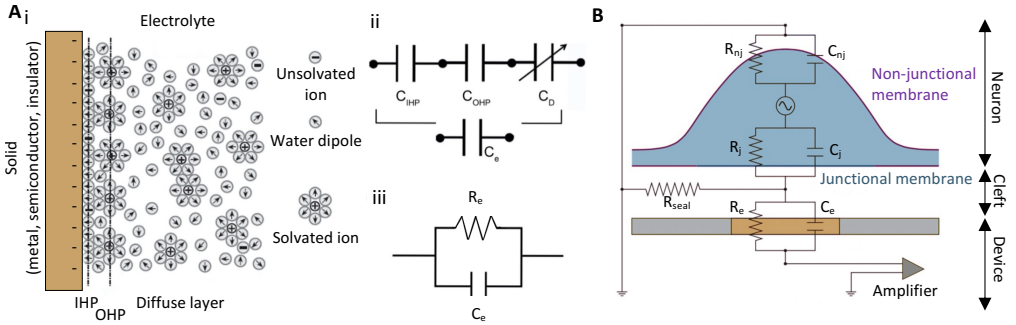

Figure 2.9.: Schematic of the electrode-electrolyte-interface (A) and the neuron-to-electrode junction as well as equivalent circuits (B). A) Schematic illustration of the electrode-electrolyte-interface (i), a series of capacitors models the charge distribution of each layer (ii), the equivalent electric circuit of the electrode-electrolyte-interface consists of the charge-transfer resistor R_e and the double-layer capacitor C_e (adapted from [76]) B) The cell body of a neuron (depicted in blue) is situated on a sensing electrode (shown in gold). The electrode is linked to an amplifier. A cleft, filled with an electrolyte solution (e.g., culturing media), is situated between the cell membrane and the electrode–substrate interface. The neuronal plasma membrane is subdivided into two distinct regions. The junctional membrane that faces the electrode (depicted in blue) is represented by the junctional membrane resistance (R_j) and the junctional membrane conductance (C_j). The remaining portion of the membrane, designated as the non-junctional membrane (violet), is represented by the non-junctional resistance (R_{nj}) and the non-junctional capacitance (C_{nj}). The solution within the cleft generates the seal resistance (R_{seal}), which is in turn connected to the ground. The impedance of the electrode is represented by the electrode resistance (R_e) and capacitance (C_e) (adapted from [77]).

Neural recordings

At the neuron-to-electrode junction (illustrated in Figure 2.9B), there is a passive electrical circuit in the cleft which couples the biological membrane to the recording electrode and thereby enables neural recordings. The cleft is filled with ionic solution, the extracellular fluid, and creates a resistance R_{seal}, which directly influences the distribution of charge across the passive metal electrode. R_{seal} is mainly characterized by the size of the cleft by

$$R_{seal} = \frac{\rho_s}{d} \cdot \delta \tag{2.1}$$

where ρ_s is the resistivity of the electrolyte, d is the distance between neuron and electrode. δ is a factor defining the overlap of the neuron's A_N and electrode's A_E membrane area

$$\delta = \begin{cases} \frac{A_N}{A_E} & \text{for} \quad A_N < A_E \\ 1 & \text{for} \quad A_N \geq A_E \end{cases} \tag{2.2}$$

The neuron is divided into a junctional membrane facing the electrode and a non-junctional membrane. Action potentials and synaptic potentials produce complex current flows between membrane compartments and extracellular fluid. The fraction of current flow that thereby passes between the junctional and non-junctional membrane is here described by the resistance R_j (or R_{nj}) and capacitance C_j (or C_{nj}) of a membrane patch. Finally, the electrode-to-electrolyte interface is modeled by a resistive-capacitive parallel circuit derived from the description of the EDL (section 2.2.2) [76][77]. This simplified model shows how microelectrodes can detect potential changes in the extracellular field which are caused by ionic processes of nearby cells. Here, the detected potential mainly depends on the magnitude and sign of current flow as well as on the distance to the recording site [60].

The term "spike" is used to describe a signal generated by a putative AP. In intracellular recordings, APs are detected by direct access to the neuron, for example, using patch-clamp techniques.

These recordings typically exhibit a first positive peak with high amplitude and a negative volley. In contrast, extracellularly, APs can be identified when electrodes are placed in close proximity (approximately 100 micrometers) to the source, for example, around the soma or near the axon hillock. They are typically identified when surpassing a threshold value after improving the signal-to-noise ratio (SNR) by filtering the raw data with a 300 – 3000 Hz [60] or 100 - 3000 Hz bandpass [78]. Timed spiking activity can be classified as either individual neuron activity (single-unit activity (SUA)) or activity from a local population of neurons (multi-unit activity (MUA)) [60][79].

Local field potentials (LFPs) are assessed in the low-frequency band (less than 300 Hz). They reflect subthreshold and spiking activities that are summed up over a larger population of neurons and usually do not display discernible spikes. The relationship between spikes and LFPs is currently under discussion. However, it is believed that synchronized APs can contribute to the generation of LFPs [60][79].

Neural stimulation

To excite neurons through electrical stimulation, the delivered current by the stimulating electrode, the electrical properties of the tissue, as well as the electrochemical processes at the EDL should be considered [80].

Stimulators are either voltage- or current-controlled. During voltage-controlled stimulation, the impedance of the entire circuit manipulates the amount of current that flows through the neural tissue. On contrast, in current-controlled stimulation a defined amount of current is delivered, regardless of the impedance [80].

The conductivity of neural tissue is not homogeneous but rather exhibits inhomogeneity and anisotropy. This phenomenon is not solely attributable to anatomical variations between regions, such as those observed in the cortex and retina, but is also influenced by encapsulating tissue surrounding the implant. In most computational models, the conductivity is assumed to be homogeneous and isotropic to facilitate the calculation of generated potentials. However, the actual conductivity plays a significant role in neural activation [80].

Faradaic and non-Faradaic reactions are the primary mechanisms of charge transfer at the electrode-electrolyte interface. These reactions are initiated by a forced potential change at the interface from equilibrium, which then results in electrochemical processes and a subsequent flow of current. Non-Faradaic reactions do only involve the distribution of charges at the EDL, such as charging or discharging the double-layer capacitance. In contrast, Faradaic reactions involve an electron transfer (oxidation-reduction reactions), which might not be reversible and can result in the release of cytotoxic chemical substances [73][75].

Stimulation parameters should be selected with caution to excite neurons while avoiding any damage to the neural tissue. A stimulating electrode can be either an anode (positive source) or a cathode (negative source). The latter is more effective at exciting neurons due to the negative membrane potential. Moreover, the current stimulation pulses should be charge-balanced. In the absence of sufficient time for the electrode to discharge, the driving force for irreversible chemical reactions may be increased, potentially leading to electrode degradation and tissue damage. Moreover, specific waveform shapes may facilitate selective stimulation of specific neural elements, such as soma or axon. Furthermore, the threshold current I_{th} required to excite a neuron

increases rapidly with distance r to the electrode. The relationship can be expressed by

$$I_{th}(r) = I_0 + kr^2 \tag{2.3}$$

with the constant I_0, the minimum current to initiate an AP when $r = 0$, and the parameter k which depends on the axon diameter and controls how quickly the threshold increases. In practice, the stimulation current is often selected well above the threshold, thereby exciting a large population of neurons in the vicinity of the electrode. However, there is also an upper limit to the stimulation current, beyond which AP propagation is blocked [80].

2.2.3. Non-invasive electrophysiological testing

Electrophysiologic testing provides objective, quantitative measurements of electrical activity within the neural system, thereby complementing anatomical analysis and offering enhanced precision relative to traditional diagnostic methods. These non-invasive diagnostic procedures allow for earlier detection of potential pathologies, facilitating more precise assessments.
Specifically, electroretinography (ERG), and visual evoked potential (VEP) tests are capable of detecting subtle alterations in retinal electrical activity, often preceding the manifestation of observable symptoms or structural changes. These techniques measure large-population-level cell responses (LFPs). The ERG, recorded at the cornea, represents retinal light responses, which are mass responses of cells discharging in the retina in response to both light flashes and changing patterned stimuli. The signal typically consists of an a- and b-wave (Figure 2.10A). The a-wave is the result of an extracellular radial current, the polarity of which can be explained, at least in part, by its being the result of the reduction of a constantly flowing photocurrent in the dark. This reduction is attributed to light absorption in the photoreceptor outer segments and closure of cation channels. Rod bipolar cells are the source of the b-wave in the dark-adapted retina. The b-wave manifests with less luminous stimuli than the a-wave, in part due to the amplification of rod signals by bipolar cells, which arise from the convergence of rod signals onto bipolar cells. Oscillatory potentials emerge within the inner retina [81][82][83].

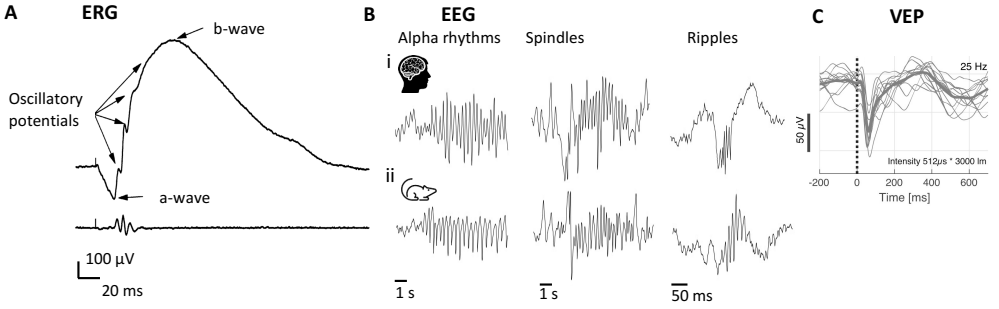

Figure 2.10.: The ERG, EEG and VEP. A) Corneal ERG response recorded from a WT rat. In the dark-adapted retina of a WT rat, the ERG consists of an a- and b-wave and oscillatory potentials. (i) shows the ERG filtered at 0.1 - 1000 Hz, while (ii) illustrates the signal filtered between 100 - 1000 Hz to isolate the oscillatory potentials (modified from [81]. B) Alpha rhythms, spindles and ripples in human (i) and mouse (ii) measured by means of EEG (modified from [42]), C) VEPs in the mouse using electrodes placed on the skull (modified from [84])

EEG is a well-established procedure that provides insight into the metabolic and electrical status of the brain. This technique finds application in diagnostics and monitoring of the human cognitive system - a field of investigation that encompasses conditions such as epilepsy, impaired consciousness, and sleep disorders [85]. Typical EEG electrodes are made of silver/silver chloride (Ag/AgCl). These electrodes are positioned on the subject's skin, and the addition of saline

gel is typically employed to enhance the electrical connection between the electrode and the skin. The strategic placement of these electrodes is contingent upon the specific investigation [86]. The classification of EEG rhythms is based on their frequency range and denoted by Greek letters. High-frequency, low-amplitude rhythms are typically associated with levels of alertness or with the initial stages of sleep. In contrast, low-frequency, high-amplitude rhythms have been observed to be associated with non-dreaming sleep states, specific drugged states, and coma. For instance, delta rhythms (< 4 Hz) are frequently characterized by substantial amplitude and are associated with deep sleep. Conversely, alpha rhythms, ranging from 8 to 13 Hz, are associated with quiet, waking states. Gamma rhythms, with a frequency range of approximately 30 to 90 Hz, indicate an active cortex. Further typical rhythms are spindles, brief 8 - 14 Hz waves commonly observed in sleep, and ripples, which are short oscillations between 80 and 200 Hz. A notable finding is the high degree of similarity observed in EEGs of various mammalian brains, including those of mice and humans, despite considerable disparities in brain mass (Figure 2.10B) [87]. In addition to measuring typical rhythms, EEG can also be used to assess the activity of cells reacting to different types of stimuli. One example of this application is the use of VEP recordings to evaluate the integrity of the visual system. VEPs are potentials generated by cells in the visual cortex, providing a comprehensive assessment that spans from sensory transduction to the visual cortex. In mice, the implantation of electrodes beneath the skull, directly above the cortex, enables the recording of VEPs (Figure 2.10C) [84].

2.2.4. Challenges and requirements for invasive neural interfaces

A more comprehensive understanding of brain functions is essential for enhancing the accuracy of diagnoses and improving the efficacy of treatments for neurological disorders. While researchers have previously relied on electrodes placed on the skin, such as for electroencephalography (EEG) and electroretinography (ERG), there is an increasing desire to interact with the neural tissue on individual cell-level, which can be achieved through the use of densely packed electrode arrays placed on the surface, or even by penetrating devices to capture activity from deeper neural layers. Nevertheless, currently established treatments rely on pharmacotherapy or bulky implantable electrodes, for instance, to identify the source of seizures in epilepsy or to reduce Parkinson's syndrome through neuronal stimulation, which is not subtype-specific. In contrast, the large size of the electrodes typically results in the simultaneous stimulation of the surrounding tissue. Furthermore, the insertion of a synthetic neural probe triggers FBR eliciting immune responses and glial scar formation (Figure 2.11A$_{i-iii}$). Acute inflammation will turn into chronic neuroinflammation which impacts the neural network surrounding the electrodes and results in a decrease in device performance due to encapsulation (Figure 2.11A$_{iv,v}$). It is therefore necessary to interact with neuronal tissue at meaningful levels of resolution and precision, while ensuring that the mechanical properties of the neural tissue are respected and that tissue damage is avoided. In this regard, significant advancements have been made in recent years, with the development of softer and more flexible materials and micro-scale electrodes. However, the use of soft materials and micro-scale device dimensions presents a number of additional challenges and trade-offs, including considerations related to insertion and surgical approach, electrochemical properties, and seamless integration. The major challenge in developing neural interfaces is to create a long-term stable device by selecting design and material parameters which improve biological compliance by minimizing inflammatory responses [72][88][89][90]. In the following section challenges for neural implants as well as requirements and failure modes will be discussed. An overview of the challenges and requirements is provided in Figure 2.11.

FBR occur as a consequence of the implantation of synthetic devices into the body and are an unavoidable consequence of this procedure. Shear motions between the implants and the

surrounding tissue have the potential to damage neurons, particularly during the insertion of a penetrating probe (Figure 2.11A). Following implantation, inflammatory cells, including microglia, astrocytes, neurons and oligodendrocytes, will be released in response to the mechanical properties of the surrounding environment. In particular, neurons demonstrate a tendency to preferentially grow and branch in regions of relatively low stiffness, whereas oligodendrocytes exhibit a preference for areas with a Young's modulus of approximately 700 Pa. In contrast, microglia and astrocytes are activated in regions with a Young's modulus greater than 10 kPa [90]. As a consequence of the inflammatory response, neurons in the vicinity of the electrode may undergo necrosis, and reactive microglia and astrocytes drive further neurodegeneration, which can eventually result in signal loss. Over week-long implantations, chronic inflammatory responses provoke the secretion of proinflammatory cytokines and glial fibrin, thereby leading to the accumulation of glial scars which encapsulate the synthetic device and incorporate neurotoxic substances that impede tissue regrowth (see Figure 2.11A$_{iv,v}$) [72][91].

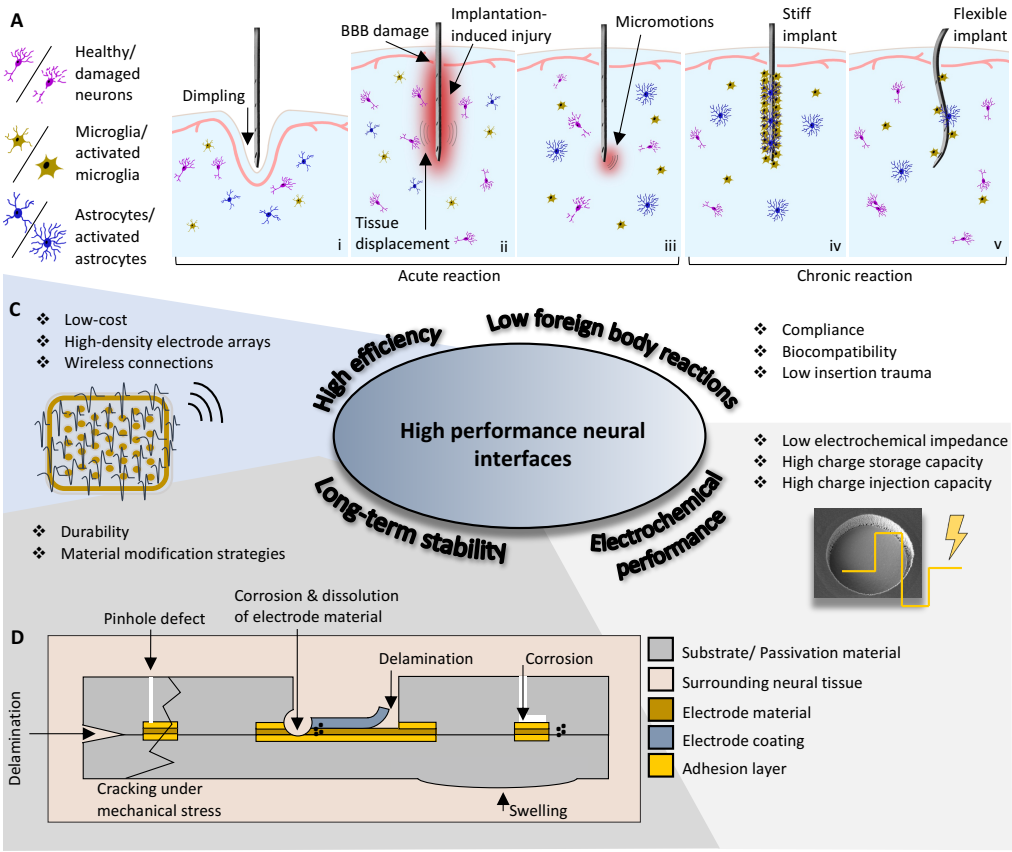

Figure 2.11.: Challenges and requirements for high-performance neural interfaces. A) Acute and chronic tissue reactions may occur. Dimpling may take place prior to penetration of the neural tissue (i). Damage to the blood-brain barrier may result, which can lead to implantation-induced injury (ii). Micromotions can further enhance FBR. In chronic implantation, more microglia encapsulate stiff implants (iv) in comparison to flexible (v) implants due to the tissue-device density mismatch (according to [**boulingreBiohybridNeuralInterfaces2023**]). B) Summary of the challenges, requirements and aims for high performance neural interfaces. C) Challenges influencing the long-term stability of flexible neural probes (modified from [91]).

Micromotions have been demonstrated to affect implanted devices (Figure 2.11A$_{iii}$). These are minor movements (submicrons to microns) of the device with respect to the neural tissue, resulting from mechanical interactions between the implant and the tissue, vibrations associated with body movements, and movements caused by vital activity such as heartbeats, breathing, and vascular pulses. It has been shown that micromotions can enhance FBR. Therefore, it would be optimal for implants to be tethered to connectors by flexible cables (electrical coupling), allowing for unrestricted movement (mechanical decoupling) and greater resilience to micromotions [72].

Electrochemical requirements

The electrochemical properties are affected by the electrode surface, which restricts the charge transfer. Electrodes are typically characterized by their impedance, the safe charge injection capacity (CIC), which is the maximal charge per pulse before water splitting occurs, and the charge storage capacity (CSC), which is the total amount of charge that can be transferred by the electrode [92]. A smaller surface area results in an elevated impedance, which consequently leads to a greater energy consumption during electrical stimulation and an increase in noise. Furthermore, the higher current density resulting from the smaller surface area exerts greater stress on the material, and the probability of electromigration is higher [91]. To study SUA, electrodes need to be small enough to distinguish spatially close neurons. But, higher impedance reduces the recording quality, evaluated by the SNR and amount of artifacts. In addition, working with lower current thresholds may not meet the clinical requirements for recordings and stimulation. Thus, there is a trade-off between electrode size and electrical performance which might be overcome by applying surface coatings on the electrode, such as PEDOT:PSS or sputtered iridium oxide film (SIROF), to effectively improve the electrochemical characteristics [93].

Crosstalk occurs when the electric fields of neighboring electrodes overlap in time and space during simultaneous stimulation. Crosstalk can lead to complex neural interactions, an overshooting of the upper limit of stimulation threshold, or damage to electrodes. For neural recordings and stimulations, a crosstalk > 1% can not be neglected and minimizing crosstalk should be considered when deciding for electrode geometry and insulation [91].

Mechanical requirements

In addition to the implantation site and the electrochemical properties of the implant, the physical dimensions and material choices also influence FBR. In the case of surface implants, such as ECoG electrodes, it is essential to ensure that the mechanical properties are aligned with the convoluted surface of the brain [90]. In contrast, the lifespan of a penetrating neural implant can be divided into three main phases, each of which requires a different set of requirements that are, at times, contradictory. Initially, during the implantation procedure (Figure 2.11A$_{i}$), the penetrating implant encounters peak forces during tissue dimpling due to the hyper/viscoelastic properties of the neural tissue. These forces depend on the speed of insertion, the number and dimensions of the shanks, and the geometry of their tips. An insertion force of 0.5 - 2 mN is required to penetrate neural tissue such as the brain or retina. If the insertion force exceeds the critical buckling load P$_{cb}$ of the implant, there is a significant risk of insertion failure due to bending [94].
Subsequently, during the displacement phase (Figure 2.11A$_{ii}$), the implant traverses the neural tissue to reach the intended position. In this phase, the forces typically increase with depth through compression and shear during viscoelastic relaxation of the tissue. However, this increase occurs at a slower rate in comparison to the penetrating phase. The surgical trauma is generally reduced during this phase by the use of a small feature size for the implant and a carefully selected insertion speed [90]. During the device implantation procedure, evidence of vascular damage was

observed, including fluid displacement, vessel rupture and incision, and the dragging of blood vessels by the device [95]. The disruption of the blood-brain barrier (BBB) gives rise to local ischemia and notable alterations in the concentrations of ions and proteins [96]. Injecting ultra-flexible electronics with a low cross-sectional footprint is a strategy to reduce FBR. However, this results in smaller critical buckling loads, which can lead to insertion failure. To overcome this challenge, various strategies have been proposed to facilitate the implantation of ultra-flexible implants. These include the use of insertion shuttles out of Si [97], using needles [93] or microwires [98][99] attached to the shanks possibly in combination with a "sewing" [31][100] or "mosquito" device [101], the use of a dissolvable brace made from polyethylene glycol (PEG) [33][102], and the incorporation of mechanical adaptable materials, such as hydrogels [103]. Finally, the third phase is the chronic state of the implant in the neural tissue, wherein it is either tethered or floating (Figure 2.11A$_{iii}$). The implant now experiences stress due to micromotions and behavior, which can reach tens to hundreds of Pascal [96]. During the chronic implantation phase (Figure 2.11A$_{iv,v}$), FBR are less pronounced when the device exhibits mechanical properties that closely align with those of the surrounding tissue. The term "compliance" refers to the ability of a device to deflect upon axial forces exerted by the surrounding tissue. Compliance is closely associated with Euler's formula and can be achieved through a low effective Young's modulus, a small cross-sectional footprint, and a loose fixation to the skull [94]. The bending stiffness K is often used to analyze the mechanical characteristics of the tissue-electrode interface. K can be estimated by the product of the Young's modulus E and the second moment of inertia I

$$K = E \cdot I \tag{2.4}$$

and describes the resistance of a implant against deflection, which results from longitudinal forces and displacement [104].

Electrode failure

A variety of factors, including corrosion, delamination, cracking and swelling, have the potential to impact the electrode material and flexible substrate, thereby influencing the lifespan of neural implants (Figure 2.11C).

Corrosion of electrode material can be caused by too high or unbalanced charge upon electrical stimulation. High potentials can lead to water electrolysis, which can alter the local pH. Here, reactions involving Cl^- can be harmful to the tissue and accelerate electrode-dissolution processes. Electrolysis also leads to oxygen bubbles at the electrode-electrolyte interface which impacts the stimulation efficiency negatively and can physically damage the electrode. Additionally, corrosion is accelerated by inflammation-induced hydrogen peroxide (H_2O_2) which changes the local pH [71][72][91].

Cracking may result from the bending of the material in response to micromotions and the subsequent mechanical stress. This can result in a change in resistance or capacitance between the electrode and target tissue, or, in the most adverse scenario, signal loss when electrodes become disconnected. Delamination between the electrode and the substrate can lead to an increased current density, which drives corrosion and dissolution of electrode material. In devices with polymer encapsulation, water absorption may result in substrate or passivation layer expansion, which subsequently induces stress in the neighboring layers, thereby causing cracks and delamination [91].

Long-term stability analysis

The combination of a mechanical mismatch and chronic immune responses (FBR) of penetrating neural implants, in conjunction with shear motion and the subsequent formation of glial scars and neuron depletion at the probe–brain interface, can result in the degradation of recording and stimulation capabilities. Therefore, failure can be attributed to a combination of biological, material, and mechanical factors [105]. Consequently, electrode failure has been documented to occur as early as days or weeks [106][107][108], or in some cases as late as months [109][110]. It is notable that there has been no demonstration of continuous functionality for neurostimulation electrodes over a period of ten years or more, which is generally accepted as the benchmark for clinical viability, particularly when the surgical method is complex and carries inherent risks [111]. It is unfortunate that research into the causes of failure of these implants is not a priority, given that studies in this area are not easily funded, require significant effort to perform and are challenging to publish. It is therefore essential to conduct not only pre-implantation studies on the functionality of the electrodes, but also post-implantation studies to analyze the failure mechanisms and gain a deeper understanding of them. This will facilitate the formulation of strategies to circumvent such failures in the future. Inspections should be conducted using microscopic and histology inspection methods, as well as material and electrode characterization analysis. In order to analyze the surface topography of the neural probe with regard to delamination and cracks, scanning electron microscope (SEM) or atomic force microscopy (AFM) may be employed. Furthermore, elemental composition analysis, such as energy-dispersive X-ray spectroscopy (EDS) or X-ray photoelectron spectroscopy (XPS), should be employed to observe dissolution, contamination, and delamination of the stimulating electrodes. In particular, adhesion testing is of great importance for thin-film electrodes based on flexible polymers, as it serves to analyze the occurrence of pinhole effects in the insulating layer [112].

2.2.5. 3D penetrating neural implants

Interacting with the 3D space of neural tissue to capture electrophysiological activity from all three dimensions can be achieved through the use of 3D implants. Traditionally, MEAs comprise one- or two-dimensional arrangements of electrodes. Nevertheless, there are methods for creating 3D recording sites from a two-dimensional plane (Figure 2.12):

- Nanoneedles and pillars with typically only one recording site per needle/ pillar
- Several implanted neural threads with multiple electrodes
- Stacks of overlaying 2D arrays with spacers in between
- Cut-and-fold techniques (kirigami)

Nanoneedles and pillars are 3D structures, but typically allow only to record from one neural layer (x - y plane) at a certain depth of the neural tissue, due to the fact that they possess only one electrode per pillar/needle. One standard approach is the Utah array which consists of microfabricated silicon (Si)-needles with metal-based or conductive polymer tips and a biocompatible polymer encapsulation [24]. A design with slanted needles offers the possibility to record from several neural depths within one device [119]. Similarly, Zardini et al. employed silicon microfabrication techniques to fabricate an array comprising an impressive number of 5184 pillars, with a length of 1200 µm [115]. However, the high Young's modulus of silicon (Si) (160 GPa [120]) and the tethered design of Utah-like arrays have been observed to result in the formation of fibrosis tissue around the pillars, a phenomenon that has been documented on multiple occasions. The encapsulation

	Approach	Fabrication process	Substrate/ Passivation	Electrode material	Electrode dimensions	Electrode count
3D nanoneedles/ pillars						
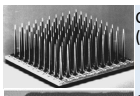	Campbell et al, 1991 (Utah array)	Silicon-based microfabrication	Si needle PI encapsulation	Au/ Pt	1500 µm long, 90 µm thick at the base	Typically 64
	Grob et al., 2021	Inkjet-printing	Ag nanoparticle ink (AgNP ink)	Electrodep. Au/ Pt	Up to 560 µm long pillars, 32 µm diameter	64
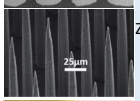	Zardini et al., 2021	Silicon-based microfabrication	Poly-Si, Oxide-nitride-oxide insulation	Cr/ Au	1200 µm long, 20 µm at the base	Up to 5184, < 100 used *in vivo*
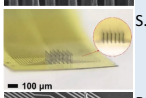	S. H. Lee et al., 2022	Photolithography	Si needles on PI, PaC passivation	Pt nanomesh or electrodep. PEDOT:PSS	10-200 µm long needles	32 or 1024
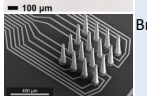	Brown et al., 2022	Si thin-film processing, 2-photon-lithography	PI substrate, PaC passivation, OrmoComp pillars sputtered with Ti/Pt	Pt	300 µm pitch, 350 µm long, 20 µm at the base	16
Neural Threads						
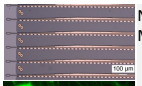	Neuralink and Elon Musk, 2019	Thin film technology, photolithography „and other"	PI substrate, Au feedlines	PEDOT:PSS, IrOx	4 - 6 µm thick threads, 5- 50 µm wide, 20 mm long	3072 distributed across 96 threads
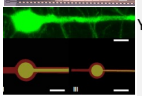	Yang et al., 2019	Photolitography, e-beam evaporation	SU-8 Au feedlines	Pt	Polymer/metal/ polymer width 4/2/4 or 1/0.6/1 µm, 0.9 µm thick	16
3D stacks of Michigan-like arrays						
	Wise et al., 2004 (Michigan array)	Silicon-based microfabrication CMOS technology	Si substrate, SiO_2 insulation	Au/Pt/IrOx	Typically 25 – 50 µm shank diameter	Up to 1024 electrodes, 128 Ch
	Rios et al., 2016	Silicon-based microfabrication CMOS technology	Si shanks and spacer, Parylene HT encapsulation	Electrodepos. Au	100 µm width at the base, 20 µm at the tip of the shank	1024
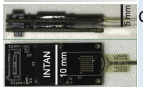	Chung et al., 2019	Thin film technology, photolithography	PI substrate, Si stiffener for insertion	Pt with electrodepos. PEDOT:PSS	14 µm thick, 61 to 80 µm wide shanks	Up to 1024,
***Kirigami* structures**						
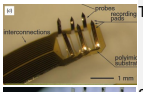	Takeuchi et al., 2003	Thin film technology, photolithography, folding: magnetic fields	PI substrate, electroplated nickel (magnetic)	Ti	1200 µm long, 160 µm wide, 20 µm thick shanks	18
	Soscia et al., 2020	Thin film technology, photolithography, folding: mechanical actuation	PI substrate, Ti/Au/Ti feedlines	Electrodepos. Pt	1100 µm long, 90 µm wide, 15 µm thick shanks	Up to 80 electrodes per array, chip with up to 256 electrodes
	J.Y. Lee et al., 2022	Thin film technology, photolithography, folding: pop-up process	PI substrate, SU-8 encapsulation, Cr/Au feedlines	Electrodepos. Pt	1500 µm long, < 20 µm thick shanks	24 electrodes on shanks, 9 surface electrodes

Figure 2.12.: Examples of 3D neural implants. Nanoneedles and pillars (Utah array by Campbell et al., 1991 [24], picture from [113], Grob et al., 2021 [114], Zardini et al., 2021 [115], S. H. Lee et al., 2022 [116], Brown et al., 2022 [117]), neural threads (Neuralink and Elon Musk, 2019 [31], Yang et al., 2019 [32]), 3D stacks of Michigan-like arrays (Wise et al., 2004 [26], Rios et al., 2016 [28], Chung et al., 2019 [118]), and kirigami structures (Takeuchi et al., 2003 [34], Soscia et al., 2020 [36], J.Y. Lee et al., 2022 [37]).

process results in an increase in impedance and elevated energy consumption. Consequently, the efficiency of both stimulation and recording is diminished until the device ultimately fails [30][121].

More recently, new fabrication processes have emerged, such as inkjet-printing [114] or 2-photon-polymerization (2PP) [117], enabling the fabrication of thin (20 µm at the base [117]) pillars with the use of less stiffer materials to decrease the insertion damage. An alternative approach by S. H. Lee involved the use of silicon needles on a flexible polyimide (PI) substrate, which allowed for greater conformity with the curvature of the brain [116]. All of the aforementioned approaches utilize stiff needles that can only record from a single z-location within the neural space. This enables single-unit recordings due to the small electrode size and distance to the target cells. However, it does not fully allow the capturing of the entire 3D complexity of the neural tissue.

Neural threads are very thin single-shank devices (1D) based on flexible polymers (such as polyimide (PI) [31] or SU-8 [32]). They are implanted either in a serial manner using neurosurgical robots [31] or multiple at a time by a controlled stereotaxic injection using a syringe pump [32] to enable access of the 3D space. The configuration of the bioinspired threads, as devised by Yang et al., aligns with the dimensions of both soma ($\sim$10 µm) and neurites (2.6 wide and 0.9 µm thick thread) of a pyramidal neuron, thereby ensuring conformity with the neural tissue. The device developed by Neuralink, with its CEO Elon Musk, is currently the subject of considerable media interest following the announcement of the commencement of human trials. The objective is to implant a 1024-channel device comprising 64 threads, which are thinner than human hair, into a human subject [122]. Although the company has made claims about its innovative technology, there are still concerns. The Physicians Committee for Responsible Medicine has stated that comments made by Musk about primate deaths used in preclinical studies may have been misleading. Subsequently, they have requested that the U.S. Securities and Exchange Commission investigate the medical device company, Neuralink, due to their concerns about the safety of the device for human trials [123].

3D stacks of Michigan-like arrays are stacked 2D-MEAs with spacers in between. The original Michigan design, created in 1970, comprises Au electrodes on Si shafts with an insulation by silicon dioxide (SiO2) [25]. The creation of 3D MEAs containing up to 1024 electrodes and 128 Ch was achieved by the stacking of 16 2D Michigan arrays [26]. Nowadays, Michigan-style probes are further commercialised by the spinoff company NeuroNexus including on-chip complementary metal-oxide semiconductor (CMOS) circuitries and a large range of shank configurations. A comparable approach by Rios et al. from 2016 resulted in the development of a shank with a width of 20 µm, which was still capable of holding 1024 electrodes [28]. However, traditional Michigan-style probes are composed of rigid Si, which has been associated with FBR comparable to those observed in the Utah array [29]. Consequently, flexible Michigan-style arrays comprising a 14 µm-thick PI. However, the use of a Si stiffener temporarily fixed to the flexible shanks by PEG is necessary to overcome insertion failure due to buckling [118].

Kirigami structures employ the cut-and-fold principle to construct a 3D MEA from a 2D plane. In 2004, Takeuchi et al. designed, fabricated, and tested a 3D flexible microprobe that was folded by applying an external magnetic field [34]. Magnetic fields were also utilized in the 2018 work of Sim et al., who folded 16 PI shanks with a total thickness of 7.65 µm [124]. However, their shanks have a width of 300 µm. Raising the number of recording and stimulation channels while using smaller shank dimensions, Soscia et al. 2020 fabricated 80 electrodes on, in total, eight PI shanks intended for *in vitro* recordings. The folding of their 1100 µm long and 90 µm wide shanks, was achieved through the use of mechanical actuation [36]. An alternative approach was taken by Lee et al., who employed a self-folding process for the fabrication of their 3D implant, which comprises nine surface electrodes in addition to the 24 distributed over four shanks [37]. While foreign body reactions (FBR) should be reduced in flexible kirigami probes in comparison to stiff silicon (Si)-

based probes, the electrode count is lower and the insertion is more difficult. Additionally, for the folding, cytotoxic materials, such as ferromagnetic metals like nickel were employed combined with the use of external energized equipment to induce magnetic fields that are considered hazardous (100 – 400 mT), or manual time-consuming processes.

2.2.6. Retinal prostheses

In the 1980s, the progress in micro-nano fabrication and the improvements in vitreoretinal surgery paved the way to an emerging research field in visual prostheses. Since then, several groups around the world have focused on the restoration of vision using implantable devices for the retina. Other approaches include implants for other parts of the visual pathway, such as the LGN, visual cortex or visual nerve [125]. In addition, alternatives for electrical stimulation of implantable devices to stimulate neurons are also being pursued, such as optogenetic [126], gene therapy, or cell biology approaches [127]. In the next section, the main focus is on neural implants in clinical trials intended to apply stimulation of the remaining visual pathway directly at first stage of the visual system: The retina. Retinal prostheses are distinguished by their implantation site: epiretinal, subretinal and suprachoroidal prostheses (Figure 2.13).

Epiretinal prostheses

Epiretinal prostheses are placed on the retinal surface next to the nerve fiber and ganglion cell layers (Figure 2.13A). The transvitreal sclerotomy surgical procedure is similar to other vitreoretinal surgeries and therefore the placement and removal of the implant may be less complex. By stimulating the RGCs directly, the first parts of the retinal system are bypassed. With ongoing remodeling processes, this may be a suitable approach. However, the proximity to the axonal nerve fibers possibly leads to undesired axonal stimulations [128].

Argus 2 Argus 2, developed by Second Sight Medical Products (CA, USA) is the first commercially available visual prosthesis with a CE approval in 2011 and FDA approval in 2013. It has 60 electrodes to stimulate the neurons on the epiretinal side of the retina. The visual input is thereby supplied by a miniature camera integrated on glasses [134]. More than 350 patients have been treated with the Argus 2 implant. However, Second Sight announced to stop the Argus 2 project and now focus on their cortical approach Orion [87][131].

IRIS 2 The current Pixum Vision S.A. product is called Intelligent Retinal Implant System (IRIS) 2 and consists of a 150-MEA, a pocket processor and, like the Argus 2, a glasses-mounted interface (see Figure 2.13A$_i$). It differs from Argus 2 in how the visual input is processed and uses optical methods for higher data transfer. More importantly, the device incorporates a learning encoder which allows to mimic retinal ON/OFF pathways as a result of individual calibrations [135]. IRIS 2 got CE approved in 2016. In a following clinical trial of 6 months the implant restored vision of patients to a certain level [136], but the lifespan of IRIS 2 turned out to be shorter than expected [128].

EPIRET3 and VLARS Like the other epiretinal devices, the EPIRET3 (RWTH-Aachen University, Germany) possesses an external camera and visual processor (Figure 2.13A$_{ii}$). In contrast to the Argus 2 and IRIS 2 device, EPIRET3 uses inductive links instead of a transscleral cable. The group around Peter Walter developed a bidirectional stimulation technique that allows the implant to analyze feedback from specific retinal areas and individually adjust the stimulation [137]. The research group finished a clinical trial with 6 patients [129] and their current product is called Very

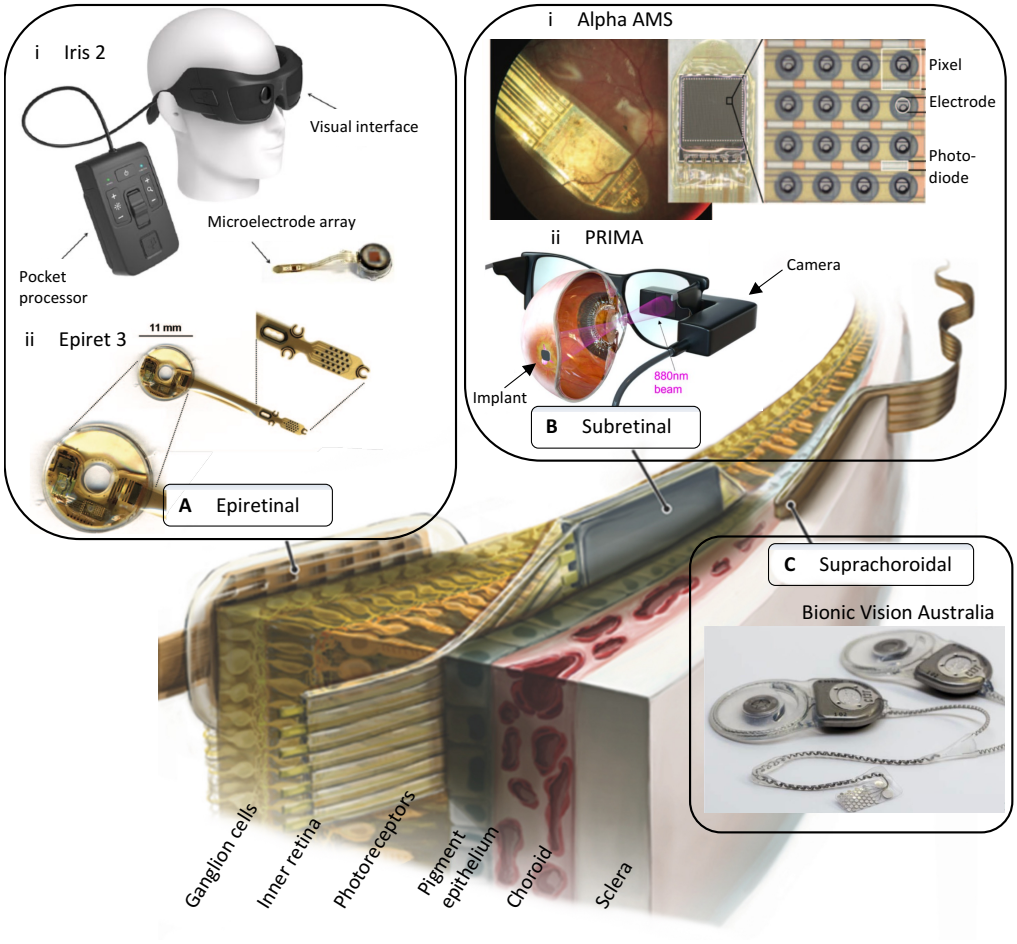

Figure 2.13.: Retinal implants and examples for epiretinal (A), subretinal (B) and suprachoroidal (C) approaches. A) The Iris2 (i) and Epiret 3 (ii) are show as example for epiretinal implants (images modified from [128] and [129]). B) The Alpha IMS (i) and PRIMA (ii) are subretinal implants (images modified from [130] and [131]). C) Bionic Vision Australia works on suprachoroidal implants [132] (overview modified from [133])

Large Array Retina Stimulator (VLARS) aiming to enhance the stimulation array to cover 37° of the field of vision [138][139].

Nano Retina The company Nano Retina is working on an implant to penetrate the retina from the epiretinal side. Their approach compromises a low-power imager that captures the natural eye image at the back of the eye and a dense 3D neural interface made out of nanoneedles. Wireless glasses provide a power source and enable communication with the implant for fine-tuning. During a first clinical trial with nine patients, visual conception was confirmed [140].

Subretinal prostheses

Here, the devices are positioned closer to the target retina, which could result in lower stimulation parameters, but requires intact retinal networks which may not be the case in degenerated retinal

diseases (Figure 2.13B). Additionally, surgical techniques are reported to be more complex [128].

Boston Retinal Implant The Boston Retinal Implant is currently in a preclinical study phase proposing a device with more than 256 electrodes that receive power from wireless inductive coupling [141]. The design is in many ways similar to the Argus 2 implant, but the implant sits in the subretinal space to avoid fixation damage.

Alpha IMS and Alpha AMS The implants by Retina Implant AG, Reutlingen, Germany got CE approved in 2013 (Alpha IMS) and 2016 (Alpha AMS). The devices consist of an array with 1500 (Alpha IMS) or 1600 (Alpha AMS) photodiode-amplifier-electrode-complexes with an inductive power source [142] (Figure 2.13B$_i$). In a clinical trial of the Alpha IMS from 2010 - 2014 86% were able to perceive light and 21% reported to have a very good improvement of their daily life reporting to recognize letters and objects [143]. Nevertheless, 28% of the patients reported sensing no benefit at all. Alpha AMS shows similar functional features, but also a longer lifespan of the product [130].

PRIMA Pixium Vision SA is additionally working in cooperation with Daniel Palanker at Stanford University, USA, on their PRIMA subretinal approach. Here, the image is also captured by camera glasses and projected onto the subretinally placed 378-pixel cells through a near-infrared laser scanner (Figure 2.13B$_{ii}$). Compared to Alpha IMS/AMS, no transcleral cables are needed which prevents the risk of residual peripheral damage during surgery [144]. The device is currently in a clinical trial with patients that suffer from age-related macular degeneration which confirmed the safety of the implant over 18 - 24 months in five patients [144][145].

Suprachoroidal prostheses

With the advantage of being more easily accessible, suprachoroidal implants are further away from the sensory retina, implanted into the sclera underneath the choroid, and consequently require higher stimulation parameters (Figure 2.13C). Another disadvantage is the high number of vessels in the suprachoroidal space provoking the risk of bleeding. There are currently no CE-approved suprachoroidal prostheses.

Bionic Vision Australia The Bionic Vision Australia (BVA) group is investigating a 44-channel implant, which is wirelessly connected by transmission coils, in a clinical trial with patients affected by RP which all reported improvements of their daily life routines [146] (Figure 2.13C).

Suprachoroidal-transretinal Stimulation System Japan's Consortium for Retinal Prosthesis has developed an implant placed in the scleral pocket next to the suprachoroidal space. The 49 protruding microelectrodes made out of Pt wires have a height of 0.5 mm. The device is currently tested on three patients with advanced RP [147].

Outlook: Next generation of retinal prostheses

The commercialization of retinal implants is a challenging endeavor, as evidenced by the experiences of Second Sight and Retina Implant AG, who discontinued their respective projects. Despite these setbacks, they were able to provide significant benefits to numerous patients through their technology. The next generation of retinal implants must leverage the insights gained from past endeavors to overcome the challenges that have been encountered. This could involve employing a larger number of smaller electrodes and targeted stimulation to address a larger visual field. One

example of this is the POLYRETINA implant, which consists of a photovoltaic array with 2215 stimulation pixels and has already been tested on *in vivo* pigs. In addition, the POLYRETINA device with its flexible material follows the curvature of the eye to lie close to the target cells [148][149]. An additional area of focus is the advancement of stimulation strategies. One promising approach is selective stimulation of RGCs, as demonstrated by the group at the Artificial Retina Laboratory at Stanford University [150]. This approach entails the use of penetrating 3D electrodes, fabricated by 2PP, for direct printing on Si. Consequently, the active region of the electrodes is positioned in close proximity to the target cell, thereby reducing the electrode-retina distance. This results in lower stimulation thresholds and enhanced selectivity [151]. Similarly, a group from South Korea currently works on a soft 3D artificial retina approach with micropillars on a soft polymer layer (PI) to adapt to the irregular surface of the retina [152].

3. Materials and methods

This study employed two methodologies for developing 3D neural implants: KiRi and PiRi. One potential solution to reduce the occurrence of FBRs is the use of flexible polymer-based neural probes [153][99][154]. Accordingly, this study employs a 2D flexible MEA with a parylene-C (PaC) substrate and passivation as the foundation for both 3D fabrication processes. The 2D fabrication process was based on preliminary work, which is summarized below. This chapter delineates the microfabrication techniques utilized for the 2D flexible MEA and 2PP for 3D printed electrodes, along with the characterization of the electrodes and the methodology employed for animal experiments.

3.1. Preliminary work

The 2D MEA fabrication process and retinal as well as cortical application protocols are based partly on preliminary work described in [102][155][156][157]. Rincon Montés et al. demonstrated the feasibility of utilizing penetrating 2D Michigan-style MEAs as a bidirectional device for stimulating the inner retina and concurrently monitoring local field potentials and spiking activity of RGCs [78][155]. As a consequence of photoreceptor degeneration, the retina undergoes a reduction in thickness and a remodeling process which leads to an increase in stimulation thresholds. This results in a reduction in the efficiency of current retinal prostheses, which lack the capacity to autonomously regulate this modification. In contrast, the penetrating shanks of the BiMEA device were designed to meet this requirement. The BiMEA device addresses this challenge by offering simultaneous recording and stimulation, thereby facilitating the adjustment of electrical stimulation parameters. To enhance biocompatibility and further optimize the implant, a flexible substrate was incorporated, transforming the Si-BiMEA[78] into a flexible BiMEA[155]. The device has been evaluated in WT and degenerated mouse retinas, demonstrating a reduced insertion footprint while penetrating the tissue [155].
Srikantharajah et al. designed and fabricated flexible PaC-based intracortical Michigan-style arrays to improve the immune acceptance in comparison to stiff Si-based neural probes. The flexible probes, which were implanted in the somatosensory cortex of mice under acute *in vivo* conditions, detected simultaneously LFPs as well as SUA and MUA [102][157].

The flexible BiMEAs for retinal applications are devices with four shanks with three (12-BiMEA) or four (16-BiMEA) IrOx electrodes per shank. As a first fabrication step, a $\sim$3 µm thick layer of PI or PaC was coated onto a four-inch Si wafer. In the first metallization step, a titanium (Ti)/Au layer formed the feedlines, contact pads, and electrodes. A $\sim$1 µm thick flexible layer was then deposited and corresponding openings for the electrodes were etched using reactive ion etching (RIE). Then, a sputtering process formed a stack of Ti/Pt/IrOx/Ti to build up the electrodes on the Ti/Au base. Afterwards, a $\sim$3 µm third flexible layer served as a second passivation layer for encapsulation. Etching for contact pads and electrodes followed likewise. Eventually, soldering of the flexible probes to a 16-channel printed circuit board (PCB) via flip-ship bonding finalized the fabrication of the flexible BiMEA [155]. The design of the flexible BiMEA was adjusted for applications with mouse retina. In this case, the target tissue can be $\sim$200– 220 µm thick in healthy mice retinas and $\sim$100–120 µm in degenerated mice retinas. Therefore, each flexible BiMEA probe consists of four shanks with a length of 140/145, 180/185, or 220/255 µm. The

shanks are 50 or 100 µm wide, ∼7 µm thick and have a tip angle of 30°. The inter-shank distance is 100 µm. Each shank holds 3 or 4 electrodes. The bottom electrode for electrical stimulation has a diameter of 25 µm, while the diameter of the 3 upper electrodes for electrical recording is only 15 µm [155].

The flexible MEAs for cortical applications consist of two 5 µm thick PaC layer embedding a Ti/Au/Ti or Ti/Pt/Ti layer. The electrode sites were opened using RIE. After flip-chip bonding the flexible probes to a PCB, the electrodeposition of PEDOT:PSS was used to improve the electrochemical properties of the electrode. Prior to the deposition, the electrode surface was subjected to 10 cyclic voltammetry (CV) cycles (-0.6 to +0.9 V vs. Ag/AgCl, 0.1 V/s, 0.1 M phosphate buffered solution (PBS)), rinsed with ultrapure water, and activated using oxygen plasma (80 W, 0.8 mbar, 3 min). Subsequently, the electrodes were coated via potentiostatic polymerization for a period of 7-20 seconds at a voltage of 1 V from a solution of 0.1% (w/v) 0.01 M EDOT (Sigma-Aldrich, Germany) and 0.7% (w/v) NaPSS (Sigma-Aldrich, Germany) prepared in ultrapure water [157].

3.2. Microfabrication processes

The following sections describe the microfabrication processes employed to fabricate the 3D implants, which are based on 2D flexible MEAs. Additionally, 2PP, the precise 3D printing technique needed for the pillars of the PiRiimplants and the kirigami molds, is explained. In addition, the details of the electrodeposition processes for filling the aforementioned pillars and the process of PEDOT:PSS electrode deposition are given. A detailed runsheet with all process parameters for the fabrication of 2D flexible MEAs can be found in section A.1.

3.2.1. 2D flexible microelectrode array (MEA) fabrication

The 2D MEA, which served as the base for the development of 3D neural implants consisted of a metal layer stack embedded in two flexible PaC layers. The process flow for the 2D flexible MEA is a combination of microfabrication processes, during which the substrate is modified in z-direction, e.g. through the deposition of layers. The patterns in x-y- direction are done by lithography processes using photo masks, which were designed using computer-aided design (CAD) programs, such as KLayout and CleWin.

Parylene deposition

Parylene is an established designation for polyparaxylylene (PPX), a collective term encompassing a category of linear, non-crosslinked, and semicrystalline polymers belonging to the thermoplasts. Thermoplastic polymeric materials can be molded when subjected to temperatures above their glass transition temperature (≈ 90 °C for PaC [158]) and below their melting point (≈ 290 °C for PaC [158]). The elevated temperatures induce a rearrangement of the chain structures within the amorphous regions of the polymer, thereby facilitating a softening of the material and enabling the reshaping of the molecular structure. Subsequently, the polymer will retain the newly formed shape upon cooling and removal of the mold. To prevent thermal oxidative degradation, thermoforming should be conducted in a vacuum oven [159]. Moreover, a gradual temperature increase and decrease is essential during the heating and cooling phases to prevent the thermoplastic material from failing due to thermal and mechanical stresses. In the process of optimizing a thermoforming protocol, temperature is a more critical factor than time. This is due to the observation that the crystallization reaction is completed during the initial minutes of the thermoforming process [160].

Among the PPX, PaC is the most commonly utilized, frequently employed as a substrate or encapsulation material for neural implants. Its good biocompatibility (FDA approved, USP class VI), chemical inertness, and its capacity to serve as a pinhole-free electrical insulator have collectively contributed to its selection as the substrate and passivation material in the present study [158][161]. The deposition of PaC layer on a Si-host wafer was done via chemical vapor deposition (CVD) using the PDS 2010 Labcoater 2 (Specialty Coating Systems Inc., USA). The deposition process begins with the vaporization of the solid PaC dimer at temperatures reaching up to 170 °C. Subsequently, the dimer undergoes pyrolysis, resulting in the formation of a monomeric gas at temperatures up to 690 °C. Upon reaching the deposition chamber, the gas cools to room temperature and undergoes polymerization on the target under vacuum. This enables the formation of a conformal coating on the target from all sides [161][162].

Photolithography

In photolithography, light-sensitive photoresist is applied to pattern the desired structures onto the substrate. A photolithography process commences with the cleaning and dehydration of the wafer prior to the coating process, which is undertaken to promote adhesion. Thereafter, the liquid photoresists is dispensed onto the wafer, and during spin coating, it is evenly deposited due to centrifugal forces. The spin speed is increased rapidly to a high speed at a constant rate [163]. The thickness of the photoresist h_R is inversely proportional to the square root of the spin speed ω [164]

$$h_R \propto \frac{1}{\sqrt{\omega}}. \tag{3.1}$$

The subsequent step, soft baking, entails the removal of the residual solvent from the photoresist. This is typically conducted at temperatures between 75 and 100 °C. The objective of soft baking is to enhance adhesion and facilitate stress release, which may have accumulated during the spin-coating process. Subsequently, the photoresist films are exposed to light with an appropriate wavelength at a dose D of

$$D = I_L \cdot t \tag{3.2}$$

with exposure time t in seconds and light intensity I_L in W/cm^2 [163]. During the exposure, a photo mask is employed to structure the resist, whereby, contingent on the desired design, specific structures are exposed while others are protected by the photo mask and remain unexposed. However, in this study, the MLA150 (mask-less aligner (MLA)) from Heidelberg Instruments was the primary tool employed for wafer exposure. In maskless lithography, micrometer-sized structures are written onto a photoresist-coated substrate with the aid of a 375 nm laser ("direct writing"). The use of a fabricated photo mask, typically used in a mask aligner (MA), is thus obviated, as the CAD drawing is transferred directly via the MLA150 software. This enables prototyping and fast design adjustments for various needs. The laser is capable of resolving structures down to one micrometer and achieves an alignment accuracy of less than 500 nm [165]. If exposed, the polymer chains of positive photoresists are weakened, whereas the polymer chains of negative photoresists are strengthened by photochemically induced cross-linking. This results in an increased solubility of the positive resist or a decreased solubility of the negative resist in the developer. Consequently, following exposure, the resist mask is a latent image within the photoresist layer, wherein the exposed regions exhibit chemical differences from the non-exposed sites. The necessity of a post exposure bake (PEB) is dependent upon the specific photoresist utilized. For example, the negative resist AZnLOF2020 requires a PEB for the cross-linking process, which renders the exposed structures. In chemically amplified photoresists, a PEB is necessary to amplify chemical reactions, which helps to reduce the exposure dose and accelerate development time. The soluble portions of the photoresist are then removed by immersing the wafer in a developer [163][164].

Metallization

The metal selected for the electrodes must be corrosion-resistant, as the implanted electrodes are in direct contact with the saline fluid in the body. In the absence of such properties, there is a significant risk of releasing toxic substances into neural tissues. Metals that form stable oxide layers and possess a high conductivity are therefore ideal candidates [161]. Thus, in this study, Au was chosen as the electrode material and Ti as an additional layer to promote adhesion to the PaC sheets. The Ti/Au/Ti-layer was deposited via e-beam assisted evaporation using the Balzer PLS 570 onto the patterned wafer. The subsequent lift-off process removed the resist structures in conjunction with the overlying metal layer, resulting in the formation of a structured metal layer that was directly deposited on the substrate [164].

Reactive ion etching

Another possibility to structure layers is using wet or dry etching. In this work, RIE was used to structure the PaC layer using the Oxford PL 100 / ICP (Oxford Instruments, UK) with an etch rate of 800 nm/min for PaC and 6.6 - 10 for Ti nm/min [156]. The process parameters are given in the tables A.1 and A.2.

Packaging

To complete the fabrication process, the flexible probes were detached from the silicon wafer using droplets of water. Subsequently, the probes were affixed to a customized 16- or 32-channel printed PCB via flip-chip bonding. The process was conducted using a hotplate set to 180 °C to heat the PCB. The solder paste Sn42/Bi58 (AMTECH, USA) was deposited, and the high temperature caused droplets to form at the contact pads of the PCB. The temperature was then lowered to 160 °C, which is below the melting temperature of PaC, and the contact pads of the flexible MEA were aligned to the contact pads. To improve the packaging stability, the probe-PCB interface was coated with 1:10 polydimethylsiloxane (PDMS) and subsequently cured at 120 °C for 30 min [156].

3.2.2. 2-photon-polymerization for 3D printed electrodes

For the fabrication of 3D neural implants, the printing of pillars was achieved through the utilization of two-photon lithography, a technique that shares similarities with conventional photolithography methods. Similarly, the structuring process is achieved through the illumination of negative or positive photoresists with light of a precisely defined wavelength. The standard photolithographic process, which is widely used for the fabrication of 2D structures, is based on the principle of one-photon absorption (OPA). In contrast, two-photon lithography is a process based on two-photon absorption (TPA), where a molecule is excited from its ground state to a higher energy level by the simultaneous absorption of two photons. Two-photon lithography can be considered as an additive manufacturing technique. It allows for the fabrication of arbitrary 3D structures with a resolution of 100 nm. In comparison to conventional photolithography, there are three primary advantages: (i) superior resolution, (ii) with high aspect ratios (iii) and the fabrication of complex 3D structures directly from a CAD design. Two-photon lithography is regarded as one of the most versatile and precise additive manufacturing processes and has been employed in a number of bioapplications, including microneedles and microfluidic devices [40].

Two-photon absorption is achieved through the use of an ultrafast laser beam with a high intensity pulse peak. In most cases, near infrared femtosecond lasers, which operate at a wavelength longer than that of ultraviolet (UV) light, are employed as light sources [166]. Upon focusing the

light beam on a small volume of liquid resin, a photosensitizing chromophore is stimulated by the simultaneous absorption of two photons, which then initiates a chain reaction leading to the formation of a polymer. Once a certain threshold of energy is exceeded as a consequence of the absorption, the area around the focus of the light beam undergoes polymerization. While OPA can be considered a linear process, with energy absorption proportional to the intensity of the light, the mechanism of TPA is inherently non-linear. Instead, the absorption is proportional to the square of the laser intensity. Consequently, the absorbed intensity at a distance from the center of the spot, in the case of TPA, exhibits a decay rate that is twice that of OPA, thereby providing a notable enhancement in resolution upon absorption by the photoactive polymer [40][167].

Two-photon lithography was conducted using the Photonic Professional GT2 (PPGT2), a device manufactured by NanoScribe GmbH. The Photonic Professional GT2 (PPGT2) is equipped with a 780 nm pulsed femtosecond fiber laser. The system is calibrated to deliver 50 mW, a power scaling of 1.0, and a laser power of 100%. The selection of an appropriate lens is of great consequence with regard to the resolution capabilities and processing times associated with polymerizations. The use of higher magnification objectives results in enhanced resolution of the fabricated microstructures, although this is accompanied by an increase in processing time. In accordance with the aforementioned considerations, the 25x NA0.8 objective was utilized for micro-scale structures, whereas the 63x NA1.4 objective was employed for high-resolution printing. The PPGT2 is equipped with a galvo scanner, which enables the navigation of the laser through the objective in the xy-direction over the substrate. The resins were employed in the "dip-in" configuration, wherein the objective lens is in direct contact with the resin. Consequently, the photoresist was applied to the substrate, inserted into a holder, and positioned in an inverse orientation over the objective lens, with the system printing in the negative z-axis direction. Subsequently, the photoresist–substrate interface was identified as the origin of the print, either automatically or manually. To achieve efficient polymerization by 2PP processes, parameters must be optimized. The writing speed of the system is inversely proportional to the laser dose, while the laser power is proportional to it. These two factors and the focusing of the laser source control the dose delivered to any volume. Fine features are best suited to lower powers to avoid damage when focusing the laser source. Damage may occur when a given area is overexposed, resulting in heat and gas buildup, which is typically observed as bubbling in the print. When establishing designs for 2PP, it should be considered that it is a fundamental property of voxels that they naturally extend in the z-axis due to the contraction and expansion of the beam around the focus point. Consequently, a mirrored volume is formed above and below the focus point, undergoing polymerization. The x–y geometry is not mirrored, thereby allowing for higher resolutions to be achieved in the x–y plane in comparison to the z-axis [166].

3.2.3. Electrochemical deposition of electrode material and coating

Electrochemical deposition was used in order to fill the 3D printed pillars with a conductive metal, here Au, to form the electrodes. To improve the electrochemical characteristics of the electrodes, PEDOT:PSS was employed as electrode coating for 3D printed electrodes as well as for kirigami electrodes.

Electrochemical depositon of Au

Prior to the electrodeposition of Au, the electrode surface was exposed to oxygen plasma activation at a power of 100 W and a pressure of 0.8 mbar for a duration of one minute. The term electrochemical deposition describes a process whereby active material is deposited on a substrate via a redox reaction. The process was performed with the aid of a multichannel potentiostat (CH

Instruments Inc., USA). To this end, a three-electrode system was employed, comprising a working electrode (an Au electrode of the 2D flexible MEA that will be coated), an Ag/AgCl reference electrode, and a Pt counter electrode. Electrochemical deposition allows for the transformation of metallic ions into a solid metal state, which then deposit onto the surface of the working electrode. This occurs when a sufficient quantity of electric current traverses the electrolyte solution, comprising charged ions generated through the dissolution of an appropriate metallic salt in water [168]. In this experiment, 50 mM $AuCl_4$ in a liquid Au bath aqueous solution was used as the electrolyte. The application of a voltage is a crucial step in achieving effective localized deposition on the desired electrode surface. The deposition then follows the reaction [169]

$$AuCl^-_{4(aq.)} + 3e^- \rightarrow Au_{(s)} + 4Cl^-_{(aq.)} \tag{3.3}$$

The deposition of materials in a controlled area can be achieved through the use of non-conductive masking, whereby the printed hollow pillars are employed as templates. By optimizing the process parameters, it is possible to control the porosity and accuracy of the resulting electrochemically deposited structure. Thus, the deposition of Au was conducted in two stages. In the initial phase, a constant potential of -1.3 V was maintained until the current reached a value of -100 nA, indicating that the pillar was filled with Au. Subsequently, a second step was conducted using a constant current of -100 nA for a duration of 20 seconds to form a conform Au cap [41].

Electrochemical deposition of PEDOT:PSS

PEDOT:PSS is the most commonly utilized conductive polymer due to its biocompatibility, high charge capacity, chemical stability, and commercial availability. Among the characteristics of the poly(3,4-ethylenedioxythiophene (PEDOT) polymer chains is their inherent non-conductivity, their insolubility in common solvents, including water, and their susceptibility to rapid oxidation in air, thereby displaying instability under these conditions. In order for the PEDOT polymer backbone to become conductive, it must undergo oxidation to its cationic form. Consequently, the polymerization process commences with the oxidation of the 3,4-ethylenedioxythiophene (EDOT) monomer, resulting in the formation of positively charged chains. When a current or voltage is applied, two activated monomers combine to create two protons, allowing the positively charged PEDOT chains to emerge. The resulting PEDOT+ is a semiconductive polymer. To balance the positive charge of the PEDOT+, a counter ion is then required. The polymerization in the presence of the negatively charged poly(sodium 4-styrenesulfonate) (PSS) serves as a counter anion to compensate for the positive charge of the PEDOT+ by forming an electrostatically stable bipolymer thin film on the electrode surface [65][170]. Electrodeposition is typically conducted in a three-electrode cell, wherein deposition occurs at the working electrode when the electrode potential exceeds the potential for EDOT oxidation. Electrodeposition may be performed using constant or varying potential, or galvanic deposition with constant or varying current. The structure of PEDOT conductive coatings is dependent upon the materials and methods employed in PEDOT electrodeposition. The choice of co-ion and deposition parameter have an impact on the various stages of polymer growth, with the potential to yield coatings that are smooth and compact or rough and porous [65]. The morphology of PEDOT coatings has been demonstrated to directly influence their electrochemical performance. An increase in coating roughness has been shown to result in an expansion of the actual electrode surface area, which in turn leads to a reduction in electrode impedance [92]. PEDOT ions aggregate on the electrode surface and undergo polymer chain extension, which constitutes the 2D growth phase. When they overlap, 3D growth commences, resulting in the formation of a bulk structures. An elevated charge density at the electrode edges results in the thickening of coatings at the edge of planar electrodes [65][91].
As reported in the literature, CV deposition leads to more uniform coatings with reduced roughness [65]. The objective was to create a smooth PEDOT:PSS coating of the Au cap of the 3D-printed

electrodes. To this end, CV was employed as the deposition method, with the initial voltage set to 0 V, the final voltage set to 1 V, and the scan rate set to 0.1 V/s for 2 to 15 cycles. The solution comprised 0.1 M of EDOT and 75 g/ml of PSS. The deposition process was conducted using a multichannel potentiostat (CH Instruments Inc., USA) with a three-electrode setup, comprising an Ag/AgCl reference electrode and a Pt counter electrode.
In contrast, the objective for planar kirigami electrodes was to enhance the electrochemical characteristics, thereby increasing the surface area and reducing the impedance. Consequently, a constant potential of 1 V was applied for 20 s via chronoamperometry. An EDOT:PSS solution was prepared with EDOT and PSS at concentrations of 0.1% (w/v) and 0.7% (w/v) in deionized water. Prior to the deposition, electrochemical cleaning of the probes was performed in 1x PBS. This involved the application of 10 cyclic voltammetry cycles to all electrodes, utilizing a sweep rate of 100 mV/s and potential limits between -0.6 and 0.9 V versus an Ag/AgCl reference electrode. Subsequently, the surface of the 3D kirigami device was activated with oxygen plasma at a pressure of 0.8 mbar and a power of 80 W for a period of 3 min. Thereafter, the electrochemical polymerization of the EDOT:PSS on the gold-based electrodes was conducted.

3.3. Characterization of neural interfaces

3.3.1. Electrochemical characterization

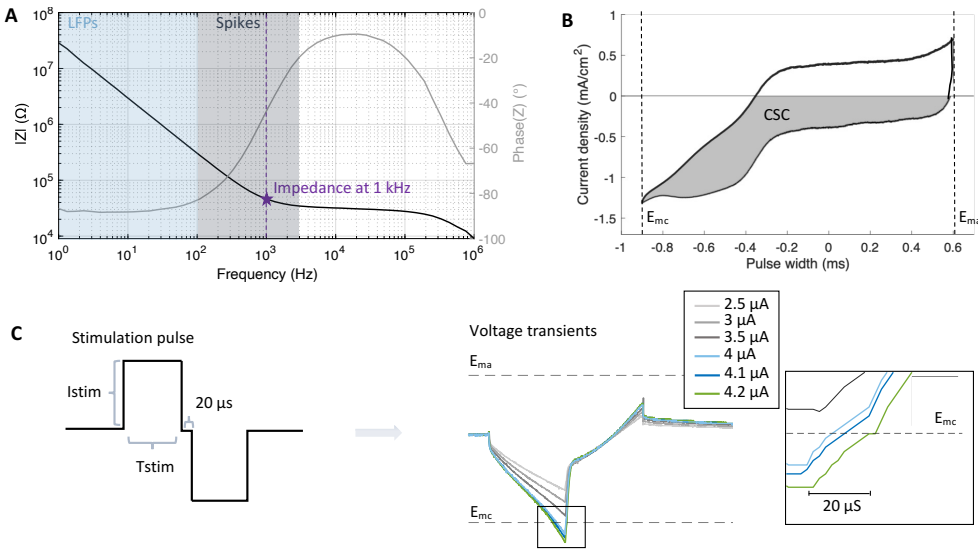

Figure 3.1.: Electrochemical characterization methods of neural implants. A) The bode plot is used to illustrate the impedance of the electrodes, where typically the value at 1 kHz is extracted for comparison. LFPs are measured in the low-frequency range (< 100 Hz) and spikes in the frequency band of 100 to 3000 Hz. B) The CSC is calculated by extracting the integral of the cathodic current I between the potential limits E_c and E_a. C) To define the CIC, voltage transients are measured upon stimulating pulses with varying pulse width T_{ph} and amplitude T_{stim} until the potential limits (cathodic E_{mc} or anodic E_{ma}) are reached.

The impedance of the electrodes was analyzed using electrochemical impedance spectroscopy (EIS) and the VSP-300 potentiostat (BioLogic Science Instruments, France). Here, the microelectrode to be characterized was placed in PBS solution as WE together with a Pt wire as CE and

an Ag/AgCl electrode as RE. During the EIS analysis the response of the microelectrode to a harmonic sinousoidal at a range of frequencies from 10 Hz to 100 kHz was measured. The amplitude of the sinusoidal signal was kept at 10 mV to prevent undesired electrochemical effects at the electrode-electrolyte boundary. The electrochemical impedance $\underline{Z}$ of the system is typically visualized using a Bode plot. An example is shown in Figure 3.1A. Typically, the impedance is evaluated at 1 kHz to facilitate comparison with other research studies [92].

Noise is defined as 'a usually unwanted disturbance, which affects the quality or usefulness of a signal typically by superimposing the signal and thereby obscuring its information content' [171][172]. The noise of an electrode is primarily influenced by intrinsic and external factors. Interference from external power or light sources, or biological noise through the activity of more distant neurons, falls into the former category. Additionally, noise may result from instrumentation noise, which originates from recording hardware, including amplifiers and analog-to-digital converters. With regard to intrinsic noise, the thermal noise is the most significant contributor. The thermal noise, designated as ν_t, can be expressed as a function of the temperature T, the Boltzmann constant k_B, and the frequency range [f_1, f_2] by

$$\nu_t = \sqrt{4k_B T \int_{f_1}^{f_2} Re(Z)df} \tag{3.4}$$

where Re(Z) is the frequency-dependent real component of the complex impedance $\underline{Z}$ of the electrode [171]. When adding the constants into equation 3.4, ν_t at body temperature was estimated by

$$\nu_t|_{T=310K} = 0.13nV \cdot \sqrt{\frac{R}{\Omega}\frac{\Delta f}{Hz}} \tag{3.5}$$

within the frequency band Δf [92]. Therefore, the potential for recording with a high SNR is enhanced by lower impedance, which significantly impacts the value of ν_t [92]. In practice, however, the noise depends on the components of the neural interface at all levels, not merely on the electrode characteristics. As previously stated, the surrounding environment also plays a role. Therefore, in all characterization and electrophysiological measurements, shielding techniques such as measurements in a Faraday cage and proper grounding were employed.

The CSC was measured using CV and the VSP-300 potentiostat (BioLogic Science Instruments, France). Here, the microelectrode was again placed in PBS medium with a Pt CE and Ag/AgCl RE. During CV, the potential at the WE was driven between oxidising and reduction potentials inside the limits of the water window ([-0.9 0.6] for PEDOT:PSS electrodes [173]) at a constant rate of 100 mV/s while monitoring the current. The CSC was then estimated by the integral of the cathodic current I between the potential limits E_c and E_a

$$CSC = 1/(\nu \cdot GSA) \int_{E_c}^{E_a} I(E)dE \tag{3.6}$$

divided by the scan rate ν and the geometric surface area (GSA) of the electrode, as illustrated in Figure 3.1B [92][174].

The CIC was determined using voltage transient measurements measured with a 2208 PicoScope oscilloscope (Pico Technology, UK) which was connected in parallel to the measurement circuit consisting of the microelectrodes connected to the multi channel system (MCS)-setup (described in detail in section 3.4.1) and the Ag/AgCl RE/CE pellet in PBS medium. The maximum

current for a current-controlled stimulation was investigated for which the electrodes are safe to polarize avoiding Faradaic effects. Therefore, the current amplitude of a biphasic, symmetric pulse with 20 µs inter-phase period (i = 0 A) and a constant pulse width T_{ph} was carefully increased until the maximum cathodic E_{mc} or anodic E_{ma} potential limits in the voltage transient measurements were reached (method from [173], illustrated in Figure 3.1C). This way, I_{mc} was found for each pulse width T_{ph}, for cathodic as well as I_{ma} for anodic first symmetric pulses. Then, the CIC was calculated by

$$CIC = \frac{I_{mc} \cdot T_{ph}}{GSA}. \tag{3.7}$$

3.3.2. Mechanical characterization

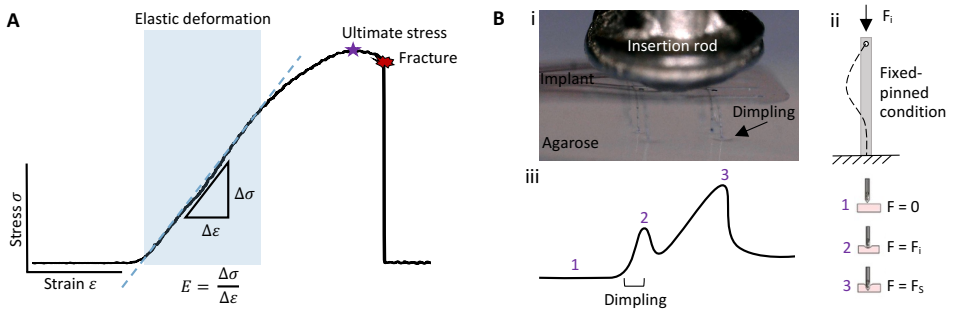

Figure 3.2.: Mechanical characterization of penetrating neural implants. A) To evaluate the Young's modulus and stress/ strain at fracture, a tensile test was performed and the stress-strain curves analyzed. B) Insertion of penetrating probes. During the insertion of penetrating shanks, tissue dimpling is typically observed. B_i shows an example where dimpling of agarose gel was observed. At this stage, a fixed-pinned condition applies (ii). When the insertion force F_i is enough to overcome tissue dimpling, the force during the measurements is rising due to shear forces F_s (iii, adapted from [94]).

The stress-strain curves of thin annealed and unannealed PaC stripes with a length of 25 mm, a width of 1.5 mm and a thickness of 10 µm with 64, 32 and without feedlines were measured using the UniVert tensile tester (Cellscale, CA) with a 1 or 10 N load cell. An example of a stress-strain curve is illustrated in Figure 3.2A. The samples were fabricated according to the protocol described in section 4.1. The probes were affixed to the clamps of the tensile test apparatus with parafilm at their extremities to prevent them from shifting out of the clamps during the course of the test. To ensure consistency in the measurement process, a starting length of approximately 15 mm was utilized, along with a preload of 0.03 N. This approach helped to establish a uniform baseline for subsequent observations. The probe was pulled at a constant velocity of 12.5 mm per minute until fracture. The Young's modulus as well as the stress and strain at fracture, as marked in Figure 3.2A, were evaluated using self-written MATLAB scripts.

The critical buckling load P_{cb} of the neural implants, which are intended to penetrate the tissue, was calculated using Euler's equation

$$P_{cb} = \frac{\pi^2 IE}{(kL)^2} \tag{3.8}$$

where E is the Young's modulus, L is the length of the shank, k is the effective length factor, which is 0.7 for a penetrating shank fixated to a measurement system (fixed-pinned condition, Figure

3.2B$_{i,ii}$) [175]. The second moment of inertia I is

$$I_{column} = \frac{wt^3}{12} \tag{3.9}$$

for a slender column with rectangular cross-section, width w and thickness t, and

$$I_{cylindar} = \frac{\pi}{4} r^4 \tag{3.10}$$

for a cylindrical implant with circular cross-section and radius r [96]. Additionally, finite element method (FEM) simulations using COMSOL Multiphysics for more complex shank or pillar geometries using the solid mechanics module were conducted. A fixed-pinned condition was assumed and an insertion force of 0.5 mN, as reported in the literature [94]. For the material properties of IP-L 780, which was used for the 3D printed electrodes, values given by the manufacturer Nanoscribe were used (Young's modulus = 4.73 GPa, Poisson's ratio = 0.3, and density = 1.17 g/cm^3). For the kirigami electrodes, the Young's modulus for thermoformed PaC (1.7 GPa) as evaluated by the tensile tests, Poisson's ratio = 0.4 [35] and a density of 1.29 g/cm^3 [176] was used.

The insertion force is needed to overcome tissue dimpling, which is typically observed during the insertion of penetrating probes (Figure 3.2B). Thus, the forces during insertion were measured during the insertion of the neural probes inside a tissue phantom (Figure 3.2B$_{iii}$). Figure 3.2B$_{iii}$ summarizes the expected forces. An implantable system should be designed to withstand the insertion force F$_i$ required to overcome tissue dimpling for insertion into soft tissues. Then, as the neural probe traverses the neural tissue, shear forces F$_s$ are occurring. For the measurements of the force-time plots, the insertion rod was mounted on a load cell (FUTEK, LSB200, 20 g) which was in turn fixated to the second micromanipulator used to push the neural probes inside the tissue or, in this case, the tissue phantom. The data acquisition was done using self-written MATLAB scripts as well as the FUTEK USB DLL provided by the manufacturer.

The bending stiffness was computed as the product of the Young's modulus E and the second moment of inertia I and was utilized as an indicator for the compliance of the penetrating probes, which are employed in an invasive electrophysiology method for chronic *in vivo* applications.

3.3.3. Accelerated aging test

Neural implants are expected to last ideally for years. However, it is not feasible to test neural implants over such a long period of time. Thus, accelerated aging tests are needed which simulate aging in a reasonable amount of time. An increase in temperature increases kinetic energy and thereby the velocity of reactions and degradation. The acceleration factor AF is determined by

$$AF = 2^{\frac{T_{ac} - T_t}{10}} \tag{3.11}$$

with the temperature of the accelerated aging test environment T_{ac} and the target temperature T_t. Using a T_{ac} of 60 °C and a T_t of 37 °C (body temperature) the AF is ≈ 5 [92]. During the aging test, the neural probes were immersed in PBS and placed inside an oven at T_{ac}. Electrochemical properties and mechanical properties of the test samples were evaluated as described in section 3.3.1 and 3.3.2 twice a week or once every two weeks, respectively. Additionally, regular inspections using an optical microscope (Keyence VK-X100) and SEM were conducted.

3.4. Cadaveric, *in vitro*, and *in vivo* experiments

The study involved a range of experimental approaches, including *in vitro* (explanted rodent retina and human brain slices), *in vivo* (somatosensory and visual cortex of mice), and cadaveric (open-sky surgery and *pars-plana* implantation with rats and rabbits) experiments (Figure 3.3). Due to the differing requirements of each experimental type, the experimental setups vary slightly. In all cases, the neural probes were inserted from the top using a micromanipulator to ensure precise movement. The ME2100 system by Multichannel Systems was employed for electrophysiological recordings and customized stimulator systems to elicit electrophysiological responses. The measurement systems for *in vitro* and *in vivo* recordings were previously described in [41][177]. Cadaveric experiments were either conducted using the *in vitro* setup (Open-sky surgery) or facilities at the Department of Ophthalmology, RWTH University Hospital (*Pars-plana* implantation).

Neural tissue	Experiment	Setting, Probe type	Model systems	Animal permit	Histology
Retina 	Spontaneous activity & optical stimulation	*In-vitro* KiRi & PiRi	RCS rats (N = 5) WT Wistar rats (N = 6)	2021.A111 2018.A190 & IBI3 OE Ratten, Forschungszentrum Jülich	-
	Spontaneous activity & EIS measurements	*In-vitro* 2D BiMEA	RCS rats (N = 2) WT Wistar rats (N = 4)	2021.A111 2018.A190 & IBI3 OE Ratten, Forschungszentrum Jülich	-
	GABA application	*In-vitro* KiRi & PiRi	RCS rats (N =2)	2021.A111, Forschungszentrum Jülich	
	Insertion footprint	*In-vitro* KiRi & PiRi	Transgenic WT TN-L15 mice (N = 8)	From IBI1, Forschungszentrum Jülich	Dead cell staining using EthD-1; Primary antibodies GFP (for RGC), Cal (for amacrine cells), PEA (for photoreceptor cones)
	Open-sky surgery	Cadaveric KiRi & PiRi	RCS rats (N = 3) WT Wistar rats (N = 4) Albino rabbits (N = 1)	2021.A111 2018.A190 & IBI3 OE Ratten Slaughterhouse	-
	Pars-plana implantation	Cadaveric KiRi & PiRi	Albino rabbits (N =2)	Slaughterhouse	-
Cortex 	Somatosensory cortex implantation and stimulation	*In vivo* KiRi & PiRi	Transgenic WT mice expressing GCaMP6s (N = 7)	81-02.04.2021.A021, RWTH Aachen	Fluorescent infrared dye (DiD) to track implant position, DAPI for cell nuclei
	Visual cortex implantation and stimulation	*In vivo* KiRi	Transgenic WT mice expressing GCaMP6s (N = 2)	81-02.04.2021.A021, RWTH Aachen	DAPI for cell nuclei; Primary antibodies NeuN (for mature neurons), IBA1 (for mature microglia), GFAP (for astrocytes)
	High-potassium stimulation	*In vitro* KiRi & PiRi	Human brain slices (N = 4)	EK067/20 & written consent, RWTH Aachen	-
	Induced epileptic-like activity	*In vitro* KiRi	Human brain slices (N = 6)	EK067/20 & written consent, RWTH Aachen	DAPI for cell nuclei Antibodies NeuN (for mature neurons), GFAP (for astrocytes)

Figure 3.3.: Overview of the conducted experiments.

The ME2100-System (Multi channel systems, USA) was used for electrophysiological recordings. The ME2100 consists of an interface board (IFB), a signal collector unit (SCU) and the headstage amplifiers (Figure 3.4). The IFB is connected to a computer. The Multi Channel Ex-

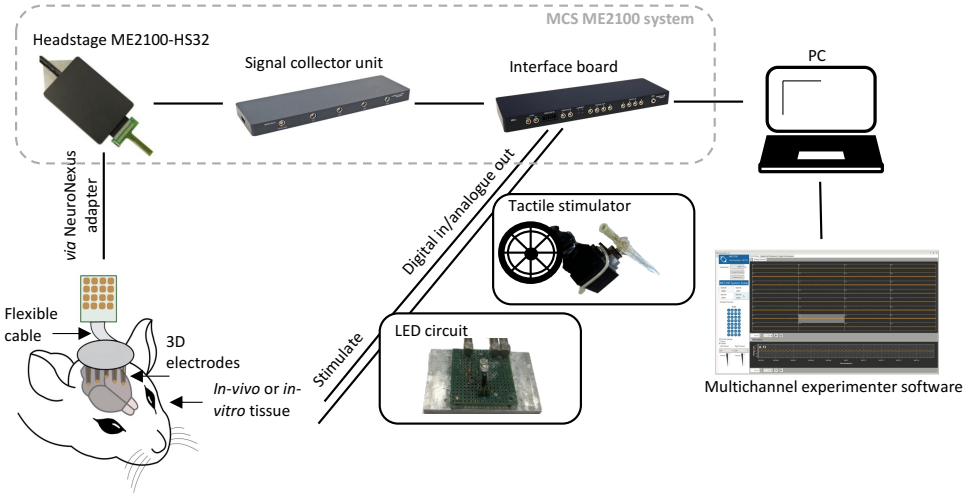

Figure 3.4.: MCS ME2100 recording and stimulation system. The ME2100 system by Multichannel systems consists of a headstage, signal collector unit and interface unit connected to a PC. A LED circuit was used to optically stimulate *in vitro* tissue while a tactile stimulator was used during *in vivo experiments*. Images from [41][178].

perimenter software (Multichannel Systems, USA) was utilized for data acquisition. The ADPT-NN-16/32 or the ADPT-NN-32 adapter from NeuroNexus (USA) was used to connect the neural probes to the ME2100-HS32-M-3m headstage. The headstage has a total of 32 channels that can each be used for recording and electrical current- or voltage-controlled stimulation.

3.4.1. *In vitro* experiments with explanted neural tissue

The *in vitro* setup

The *in vitro* setup consisted of the ME2100-System (Multi channel systems, USA), two micromanipulators (SM6 controller, Luigs and Neumann, Germany, and uMp4, Sensapex, Finland), a light-emitting diode (LED) circuit and a microscope (Keyence Deutschland GmbH, Germany) placed inside a Faraday cage. The prepared tissue was placed on a PDMS pillow inside a transparent perfusion chamber using filter paper and insect pins [155]. The perfusion with aCSF or Ames' medium (depending on the experimental type) was recycled in a closed-loop perfusion system using a REGLO Digital peristaltic pump (ISMATEC, Germany). The medium was bubbled constantly with carbogen gas during the experiments. To perform optical stimulation in retinal experiments, an LED circuit was placed underneath the perfusion chamber and connected to the digital input of the ME2100-System to synchronize the stimulus with the recorded data. To faciliate the insertion, the headstage of the MCS system was connected to a micromanipulator (Luigs & Neumann GmbH, Germany) to bring the 3D neural implant close to the surface of the neural tissue in a controlled manner. Additionally, an insertion rod was mounted on a second micromanipulator (uMp4, Sensapex, Finland) to apply the insertion force which enables the penetration of the 3D neural implant inside the neural tissue. To optically monitor the insertion procedure, a VHX digital microscope (Keyence Deutschland GmbH, Germany) was used.

In vitro retinal applications

Retinal explants from mice and rats were prepared in accordance with the methodology previously described [41][155]. Prior to decapitation, the animals were deeply anesthetized with

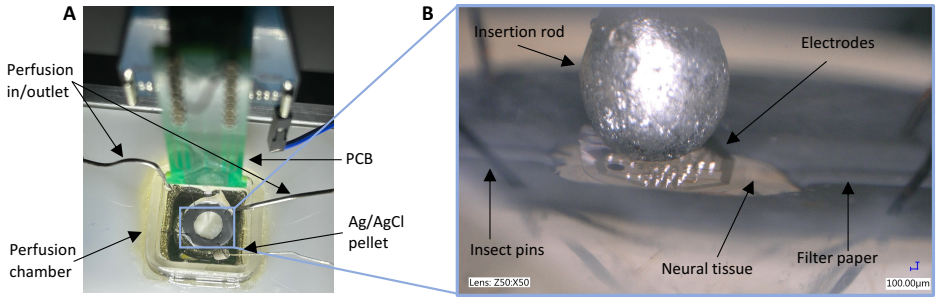

Figure 3.5.: Setup for *in vitro* electrophysiological recordings. During *in vitro* experiments the neural tissue was placed inside the perfusion chamber (A) and the neural probe was inserted from the top using an insertion rod (B). The neural tissue was fixated with filter paper and insect pins. An Ag/AgCl pellet was used as RE.

carbon dioxide or isoflurane. Immediately following the decapitation, the eyeballs were enucleated and immersed in fresh Ames' medium (see Appendix C.1.1). The medium was maintained in a state of constant oxygenation through the use of carbogen gas, comprising 95% oxygen and 5% carbon dioxide (The Linde Group, Germany), with a pH level of 7.4 adjusted through the addition of sodium bicarbonate ($NaHCO_3$). The light-adapted retinas were then isolated under a reflected-light stereomicroscope (Stemi SV-6, Carl Zeiss GmbH, Germany) in conditions of ambient light and at room temperature. An incision was made along the ora serrata to facilitate the extraction of the cornea and lens. The vitreous body was then removed with great care. Subsequently, the procedure was conducted on the second eye with the objective of ensuring constant oxygenation. Next, the posterior eyeball was bisected, and the two retinal pieces were gently isolated. One was returned to oxygenated Ames' medium, while the other was prepared for the initial experiment. At this step, the retina was positioned upon a donut-shaped piece of filter paper, with the ganglion cell layer oriented in a superior position. Subsequently, the specimen was inverted and positioned within the perfusion chamber, where it was secured with insect pins to maintain its position during implant insertion (Figure 3.5).

Optical stimulation of the retinal explants was performed using an LED-circuit consisting of a 5 mm round white LED connected in series with a 61.9 Ω resistor to provide high photopic stimuli (7.96 µW/mm^2) to activate the cones [155]. The LED was placed in close proximity to the retinal explant (below the perfusion chamber) and the circuit was connected to the IFB of the ME-2100 system. Pulses of 500 ms duration with an amplitude of 5 V were sent every 15 s to illuminate the LED.

Histological analysis of retinal explants

In order to assess the biological impact of acute intraretinal insertion of the 3D KiRi and PiRi implants, the TN-L15 mouse strain was employed. This particular mouse strain exhibits a pronounced and highly discernible fluorescence in retinal ganglion cells. Following the retraction of the 3D implants from the tissue, the biological samples were initially stored in freshly oxygenated Ames' medium. Subsequently, the samples were stained and imaged using a confocal microscope, with the resulting images undergoing further post-processing. Cell stainings and confocal imaging were performed at the Institute of Biological Information Processing-1, Molecular and Cellular Physiology (IBI-1) at Forschungszentrum Jülich with the help of Nruthyathi and Prof. Frank Müller.

Cell stainings were conducted following the removal of the 3D implants. Dead cells were stained using ethidium homodimer-1 (EthD-1, ThermoFisher Scientific Inc., USA), a fluorescent cell-impermeable DNA-binding dye. The methodology of the dead cell staining was adapted from previously published reports on *in vitro* staining of live tissue slices [155][156][179]. The staining solution was prepared by dissolving 5 µl of 2 mM ethidium homodimer-1 (EthD-1) with 1 ml of freshly prepared, oxygenated Ames' medium. Each retinal sample was submerged in 700 µl of the staining solution in a 24-well plate. To ensure the viability of the tissue, the well plate was placed within a closed, oxygenated, wet chamber for the duration of the staining process. The staining was then conducted within the wet chamber, utilizing an orbital shaker at 60 rpm for a period of 20 minutes. Subsequently, the dye was removed by washing with fresh Ames' medium for a period of 10 minutes, with constant shaking and oxygenation. Thereafter, the slices were fixed with 500 µl of 4% PFA for 20 minutes and washed in Ames' medium for 10 minutes. The samples were then mounted on a glass slide with a small amount of media for imaging. Following the initial set of confocal images, the samples were stored for subsequent staining procedures. For this purpose, the samples were incubated in 10% sucrose in phosphate buffer (PB) for one hour and 30% sucrose in PB overnight at 4 ℃. Subsequent stainings were then conducted using primary antibody: green fluorescent protein (GFP, raised in rabbit, 1:8000, Abcam- ab290), calretinin (Cal, raised in goat, 1:3000, Chemicon- ab1550), peanut agglutinin biotin (PEA, 1:200, Sigma- l6135); secondary antibody: d α rb Cy2 (1:400, Dianova- 711-225-152), d α gt Cy3 (1:1000, Dianova- 705-165-147) and S A647 (1:100, Invitrogen- S32357) to stain the retinal ganglion cells, amacrine cells and outer segments of the photoreceptor cones, respectively. The fixed retina was transferred to a multi-well plate containing PB for the immunohistochemistry staining. Subsequently, the PB was substituted with the primary antibody (in CTA (5% Chemiblocker (Chemicon International, USA), 0.5% Triton X-100 (Sigma, Germany), 0.05% NaN_3)), and the mixture was then incubated for a period of three days at room temperature. Subsequently, the retina was washed with PB for 1-2 hours and incubated overnight with the secondary antibody (in CTA) at room temperature. The retina was then washed again with PB for 1-2 hours and transferred to a glass slide with ganglion cells facing upwards. The retina was then covered with Aqua Polymount, and a glass coverslip was placed on top.

Confocal imaging of the stained retinal samples was performed using a confocal laser scanning microscope (TCS SP5 II, Leica Microsystems, Germany) to obtain both whole-mount images and images for 3D analysis of the insertion areas. For the acquisition of whole-mount images for an area of 1024x1024 pixels, z-stacks were obtained at varying focal planes with step sizes of 5 µm. 3D images of the whole mount retina were generated by zooming into 1024x128 pixels, with smaller step sizes of 0.5 - 0.8 µm. An argon laser and a helium laser were employed to stimulate the fluorescent samples. The scanning was conducted in a sequential manner using wavelengths: 458 nm to detect the live RGCs, 543 nm to detect the dead cells stained with EthD-1, 594 nm to detect the amacrine cells stained with calretinin (Cal), and 633 nm to detect the cones stained with peanut agglutinin biotin (PEA).

The image processing was conducted using the ImageJ software [180]. Firstly, the regions affected by the intraretinal insertion of each shank or pillar were each manually selected as region of interest (ROI) in the maximum intensity projections of individual and merged channels. The ROIs were delineated around areas comprising dead cells and discernible neuronal loss at the insertion sites. Subsequently, the dimensions of the aforementioned ROIs were quantified and designated as the insertion trauma area (ITA). Then, thresholding was conducted on the maximum intensity projections of the red channel to eliminate background noise. In the subsequent step, watershed segmentation was utilized to remove isolated pixels and facilitate the separation of merged cells. The "Analyze Particles" function was employed to perform an automated count of

dead cells, with a size range of 5-25,000 pixels and circularity range of 0.1-1. For 3D analysis, "3D projects" were created on the small images with numerous z-steps. This enabled the creation of a 3D visualisation of the insertion holes, specifically by rotating the stack by 90°, which resulted in the generation of a cross-sectional view of the retinal layers.

In vitro recordings from human brain slices

The preparation of human brain slices was done by the neurology clinic at Uniklinik RWTH Aachen in accordance with published protocols [181]. Approval was obtained from the ethics committee of the University of Aachen (EK067/20) and written informed consent was obtained from all patients. The human neocortical brain slices were obtained from patients undergoing surgical treatment for epilepsy. The tissue in focus is "access tissue" situated outside the epileptic focus, which has been resected in order to gain access to the pathology. To ensure the integrity of the tissue, the cortex was carefully microdissected and resected with minimal use of bipolar forceps. Subsequently, the tissue was transferred directly into ice-cold aCSF (see Appendix C.1.2), equilibrated with carbogen gas. Once the pia mater had been removed, the tissue chunks were trimmed using a Microm HM 650V vibratome (Thermo Fisher Scientific Inc.) at a vertical angle relative to the cortical surface, thereby encompassing all six layers of the cortex in the resulting slices. Afterwards, the slices were cultured according to pre-published protocols [181] or directly transferred to Forschungszentrum Jülich for acute recordings. Upon arrival at the IBI-3 laboratories at Forschungszentrum Jülich, the slices were placed into fresh aCSF at 36 °C oxygenated with carbogen. For the purpose of electrophysiological recordings, the brain slices were positioned on donut-shaped filter papers, secured with insect pins, and placed within the perfusion chamber of the electrophysiological setup.

The modulation of spiking activity by adjusting the extracellular ionic concentration of human brain slices was performed in accordance with the methodology described in [157]. The tissue was initially perfused with normal aCSF medium, and spontaneous activity was recorded. Subsequently, the perfusion system was used to administer a solution with a high concentration of potassium until a depolarization block was observed. To achieve this, an elevated extracellular concentration of K^+ was generated by supplementing the standard aCSF medium with additional potassium bicarbonate ($KHCO_3$), resulting in a K^+ concentration of at least 20 mM. Once the desired effects were observed, the perfusion with the standard aCSF medium was resumed after 2 - 3 minutes.

Epileptic-like activity was induced by adjusting the extracellular ion concentration in order to study the spread of epileptic activity through the neural tissue. In accordance with the methodology described by Pallud et al. [182], the aCSF medium was modified by increasing the K^+ concentration to 8 mM and reducing the magnesium ion (Mg^{2+}) concentration to 0.25 mM. Following the introduction of the modified aCSF medium, recordings were conducted for a period exceeding 60 min to assess the recurrence of seizure-like events.

A histological analysis was conducted using antibodies targeting the neuronal marker neuron-specific nuclear protein (NeuN) (MAB377, MilliporeSigma (Merck), 1:1000; anti-mouse A48287 (AF555), 1:750) and the microglia/ macrophage marker ionized calcium-binding adaptor molecule 1 (Iba-1) (19-19741, Wako Chemicals, 1:1000; anti-rabbit A32732 (AF488) 1:750). Additionally, the nuclear stain 4'-6-diamidino-2-phenylindole (DAPI) (D9542-1 mg, MilliporeSigma (Merck), 285, 5 nM) was utilized. The human brain slices were washed three times in PBS, incubated for one hour in 15% sucrose, washed again three times with PBS, and then blocked for two hours with

10% goat serum (with PBS-T-T). Subsequently, the samples were incubated with the primary antibodies for a period of three days, after which they were washed again in PBS. Thereafter, the samples were incubated overnight with the secondary antibodies. Following another washing step, the slices were each stained with 250 µl DAPI and then washed again before being immersed in fluoromount.

3.4.2. *In vivo* experiments

The surgical procedure for *in vivo* cortical applications was conducted in accordance with the previously described protocols in reference [41][177]. The mice utilized in the *in vivo* experiments were bred at the Institute of Biology 2 in Aachen, and the *in vivo* surgeries were performed with the help of Prof. Dr. Simon Musall (IBI3, Forschungszentrum Jülich, and Institute for Zoology, RWTH Aachen University). The *in vivo* surgeries, wide-field imaging and histology (brain sectioning and confocal imaging) were performed at the Institute of Biology 2 in Aachen with the help of Prof. Dr. Simon Musall and Peter S. Graff (IBI3, Forschungszentrum Jülich, RWTH Aachen University). The tissue stainings were performed at the Uniklinik Aachen with the support of Dr. med. Henner Koch (Department of Epileptology, Neurology, RWTH Aachen University Hospital).

Surgery for *in vivo* cortical applications

The setup for *in vivo* surgeries of anesthetized mice equally consisted of the ME2100-System (Multi channel systems, Germany) and two micromanipulators for holding the probe and the insertion rod (MTM-3, World Precision Instruments, and uMp4, Sensapex, Finland). For maintaining the mice body temperature, the setup contained a heating pad as well as a sterotaxic frame to fixate the head of the mice. A camera (Leica Microsystems, Germany) was used to capture videos and pictures during the surgery. In order to guarantee the attainment of a high SNR during electrophysiological recordings, all metallic components of the experimental apparatus were grounded.

Prior to the surgical procedure for *in vivo* cortical applications, analgesia was given to the animals by subcutaneously injecting buprenorphine (0.1 mg/kg) and carprofen (4 mg/kg). In addition, local application of bupivacaine was used for local analgesia. The mice were placed on a heating pad to maintain their body temperature and then placed in a stereotactic frame and anesthetized with 1–5% isoflurane throughout the surgical procedure (Figure 3.6A). To ensure stable and low-noise signal recordings, a reference pin was positioned on the cerebellum. The skin covering the skull of the anesthetized mice was incised and retracted laterally in a gentle and controlled manner, following the initial incision. Then, a craniotomy with an approximate diameter of 4 mm was performed on one cerebral hemisphere utilizing an orthopedic drill (Eickemeyer, Germany). Subsequently, the exposed surface of the dura was cleaned and covered with PBS. Then, a minor incision was made in the dura. Following this initial incision, the dura was carefully removed with a hooked needle in order to facilitate access to the cortex. The 3D neural implants were then implanted into the somatosensory or visual cortex, according to the experimental design. To facilitate the insertion process, the neural probes were initially positioned on the surface of the dried cortex using a 3-axis micromanipulator (MTM-3, World Precision Instruments, Germany). Subsequently, an insertion rod, fixed to a second micromanipulator (uMp4, Sensapex, Finland), was utilized to guide the implant's insertion into the neural tissue (Figure 3.6B). The insertion was conducted with incremental step sizes between 100 and 250 µm and a velocity of 200 to 4000 µm/s. Following the successful insertion of a 3D probe into the visual cortex, a glass window was affixed to the implant. Subsequently, the implant was secured to the skull using dental cement. Animals used for chronic implantation, were treated with analgesia for 3 days using a combination of oral administration (buprenorphine, 0.1 mg/ml in drinking water) and subcutaneous injections

(carprofen, 4 mg/kg). After allowing the animal to recuperate, it was utilized for visual stimulation experiments, wherein it was exposed to stimuli of varying complexity.

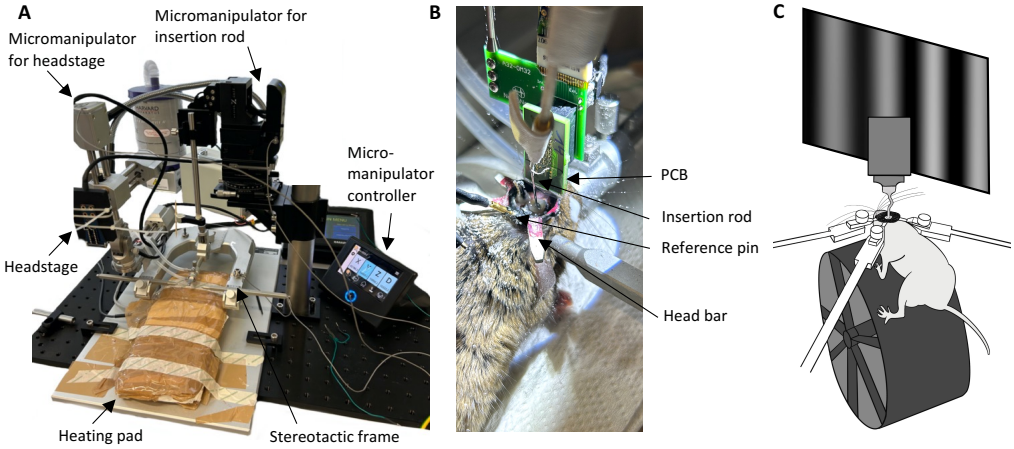

Figure 3.6.: Setup for *in vivo* electrophysiological recordings. For the *in vivo* trials the mice were placed on a heating pad and fixated with a stereotactic frame (A). Two micromanipulators were used for insertion: One to position the neural implant, which was connected to the headstage (A), and another one for the insertion rod (B). A reference pin (B) was used for low-noise signal recordings. For visual stimulation, the awake mice were placed in another setup were they could move on a turning wheel while being exposed to visual stimuli on a screen (C, image from [177])

.

Widefield imaging

Widefield imaging was performed prior to the surgeries to identify an appropriate cortical region for implantation, where a discernible stimulation response was evident. The imaging data were generated and processed at the Institute of Biology 2 in Aachen. A custom-built setup comprising a tandem-lens macroscope and two 85 mm objectives (Walimex Pro 85mm f/1.4 IF; Walimex, Gernaby) was employed for this purpose. Images were acquired with a sCMOS camera (Edge 4.2, PCO, Excelitas, USA) using a Python-based software package [183] at a frame rate of 30 Hz and a resolution of 512 x 512 pixels. The acquisition of frames was conducted under alternating illumination using a blue LED (470 nm, M470L3, Thorlabs, USA) and a violet LED (405 nm, M405L3, Thorlabs, USA). The GCaMP6s fluorescence signals were isolated using a 525 nm emission filter (86-963, Edmund Optics) in front of the camera. Images captured under violet illumination demonstrated calcium-independent fluorescence at the isobestic point of GCaMP57, which is a genetically encoded calcium indicator [184]. Thus, by subtracting the calcium-independent signal linearly rescaled from the calcium-dependent signal acquired under blue illumination, it was possible to eliminate the intrinsic signal resulting from hemodynamic fluctuations. The images were subsequently processed further through the application of self-written MATLAB scripts (MATLAB R2019b, MathWorks).

Stimulation of living mice

Tactile stimulation was used to record neural responses from the somatosensory cortex during widefield or electrophysiological recordings. The custom-built tactile stimulator (Figure 3.4), comprising a rod attached to a small servomotor (TGY-306G-HV) was controlled by a Teensy 3.6 microcontroller (PJRC LLC). The rod was programmed to apply mild pressure to the hindlimb for

a duration of one second every five seconds to elicit electrophysiological responses from the somatosensory cortex. This procedure was repeated for a total of 50 trials. The cortical responses to tactile stimulation during widefield imaging were calculated by determining the averaged cortical activity within the first 150 ms following tactile stimulation. To investigate the electrophysiological responses using 3D implants, the ON time of the stimulator was collected via the SCU of the ME2100-system. Then, the spiking activity during the stimulation was compared against the time outside of the stimulation window. The LFPs were investigated for a window of 500 ms after the onset of the stimuli.

Visual stimulation was conducted in an apparatus designed for awake mice (Figure 3.6C). The mice were permitted to move freely within a rotating wheel while being exposed to visual stimuli of varying complexity on a screen. To identify the location of visual cortical regions, retinotopic mapping [185] was performed during widefield imaging. To this end, a technique was employed involving the presentation of continuous, periodically drifting bars with a flickering checker pattern, characterized by a patch size of 20° and contrast reversal at 3 Hz. The generation of these stimuli was facilitated by the Psychtoolbox, implemented within the MATLAB environment. The patterns were masked, ensuring their visibility was constrained to a 15°-wide bar aperture, which traversed the screen at a rate of 0.5 Hz, encompassing all four cardinal directions in a randomized sequence. The stimuli encompassed approximately 120° horizontally and 80° vertically of the mouse's visual field and were pre-rendered in advance. A spherical correction was applied to compensate for distortions caused by the presentation on a flat monitor. The monitor (XL2420T, BenQ, Taiwan) was positioned at an angle of 20° to the midline and tilted 10° above the animal. The eye was positioned at the horizontal center of the monitor, 30 mm above the lower edge of the monitor, and the stimulus presentation was adjusted accordingly. By combining functional responses and anatomical landmarks, the imaging data were mapped to the Allen Common Coordinate Framework (ACF) [186] to reliably identify the location of the primary visual cortex and the surrounding higher visual areas [187]. In order to elicit diverse neural responses across cortical regions, which were captured with the 3D implants, a basic moving grating stimulus or a more complex broadband random phase texture was utilized. The initial stimulus consisted of a full-field horizontal grating with a spatial frequency of 0.04 cpd, moving with a temporal frequency of 1 Hz. The second stimulus consisted of a full-field array of localized moving gratings characterized by random positions, encompassing orientations between 0 and 45 degrees and spatial frequencies between 0.004 and 0.4 cpd. The experiment involved the pre-rendering of all stimuli in Matlab and their presentation for a duration of five seconds, followed by a five-second inter-stimulus interval. During this interval, a mean gray screen was displayed. The sequence of gratings and broadband stimuli was randomized, with a total of 50 repetitions being conducted for each condition.

Post-explantation inspection and histology

The implanted region as well as the neural interface were inspected after implantation according to the protocols published in [41][177]. The extracted implants were optically inspected using SEM and the rodent brains were sectioned, stained and inspected using confocal imaging and fluorescence microscopy.

The positioning of the implant within the brain was investigated by utilizing a fluorescent dye. To this end, the 3D MEAs were coated with a fluorescent infrared dye (DiD V22887, ThermoFisher, USA) that had been dissolved in ethanol prior to implantation. For this procedure, a 10 µL drop of the DiD solution was placed on the implant, resulting in a thin layer of DiD being deposited on all shanks or pillars after the ethanol fully evaporated. Subsequent to the insertion of the implant, the probe remained in the tissue for approximately 30 minutes. Following the slicing of the

brain, the slices were mounted on cover slides and fixed with mounting medium containing a DAPI stain (Fluoromount, Thermofisher, USA). The cover slides were then sealed with nail polish, and confocal microscope images of the cortical slices and the pillar implantation sites were obtained.

The brain was sectioned at the Institute of Biology 2 in Aachen. Prior to the initiation of perfusion, the mice were anesthetized with 5% isoflurane in oxygen and administered additional analgesia (buprenorphine, 0.1 mg/kg). Subsequently, a lethal dose of pentobarbital (150 mg/kg) was injected, and the mice were perfused with PBS following the termination of the respiratory reflex. After that, the mice were perfused with 4% paraformaldehyde (PFA). Subsequently, the implants were meticulously retracted, and the brain was carefully evacuated from the cranial cavity. The brain was then subjected to an additional period of fixation for one day, after which it was prepared for cryosectioning. For the purpose of cryoprotection, 10% sucrose in 1x PBS was used to immerse the brains overnight, followed by 30% sucrose in 1x PBS until sectioning. The frontal lobe and cerebellum were dissected and the remaining brain was immersed in Tissue-Tek O.C.T.^{TM} compound and frozen. A LEICA CM3050 S cryostat with a chamber temperature of -23 °C and an object temperature of -21 °C was used for sectioning. The frozen brain was sectioned horizontally at a thickness of 20 µm. Sections were collected on adhesive slides (Epredia^{TM} SuperFrost Plus^{TM}), dried, and stored at -80 °C until staining.

Staining of rodent brain sections was performed in a manner similar to that of human brain slices using antibodies NeuN and Iba-1 as well as DAPI staining at University Hospital in Aachen. After thawing and drying, the brain slices were washed in PBS, incubated in PBS-TT for 30 min, washed three more times in PBS, and blocked in 10% goat serum for 60 min. They were then incubated with the first antibody overnight, washed again, and incubated with the second antibody for 90 min, followed by a final wash. Samples were then stained with DAPI, washed and incubated in 200 µl TrueBlack (Cat. No. 23007, Biotium, USA) diluted 1:20 in 70% ethanol for 30 s. The samples were embedded in Fluoromount after a final wash.

Images of mouse brain slices were obtained using an Echo Revolution fluorescence microscope (ECHO, Germany) and a confocal laser scan microscope (Zeiss LSM 710, Germany). Confocal images were obtained at a 10x magnification with a pixel dwell time of 1.24 µs and laser wavelengths of 405 nm (blue), 488 nm (green), 561 nm (red), and 630 nm (far red) with laser powers of 2.6%, 2.2%, 1.0%, 3.0%, and a gain of 720, 780, 800, and 750, respectively. Confocal images at a 20x magnification were obtained with a pixel dwell time of 0.93 µs, and laser wavelengths of 405 nm (blue), 488 (green), 561 (red), and 63 3 (far red) with laser powers of 1.5%, 1.0%, 1.0%, 1.0%, and a gain of 620, 720, 800, and 670, respectively

Images were processed using ImageJ [180]. First, ROIs were selected using the wand tool. Subsequently, the image was separated into channels and the threshold was adjusted. The watershed algorithm was then employed to separate overlaying cells. The particles were enumerated for the blue (DAPI) and red (NeuN) channels. To calculate the mean gray values within the ROI and a reference ROI (500 x 500 µm, placed 500 µm away from the implantation site), the relative fluorescence intensity was determined.

3.4.3. Processing of electrophysiological recordings

The data files acquired with the ME-2100 system and the Multi Channel Experimenter software, were first converted into hdf5-files using the Multi Channel DataManager software (Mutlichannel systems, USA). The McsMatlabDataTools Matlab toolbox [188] and self-written scripts were used

to import and offline process the hdf5-files as reported in [41][177]. The raw traces were band-pass filtered with cut-off frequencies of 100 Hz and 3 kHz using a zero-phase 6th order Butterworth filter to extract spiking activity. The LFPs were low-pass filtered at 100 Hz. The high-frequency oscillation (HFO)s were filtered with a 10th order Butterworth bandpass filter with cut-off frequencies of 250 and 350 Hz. Spike sorting was done using the UltraMegaSort2000 algorithm [189].

The SNR was calculated as the ratio of the spike amplitude divided by the standard deviation of the noise, which corresponded to a 10-ms-long period of the signal devoid of any spiking activity.

More specific processing exceeding these basic descriptions are explained in the corresponding section of each application.

3.5. Statistical analysis

Throughout this work, data is shown as mean ± standard deviation if not stated otherwise. Statistical testing was performed with self-written scripts in Matlab (The MathWorks Inc., USA) using the "Statistics and Machine Learning" toolbox. Normality of data was tested applying the Lilliefors test. For post-hoc pairwise testing, Bonferroni correction was applied. All statistical tests were performed with a confidence interval of 95%. P-values less than 0.05 are indicated with an asterisk (*), p-values < 0.01 with (**), and p-values < 0.001 with (***), respectively. Table 3.1 summarizes the applied tests throughout the manuscript.

Testes parameter	Section	Applied statistical tests
Electrochemical impedance	5.1	Unpaired t-tests
Mechanical properties during aging test	5.3	One-way ANOVA and post-hoc pairwise t-tests
Insertion footprint (Dead cell count and ITA)	6.3	Unpaired t-tests
Firing rate before vs. during a seizure-like event (SLE)	7.1.2	Paired t-test

Table 3.1.: Summary of the statistical tests applied in this work.

4. Development of flexible 3D neural implants

Two types of flexible 3D probes were developed, characterized, and extensively validated in cadaveric, *in vitro*, and *in vivo* applications: A) Kirigami electrodes fabricated by a matched-die forming technique (KiRi) [177][190] and B) 3D printed electrodes on flexible substrates (PiRi) [41][191] (Figure 4.1). The PiRi process was established and the molds for the KiRis were developed in collaboration with Dr. Ing. Jamal Abu Shihada (IBI-3, Forschungszentrum Jülich, and RWTH Aachen University) [192]. The PiRis are currently fabricated and further optimized by Simon Decke (IBI-3, Forschungszentrum Jülich, and RWTH Aachen University). Further discussions of the 3D printing and electrodeposition processes of the PiRis can be found in [192].
The contents of this chapter are reproduced from the following works:

- J. Abu Shihada* and **M. Jung***, S. Decke, L. Koschinski, S. Musall, V. Rincón Montes, A. Offenhäusser. "Highly Customizable 3D Microelectrode Arrays for In Vitro and In Vivo Neuronal Tissue Recordings". Advanced Science 2024, DOI: 10.1002/advs.202305944 (**Equal contribution*)

- Patent application: Shihada, J.A., Offenhäusser, A., **Jung, M.**, Rincón Montes, V., Koschinski, L. " Herstellung dreidimensionaler Elektroden mittels schablonengestützter elektrochemischer Abscheidung ". Patent application: DE 102023102460.4; PCT/EP2024/052176, filed on February 1, 2023.

- **M. Jung**, J. Abu Shihada, S. Decke, L. Koschinski, P. S. Graff, S. Maruri Pazmino, A. Höllig, H. Koch, S. Musall, A. Offenhäusser, V. Rincón Montes. "Flexible 3D *Kirigami* Probes for In Vitro and In Vivo Neural Applications". Advanced Materials 2025, DOI: 10.1002/adma.202418524

- Patent application: Rincón Montes, V., **Jung, M.**, Shihada, J.A., Offenhäusser, A., Koschinski, L. "Herstellung dreidimensional strukturierten Elektrodenlagen, insbesondere im Kirigami-Prinzip". Patent application: DE 102023102257.1; PCT/EP2024/051829, filed on January 30, 2023.

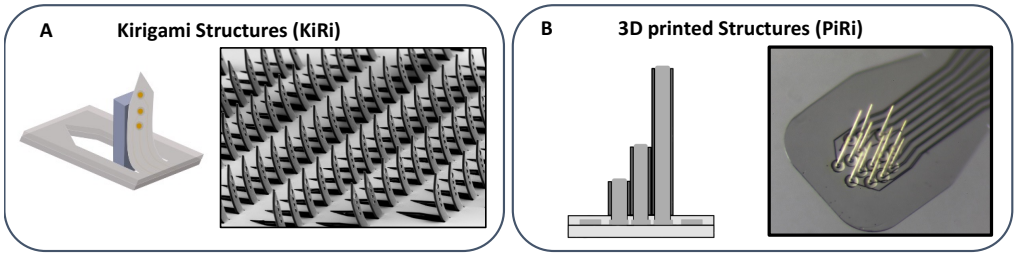

Figure 4.1.: Concepts for the development of 3D neural implants: Kirigami electrodes (A) and 3D printed electrodes (B).

The fabrication of both types of 3D flexible implants commenced with the fabrication of 2D flexible MEA as described in section 4.1. In the following sections, the KiRi and PiRi processes are described.

4.1. Fabrication of flexible MEAs for 3D implants

The fabrication of 2D flexible probes (Figure 4.2) involved the deposition of two flexible thin film layers, and one metal layer. While the 2D fabrication process is based on preliminary work as described in section 3.1, the processes were adjusted and optimized to meet the requirements for this study, as described in the following section. All steps were conducted in a certified clean room environment to ensure a stable fabrication process [193]. Further details of the fabrication process are given in the appendix section A.1.

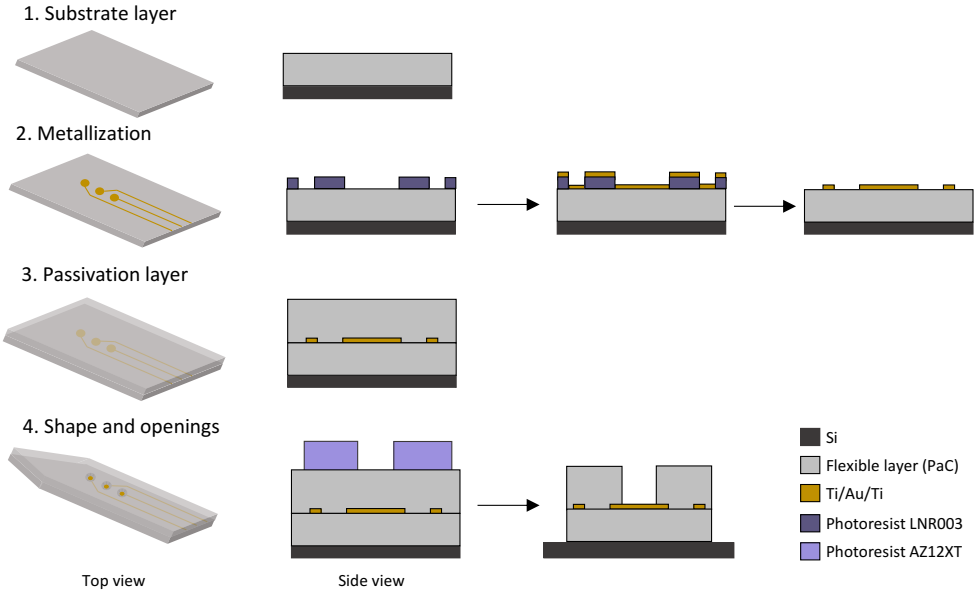

Figure 4.2.: 2D flexible MEA fabrication process flow. The process consists of the substrate deposition (PaC), a metallization step, passivation layer deposition (second PaC layer) and the etching of the shape and openings for electrodes and contact pads.

4.1.1. Fabrication protocol for a 2D flexible microelectrode array (MEA)

1. Substrate layer

For fabrication of 2D flexible MEAs, 5 µm PaC were first deposited on a host Si-wafer via CVD as described in section 3.2.1. A PDS 2010 Labcoater 2 (Specialty Coating Systems Inc., USA), 10 g of PaC dimer, and a process vacuum pressure of 25 mTorr were used for the deposition.

2. Metallization

Subsequently, a metallization process was conducted utilizing photolithography processes, e-beam assisted evaporation and a lift-off technique as described in section 3.2.1 and 3.2.1 (Figures 4.2, and 4.3A,B). In this step, the metal base layer for contact pads, feedlines, and electrodes was patterned. This was accomplished by spin-coating the negative photoresist AZ LNR-003 (Micro-Chemicals GmbH, Germany) at 4000 rpm for 45 seconds with a ramp of 500 rpm/s. AZ LNR-003 was selected as it allows for feedline widths $\leq$ 3 µm and a strong undercut for a reliable lift-off

process. This was followed by a soft-bake at 120 °C for 2 min on a direct contact hot plate. Subsequently, the photoresist was exposed at 320 mJ/cm^2 with a defoc of 2 and a critical dimension bias (CDB) of 800 using UV radiation at 375 nm with an MLA (MLA 150, Heidelberg Instruments, Germany). Then, a post-exposure bake step at 100 °C for 1.5 min on a direct contact hot plate was conducted, followed by a developing step in AZ 326 MIF (MicroChemicals GmbH, Germany) for 90 s and a cleaning step in deionized water. The results of the patterned AZ LNR-003 layer are visualized in Figure 4.3A. Subsequently, the wafer was evaporated with a metal stack comprising 20/100/10 nm of Ti/Au/Ti, utilizing an electron-beam assisted evaporation apparatus (Balzer PLS 570, Pfeiffer, Germany). In this instance, a tungsten liner was employed, with deposition rates of 0.1 and 0.5 nm/s utilized for Ti and Au, respectively. After that, a lift-off process was conducted in an acetone bath for a period of 2.5 - 3 hours, with the objective of removing the sacrificial material and photoresist (Figure 4.3B). Following the lift-off process, the wafer was rinsed in isopropanol for a period of 2 min and subsequently dried with the use of a nitrogen gun. It is also possible to perform the UV exposure step using standard UV photolithography with the aid of a broad band MA (Süss MA8/BA8, Germany), with a dose of 100 mJ/cm^2. Nevertheless, the MLA provides the advantage of rapid adaptation to design alterations due to the lack of necessity for photo masks and the direct implementation of designs via the MLA150 software.

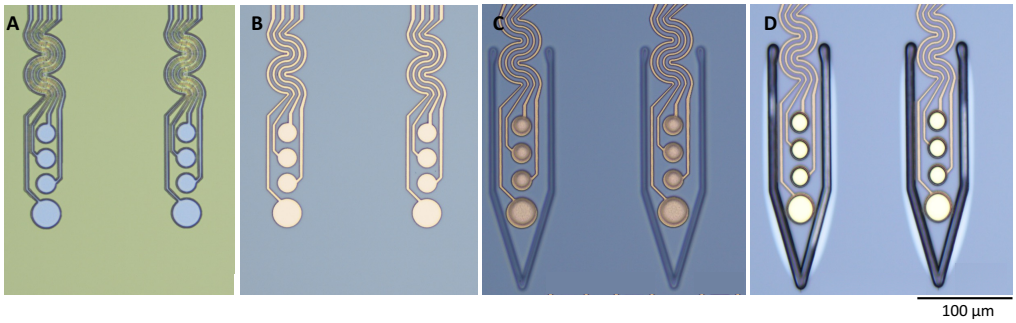

Figure 4.3.: 2D flexible MEA fabrication process results. A) Patterned LNR003 on PaC substrate, B) after lift-off, C) patterned AZ12XT, D) after RIE.

3. Passivation layer

A second flexible PaC layer with a thickness of 5 µm was deposited as described in step 1. This layer served as the passivation of the feedlines.

4. Shape and openings

In this phase, the flexible polymer passivation was removed from the electrodes, contact pads, and the device's outline. First, an etch mask was created using a thick positive photoresist (Figure 4.3C). The etch mask was patterned on the final PaC layer by spin-coating the photoresist AZ 12XT (MicroChemicals GmbH, Germany) at 1000 rpm for 180 seconds with a ramp of 200 rpm/s. After performing a soft bake using a hot plate at 110 °C for 4 min, the material was exposed to UV at 375 nm with a maskless aligner to a dose of 350 mJ/cm^2, a defoc of 2, and a CDB of -800. Subsequently, the wafer was exposed to a post-exposure bake, which involved heating it on a hot plate at 90 °C for one minute. This was followed by a developing step of 2 min, during which AZ 326 MIF was used. Following the patterning of the etch mask, a RIE step was conducted using an oxygen/carbon dioxide (O_2/CF_4) gas mixture of 36/4 sccm, respectively, with radio frequency (RF) and inductively coupled plasma (ICP) powers of 50/500 W, with the objective of etching

PaC (Figure 4.3D). A second RIE step was performed to etch the top 10 nm Ti layer using an O_2/argon (Ar) gas mixture of 20/20 sccm with an RF power of 150 W for 1:15 min. Following RIE, the etch mask was stripped using AZ 100 remover (MicroChemicals GmbH, Germany) in a two-bath system. In the initial bath, an ultrasound bath with low power was employed for a duration of 5 min, followed by a second bath utilizing fresh AZ 100 remover without ultrasound. Subsequently, the wafer underwent a rinsing process in three baths of isopropanol.

4.1.2. Challenges of the 2D microelectrode array (MEA) fabrication

During the microfabrication of the 2D flexible MEAs several challenges were encountered. As described in the following sections, most of these challenges could be addressed to a certain extent.

The photolithography step for the metallization process required optimization. In contrast to previous works, an MLA was employed in preference to an MA due to the advantage it offers of not requiring a photo mask, but only a CAD design file converted by the software. Consequently, an effort was made to optimize the photoresist AZ nLOF2020, which had been utilized in previous works (such as in [156]). Nevertheless, despite repeated attempts at optimization, residual photoresist remained at the feedlines, resulting in an unsharp feedline profile (Figure 4.4A$_i$), which may have implications. For instance, it was not feasible to pattern metal feedlines with a width of $\leq$ 3 µm (Figure 4.4A$_{ii}$). Furthermore, the formation of irregularities in the PaC passivation layer, which were observable after the stripping of the resist (after RIE), were attributed to the aforementioned resist residues and may be an indication of water entering the structure (Figure 4.4A$_{iii}$). The long-term impact of this phenomenon is yet to be determined. It was thus decided to employ AZ LNR003 instead, which led to clean feedlines without irregularities in the PaC passivation after resist stripping (Figure 4.4A$_{iv}$). Optimization of the resist was required in order to create long feedlines that were closely spaced. At a dose of 240 mJ/cm^2, AZ LNR003 was observed to lack stability between long and closely spaced (< 5 µm) feedlines (Figure 4.4A$_v$, black arrow). In contrast, a dose of 320 mJ/cm^2 resulted in the attainment of clean feedlines of width $\approx$ 2 µm (Figure 4.4A$_{vi}$). Another beneficial outcome was the reduction in exposure time for a 4-inch wafer with AZ LNR003 and a dose of 320 mJ/cm^2, which required $\sim$ 1 h, a duration that is only half of the exposure time required for AZ nLOF2020 (exposure dose of 670 mJ/cm^2).

Irregularities in the metallization layer were observed while depositing the Ti/Au/Ti layer on PaC via e-beam assisted evaporation. The utilization of a tungsten liner that was thermally insulated proved effective in eliminating the Au bumps that were observed on the PaC surface (Figure 4.4B). It is crucial to ensure that the Au surfaces are free of contamination and irregularities, such as bumps, to guarantee a uniform current density during electrodeposition of subsequent electrode coating material. Otherwise, the coating adhesion and long-term performance may be affected.

The occurrence of micro-cracks in the PaC layer during RIE was attributed to thermal stress (Figure 4.4C$_i$), a phenomenon previously documented by [194]. The majority of observed micro-cracks were located at sharp edges of the structures, from which they extended, thereby resulting in the exposure of the feedlines from the PaC passivation or even damaging them. Thus, in the design of the outline of the shape for the flexible probes, it is of great importance to utilize rounded edges in order to limit the stress. Given the etch rate of 0.8 µm/min for PaC [156], a total etching time of 15 min can be expected for a 10 µm thick PaC layer. However, the etching process was observed to exhibit inhomogeneity, with a more pronounced effect observed in the central region of the wafer in comparison to the surrounding areas. To circumvent the formation of micro-cracks,

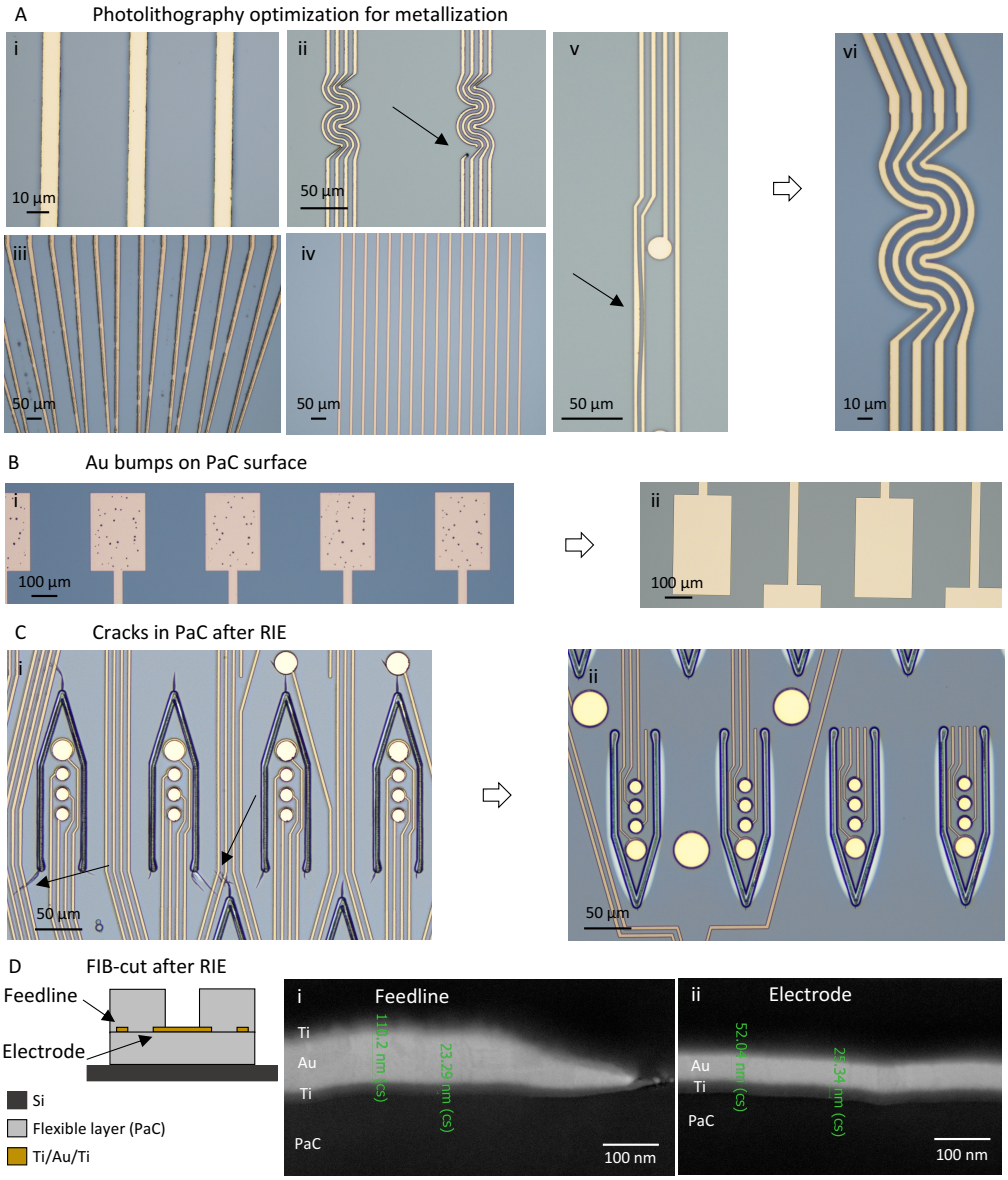

Figure 4.4.: 2D flexible MEA fabrication challenges. A) Photolithography optimization for the metallization. Optimizing the photoresist AZ nLOF2020 did not succeed using the MLA150 due to resists residues on the feedlines (i), which led to irregularities in the PaC passivation (iii) and the inability to achieve structures ≤ 3 µm (ii, black arrow). In contrast, the use of AZ LNR003 resulted in clean feedlines (iv). The exposure dose of AZ LNR003 had to be optimized for closely spaced, long feedlines (v) to at the end achieve clean feedlines down to ≈ 2 µm (vi). The metallization step itself was optimized to prevent Au bumps on PaC (B_i and B_{ii}). The RIE step needed to be optimized to avoid cracks in PaC (C_i and C_{ii}). However, the FIB-cuts after RIE revealed that the Au layer was thinner at the electrode (D_{ii}) in comparison to the feedline (D_i).

the dry etching process was conducted in a stepwise manner, with the wafer undergoing optical inspection after 12 min and subsequently at one-minute intervals. As a result, the formation of

minor cracks was largely prevented (Figure 4.4C$_{ii}$). As an alternative, the AZ12XT layer should be made thicker in order to provide additional protection for the PaC layer. Furthermore, an aluminum ring was utilized to prevent the wafer from contacting the clamps within the RIE machine chamber, where it could otherwise become stuck due to photoresist melting. However, resist-free edges of the wafer, as previously described in [156], were still employed to further minimize the thermal stress and thereby the occurrence of micro-cracks.

The thickness of the metal layer was investigated using FIB-cuts, which were employed to reveal the side profile of the samples. The electrode area, which was etched open using RIE, and the feedlines, which were embedded between two layers of PaC, were then inspected and compared using SEM. At the electrode site, a first RIE step was utilized to remove the PaC passivation. During this step, it is essential that the Ti-etch stop layer protects the underlying Au layer throughout this process. Subsequently, the Ti layer was removed in a second RIE step, thereby exposing the underlying Au layer. In contrast, the feedlines remained unaffected by the RIE steps. The FIB-cuts revealed that the Au/Ti layer was $\sim$110 nm thick at the feedlines (Figure 4.4D$_i$), which is consistent with expectations. However, the Au layer at the electrode was only approximately half as thick (52 nm) 4.4D$_i i$). This indicates that the RIE step is not functioning optimally, with a significant portion of the Au layer undergoing etching. Further investigation and improvement of this process are necessary to ensure a stable Au layer at the electrode.

4.2. 3D flexible kirigami implants

For kirigami implants, matched-die forming was used to form a 3D implant from the 2D MEA. Therefore, the design of the 2D MEA was created in such a way that mechanical actuation can be employed to fold the shanks at a 90 ° angle by sandwiching the 2D flexible probe between a lower and upper mold (Figure 4.5). The lower mold was composed of blocks positioned at the locations where the shanks are to be situated. The upper mold was constructed with walls that ensure uniform pressure upon folding. The lower and upper molds, as well as the 2D flexible probe, were designed to fit inside each other according to a key-lock principle, which facilitated alignment. The stack of molds and the 2D flexible probe were gently pressed together, resulting in the simultaneous folding of all shanks. Following the thermoforming at 160 °C, the flexible probe was separated from the molds, and the shanks maintained their folded position.

4.2.1. 2D design and fabrication for kirigami implants

For kirigami implants, three to four electrodes were positioned on a single shank, which is intended to penetrate electrogenic tissue (similar to flexible 2D BiMEA probes [155]). In order to achieve a successful parallelized kirigami approach, the design of the 2D pattern exclusively matched the molds of the lower mold enabling the parallel folding of the shanks. The 2D pattern comprised the cut-outs of the structures that were folded into the 3D dimension, in addition to openings for electrodes and contact pads, as well as the outline of the shape of the implant. The implant design included the contact pad area, which facilitated a further connection with a PCB, a flexible cable, and the shank holder, encompassing the outline of multiple shanks, each comprising multiple electrodes (Figure 4.6).

The objective was to develop an intraretinal application, which led to the design of the KiRiRet implant (Figure 4.6A). In this instance, the flexible cable was available in lengths of either 1, 1.5, or 2 cm, contingent on the intended application and the animal model (e. g., mouse, rat, or rabbit, respectively). The shank holder (Figure 4.6A$_{ii}$ and Figure 4.7A$_i$) was composed of 32 shanks,

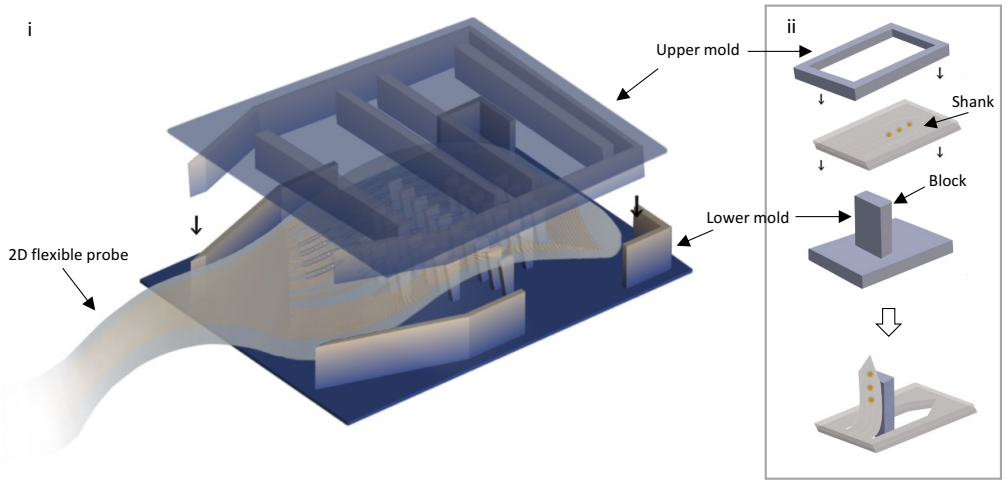

Figure 4.5.: Fabrication of a 3D kirigami implant from a 2D MEA. The 2D flexible MEA is sandwiched between two molds which allows for the simultaneous folding of all shanks in an upright position (modified from [177]).

each measuring 50 µm in width and 225 µm in length (Figure 4.6A$_{iii,iv}$ and Figure 4.7A$_{ii,iii}$), distributed in a uniform manner at intervals of 100 µm across the shank holder. Each shank (i.1, i.2, i.3, and i.4) contained three or four electrodes with a vertical inter-electrode distance of 12 µm. The diameters of the stimulation and recording electrodes were 25 µm for i.1 and 15 µm for i.2-4, respectively. At the folding point, the feedlines were less than 3 µm wide, whereas at the holder's remaining regions, they had a width of 4 µm and 5 µm at the cable. Furthermore, to mitigate the mechanical stresses associated with folding, meander structures were incorporated into the feedlines at the folding point of the shanks (Figure 4.6A$_{iii}$) and compared with straight feedlines (Figure 4.6A$_{iv}$).
To facilitate access to all three dimensions of the target tissue (including the surface), the KiRiRet implant incorporated surface electrodes for epiretinal coupling. Additionally, a surface electrode with a diameter of 230 µm was implemented which can be used as a reference/counter electrode during electrical stimulation or recording, or for impedance measurements. To ensure the proper functionality of the internal reference/counter electrode (low impedance), a geometric surface area of $\sim$ 1.5 times the surface of all the recording/stimulating electrodes was considered.
The KiriCor implant (Figure 4.6B) was designed for intracortical applications. The device comprised eight or ten shanks with three or four electrodes positioned over the shank holder (Figure 4.6B$_{ii}$), with an inter-shank distance of 250 µm. As a proof of concept, the electrodes were distributed along the 500 µm long shanks with a pitch of 80 µm with the objective of recording from different cortical layers (Figure 4.6B$_{iii,iv}$). It is important to note that breaking points were added along the length of the KiriCor shanks to prevent them from moving due to electrostatic forces after the formation of the cut-outs and before the assembly of the folding process. This ensured the correct alignment of the 2D pattern of the flexible probe onto the lower mold. Then, under the influence of the mechanical forces exerted during the folding process, the breaking points were subject to cracking, thereby facilitating the upright folding of the shanks. The width of the breaking points and the width of the cut-out were optimized in order to create a thin breaking point that would be strong enough to survive the mechanical forces until the folding process, while also being able to break easily upon folding. Here, the dimensions of the breaking points were influenced by the limited resolution of the etching step. After patterning the etch match, the widths of the cut-outs were 3 µm, while the breaking points were 5 µm wide. However, after dry etching, the

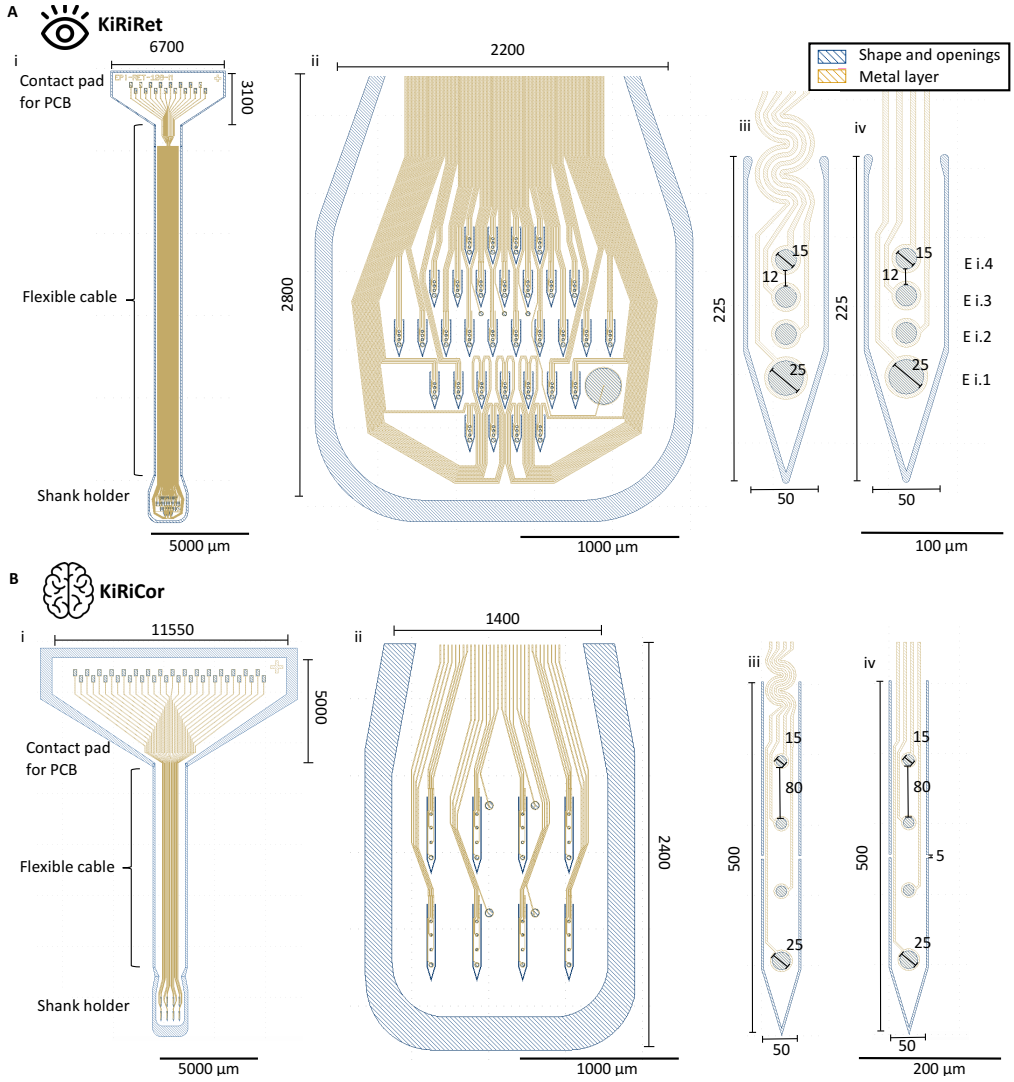

Figure 4.6.: 2D MEA for kirigami implants: Design overview. Kirigami probes are either designed for retinal (KiRiRet, A) or cortical (KiRiCor, B) applications. The probes consist of a contact pad area to connect the PCB, a flexible cable and a shank holder (A_i and B_i) in both cases. The shank holder of the KiRiRet example holds 32 x 225 µm long shanks (A_{ii}) with 3 or 4 electrodes while the KiRiCor example holds eight shanks with a length of 500 µm (B_{ii}). The shanks have either meander-shaped (A_{iii} and B_{iii}) or straight (A_{iv} and B_{iv}) feedlines at the kink area (C) (modified from [177]).

resulting breaking points were only $\leq$ 1 µm wide (Figure 4.7$B_{i,ii}$, red arrow). As with the KiRiRet, the KiriCor shank holder was equipped with surface electrodes for µECoG (micro electrocorticography) recordings (Figure 4.7B_i, green arrow).
For KiRiRet as well as KiRiCor implants, additional designs were tested to investigate the limitations of the process, to adjust to the needs of a certain application or to determine the influence of certain design parameters regarding the insertion impact. An overview of the designs is shown in Figure A.3.

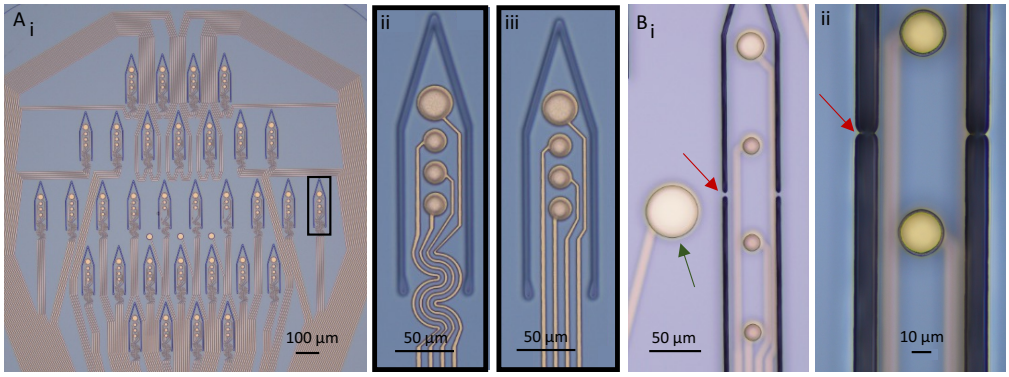

Figure 4.7.: 2D MEA for kirigami implants: Fabrication results. A) The shank holder with 32 x 225 µm long shanks after resist stripping and zoomed-ins of meander-shaped (ii) and straight (iii) feedlines. B) The probes also have surface electrodes (green arrow). For long shanks ($\geq$ 500 µm) breaking points were employed (red arrow). The images were taken before (i) and after RIE (ii).

4.2.2. Mold design and fabrication

The molds were utilized to facilitate the folding of the kirigami structures. Two molds were designed for each implant type (KiRiRet and KiriCor) and for each specific design configuration. Figure 4.8 depicts the CAD models of the lower (Figure 4.8A) and upper (Figure 4.8B) molds utilized for the folding approach, serving as illustrative examples of the mold designs for the KiRiRet implant. The positioning of the blocks responsible for the upward folding of the shanks was precisely aligned with the location of the shanks within the two-dimensional pattern. The blocks on the lower mold had a height of 260 µm (slightly higher than the shanks) and a width of 46 µm (slightly smaller than the shanks). To reduce the contact surface area between the blocks and the shanks, ramped sidewalls were implemented, with a length of 120 µm at the top and 60 µm at the bottom (Figure 4.8A$_{ii}$). In addition to the aforementioned blocks, the lower mold also contained sidewalls that correspond to the outline of the shank holder of the 2D flexible probe. This configuration allowed for the straightforward manual placement of the 2D flexible probe into the mold, obviating the necessity for a complex alignment setup. In addition to the features described for the lower mold and the 2D flexible probe, the upper mold contained straight structural elements between the outer boundaries. These elements ensure uniform pressure distribution across the 2D flexible probe when it is pressed inside the lower mold in a controlled manner. The outer boundaries of the upper mold fit perfectly inside the lower mold, ensuring facile alignment and the folding of all shanks simultaneously. This facilitated manual manipulation of the folding process using tweezers and a microscope, obviating the necessity for a micromanipulator. The outer boundaries of the lower mold were not continuous in order to facilitate the removal of the 3D probe after folding and thermoforming. The total area of the molds was approximately 2 x 2.3 mm for the upper molds and 2.2 x 2.8 mm for the lower molds.

The fabrication of the molds was conducted using a 2PP 3D printer, the Photonic Professional GT2 from NanoScribe GmbH. In this process, an erbium-doped femtosecond laser source (center wavelength 780 nm) is focused into a liquid droplet of a 2PP negative photoresin. If the laser power exceeds a certain threshold, the photoresin will undergo polymerization only in the focal spot of the laser, thereby printing a single voxel of $\approx$ 600 nm in x-y and 2.5 µm in z direction (using a 25x objective). By printing several voxels the fabrication of highly complex structures with high resolution is enabled. To achieve such molds, three main steps were followed:

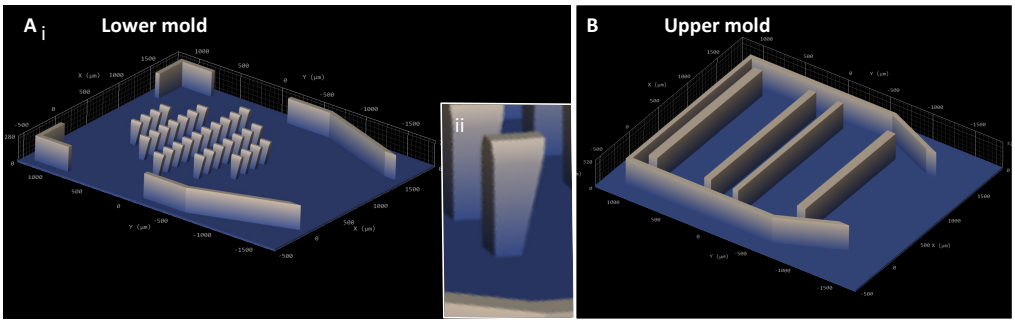

Figure 4.8.: Lower and upper mold for folding a KiRiRet implant. A) Lower mold (i) and zoom-in on one of the blocks (ii), B) upper mold (modified from [177]).

1. Conversion of the 3D design: The molds were designed using CAD software and subsequently converted to print job instructions using Describe (NanoScribe GmbH, Germany).

2. 3D printing: A Zeiss 25X NA0.8 objective was utilized, and IP-S (NanoScribe GmbH, Germany) was employed as the photopolymer material. The print recipe provided by NanoScribe, designed for use with the 25X objective and IP-S, specifies a slicing distance of 1 µm and a hatching distance of 500 nm. A scan speed of 100,000 µm/s, a laser power of 100%, and a power scaling of 1.2 yielded the optimal printing result, exhibiting sufficient resolution and stability of the printed structure. As the mold is considerably larger than the dimensions of a single printed block, which are defined by the print field of the objective (400 µm x 400 µm x 400 µm for the 25X objective) without stage movement, numerous blocks are printed in close proximity to construct the entire structure. To guarantee the adhesion of the individual blocks, the block overlay was set to 2 µm in all dimensions. The height of each block was set to 200 µm to prevent the objective, which has a working distance of 380 µm, from moving into the structure. Alternatively, the molds were printed using a 10X microscope to decrease the printing time. Here, a scan speed of 50,000 µm/s, a laser power of 100%, and a power scaling of 1 were employed. The molds were printed onto a 2.5 cm x 2.5 cm ITO (indium thin oxide) coated glass substrate (NanoScribe GmbH, Germany) that has been previously coated with 3 µm PaC, as described in section 3.2.1. The PaC coating ensures high adhesion of the printed structure to the glass substrate.

3. Development: Following the printing process, a subsequent step entailed the removal of residual photopolymer that has not undergone polymerization. This was achieved by immersing the samples in a bath of Mr-Dev 600 developer for a period of 15 min, followed by another 5 min in fresh Mr-Dev 600 solution. Subsequently, the molds were placed into isopropanol (IPA) for an additional 5 min, after which they were air-dried.

4.2.3. 3D assembly

After the 2D flexible MEA was flip-chip bonded to a PCB as described in section 3.2.1, the probe was subject to folding and subsequent thermoforming to create a 3D MEA out of the 2D flexible MEA.

Folding

Once the 2D flexible probes and the molds had been fabricated, the assembly of the components was carried out in order to construct the 3D device. To facilitate the folding of the shanks, two molds were employed. Initially, the 2D probe was positioned on the lower mold (Figure 4.9A). This process was completed manually, utilizing tweezers and an appropriate microscope (Stereo microscope Stemi DV 4, Carl Zeiss GmbH, Germany). A second pair of tweezers was employed to align the 2D probe with the lower mold. The alignment was facilitated by the edges of the lower mold, which allowed for precise positioning of the 2D probe within the mold and ensured that the 2D probe remained in place. In the subsequent phase, the upper mold was retrieved and oriented with its edges in a downward position. It was then gradually lowered until it was aligned with the lower mold. The precise fit of the upper mold's edges within the lower mold's side walls facilitated the alignment process. Once the upper mold was correctly positioned, it was lowered until all shanks were folded simultaneously (Figure 4.9B). In the case of the long shanks (> 500 µm), the breaking points tore at the mechanical force that allowed the folding of the long shafts in the upright position (Figure 4.11A$_{i,ii}$).

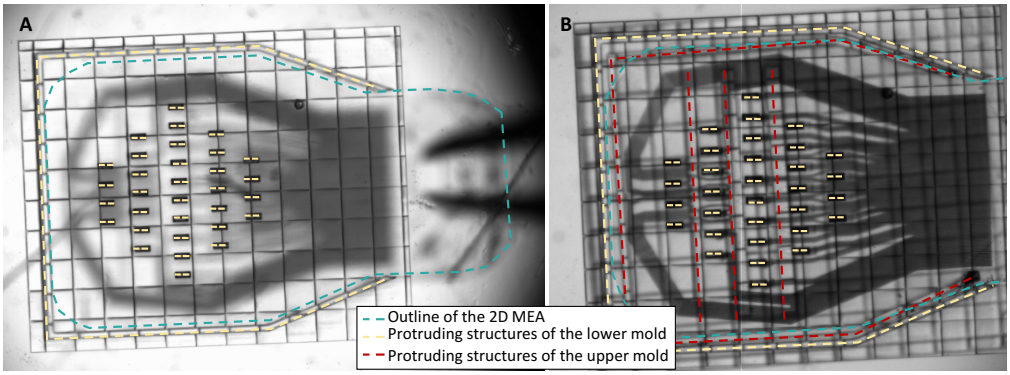

Figure 4.9.: Schematic of the folding process for kirigami implants. 2D flexible kirigami MEA in lower mold (A) and with upper mold placed on top for folding of the shanks (B) (modified from [177]).

When a shank bends upwards, the top surface undergoes compression while the lower surface experiences tensile strain. In accordance with the aforementioned observations, FEM simulations conducted in COMSOL using the shell module indicate a maximum volumetric strain of -2.3% at the center of the kink region on the top side and 1.2% on the bottom side. Figure 4.10 shows the front side as well as the back side of a folded shank considering only PaC as material and neglecting the metal structures. The maximum strain of 2.3% that occurs during folding does not damage the PaC layer, as it remains within the linear elastic region of the material (Figure 4.11C). Therefore, assuming a homogeneous volumetric strain distribution, the metal layer situated at the center of the two 5 µm-thick PaC layers is subjected to a strain of 0.55%, which is insufficient to cause damage to Au [195]. Following the folding process, a PaC-metal-PaC sandwich structure devoid of cracks was observed at the kink region of the shanks, as evidenced by SEM analysis (Figure 4.13). This finding suggests that the feedlines, including both straight and meander-shaped configurations, remain intact despite the folding procedure.

An alternative approach was also considered, in which an upside-down process was explored. In the alternative approach, the lower mold was designed with encompassing edges that could accommodate the 2D flexible probe (Figure A.4A) [190]. Furthermore, the lower mold was equipped with crossbars to guarantee an uniform distribution of pressure throughout the folding process. The lower mold was positioned on an assembly table to create space for the shanks to fold. Then, the 2D probe was placed on top of it. Subsequently, the upper mold was placed on the 2D probe

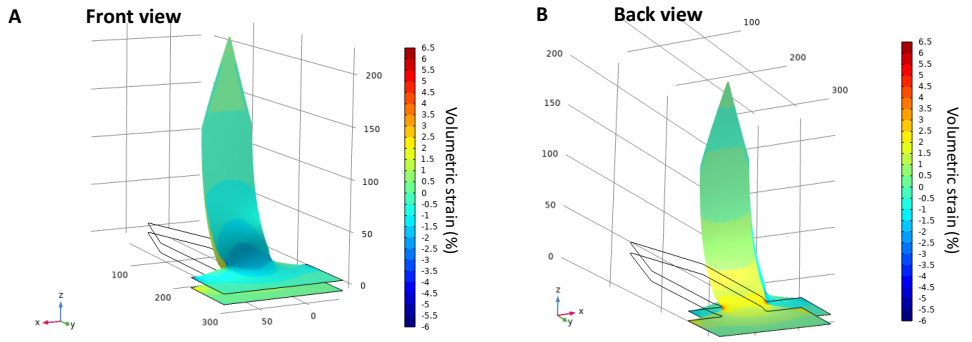

Figure 4.10.: Simulation of the kirigami folding procedure using COMSOL Multiphysics. Front (A) and back (B) view of the probe which was subjected to a displacement at the tip resulting in the displayed volumetric strain (in %) (modified from [177]).

with the blocks oriented downward (Figure A.4D). The edges of the lower mold once more facilitated the alignment. Once the upper mold was correctly situated, it was pushed downward to fold all shanks simultaneously.
Nevertheless, the conventional folding methodology yielded more reproducible outcomes and was therefore selected for the fabrication of 3D kirigami implants.

Thermoforming

PaC, which was utilized for the kirigami devices, is a thermoplastic material. The elevated temperatures facilitate the rearrangement of the amorphous regions of the PaC, which results in the softening of the material and enables the reshaping of its molecular structure. Thus, the folded flexible MEA was thermoformed inside the lower mold (Figure 4.11A$_{i,ii}$). The polymeric material then retained the new shape upon cooling and removal of the mold. The thermoforming protocol was optimized to achieve an optimal balance between temperature and thermoforming time (Figure 4.11B). It is crucial for the thermoplastic material to possess a melting point that is inferior to the glass transition temperature of the mold material. The potential for failure exists in the event of elevated temperatures (> 170 °C), which may result in the PaC adhering to the mold even at short dwell times (Figure 4.11B). The upper mold was removed to improve heat circulation during thermoforming and to reduce the risk of the PaC adhering to the mold material. To prevent adhesion further, it may be beneficial to coat the molds with a thin metal film, or a soap such as Micro90. However, in the case of PaC, it is necessary to consider that high temperatures (> 300 °C) permanently alter the material's mechanical and optical properties, as reported in the literature [196]. Conversely, if the temperature is insufficient or the dwell time is too brief, the shanks fold back immediately following their separation from the mold (Figure 4.11B). Accordingly, a thermoforming protocol was devised comprising a gradual temperature increase of 4 °C per minute from room temperature to 160 °C, a 60-minute dwell time at 160 °C, and a slow cooling phase (> 120 min) until room temperature was reached. Subsequently, the 3D flexible probe and the lower mold were separated using water droplets to facilitate the separation process.

To ascertain whether the mechanical properties of the PaC would undergo significant alteration as a result of the thermoforming protocol, a tensile test was conducted on flexible PaC samples that had been subjected to thermoforming processes at maximum temperatures of 160 °C or 200 °C. The results obtained were then compared to those of the untreated samples. The mechanical properties of 10 µm thick PaC stripes were assessed in accordance with the methodology outlined in section 3.3.2. From the stress-strain curves (Figure 4.11C), the Young's modulus of a 10 µm thick PaC layer thermoformed at 160 °C, yielded a value of 1.70 GPa ± 0.32 GPa. Accordingly, a

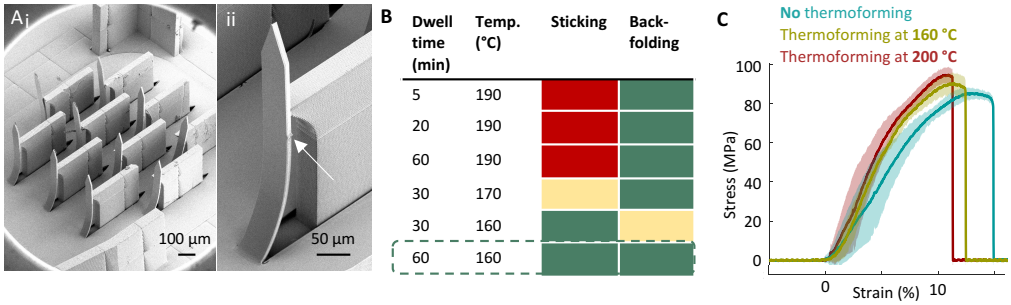

Figure 4.11.: Thermoforming of the flexible kirigami MEA in the lower mold. A) A flexible probe with 500 µm long shanks is positioned inside the lower mold (i). The zoom-in (ii) shows the remaining structures of the breaking points at the side of the shank (white arrow). B) Optimizing the thermoforming protocol according to dwell time and temperature evaluating the sticking of the flexible probe to the mold and the back-folding of the shanks (green: no, yellow: medium, red: high risk of sticking/back-folding). C) Stress-strain curves of untreated (blue), thermoformed at 160 °C (green) and at 200 °C (red) (mean ± standard deviation of N = 7 or 8) (modified from [177]).

strain of up to 13.93% ± 11.25% and a stress of 89.07 ± 6.92 MPa at break were achieved. At 200 °C, the Young's modulus, as well as the stress and strain at break, exhibited statistically significant differences in comparison to the untreated PaC stripes using a one-way ANOVA test with 95% confidence interval. Conversely, thermoforming at 160 °C did not result in a notable alteration in the Young's modulus (Table 4.1). This finding supports the selection of 160 °C as the optimal thermoforming temperature.

	Untreated (no thermoforming)	Thermoformed at 160 °C	Thermoformed at 200 °C
Young's modulus (GPa)	1.66 +/- 0.22	1.70 ± 0.32	2.08 ± 0.34* (p = 0.03)
Stress at fracture (MPa)	83.82 ± 2.02	89.07 ± 6.92* (p = 0.034)	91.45 ± 6.3** (p = 0.006)
Strain at fracture (%)	14.15 ± 4.65	13.93 ± 11.25	9.56 ± 9.5* (p = 0.022)

Table 4.1.: The mechanical properties of untreated (i.e., thermoformed at 160 °C) and thermoformed (at 200 °C) 10 µm thick PaC stripes. The data is presented as the mean ± standard deviation. P-values less than 0.05 are indicated with an asterisk (*). The statistical analysis was conducted using one-way ANOVA with 95% confidence intervals. The number of samples (N) was seven or eight for each group.

4.2.4. PEDOT:PSS deposition on kirigami electrodes

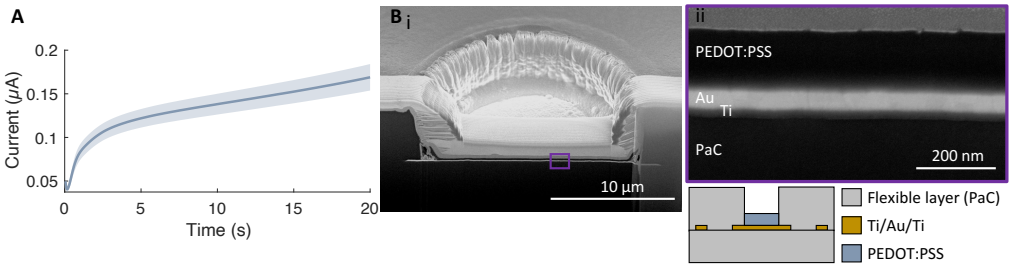

Figure 4.12.: PEDOT:PSS deposition on Au electrodes on kirigami implants. A) Current measurement during the deposition (mean ± SE, N= 75 implants), B) FIB-cuts showing the PaC substrate, Au, and PEDOT:PSS layer [197].

As outlined in section 3.2.3, a PEDOT:PSS coating was electrochemically deposited on the Au electrodes with the objective of enhancing the electrochemical performance of the 3D kirigami implants. During the 20-second deposition period, the current was monitored. Figure 4.12A depicts

the current averaged ± SE during the deposition of 75 implants. After 20 s, the maximum current reached was 0.17 ± 0.13 µA (mean ± standard deviation of N = 75 implants). The observed high standard deviation is potentially associated with the quality of the underlying Au layer, which may exhibit variability across different fabrication runs. The FIB-cut analysis of a kirigami electrode with a diameter of 25 µm and one with a diameter of 15 µm revealed a homogeneous layer with a thickness of 178 ± 7 nm (Ø15 µm electrode) and 179 ± 7 nm (Ø25 µm electrode). Figure 4.12B shows an example FIB-cut SEM-picture of a Ø15 µm electrode. The observed standard deviation in the measurements can be attributed to minor variations in the electrodes' central and peripheral regions. As documented in the literature, the enhanced electric field surrounding the electrode edges results in increased material deposition [91].

4.2.5. Design variations and limitations

The kirigami-based process developed in this work allows for the straightforward customization of 3D flexible probes to meet varying laminar and spatial requirements. The fabrication of KiRi implants yielded 96% success (N = 100) for the folding process, wherein successful folding was defined as the probe being separated from the molds without any difficulties (e.g., without sticking to the mold) and all shanks being folded upright. Subsequently, the 3D flexible probes underwent a coating process with PEDOT:PSS via CV, with the objective of improving the electrochemical properties of the underlying Au electrodes. Following electrodeposition, the resulting overall yield was 52%. However, when the yield was evaluated according to the fabrication runs, a yield of 47% ± 16% was achieved across seven fabrication runs. The high standard deviation indicates that the success of the process is contingent upon the precise handling of the 2D kirigami template, in addition to the quality of the underlying metal layer. While the folding process has the potential to be automated, for instance through the use of micromanipulators and pick-and-place techniques, the alignment of the 2D flexible probe with the corresponding molds and the folding were conducted manually in this study. During the folding process, rapid movements during alignment can result in the formation of cracks in the PaC layer, which can subsequently extend to the metal layer. In consideration of the aforementioned learning curve and the underlying Au layer, a yield of 80% (N = 271 electrodes) was achieved in the final fabrication run.
The maskless lithography used for the 2D MEA fabrication enables rapid prototyping, facilitating the adaptability of design choices to accommodate diverse requirements, such as the utilization of various animal models. Similarly, the 2PP used to fabricate the molds has a high degree of design freedom, allowing for straightforward adaptation to the design requirements. Thus, for each kirigami design, a matching mold was created. The dimensions are summarized in table 4.2. For successful folding, the protruding structures of both the lower and upper molds must be mechanically stable, which depends on the mechanical properties of the materials that compose the mold and the lithographic methods used. An aspect ratio of 16.3 could be achieved by considering the ending stiffness (Table 4.2).

Design	Block height (µm)	Shank length (µm)	Ratio block/ shank length	Block width (µm)	Shank width (µm)	Ratio block / shank width	Block aspect ratio
KiRiRet	250	225	1.11	46	50	0.92	5.43
KiRiCor	300	500	0.60	45	50	0.9	6.67
KiRiCor	750	1000	0.75	46	50	0.92	16.3

Table 4.2.: Dimensions of the lower mold for the folding of different kirigami designs.

Consequently, the 3D probes can be designed to satisfy the spatial requirements for a multitude of neural applications. For instance, KiRiRets were constructed with shanks reaching 225 µm in length, with the objective of addressing the laminar structure of rodents' retinas. In order to enhance resolution or, ultimately, to extend the implant across the entire retina, the design was tested with smaller inter-shank distances (50 µm) or an increased number of shanks. This ap-

proach resulted in a total of 512 electrodes distributed over 128 shanks with 100 µm spacing. For the KiRiCors, designs with up to 10 x 500 µm long shanks were explored. To reach even deeper cortical layers, a design with up to 1000 µm long shanks was tested.

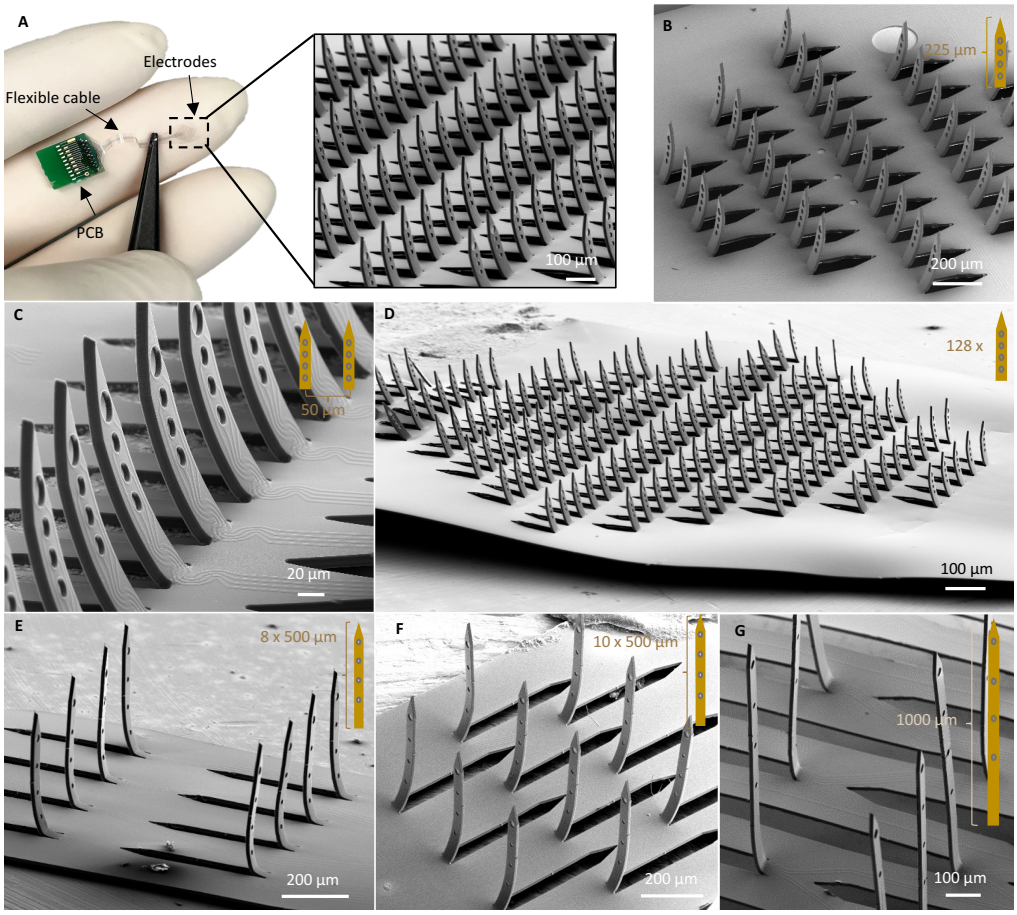

Figure 4.13.: Finalized 3D kirigami neural implant and design variations. A) Finalized probe connected to a PCB. B) - D) KiRiRet designs with 32 x 225 µm long shanks with 100 µm (B) and 50 µm (C) spacing and with up to 128 shanks (D). E) - G) KiRiCor design with 8 x (E) or 10 x (F) 500 µm long shanks. Up to 1000 µm long shanks were folded (G) (modified from [177]).

The success of the folding procedure is constrained by the remaining area in the 2D kirigami MEA, particularly the inter-shank spacing, which provide mechanical support during the key-lock folding process. Consequently, as the shanks are positioned in closer proximity, the inter-shank area is reduced, while the compressive stress is augmented. This has the potential to result in structural instability and ripping of the 2D flexible MEA, which in turn leads to an unsuccessful folding procedure. Furthermore, a considerable number of long, closely spaced shanks present a challenge in separating them from the lower mold, given the limited remaining area in the flexible MEA. To avoid damaging the shanks, particularly at the kink, it is essential to lift the flexible probe in a predominantly straight manner. However, the less mechanically stable the probe is, the more difficult this procedure becomes. Accordingly, the design incorporating 30 x 1000 µm elongated shanks with a spacing of only 125 µm could not be folded in a satisfactory manner. The folding

procedure either resulted in the tearing of the flexible MEA or the shanks were not folded into an entirely upright position (Figure 4.14).

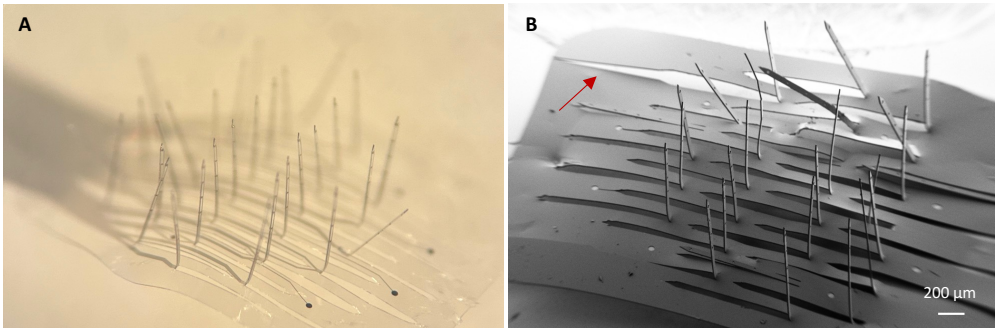

Figure 4.14.: Folding of a KiRiCor probe with 30 x 1000 µm long shanks. The folding process was not entirely successful, as evidenced by the tilting of some shanks (A) and the tearing of the flexible MEA substrate (B, red arrow) under the mechanical forces applied during the folding procedure (modified from [177]).

4.3. Printing 3D electrodes on a flexible microelectrode array (MEA)

To create a 3D microelectrode structure from a 2D flexible MEA, polymer templates were printed around the electrodes using a biocompatible photoresin and 2PP. The hollow pillars then served as templates for the electrodeposition of Au and PEDOT:PSS (Figure 4.15) and at the same time as electrode passivation. Hollow polymer pillars were fabricated according to custom specifications and are addressable on an individual basis, thereby allowing maximum flexibility to meet the requirements of various types of neural tissue. The following sections describe the 2D MEA design, as well as the results and limitations of the 3D printing and electrochemical deposition processes.

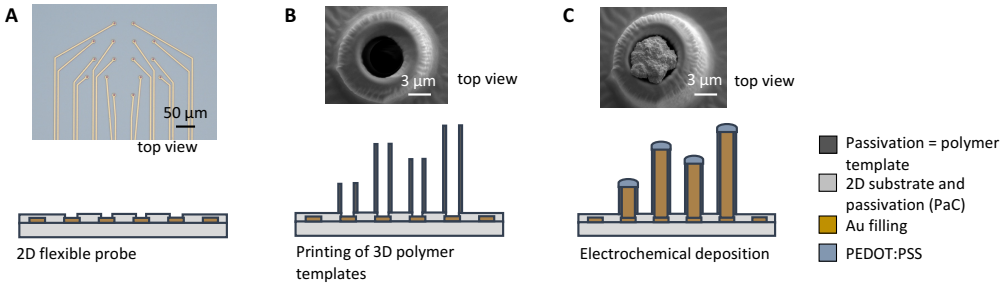

Figure 4.15.: The fabrication process for 3D printed electrodes on 2D flexible MEA. Hollow polymer cylinders (B) were printed using 2PP on flexible MEA (A) and were filled with metal via electrodeposition (C) (modified from [41]).

4.3.1. 2D flexible microelectrode array (MEA) for 3D printed implants

As with the 2D flexible MEA for the kirigami implant, the 2D flexible MEA of the 3D-printed implant (PiRi) was fabricated in accordance with the process outlined in section 4.1. Similarly to the KiRi design, the PiRi implant comprised a contact pad area for PCB connection with dimensions of 3100 x 6700 µm, a flexible cable, and an electrode holder area (Figure 4.16A). The dimensions of the flexible cable were contingent upon the specific animal model and experimental design. The shank holders of size 650 x 1200 µm (Figure 4.16B) were capable of accommodating up to 16 electrodes with a diameter of 6 µm (Figure 4.16C), around which the 3D-printed pillars were subsequently fabricated. The inter-electrode distance could be tailored to align with the specific experimental requirements, with distances ranging from 10 to 200 µm (Figure 4.17).

4.3.2. Printing of polymer pillars via 2-photon-polymerization (2PP)

Design of 3D printed pillars

In the subsequent phase, hollow polymer pillars were produced at the electrode locations of the flexible 2D MEA using 2PP and a biocompatible photoresin. In this phase of the process, a polymer disk (base plate) was first printed on the MEA surface in order to enhance adhesion. Typically, the base plate comprised a diameter d_B of 50 µm and a thickness T_B of 3 or 5 µm. An opening of 8 µm was left for the microelectrode, which itself had a diameter of 6 µm. This allowed for a tolerance of 1 µm for the printing process. Subsequently, the hollow polymer pillars were printed on the disk during the same printing step. This process permitted the fabrication of thin pillars with outer and inner diameters of 12/8 µm (and a wall thickness of 2 µm). Pillars of varying design configurations (height h and inner and outer diameters, d_i and d_o, respectively) and comprising different pitches were printed in a straight or conical configuration. Moreover, a multisite approach was utilized

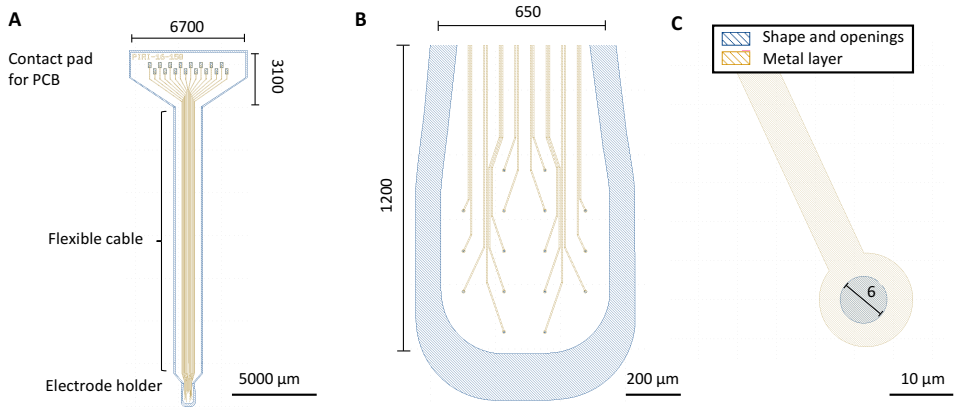

Figure 4.16.: 2D flexible MEA design for 3D printed implants. The probe consists of a contact pad area for a PCB, a flexible cable and a shank holder (A). The shank holder (B) accommodates up to 16 electrodes with a diameter of 6 µm (C).

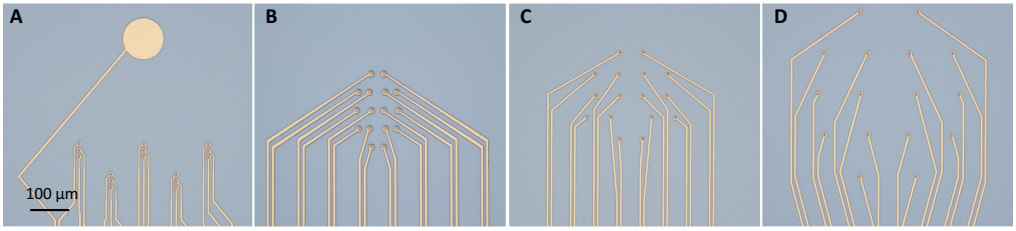

Figure 4.17.: 2D flexible MEA for 3D printed implants fabrication results. The probes consist of 16 electrodes with inter-electrode distances of for example 10 (A), 16 (B), 56 (C) or 106 (D) µm.

with the objective of recording from disparate depths within a layered neural structure, such as the retina (Figure 4.18).

Printing process for 3D printed pillars

The 3D structures were fabricated in accordance with the methodology outlined in section 3.2.2.

1. Conversion of the 3D design: The designs were created using a CAD software and subsequently transformed into print job instructions using Describe, a software program developed by NanoScribe GmbH.

2. 3D printing: The IP-L 780, developed by NanoScribe for high-resolution prints down to 200 nm, was employed for the 2PP process. Two objectives were utilized for the printing of the pillars, namely a Zeiss 25XNA0.8 and a Zeiss 63XNA1.4, contingent upon the electrode layout. A scan speed of 50,000 µm/s, a laser power of 100%, and a power scaling of 1.2 were employed when utilizing the 25X objective. The slicing distance was set to 700 nm, and the hatching distance was set to 400 nm. For the 63X objective, a scan speed of 8000 µm/s, a laser power of 100%, a power scaling of 1.0, a slicing distance of 300 nm, and a hatching distance of 200 nm were employed. Due to the similarity in optical properties between the printed polymer and the PaC passivation, the interface between the two could not be identified automatically by the 3D printer. Consequently, the interface must be identified manually by adjusting the laser focus to guarantee

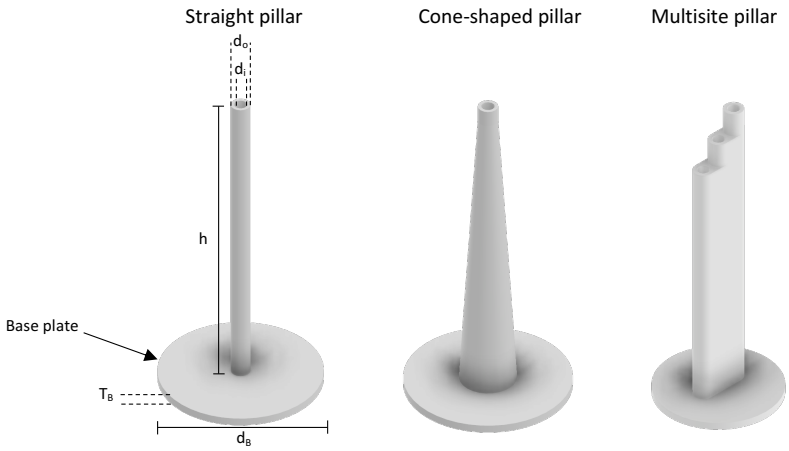

Figure 4.18.: Designs for 3D printed pillars on flexible 2D MEAs: Straight, cone-shaped and multisite pillars. Different heights h, and inner and outer diamaters, d_i and d_o, respectively, were explored. A base plate (black arrow) was printed around the pillar to promote adhesion to the substrate.

optimal adhesion between the 3D printed object and the substrate. It was imperative that the manual interface finding was precise, as otherwise the adhesion to the substrate resulted to be insufficient. Consequently, this could lead to an improper Au deposition. Alternatively, the reflection of the laser by the underlying metal feedlines could result in an overdose and thereby in burning of the resist.

3. Development: Following the printing process, a developing procedure was employed to remove any residual unpolymerized photopolymer. The samples were immersed in a Mr-Dev 600 developer solution for 10 min, followed by an additional 10 min in a fresh Mr-Dev 600 solution to ensure comprehensive development. Subsequently, the samples were placed in a fresh isopropanol solution for an additional 5 min and then allowed to air dry.

4.3.3. Template-assisted electrodeposition

After flip-chip bonding, the polymer pillars, which served as both templates and passivation layers, were filled via two steps of electrochemical deposition of Au, followed by a third deposition step during which the formation of an electrode coating cap through the electropolymerization of PEDOT:PSS was achieved.

First Au deposition step: In the initial electrodeposition phase of Au, a potential was applied between the 2D MEA electrodes, which were encapsulated by the 3D-printed pillars, a Pt counter electrode and an Ag/AgCl reference electrode submerged in an aqueous solution containing $AuCl_4$. To facilitate the electrodeposition of solid Au within the hollow pillar template, a constant potential of -1.3 V was employed, while the electrical current was monitored and subsequently used to determine the growth rate through the printed pillars. Upon reaching the top edge of the pillar template, an exponential increase in current was observed, which is indicative of the onset of cap growth. Therefore, the deposition of gold was terminated when a threshold current of -100 nA was reached. This resulted in an Au strain within the hollow pillar, which terminated several micrometers below the top edge of the pillar (Figure 4.19A).

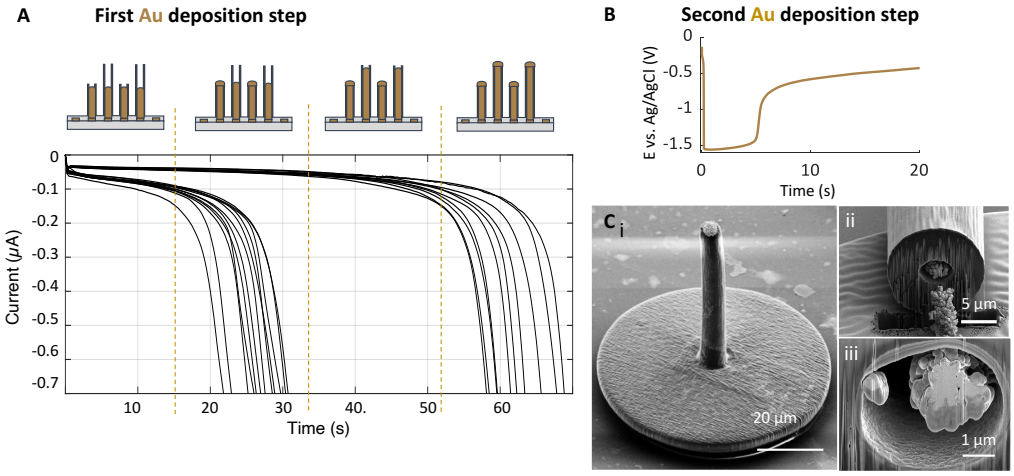

Figure 4.19.: Filling of the 3D printed pillars with Au via electrodeposition. A) The initial deposition process was conducted with a constant potential of -1.3V, with the current flow being monitored. Upon reaching a threshold current of -100 nA, the deposition was terminated. Otherwise, an exponential current was observed, accompanied by the formation of Au caps on the edges of the pillars. During the second deposition phase (B), the current of -100 nA was maintained for a period of 20 s, with the objective of creating smooth Au caps on the pillars (C_i). FIB-cuts revealed of one pillar at the base (i) and top end (ii) revealed a wall-thickness of around 4 µm (modified from [41]).

Second Au deposition step: A second deposition step was performed, wherein the current was fixed at -100 nA for a time of 20 s (Figure 4.19B_i). This step was undertaken to ensure that the remaining template was filled with a more uniform gold morphology. The objective of this step was to create small caps on top of the pillars, which would increase the electrode area (Figure 4.19C_i). This is beneficial for the electrochemical properties, thereby improving the recording qualities from the neural target cells. The FIB-cut (Figure 4.19$C_{ii,iii}$) revealed a comparatively coarse morphology of the Au strain within the pillar in comparison to the tip (Figure 4.15C). These findings provide further evidence that the morphology of Au is dependent on the deposition process.

PEDOT:PSS deposition: To further enhance the electrochemical performance of the 3D electrodes, a layer of PEDOT:PSS was electrodeposited onto the Au surface. By employing CV, the dimensions of the resulting PEDOT:PSS electrode coating cap could be meticulously calibrated and tailored to the desired specifications through the modulation of the number of CV cycles. The CV deposition was performed with an initial voltage of 0 V, the final voltage of 1 V and a scan rate set to 0.1 V for 2 – 15 cycles. Figure 4.20A illustrates the deposition curves, where the potential of the pillar electrodes vs. the Ag/AgCl reference electrode was measured over the deposition time. Here, 10 CV cycles were employed to create a smooth, round PEDOT:PSS cap with a diameter of 20 µm (Figure 4.20B). Figure 4.20C illustrates the growth in diameter of the PEDOT:PSS cap with each deposition cycle. In this example, < 10 µm in diameter were achieved when using 2 cycles to > 30 µm in diameter with 10 cycles, respectively. The morphology of the underlying gold significantly influences the morphology of the deposited PEDOT:PSS. It was observed that rather inhomogeneously distributed potential fields at rough, dendrite-shaped gold surfaces result in a rather rough and inhomogeneous PEDOT:PSS growth, a phenomenon that has also been previously reported [198]. Thus, the different morphology of the PEDOT:PSS cap in Figure 4.20B, which is smoother in comparison to the PEDOT:PSS caps in Figure 4.20C, was dependent on the quality and morphology of the underlying Au layer.

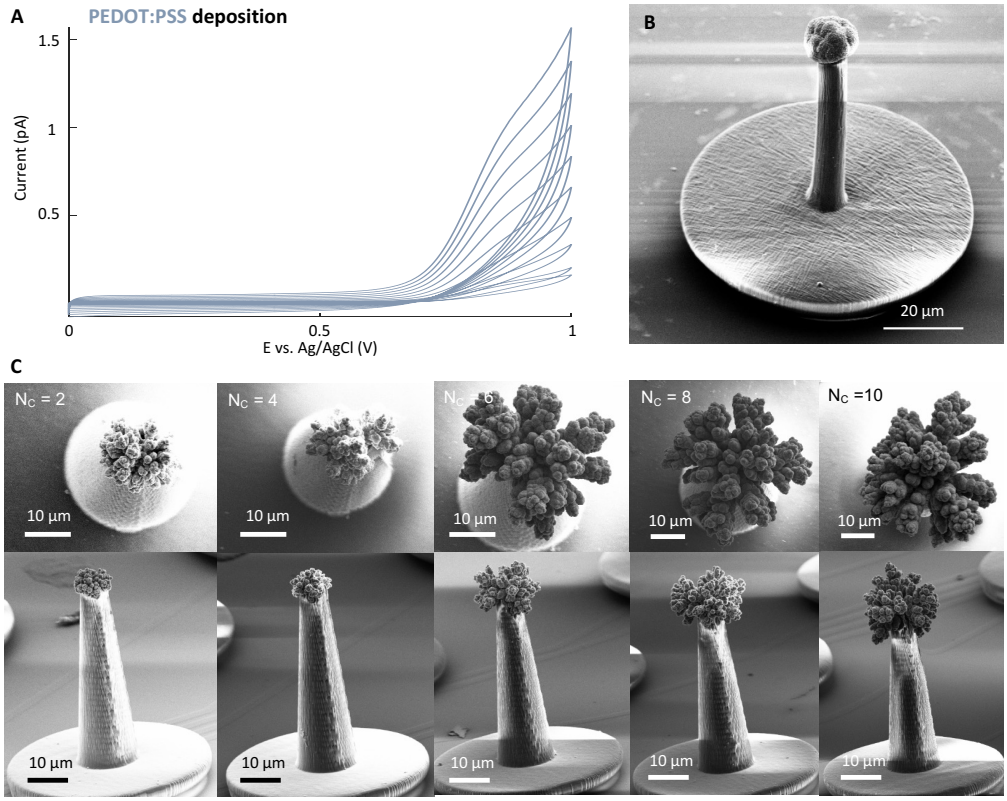

Figure 4.20.: PEDOT:PSS coating on top of the 3D printed pillars Au cap via electrodepostion. A) The deposition process was conducted using CV with and initial voltage of 0 V, the final voltage of 1 V and a scan rate set to 0.1 V for 10 cycles to create a PEDOT:PSS coating on the Au cap (B). The number of cycles (N_c) was found to be a determining factor in the growth of the PEDOT:PSS caps, with an increase in the number of cycles resulting in a corresponding increase in diameter (C) (modified from [41]).

4.3.4. Design variations and limitations of 3D printed implants

Figure 4.21A illustrates a final PiRi implant in comparison to a 1-cent coin. Upon closer examination, the image reveals the presence of pillars with a height of 500 µm (Figure 4.21B). In addition to probes with up to 16 cone-shaped (Figure 4.21C) or straight pillars, a multisite design was fabricated with the intention of using it for layered neural structures. Figure 4.21D depicts the top-view and 4.21E presents a side view of a multisite pillar with a PEDOT:PSS coating. Overall, PiRi implants were fabricated with a yield of 85% in the 2PP printing process and 55% after the electrodeposition process.

In the 2PP printing process, the mechanical stability of the pillars is contingent upon a number of factors, including not only the mechanical properties of the photoresin itself, but also the geometry of the pillars, as well as aspects of the microfabrication process. Polymer structures fabricated by 2PP often exhibit shrinkage and collapse during the fabrication process, particularly when fabricating delicate structures. These structures are particularly susceptible to mechanical instability due to insufficient resistance against capillary forces, which predominantly arise during the fabrication process as a consequence of the evaporation of the developer and rinsing liquids,

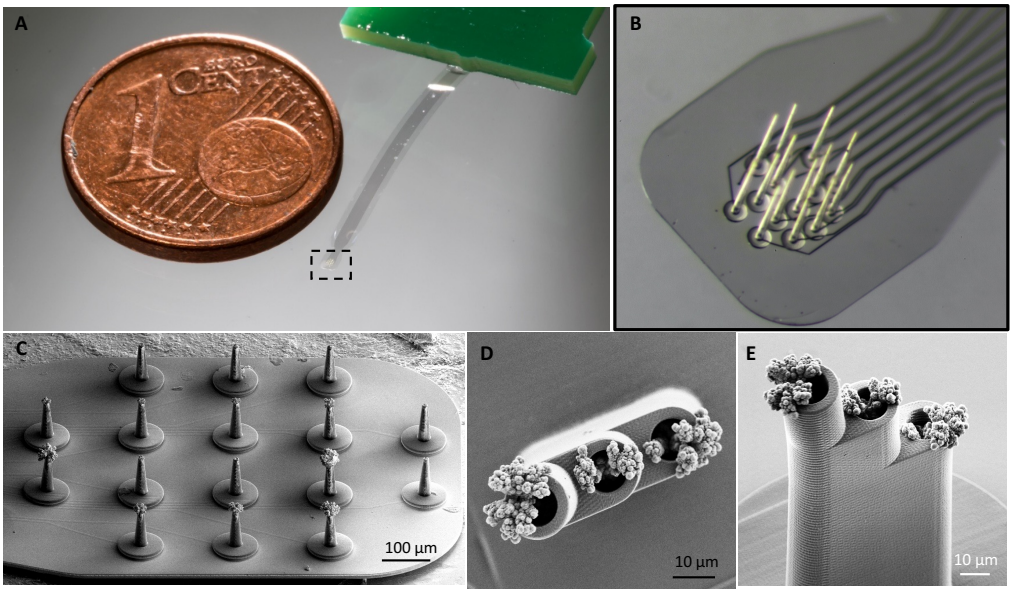

Figure 4.21.: Finalized PiRi probe. PiRi probe in comparison to a 1-cent coin (A) and zoom-in on the electrode holder (B). C) Probe with 16 cone-shaped pillars. Top-view (D) and side-view (E) of a multisite pillar with three electrodes (modified from [41]).

such as isopropanol in this case (Figure 4.22A). The capillary forces are defined by

$$F_C = \frac{\pi\gamma r^2}{p - 2\delta} \cdot cos(2\Theta) \tag{4.1}$$

where γ represents surface tension of the liquid, which in this case is isopropanol. r is the radius and p the pitch of the pillars. The variable Θ refers to the advancing contact angle, while δ denotes the deflection of the pillar. The term (p - 2δ) serves to quantify the actual inter-pillar spacing, which is subject to dynamic alteration when the pillars undergo bending [199][200]. In the absence of bending of the pillars (when δ = 0), F_C is inversely proportional to the pillar pitch, p. Consequently, the higher the density of the array of pillars, the greater the value of F_C. In the event that the pillars are unable to withstand F_C, they begin to bend towards one another. Subsequently, F_C increases in accordance with the value of δ, reaching its peak just prior to the moment at which two neighboring pillars make contact. The opposing force to F_C is the elastic restoring force F_E of the pillars, which is described by

$$F_E = \frac{3E \cdot I\delta}{h^3} \tag{4.2}$$

where E is the Young's modulus of the polymer and h is the height of the pillars. I is the 2nd moment of inertia, which is $I = \pi/4 \cdot (r_o^4 - r_i^4)$ for hollow pillars [201]. Thus, the value of F_E increases in a linear manner with respect to that of δ. In the event that the value of F_E exceeds that of F_C, the pillars will exhibit a high probability of remaining in an upright position within the dried array due to their capacity to resist capillary forces. Conversely, if the value of F_E is less than that of F_C, the pillars will be subjected to bending that could potentially result in their collapse. Once the liquid has undergone complete evaporation, the primary forces responsible for maintaining the attachment of the pillars are van der Waals forces F_W. Consequently, the stability of clustered structures formed by capillary action is contingent upon the ratio of F_E and F_W. When F_E is greater than

F_W, the pillars are likely to revert to a vertical position, although slight bending of the tips may persist due to plastic deformations. Conversely, when the value of F_E is less than that of F_W, the pillars remain attached [199]. Figure 4.22C holds an example SEM picture of high, straight pillars that were unable to withstand F_C. Some pillars remained attached after the drying process (Figure 4.22B,C), while others exhibited a tilted tip.
In order to evaluate the constraints of the 2PP printing process, an initial series of tests was conducted to identify the maximum pillar heights that could be achieved with the thinnest possible wall thickness (Figure 4.22D). To this end, 500 µm high pillars with varying wall thicknesses (outer/inner diameter of 12/8, 6/2, 6/4, 2/1, 4/2 µm) were subjected to testing. The distance between the pillars was set to 200 µm. Only the pillars with a wall thickness of 2 µm and an outer diameter of 12 and an inner diameter of 8 were able to withstand F_C during the development step. However, the resulting tips exhibited a slight tilt. Based on equation 4.1, a larger pitch would be necessary to eventually create straight 500 µm high pillars, which should be tested in the future. An additional option would be to consider alternative design criteria, such as a larger outer diameter, cone-shaped pillars, or the incorporation of supporting structures around the pillars. Nevertheless, for pillars with a length of 400, 300, and 200 µm and an outer diameter of 12 µm and an inner diameter of 8 µm, the formation of entirely straight pillars with a pitch of 200 µm was achieved (Figure 4.22E).
Subsequently, an investigation was carried out to ascertain the influence of varying pillar pitches for different heights. The objective was to determine the maximum height that could be attained for a given pitch. An array of pillars with a height of 50 µm and a pitch of 20 µm (Figure 4.22F) exhibits a few pillars, which bend towards each other around the edges. In contrast, an array of pillars with a height of 150 µm and a pitch of 25 µm (Figure 4.22G), as well as an array of pillars with a height of 200 µm and a pitch of 35 µm (Figure 4.22H), show only pillars without any bending.
The electrodeposition method permitted the filling of pillars up to 400 µm in height and 12/8 µm in outer/inner diameter, which was sufficient for the applications required by this work. Figure 4.22I shows the deposition curve of the filling of such a pillar and the resulting Au tip. The filling of pillars is contingent upon a number of factors, including the results of the 2PP process and the integrity of the pillars. The electrodeposition process itself also plays a significant role in this regard. The filling of taller pillars presents a notable challenge, as the electrodeposition process is constrained by ion diffusion and ion charge transfer mechanisms that shape the morphology of the deposited Au. To further enhance the efficiency of the electrodeposition process, strategies such as heating the Au solution or utilizing higher ion concentrations to accelerate the rate of deposition can be employed.

Parameter	**Explored configurations and tested values**	
Substrate Materials	Parylene-C and SU-8 on quartz	
Pillar height	Up to 500 µm straight pillars with 12 µm outer diameter and 200 µm pitch	
Pillar diameter and wall thickness	Down to 12/8 µm outer/inner diameter (2 µm wall thickness) for straight pillars of 500 µm height	
Pillar pitch and height	The pitch highly depends on the pillar geometry and height:	
	Pitch (µm)	Maximal possible height (µm)
	20	50
	25	150
	35	200
	200	500
Electrochemical deposition	Au-filled pillars of up to 400 µm height with an inner diameter of 8 µm	

Table 4.3.: Tested limitations of 3D printed electrodes on flexible 2D MEA (PiRi).

In table 4.3, the aforementioned design constraints are summarized. Thus, this technological approach enables the fabrication of 3D-printed pillar electrodes exhibiting high aspect ratios, reaching up to 33:1 (400 µm height and 12 µm outer diameter). These results surpass the aspect

ratios and electrode diameters previously reported in the literature when using 2PP printing processes, which were up to 11:1 and 10 µm, respectively [117][151].
Although high aspect ratios of up to 500:12 were achieved following 2PP printing, future applications, including targeting deeper cortical regions, utilizing larger animal models, or even human applications, necessitate the incorporation of pillars exceeding 500 µm in length. Accordingly, an additional UV-exposure during 2PP processing, as proposed by Purtov et al. [199], may be an effective method to enhance mechanical stability. The aforementioned process has the potential to enhance the cross-linking of the polymer, thereby augmenting its Young's modulus and consequently reinforcing the mechanical stability of the pillars throughout the fabrication process [199].

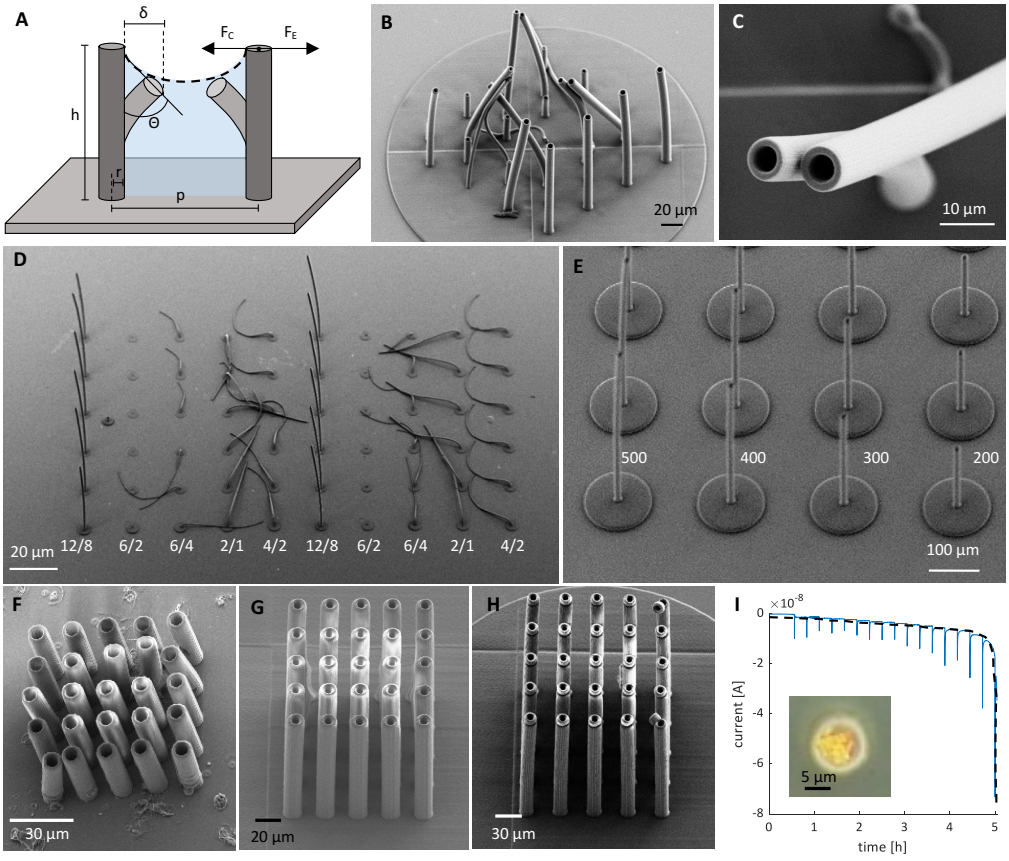

Figure 4.22.: Limitation of 3D printed pillars on PaC substrate. Mechanical instability due to capillary forces during the fabrication process (A) can lead to bent or collapsed pillars (B, C). D) Outer and inner diameter test parameters, where the first number denotes the outer diameter in micrometers, and the second denotes the inner diameter. The pitch of the pillars is 200 µm. E) Testing the pillar height of a straight pillar design with an outer diameter of 12 µm, an inner diameter of 8, and a pitch of 200 µm. F) An array of pillars with a height of 50 µm and a pitch of 20 µm. G) An array of pillars with a height of 150 µm and a pitch of 25 µm. H) An array of pillars with a height of 200 µm and a pitch of 35 µm. I) Current-time curve of the electrochemical deposition of Au for a 400 µm high pillar (modified from [41]).

4.4. Summary and outlook

Two distinct types of 3D neural implants were successfully fabricated via the integration of kirigami or 3D printing technology.
The implants are both customizable with respect to different neural targets (here retina and cortex). In both cases, modifications were made to the height of the shank/pillars, their width, and the pitch. To adapt the device design to the desired application for both designs, it is necessary to implement modifications to the 2D MEA as well as the CAD file for the print job, which serve as molds for KiRis and pillars for PiRis, respectively. However, the customizability is slightly higher for the PiRi, as different pillar dimensions and design configurations (e.g., straight or cone-shaped) can be printed on the same 2D flexible MEA design. In contrast, the 2D MEA as well as the molds must be adjusted for varying shank heights, widths, and distances between the shanks for the KiRis. Besides the customizable pillar design configuration, the PiRi process has been demonstrated to be capable of printing on a variety of substrates, including stiff MEA substrates [41]. This increases the range of possible applications, as it facilitates the utilization of the probes for cell cultures or organoids.
Both fabrication processes demonstrate high efficiency, necessitating only a minimal number of fabrication steps. The 2D flexible MEA is produced for both probe types in an identical manner and is typically manufactured in the same production cycle. Although 3D printing is a relatively rapid process, it is essential to consider the potential increase in printing time when utilizing objectives for high resolution. To illustrate, the printing of KiRi molds with a 25X objective can take a period of several days. For instance, the lower KiRiCor mold for 500 µm long shanks requires a printing time of 26 hours and 30 min with the 25X objective and only 3 hours with the 10X objective. Nevertheless, the 10X objective needs the manual identification of the interface during the printing process. Consequently, only a single mold can be printed at any given time. Furthermore, the dimensions of the molds allow for fabrication with any additive manufacturing process capable of achieving a resolution of µm-mm (e.g., digital light processing printers [202] or projection micro stereolithography [203]). Another advantage is that the molds are reusable. When handled correctly, they are not damaged during the folding procedure. The folding process itself is rapid, with a completion time of less than one minute for one KiRi probe. In contrast, the dimensions of the PiRi probes necessitate high resolution, which is provided by the 2PP process. The printing of a PiRi probe with 60 x 80 µm high pillars using a 25X objective is a fast process and requires < 3 min. However, if higher resolutions are required for more complex structures, the considerably greater investment of time for the use of a 63X objective should be considered. In addition, the filling of the pillars is a time-consuming process that scales with the pillar height. For instance, the filling of 100 µm long pillars takes on average 23 min. In conclusion, the processing time required to fabricate a single PiRi probe is significantly higher than that of a single KiRi probe, with the former taking over 20 min and the latter less than one minute. It should be noted that the processes that are identical for both samples, such as the 2D MEA fabrication and flip-chip bonding, as well as the time spent for several probes simultaneously, which is the development step following printing for the PiRis and the fabrication of molds for KiRis, were not included in this analysis.
To further decrease the fabrication time, from an engineering perspective, the KiRi process could be scaled up to meet the demands of larger production volumes, assuming the necessary resources and infrastructure are available. In this case, the deployment of a machine would be necessary for the automation of the folding process, with the objective of fabricating multiple probes simultaneously. In contrast, the PiRi process will necessarily entail a linear printing process with 2PP. Therefore, scalability is inapplicable to this process.
The yield of the probes is comparable, with yields of approximately 52% for the KiRis and 55% for the PiRi, respectively. However, when considering only the most recent fabrication run of the KiRis, which occurred subsequent to a substantial learning curve, a yield of 80% could be ac-

complished. This yield exceeds that of all fabrication runs of the PiRi implants. The folding of a complete implant with 1000 µm long shanks was not entirely successful. Accordingly, for experimental purposes, shanks of a maximum length of 500 µm were considered. In comparison, PiRi pillars with up to 400 µm could be filled with Au. However, the filling of such long pillars was a time-consuming process and was only successful for individual pillars, not for complete probes. Therefore, only pillar lengths of up to 250 µm, which could be reliably produced, were considered during the experiments.
It would be beneficial to consider ways to enhance the yield in order to achieve a more reliable fabrication process. This should be done not only by considering or implementing the aforementioned processes for the fabrication of 3D devices, such as the use of micromanipulators during the folding process for KiRis or the improvement of Au electrodeposition for PiRis, but also by considering the 2D MEA fabrication process. The quality of the electrodes is significantly influenced by the underlying metal layer of the 2D MEA, which in turn affects the yield and functionality of the electrodes. As previously discussed in section 4.1.2, it is of the utmost importance to consider the fabrication challenges of the 2D MEA in order to guarantee optimal fabrication of 3D kirigami or 3D printed implants.
For comparison, the cross-section of a shank was 500 µm² (50 µm in width and 10 µm thick), whereas the cross-section of a straight PiRi pillar with an outer diameter of 12 µm was only 110 µm². Nevertheless, the density of the shanks must be taken into account. While KiRi shanks contain up to four electrodes, a straight or cone-shaped pillar has only one recording/stimulation site. Therefore, they are only capable of recording from a single depth within the neural tissue at any given time, which constrains their ability to perform 3D neural tissue recordings. Consequently, a multisite approach was employed for the PiRis with the objective of recording from multiple neural depths. By utilizing multisite pillars, three recording sites were utilized, resulting in an increased cross-section of 250 µm².

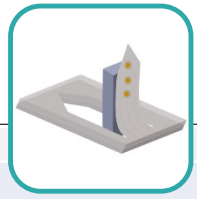

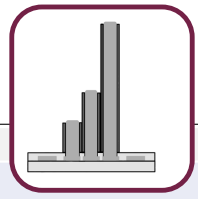

	KiRi	PiRi
Customizable design	+	+ +
Fast fabrication process	+ + +	+
Scalability of the process	+ + +	-
Yield	52 % (80 % in the latest fabrication run)	55 %
Max. shank/pillar height for implantation	500 µm	250 µm
Shank/pillar cross-section at centroid	500 µm²	Straight pillar: 110 µm² Cone-shaped pillar: 541 µm² Multisite pillar: 250 µm²

Figure 4.23.: Comparison of KiRis and PiRis for the development and fabrication of 3D neural implants.

Further improvements to the KiRi and PiRi samples could be made by utilizing longer shanks or pillars, enabling deeper penetration into the cortical layers. As discussed in section 4.2.5, it is necessary to investigate whether the folding approach for KiRis with shank length exceeding 1 mm is feasible. One potential method for achieving this could be the "upside-down approach". To further reduce the insertion footprint of the KiRis and enhance their conformability to neural tissue, it would be beneficial to investigate the feasibility of fabricating smaller shank dimensions in terms of thickness and width. Similarly, printing of higher pillars for the PiRis should be feasible by slightly increasing the diameter of the pillars at the base, or by adding supporting structures close to the base. However, filling pillars higher than 400 µm is challenging, as discussed in section 4.3.4. An

alternative approach would be to utilize 2PP printing of conductive structures, which may potentially result in a reduction in the spatial resolution of the electrodes in the future. Nevertheless, the insertion of longer pillars and shanks will be challenging due to the low bending stiffness and consequent buckling. It is therefore necessary to investigate the implantation techniques that will be required for *in vivo* applications. In this context, the available strategies range from the use of insertion shuttles made of Si [97], needles [93], or microwires [98][99], the use of a biodegradable polymers, e. g. PEG, to reduce the effective length of the implant [33][102], or the incorporation of mechanical adaptable materials, such as hydrogels [103].
KiRi probes with up to 512 electrodes have been manufactured. To augment the electrode count even further, two strategies may be pursued without an increase in processing time. The first strategy entails reducing the width of the feedlines and electrode diameter. Consequently, the number of feedlines and electrodes that can be accommodated not only within a single shank but also on the x-y-plane of the KiRi probe will be augmented. Concurrently, a three-layered probe comprising a single metal layer embedded between two PaC layers can be retained. However, the resolution is constrained by the lithographic techniques employed. In this particular case, feedlines with a width of approximately 2 µm and electrodes with a diameter of up to 25 µm were successfully implemented using maskless lithography. It is important to note, however, that submicron features are achievable with other techniques, such as electron-beam lithography, as demonstrated by others [204]. A second strategy is to increase the shank density. However, the success of the mechanical pressing is limited by the remaining area of the flexible probe, as discussed in section 4.2.5. In addition to the folding procedure itself, the primary bottleneck is the separation of the 3D flexible probe from the lower mold. Therefore, for probes with a high amount of long shanks, a device should be implemented to lift the flexible probe uniformly.
However, the interconnection of all 512 electrodes on a KiRi implant is a challenge. Thus, at present, the contact pad facilitates a connection to a restricted number of electrodes (16, 32) due to the limitations of the data acquisition system. An ideal solution would be a wireless, high-channel connector design, which would be advantageous for long-term recordings. However, wireless front ends with 512 channels are currently not commercially available. Thus, the issue of acquiring thousands of channels for measurement and stimulation is not solely contingent upon the electrodes themselves. Rather, it is primarily contingent upon the (electronic) components for data acquisition, recording and electrical stimulation. This gives rise to a number of challenges. Firstly, establishing a connection between the numerous electrodes and a PCB represents a significant challenge when the number of electrodes is increased, particularly in terms of spatial constraints, as each electrode requires an individual connection. In addition, the PCB itself should be of a reduced size. To illustrate, a compact Omnectis connector with the capacity to connect 32 channels has a size of 14.6 x 4.4 x 1.8 mm. It would be prudent to explore the use of smaller alternatives in this instance. One such alternative could be the use of flexible PCBs, or alternatively, the establishment of a wireless solution. Subsequently, the data acquisition system (DAQ) must be capable of accommodating a considerable number of channels. The MCS system currently in use is limited to 64 channels, but allows for the connection of eight 32-channel head stages, which equates to a total of 256 channels. It may therefore be necessary to consider alternative commercial DAQ systems or to develop a new system in-house. Finally, the vast quantity of data produced by a large number of electrodes should not be underestimated. It is of the utmost importance that considerations regarding efficient data management, fast processing and storage capacities are explored in conjunction with the increase in channels.

5. Performance of 3D implants

In order to ascertain the performance of 3D implants and ensure that their properties are suitable for electropysiological experiments, a comprehensive evaluation of several electrochemical and mechanical characteristics was conducted.
This chapter is partly reproduced from the following publications:

- **M. Jung**, M. Kasavetov, N. Nruthyathi, J. Abu Shihada, S. Decke, L. Koschinski, F. Balcewicz, T. Lohmann, P. Walter, F. Müller, A. Offenhäusser, V. Rincón Montes. “Towards the in vivo validation of 3D retinal implants: an in vitro and cadaveric validation” (in preparation)
- **M. Jung**, J. Abu Shihada, S. Decke, L. Koschinski, P. S. Graff, S. Maruri Pazmino, A. Höllig, H. Koch, S. Musall, A. Offenhäusser, V. Rincón Montes. "Flexible 3D *Kirigami* Probes for In Vitro and In Vivo Neural Applications". Advanced Materials 2025, DOI: 10.1002/adma.202418524
- J. Abu Shihada* and **M. Jung***, S. Decke, L. Koschinski, S. Musall, V. Rincón Montes, A. Offenhäusser. "Highly Customizable 3D Microelectrode Arrays for In Vitro and In Vivo Neuronal Tissue Recordings". Advanced Science 2024, DOI: 10.1002/advs.202305944 (**Equal contribution*)

5.1. Electrochemical properties

The electrochemical characterization was performed according to section 3.3.1 for KiRi as well as PiRi electrodes.

5.1.1. Impedance

The EIS characterization of the electrodes revealed a notable reduction in impedance following the deposition of the PEDOT:PSS coating. At 1 kHz, the impedance of the electrodes was reduced by 59-fold for the PiRis and by 28-fold for the KiRis. Figure 5.1 illustrates the impedance spectra for a single KiRi probe with electrodes (Ø= 15 µm) and a PiRi probe (straight pillars with a 8 µm opening). The spectra are presented for the following cases: Figure 5.1A after cleaning the Au electrodes and electrodeposition of PEDOT:PSS in the case of the KiRis, and Figure 5.1B following the Au as well as the PEDOT:PSS electrodeposition in the case of the PiRis.

In this example, the impedance of the PiRi electrodes was observed to be 2.1 MΩ and 35.1 kΩ at 1 kHz following the electrodeposition of Au and PEDOT:PSS, respectively. In the case of the KiRi electrodes, the impedance exhibited as well a notable decrease, from 1.6 MΩ to 46.1 kΩ at 1 kHz. The impedance values of the Au electrodes at 1 kHz are slightly higher compared to standard 2D electrodes with 10 µm diameter (1 MΩ at 1 kHz [205]). This suggests that the Au does not overgrow the PiRi pillars, which would have been indicated by a lower impedance value due to the increased surface area. Instead, it is observed to cover only the 8 µm wide pillar opening. The impedance amplitude of both electrode types demonstrates a decline as the frequency increases, exhibiting the characteristic profile of an Au electrode as observed in previous studies [205]. Upon depositing PEDOT:PSS onto Au, the electrochemical performance of the electrodes exhibits the anticipated resistive behavior of PEDOT:PSS electrodes within the high frequency band relevant for spiking activity (1 kHz to 100 kHz). Furthermore, it exhibits capacitive behavior at low frequencies, where

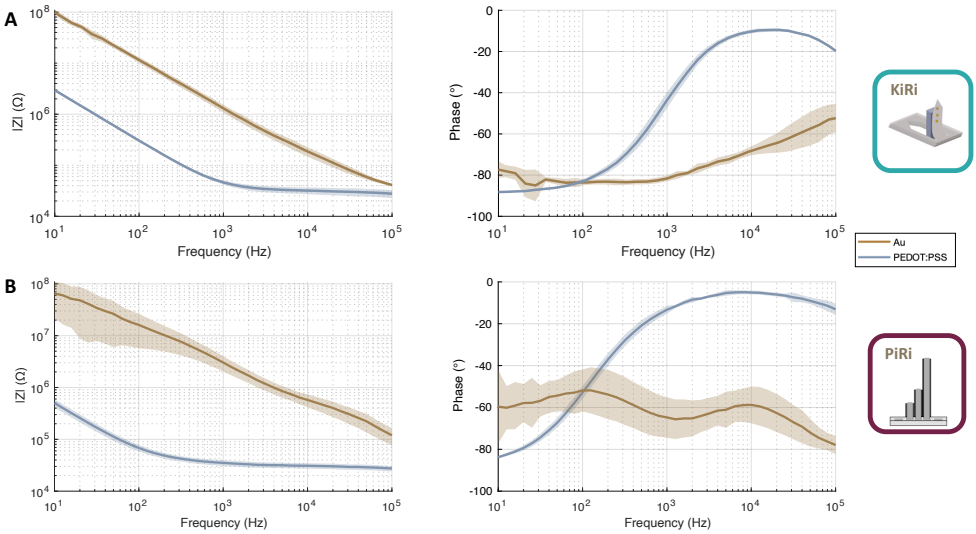

Figure 5.1.: EIS of PiRi (A) and KiRi (B) Au electrodes and after electrode coating with PEDOT:PSS. A) The impedances of the PiRi electrodes were measured after the electrodeposition of Au and again after the following electrodeposition of PEDOT:PSS(N = 11). B) The Impedances of the KiRi electrodes were measured after cleaning the Au electrodes and after the deposition of a PEDOT:PSS electrode coating (N = 7) (modified from [197]).

the phase angle is approximately - 90° (below 10 Hz), which is the typical range for measuring LFPs. This shift can be attributed to the enhanced ionic conductivity of PEDOT:PSS, and aligns with the observations documented in the literature [205][206][207][208].

When comparing the impedance values at 1 kHz between PiRi probes and KiRis, there are notable differences in some cases. Figure 5.2A shows the mean ± standard deviation of the amplitude (|Z|) and phase (°) of the complex impedance Z of KiRi electrodes with Ø25 µm (N = 33) and Ø15 µm (N = 60), as well as PiRi electrodes (N = 66). For the Ø25 µm KiRi electrodes, the impedance at 1 kHz of 28.9 ± 9.9 kΩ is significantly lower in comparison to the Ø15 µm electrodes with 38.7 ± 6.9 kΩ. This is due to the increased surface area. Furthermore, the KiRis were separated according to the type of feedline employed (meander-shaped or straight) to facilitate a more detailed analysis. For the meander-shaped feedlines, electrodes with Ø15 µm had an impedance of 38.4 ± 9.0 kΩ (N = 32) and 39.1 ± 3.4 kΩ (N = 28) for straight feedlines, respectively. For electrodes with Ø25 µm the impedance was 30.8 ± 11.9 kΩ(N = 19) for meander-shaped feedlines and 27.5 ± 8.1 kΩ for straight feedlines, respectively (N = 14). The analysis revealed no significant difference between meander-shaped and straight feedlines when electrodes of varying sizes were considered independently (Figure 5.2B). However, the slight increase in the standard deviation of the meander-shaped feedlines points to a more stable fabrication process for the straight feedlines. Consequently, they were selected for further experiments. The primary reason for the noted instability appears to be the proximity of meander-shaped feedlines to the edge of the shanks, which raises the possibility of exposure to minor cracks. This phenomenon is a direct consequence of the RIE processing stage, as discussed in section 4.1.2. The impedance was determined to be 30.3 ± 12.6 kΩ for the PiRis. No statistically significant difference was observed between the large KiRi electrodes (25 µm) and the PiRi, indicating comparable electrochemical performance. A statistically significant difference was observed when comparing the small KiRi electrodes (15 µm) with the PiRis, which is likely attributable to the differences in electrode surface area. Additionally, the standard deviation of PiRi electrodes was marginally higher than that of KiRi electrodes, potentially due to the unequal surface when comparing different PiRi electrode caps in

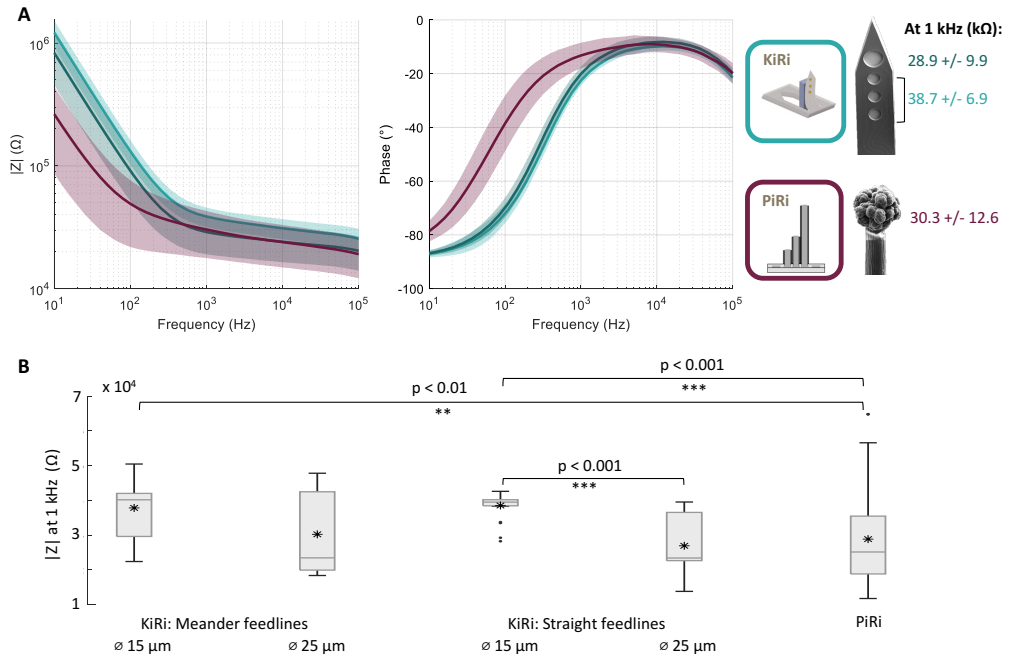

Figure 5.2.: EIS analysis and comparison of KiRi and PiRi electrodes. A) EIS measurements of KiRi electrodes with Ø25 µm (N = 33) and Ø15 µm (N = 60), as well as PiRi electrodes (N = 66) showing the mean ± standard deviation of the amplitude (|Z|) and phase (°) of the complex impedance Z. B) Box plot of the impedance values of KiRi probes with meander and straight feedlines. Electrodes with Ø15 µm had an impedance of 38.4 ± 9.0 kΩ (N = 32) for meander and 39.1 ± 3.4 kΩ (N = 28) for straight feedlines, respectively. For electrodes with Ø25 µm the impedance was 30.8 ± 11.9 kΩ(N = 19) for meander-shaped feedlines and 27.5 ± 8.1 kΩ for straight feedlines, respectively (N = 14). For the PiRis, the impedance was 30.3 ± 12.6 kΩ. The mean values are indicated with black stars inside the box plots. Statistical analysis was conducted using pairwise unpaired t-tests with Bonferroni correction (modified from [197]).

contrast to the well-defined KiRi electrodes.
For this reason, the KiRi as well as the PiRi exhibit an electrochemical performance that is optimal for electrophysiological recordings, as low impedance values improve the recording quality of neural implants [93].

The thermal noise of PiRi and KiRi electrodes was computed according to equation 3.5. Given the low impedance after PEDOT:PSS electrodeposition, the PiRi as well as the KiRi electrodes exhibited a thermal noise of 1.3 µV for a bandwidth of 300 Hz to 3 kHz.

5.1.2. Charge storage capacity (CSC)

The cathodic CSC_C was examined for KiRi electrodes with Ø25 µm, which were designed to use for electrical stimulation, as well as for PiRi electrodes. Figure 5.3 depicts the CV response in the form of current density at different electrode potentials (E) versus the Ag/AgCl RE. From the CV curve the CSC_C was computed according to equation 3.6. In order to achieve this, it was necessary to calculate the GSA of the electrodes. For the KiRi electrodes, the GSA was calculated as the area of a circle by

$$GSA_{KiRi} = \pi \cdot (0.00125cm)^2. \tag{5.1}$$

However, the surface morphology of the electrodes is more irregular for the PiRis, with significant

variation between electrodes. Therefore, the radius r, which differs for each electrode, was measured using an optical microscope. Then, the GSA was estimated as the area of a sphere for each electrode by

$$GSA_{PiRi} = 4\pi \cdot r^2. \tag{5.2}$$

For the KiRis, the CSC_C was 6.9 ± 3.8 mC/cm^2, which was slightly lower in comparison to the PiRis at 9.1 ± 1.5 mC/cm^2, respectively. Thus, for KiRi electrodes the mean value is lower and the standard deviation is higher in comparison to the PiRis. This might be attributed to the different deposition methods, which was chronoamperometry for the KiRis and CV for the PiRis. Thus, using CV may lead to a more homogeneous deposition of PEDOT:PSS.

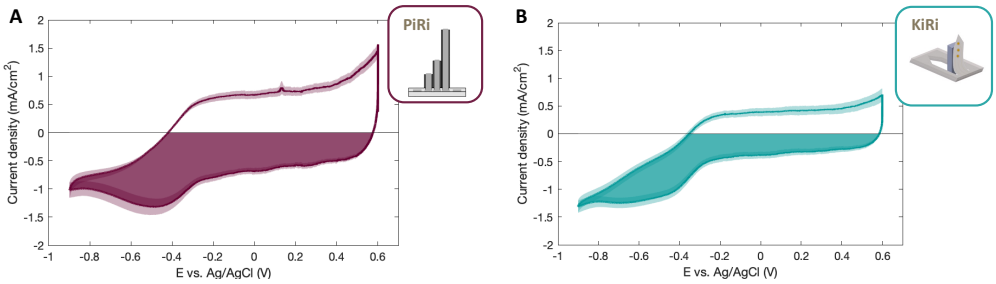

Figure 5.3.: CV (current density) responses of KiRi (A) and PiRi (B) electrodes. The current density (mean ± SE) at different electrode potentials (E) versus an Ag/AgCl RE, as well as the cathodic CSC_C (colored areas) is marked in the CV curve (N = 10 for PiRi and N = 11 for KiRi electrodes, modified from [197]).

5.1.3. Charge injection capacity (CIC)

Furthermore, the maximum CIC of the KiRi and PiRi electrodes was examined by determining the current and charge injection thresholds, with the objective of preventing electrode polarization beyond the limits of the water window. In order to characterize the voltage transients, a maximum cathodic polarization voltage of -0.9 V and a maximum anodic voltage of 0.6 V were considered, as these values are commonly reported in the literature for PEDOT:PSS electrodes [173][209]. The current limits of biphasic pulses with varying pulse widths, designated as T_{ph}, were assessed through the utilization of either an anodic or cathodic first pulse. Figure 5.4A depicts the measured voltage transients for the KiRi and PiRi electrodes when employing either anodic or cathodic first pulses for varying T_{ph} using the maximum anodic I_{ma} or cathodic currents I_{mc}. The cathodic potential limit E_{mc} was set to -0.9 V, while the anodic potential limit E_{ma} was set to 0.6 V. These limits were reached 20 µs after the peak of the pulse. In the case of anodic first stimulation, the anodic potential limit E_{ma} was typically reached before the cathodic potential limit E_{mc}. Conversely, the opposite behavior was observed for cathodic first pulses. The employed pulse widths spanned a range of values, from 0.1 to 10 ms. The specific widths utilized were 0.1, 0.5, 0.8, 1, 2, 3, 4, 5, and 10 ms. The mean and standard deviation of the current limits were evaluated for each pulse width (Figure 5.4B and table B.1). It was observed that, in general, a smaller T_{ph} resulted in a higher I_{ma} or I_{mc} compared to a larger T_{ph}, while indicating a nonlinear relationship between these parameters. Furthermore, the current limits and pulse width exhibited an inverse exponential correlation, which, when plotted on a logarithmic scale, revealed a linear decreasing trend. These general findings are consistent with the literature [209]. For PiRi electrodes, it was also evident that enlarging the electrode cap permitted greater current injection with respect to anodal and cathodal threshold potentials (Figure 5.4C). Due to the differing electrode sizes, the standard deviations of the current limits are generally higher for PiRi electrodes than for KiRi electrodes, which have a more uniform surface area that is typically comparable between electrodes.

Subsequently, the CIC, defined as the product of the current limits(I_{mc} or I_{ma}) and T_{ph} divided by the GSA of the electrode (equation 3.7), was evaluated. Similarly, for the CSC calculations, the GSA was estimated as a circle with a diameter of 25 µm for KiRis and as a sphere with a diameter measured with an optical microscope for the PiRi electrode caps. It should be noted, however, that the actual surface area is dependent on the underlying morphology of the PEDOT:PSS layer and may differ from the estimated values. Figure 5.4D and table B.2 contain the CIC measurements for KiRis and PiRis and anodic and cathodic first pulses for different T_{ph}. The CIC was, in general, higher for PiRi electrodes in comparison to KiRi, as well as for anodic first pulses relative to cathodic first pulses. It was observed that an increase in the pulse width (T_{ph}) generally resulted in a greater amount of injected charge, as reflected by the higher CIC value. In particular, the CIC for KiRi electrodes was enhanced by approximately 51% when the pulse width was increased from 0.1 ms to 1 ms, and by approximately 150% when the T_{ph} was increased from 0.1 ms to 10 ms for anodic first pulses. For cathodic first pulses, the enhancement was approximately 37% and 132%, respectively. For PiRi electrodes, the CIC was enhanced by 69% when the pulse width was increased from 0.1 ms to 1 ms and by 153% when the pulse width was increased from 0.1 ms to 10 ms for anodic first pulses. For cathodic first pulses, the enhancement was 35% and 126%, respectively. Therefore, clinical stimulation protocols requiring a sustained pulse duration are permitted a higher CIC limit, whereas those necessitating brief pulse widths are permitted a lower CIC limit. This compromise between immediate electrical stimulation, which employs shorter T_{ph} and consequently a higher frequency, and safe stimulation (limitation of the CIC) has been previously elaborated upon in the literature [209].

5.2. Mechanical properties

5.2.1. Insertion of 3D implants

The objective of the two types of 3D implants, KiRis and PiRis, is to record from beyond the superficial layers of neural tissue without compromising the viability of the surrounding tissue. Accordingly, in the design considerations, the smallest cross-sectional footprints that could be constructed with the aforementioned fabrication techniques were taken into account. As reported in the literature, an insertion force (F_i) between 0.5 and 2 mN is required to penetrate neural tissue [94].

The critical buckling load P_{cb} was analyzed as a matter of insertion probability. If F_i exceeds the critical buckling load P_{cb} of the shanks or pillars, they will fail due to bending while attempting to penetrating the tissue. Consequently, in order to evaluate the probability of insertion of KiRis and PiRis into neural tissue, an investigation of P_{cb}, which is dependent upon their physical properties and dimensions, was conducted using Euler's equations (equation 3.8). Figure 5.5A shows the critical buckling load plotted against the height of pillars of varying PiRi designs or KiRi shanks (slender columns), with the insertion threshold marked according to the literature. Figures 5.5B and 5.5C illustrate the Von Mises' stress due to critical buckling, considering an F_i of 0.5 mN and the maximum possible height for KiRi shanks and PiRi pillars.
In order to ascertain the optimal design for the PiRis, a comparison was conducted between the three distinct pillar configurations: straight, cone-shaped, and multisite. The straight pillars exhibited an inner diameter of 8 µm and an outer diameter of 12 µm. The cone-shaped pillars exhibited an outer diameter of 35 µm and an inner diameter of 30 µm at the base, while the outer diameter was 12 µm and the inner diameter was 8 µm at the end of the pillar. For the multisite pillars, three straight pillars were selected in a linear configuration, with an inner diameter of 8 µm and an outer diameter of 12 µm. Simulations conducted using COMSOL Multiphysics indicate that cone-shaped and multisite pillars exhibit reduced stress along the z-axis and at the

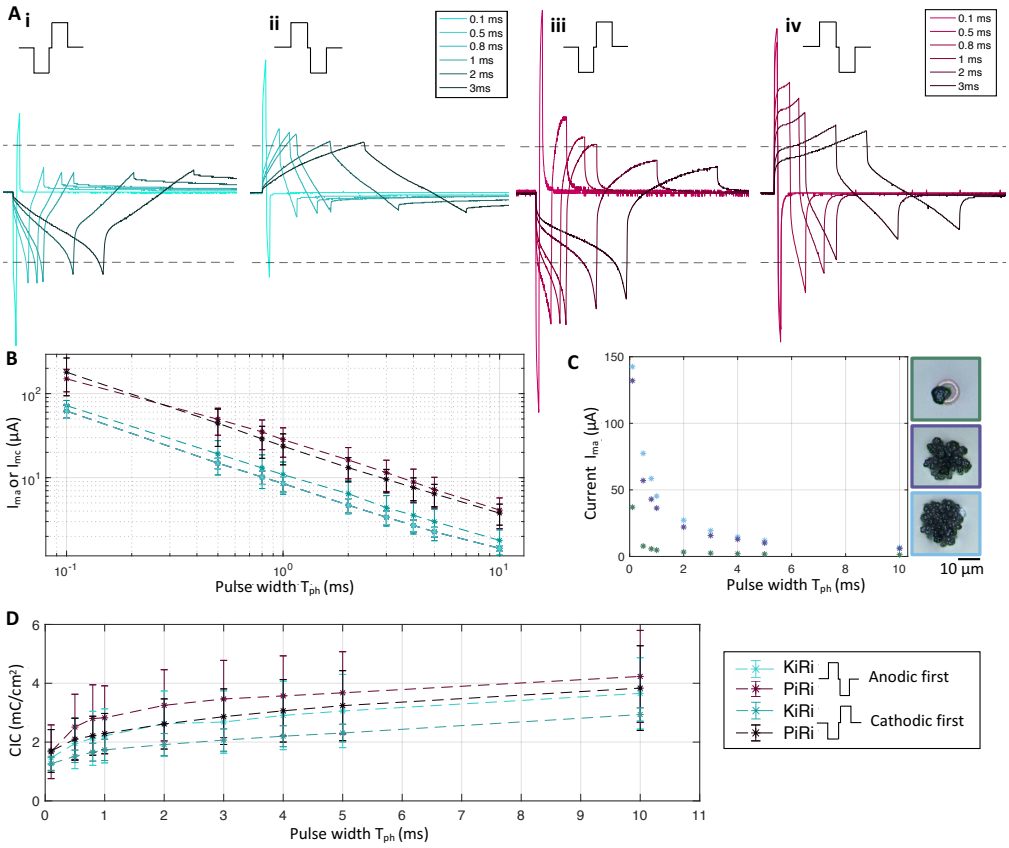

Figure 5.4.: Analysis of the voltage transients and CIC using biphasic anodic and cathodic first stimulation pulses. A) Voltage transients for different pulse widths T_{ph} for KiRi (i, ii) and PiRi (iii,iv) electrodes using first cathodic (i, iii) and first anodic (ii, iv) biphasic pulses. B) The maximum anodic I_{ma} or cathodic currents I_{mc} of the first pulse at which the maximum polarization voltages (-0.9 V, 0.6 V) were reached for different pulse width T_{ph}. C) The maximum current depends on the size of the electrode cap of the PiRi electrodes. Here, three example measurements and the corresponding microscopic images are shown in green, violet and blue. D) Calculated CIC for the different pulse width T_{ph} of KiRi and PiRi electrodes using anodic or cathodic first biphasic pulses (N = 14 for PiRi and N = 9 for KiRi electrodes, modified from [197]).

base of the pillars. This suggests enhanced stability and less risk of pillar breakage compared to straight pillars when penetrating neural tissues (Figure 5.5B). The simulations revealed that when considering a F_i of 0.5 mN, pillar heights of 390, 910 and 1150 µm are achievable before buckling of straight, multisite and cone-shaped pillars, respectively. Furthermore, as the wall thickness at the base of the pillars was determined to be 4 µm as revealed by the FIB-cut analysis (Figure 4.19), the simulations were conservatively conducted with an assumption of a 2 µm wall thickness. It is notable that a 4-µm wall thickness results in a 75% increase in the P_{cb}, indicating that the theoretical stability of the pillars is likely to exceed the observed values.

To evaluate the potential for penetration of the shanks of a KiRi probe, simulations were conducted using slender columns with a width of 50 µm, a thickness of 10 µm, and varying lengths. Once more, Euler's equations were employed to ascertain the feasibility of inserting a 10 µm-thick PaC layer stack thermoformed at 160 °C with a Young's modulus of 1.7 ± 0.32 GPa and a length up to 530 µm into neural tissues (Figure 5.5C).

The simulations were conducted without the use of additional insertion aids, such as shuttles or

dissolvable braces, under the assumption of a maximal insertion force of 0.5 mN to penetrate neural tissues, such as brain tissue without meningeal layers, such as the dura. The analysis demonstrated that KiRi shanks and PiRi pillars can be inserted into deeper neural layers, with the potential for even higher insertion depths achievable with PiRi pillars.

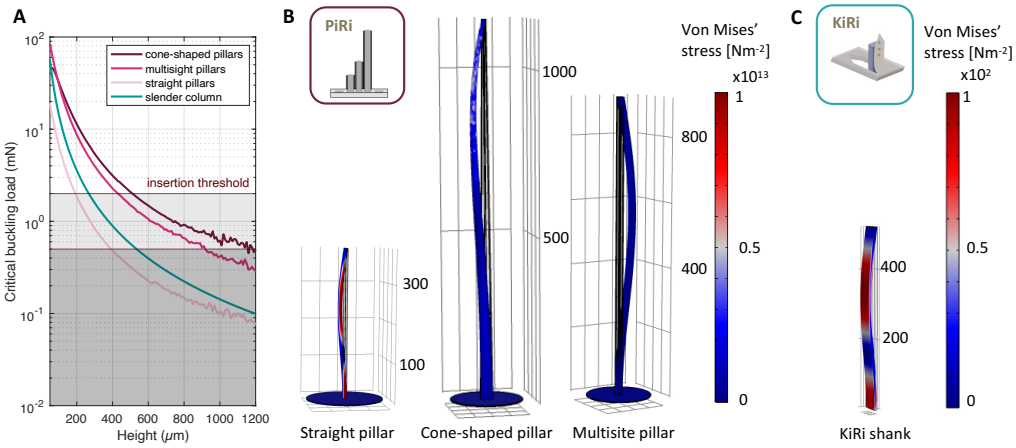

Figure 5.5.: Buckling load and Von Mises' stress simulated using COMSOL multiphysics. A) Results from the simulated buckling load according to the pillar or shank height for different PiRi designs and KiRi shanks (slender column). B) Von Mises' stress for the different PiRi design. C) Von Mises' stress of a slender columns (KiRi). B) and C) show the highest pillar/shank configuration possible before the critical buckling load is exceeded (modified from [177][41]).

Insertion tests using tissue phantoms were performed prior to animal experiments to ensure safe insertion. Agarose gel, which exhibited a comparable Young's modulus of 2–10 kPa, was selected to simulate the mechanical properties of neural tissue [157]. The agarose mold was prepared according to the method described in [157], using agarose powder (A9539-256, Sigma Aldrich, Germany) and 0.1 M PBS. The KiRi and PiRi probes were then inserted into the agarose. The probes were mounted on a micromanipulator and lowered at a slow and controlled rate until they reached the surface of the agarose. Subsequently, an insertion rod, which was fixed to a second micromanipulator, was lowered until it was in close proximity to the upper portion of the neural probes. Then, the insertion rod was lowered in a stepwise manner to exert pressure on the neural probe and facilitate its insertion into the agarose. The aforementioned methodology was employed to successfully insert KiRi probes with 128 x 225 µm long shanks (Figure 5.6A$_i$ and zoom-in A$_{ii}$), as well as probes with 8 x 500 µm long shanks (Figure 5.6A$_{iii}$), into agarose gel, as illustrated in Figure 5.6. The insertion of PiRi probes was also tested using a multisite probe with heights of 500, 480, and 460 µm (Figure 5.6B$_i$) and probes with 16 x 350 µm high cone-shaped pillars (Figure 5.6A$_{ii}$). While the insertion of the multisite probe was successful, the insertion of the cone-shaped probe frequently resulted in tissue dimpling (Figure 5.6A$_{ii}$, black arrow), indicating that the pillars were not fully inserted.

The insertion forces were quantified during the insertion of the KiRi and PiRi probes (Figure 5.8A). The probes were inserted into neural tissue at a constant rate of 200 µm/s, while the insertion forces were measured in accordance with the methodology outlined in section 3.3.2. Typically, the force increased linearly reaching its peak until the insertion stopped. Thus, the main contribution to the force observed was the frictional force and no additional peak was observed that would correspond to penetration force to overcome tissue dimpling. Subsequently, as the tissue

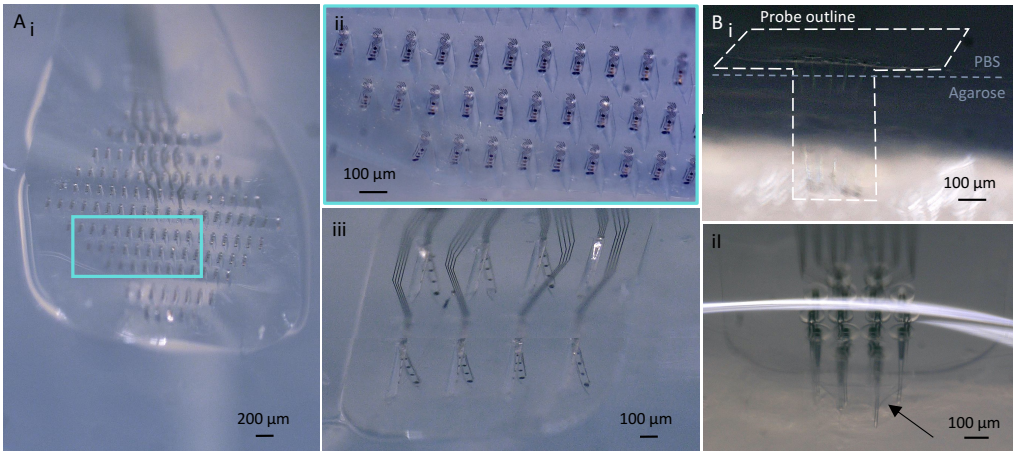

Figure 5.6.: Insertion into agarose gel of KiRi (A) and PiRi (B) probes. The insertion of a KiRi probe with 128 x 225 µm long shanks (A_i and zoom-in in A_{ii}) as well as a probe with 8 x 500 µm long shanks (A_{iii}) was tested. For the PiRi probes, a multisite design with length of 500, 480 and 460 µm was successful (B_i), while using 16 x 350 µm long cone-shaped pillars often led to tissue dimpling (B_{ii}, black arrow) (modified from [177][41]).

relaxed, the force measurement exhibited a decrease until it stabilized after a couple of minutes. This behavior is consistent with the observations reported in the literature regarding the insertion force measurements using flexible neural probes [210][211]. The KiRi probes, comprising eight 500 µm long shanks, were subjected to measurement, exhibiting a peak force of 1.1 ± 0.2 mN (N = 7). During the insertion process, no bending of the flexible shanks was observed, and thus the probe design was selected for testing *in vivo* cortical application. In comparison to the KiRis, the insertion force is with 2.7 ± 0.9 mN (N = 6) higher for the PiRis. As previously stated, the insertion of 16 x 350 µm long cone-shaped pillars occasionally resulted in tissue dimpling, which can necessitate a greater force for penetration of the tissue. This also explains the high standard deviation, as the occurrence of tissue dimpling was not consistent. Furthermore, the PiRi probes consist of 16 pillars with a collective cross-sectional area of 16 x 541 µm^2 = 8656 µm^2. In comparison, the total cross-sectional area of an individual KiRi probe shank is 500 µm^2, while that of an entire probe is 4000 µm^2. Notably, this was maintained while the number of electrodes remained consistent with the PiRi probes. This discrepancy in cross-sectional area also contributes to the increased insertion force observed in the PiRi probes.

The reusability of the KiRi and PiRi probes was evaluated after performing *in vitro* as well as *in vivo* insertions. The insertion of the probes into neural tissue was performed on multiple occasions (greater than 10) for both the KiRi and PiRi probes, which demonstrated the feasibility of reusing them without compromising their functionality. The mean number of *in vitro* insertions for PiRi probes was 3.2. Figure 5.7A presents a PiRi multisite probe that was utilized 10 times in retinal tissue. As can be observed in the SEM image, residual retinal tissue is present, having been extracted along with the probe (Figure 5.7A_{ii}, white arrow). It should be noted that two of the pillars do not contain electrode tips. However, these have not been present prior to the use of the probe (Figure 5.7$A_{i,iii}$, white dashed circles). The utilization of KiRi probes exhibited equal repetition, with an average of four insertions per probe. Subsequent to four insertions, the impedance of the electrodes was assessed for both KiRi and PiRi probes. While the impedance demonstrated a minimal increase for the PiRis (from 34.7 ± 14.1 to 35.6 ± 19.9 kΩ at 1 kHz (N = 20)), the increase was more pronounced for the KiRis (from 41.1 ± 18.1 to 120.9 ± 132.1 kΩ at 1 kHz (N = 31)) (Figure 5.7C). The study found that 95% of the PiRi electrodes and 94% of the KiRi

electrodes retained functionality after four insertions, suggesting, together with the impedance measurements, that the stability of PiRi electrodes upon multiple insertions is higher than that of KiRis. However, a KiRi probe that underwent 16 insertions during *in vitro* trials exhibited 100% electrode functionality, despite an increase in impedance to 176.3 ± 165.5 kΩ at 1 kHz (N = 16). Furthermore, the KiRi probes were examined following their *in vivo* implantation into mouse cortex for a period exceeding four weeks. Inspection using an optical microscope and an SEM (Figure 5.7B$_{i,ii}$) revealed that the shanks remained in an upright position. While the angle was not 90°, the forces applied during extraction must be considered. Upon inspection, the electrodes exhibited no signs of delamination (Figure 5.7B$_{iii}$).

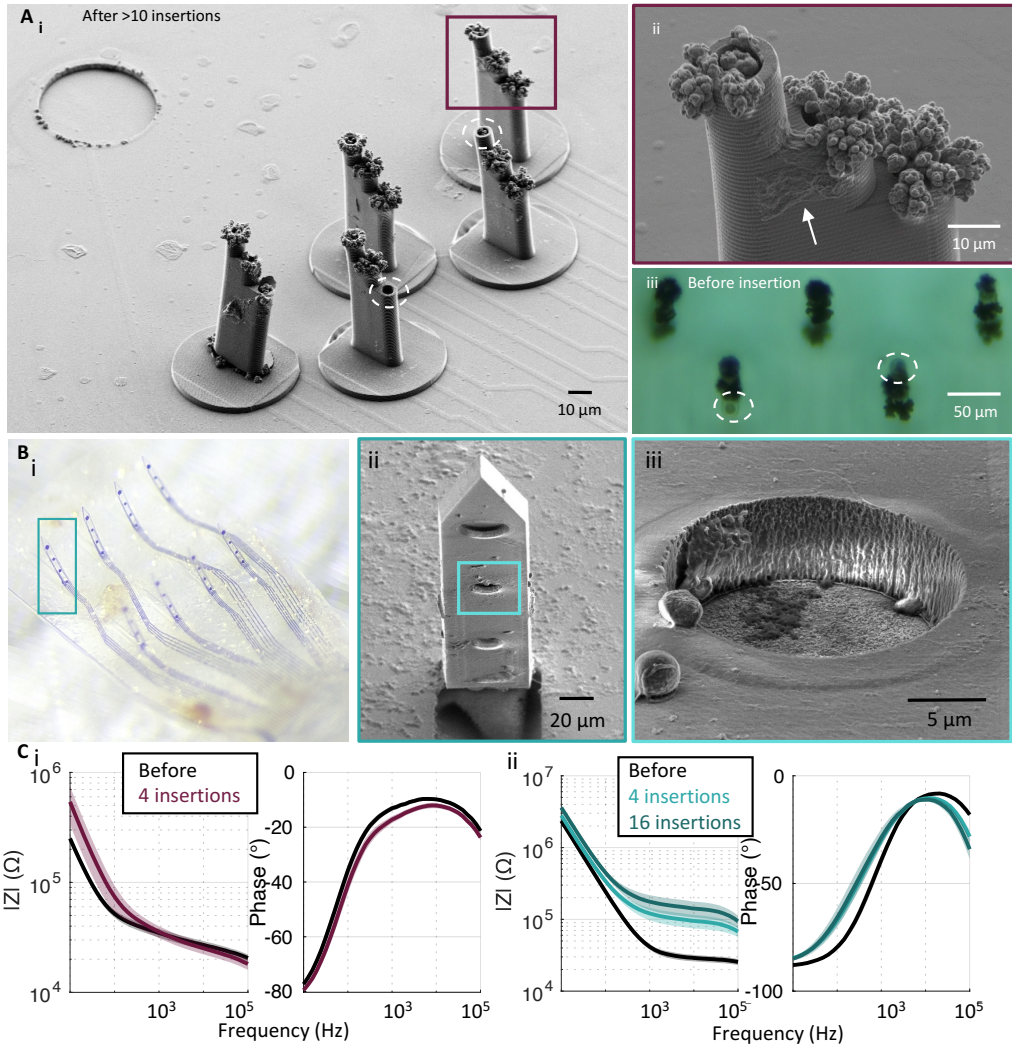

iii

Impedance at 1kHz (kΩ)

	PiRi	*KiRi*
Before	34.7 +/- 14.1 (N = 20)	41.1 +/- 18.1 (N = 47)
After 4 insertions	35.6 +/- 19.9 (N = 20)	120.9 +/- 132.1 (N = 31)
After 16 insertions		176.3 +/- 165.5 (N = 16)

Figure 5.7.: Post-experiment optical inspection of a PiRi probe used during *in vitro* trials (A) and a KiRi probe used for an *in vivo* implantation (B). A) SEM picture of a PiRi multisite probe with five shanks comprised of three electrodes each with heights of 80, 100, and 120 µm after it was inserted >10 times into retinal tissue (i). Retinal tissue residues are visible (white arrow) in the zoomed-in picture (ii). (iii) shows a top view of the probe with a light microscope picture before the insertion revealing that two pillars did not possess a PEDOT:PSS cap (marked with white dashed circles) (modified from [41]). B) KiRi probe after being implanted into mouse cortex for four weeks. The shanks were still standing in an nearly upright position after explantation (optical image in (i), and SEM zoom-in (ii)) and the electrodes did not express delamination (iii) (modified from [177]). C) Impedance measurements before and after 4/16 insertions using PiRi (i) and KiRi (ii) electrodes. The impedance at 1 kHz was extracted for each case (iii).

5.2.2. Bending stiffness and literature comparison

Once implanted within the tissue, the probe should exhibit optimal compliance to minimize the potential for FBR. For that the bending stiffness was analyzed. The effective bending stiffness is proportional to the Young's modulus of the material and the second moment of inertia of the probe, which in turn depends on the cross-sectional area. The bending stiffness is a common metric used to evaluate the mechanical properties of the tissue-electrode interface, specifically to assess the resilience of an implant against deflection induced by longitudinal forces and displacement. Accordingly, a reduction in bending stiffness facilitates compliant tissue integration by minimizing the mechanical mismatch between the probe and the tissue [104].

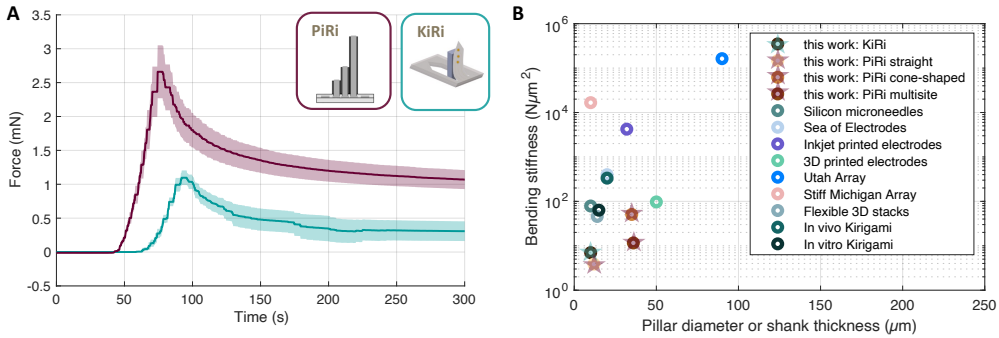

Figure 5.8.: Insertion forces (A) and bending stiffness (B) of KiRi and PiRi implants. A) The insertion force of a KiRi probe with 8 x 500 µm long shanks (N = 7) and a PiRi probe with 16 x 350 µm long shanks (N = 6) implants (mean ± SE). B) The bending stiffness of different pillar configuration of PiRis and KiRi shanks in comparison to selected state-of-the-art 3D stiff and flexible neural probes (Si microneedles [116], 'Sea of electrodes' [115], inkjet printed electrodes [114], 3D printed electrodes [117], Utah arrays [24], flexible [118] and stiff [25] Michigan-style arrays, and kirigami approaches used for *in vitro* [36] and *in vivo* [37] applications.

Figure 5.8B (and table B.3) illustrates the effective bending stiffness of the PiRi pillars (including straight, multisite, and cone-shaped pillars), as well as the KiRi shanks, in comparison to state-of-the-art 3D neural probes. The bending stiffness of straight PiRi pillars is with 3.9 Nµm^2 the smallest in comparison to the other PiRi designs with 50.7 Nµm^2 for the cone-shaped and 11.6 Nµm^2 for the multisite pillars, respectively. The bending stiffness of the KiRi shanks, is with 7.1 Nµm^2 smaller than cone-shaped and multisite PiRi pillars. The comparative analysis was conducted with state-of-the-art probes, including those of the Utah and Michigan arrays, as well as novel approaches utilizing 3D printing technology, flexible Michigan-style probes or other kirigami approaches using mostly PI or PaC as substrates. Although the Young's modulus of IP-L (4.7 GPa, according to the manufacturer), which is the material for the PiRi pillars, is relatively high compared to softer materials such as PaC (here 1.7 GPa), the small dimensions of the pillars led to an optimized cross-sectional footprint that reduces the effective bending stiffness of the probes. The multisite design, which enables recordings from three different depth locations within neural tissue, also maintains a low cross-section (250 µm^2). In the case of kirigami, the low Young's modulus of PaC and the small dimensions result in a lower bending stiffness in comparison to the state-of-the-art probes. Consequently, the combination of low bending stiffness and small dimensions distinguishes the KiRis and PiRis from those previously reported in the literature.
The only probe type that exhibits a smaller bending stiffness than the KiRis and PiRis are the neural threads, which are extremely thin SU-8-based implants and reach with 0.14 mNµm^2 a bending stiffness nearly comparable to that of an axon (0.00058 - 0.76 mNµm^2) [32]. However, each thread is only capable of accommodating a single recording or stimulation site. Consequently, recordings from different depths within the neural tissue can only be achieved through the implantation of multiple threads.

5.3. Long-term stability test

As outlined in section 2.2.4, the long-term stability is contingent upon mechanical, material, and biological failures. To analyze the stability prior to implantation, accelerated aging tests were employed to evaluate the electrochemical performance of the electrodes over time, as well as the mechanical properties of thin-film samples comprising a stack of PaC-metal-PaC to ascertain the adhesion, which has been identified as a significant failure mode for thin-film electrodes [112]. Moreover, the implants were subjected to examination post-use *in vitro* and post-implantation under *in vivo* conditions using SEM. To analyze the impact of insertion into neural tissue and the immune responses, histological experiments were conducted using retinal and cortical tissue after explantation of the neural implants, as detailed in sections 6.3 and 7.2.4, respectively.

5.3.1. Electrochemical stability in accelerated aging tests

The electrochemical stability of the electrodes was investigated through the implementation of a series of aging tests, the results of which are presented and discussed in the following sections. The primary objective was to conduct an aging test with the aim of optimizing the fabrication of the 2D MEA, which is crucial for the long-term functioning of the electrodes. Modifications to the established protocol, as outlined in section 4.1, were implemented with the objective of enhancing electrode stability. A review of the relevant literature revealed that the following techniques should be employed: oxygen plasma treatment [212][213], saline [212][214][215] and annealing [196][212]. Subsequently, the 2D MEAs were subjected to an accelerated aging test, with impedance analysis conducted at two- to three-day intervals over a period of 30 days, equivalent to 150 days according to the specified aging test factor (Equation 3.11). The results of this initial trial enabled the optimal fabrication techniques for the 2D MEA to be identified. A second test was conducted to analyze the PEDOT:PSS electrode coating in the accelerated aging process using KiRi electrodes.

Modifying the 2D MEA fabrication to enhance the long-term stability was tested with several approaches as illustrated in Figure 5.9. A design with a single shank which accommodated 16 electrodes was used (Figure A.1). The samples were fabricated with the assistance of Lina Koschinski (HNF and IBI-3, Forschungszentrum Jülich, and RWTH Aachen University) and Kelsey Varodom (DAAD internship) contributed to the measurement of the samples. In accordance with the established standard protocol, for Type A probes, a metallization step was conducted following the deposition of the PaC on the Si host wafer. For all samples, a Ti-Au-Ti metal layer stack was used, as Ti is known to improve the adhesion of the metal layer on the PaC surface [112][215][216][217]. Subsequently, the deposition of the PaC passivation layer and the etching of the electrode openings and contact pads were conducted. In order to improve the adhesion of the PaC layers, modifications were performed. The modification of Type B was conducted in accordance with the aforementioned process, with the exception that the samples were placed in an oxygen plasma oven (TePl Gigabatch 360 flow of O_2 plasma at 80 sccm, power of 50 W for 2 min) subsequent to the deposition of the initial layer of polymer. The third set of samples, designated Type C, underwent the same fabrication process as the preceding two types. However, before the deposition of the PaC passivation layer, $\approx$ 1 ml of the adhesion promoter silane A-174 (Specialty Coating Systems Inc., USA) was applied to the walls of the deposition chamber prior to the commencement of the CVD process. The fourth and final type of sample, designated D, was fabricated in accordance with the aforementioned process. However, at the conclusion of the fabrication process, the sample was subjected to an annealing treatment for 48 hours at 200 °C in nitrogen environment.

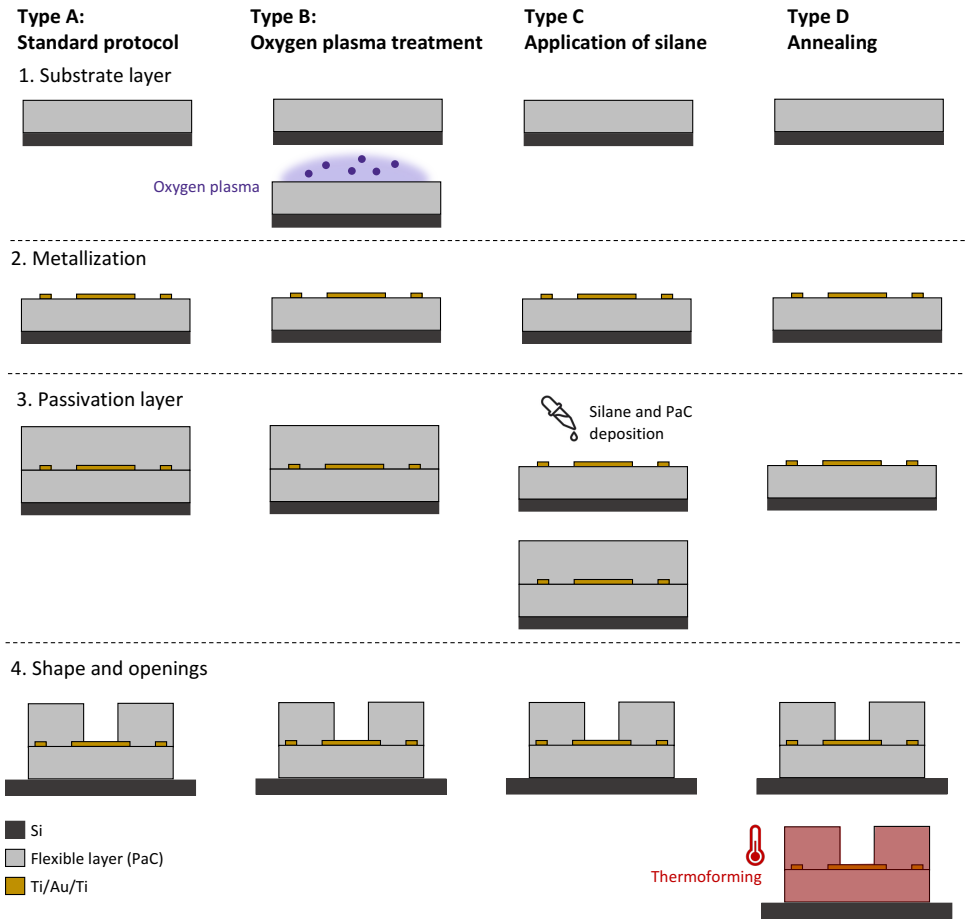

Figure 5.9.: Modifications to the 2D MEA fabrication to improve the long-term stability. A) Standard protocol, B) Oxygen plasma treatment before the metallization step, C) Use of silane during the deposition of the passivation layer, D) Annealing step after the fabrication.

Three samples were subjected to the accelerated aging test for a period of 30 days, with three samples per condition and 16 electrodes per sample. During the course of the test, the impedance of the electrodes was monitored, and an optical inspection was conducted using an optical microscope (Keyence VK-X100, Germany). The number of working electrodes was evaluated in accordance with their impedance value, with a threshold of 0.4 MΩ selected, representing approximately 10% of the overall mean impedance of 4.12 ± 1.2 MΩ prior to aging. Figure 5.10A illustrates the percentage of working electrodes versus time in the accelerated aging test for each condition. The number of working electrodes for the standard probes (untreated, type A), the probes treated with oxygen plasma (type B), and the probes treated with silane (type C) exhibited a significant decline during the initial stages of the aging process. On days 9 and 12, the number of working electrodes for types B and C, respectively, fell below 20%. In contrast, the annealed samples (type D) exhibited 100% functionality of the working electrode until day 12. Subsequently, the number of functional electrodes declined to approximately 75% until reaching 67% at the end of the experiment. Figure 5.10B presents the mean ± standard deviation of the impedance values for each probe type. With the exception of the annealed samples (type D, red trace), a general trend of

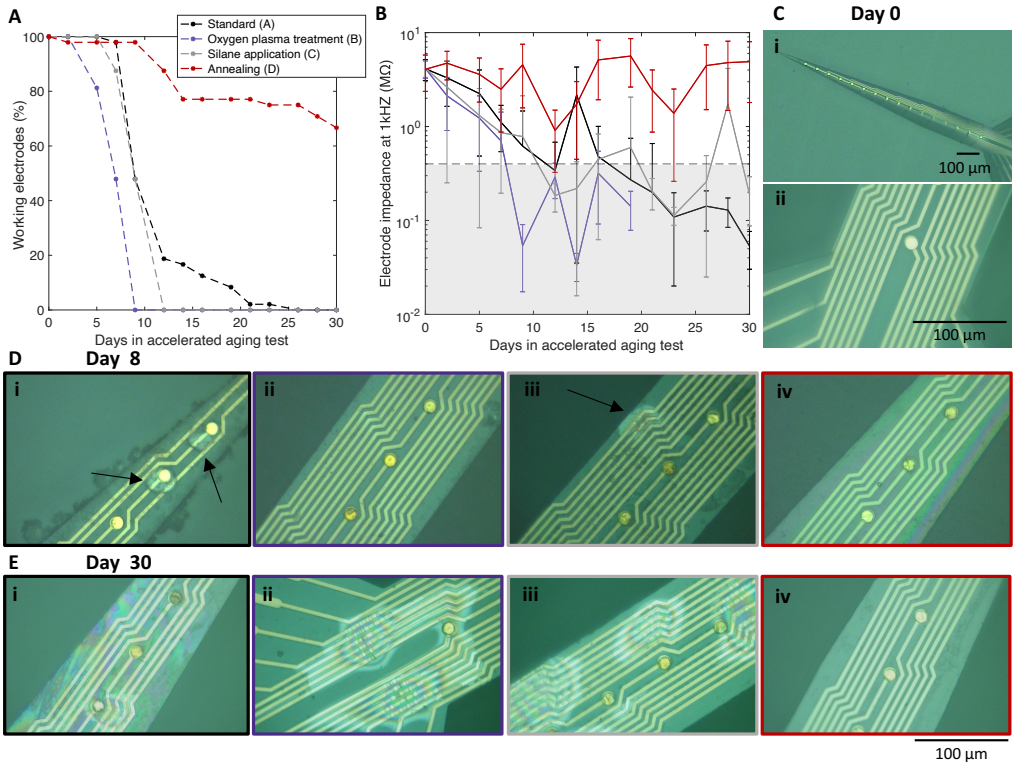

Figure 5.10.: Results of the first electrochemical aging test. A) Number of working electrodes per day for each group. B) Impedance of the electrodes throughout the duration of the aging test. C) Probes before the start of the aging test with no notable electrode degradation or layer delamination. Inspection of the probes at day 8 (D) and day 30 (E) of the aging test, type A (i), type B (ii), type C (iii), type D (iv) (N = 48 electrodes per condition).

reduced impedance values is observed. Prior to the commencement of the test, the probes were observed to be free of delamination, cracks, and corrugation (Figure 5.10C$_i$ and zoom-in C$_{ii}$). At day 8 (Figure 5.10D), an optical inspection revealed the presence of water between the PaC layers in sample types A (Figure 5.10D$_i$) and C (Figure 5.10D$_{iii}$). The ingress of water was observed to occur either at the electrodes (Figure 5.10D$_{ii}$) or at the edges of the sample (Figure 5.10D$_{iii}$). In samples of type B (Figure 5.10D$_{ii}$) and D (Figure 5.10D$_{iv}$), no evidence of water ingress or delamination of the PaC layers was noted. However, a change in color and modification of the surface of the electrodes was observed, which is indicative of degradation and delamination from the PaC substrate. This phenomenon was more pronounced in types A, B, and C in comparison to type D. After 30 days of aging (Figure 5.10E), sample types A, B, and C (Figure 5.10E$_{i,ii,iii}$) exhibited a significant amount of water between the PaC sheets, a clear indication of poor adhesion and delamination. In contrast, the annealed samples (types D) remained free of water. However, the surface of the electrodes in these samples also appears to have undergone alteration.
In conclusion, the annealed samples exhibited a distinct advantage over the other sample types. As previously reported, annealed samples exhibited superior performance compared to untreated samples during aging tests [196]. Nevertheless, electrode degradation was still evident and requires further optimization for enhanced long-term stability.

The long-term stability of the PEDOT:PSS coating was subsequently assessed. In this experiment, the KiRi samples were evaluated. It should be noted that the thermoforming step is, in fact, an annealing procedure, which resulted in the most promising outcomes in the initial test. A total of 38 working electrodes on three probes, with an initial impedance of 35.2 ± 13.7 kΩ, were subjected to an accelerated test. The impedance was measured for a total period of 17 days, with measurements taken every two to three days (Figure 5.11A). Furthermore, the implants were inspected using an optical microscope on the days of impedance measurements and SEM after 45 days. An electrode was identified as having failed when its impedance exceeded a value of 1 MΩ, which is equivalent to the impedance of a plain Au electrode [205]. The impedance measurements indicated that approximately 20% of the electrodes exhibited an impedance greater than 1 MΩ after just two days, which is indicative of degradation of the PEDOT:PSS layer. Subsequently, the number of functional electrodes declined, reaching 34% at day 17 of the accelerated aging test. The degradation of PEDOT:PSS was additionally noted during the optical inspection. Figure 5.11B illustrates the electrode's progression over the course of the aging test. The color change is an indication of surface alterations. Furthermore, it is evident that the electrode is delaminating, with the process commencing slowly from day two and becoming increasingly pronounced by day 45 of the aging test. At day 45, however, there was no evidence of water between the PaC layers or corrugation at the feedlines, indicating an intact passivation (5.11C$_i$ and C$_{ii}$). An additional inspection was conducted using SEM. Figure 5.11D shows electrodes without (Figure 5.11D$_i$) and with PEDOT:PSS (Figure 5.11D$_{ii}$) coating, which both showed a comparable amount of delaminating. However, most of the KiRi shanks were still standing (Figure 5.11D$_{iii}$ and D$_{iv}$) in an upright position.

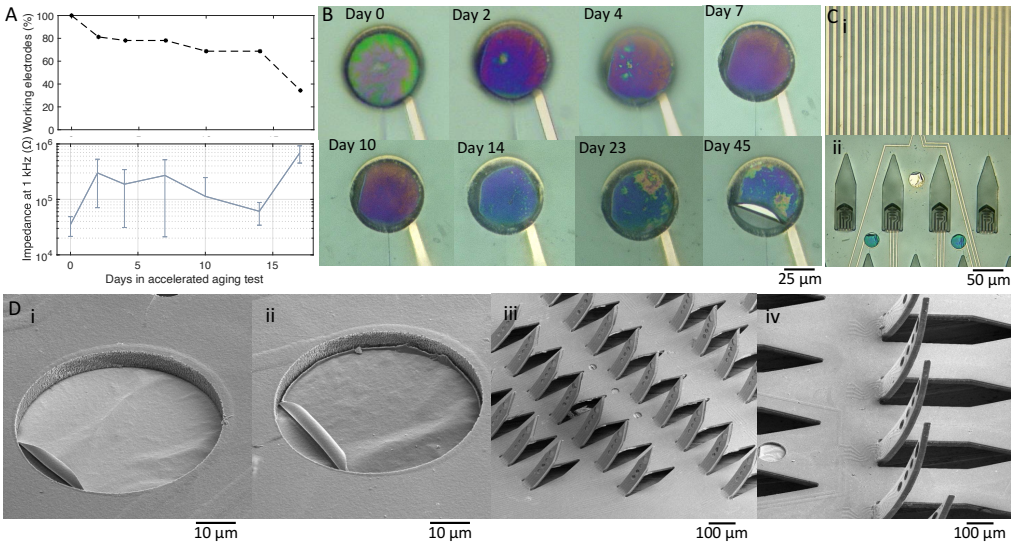

Figure 5.11.: Results of the accelerated aging test using PEDOT:PSS coated KiRi electrodes. A) Number of working electrodes (black) and impedance of working electrodes (blue) during the course of the aging test. B) Optical inspection of one electrode during the course of the aging test, which exhibits surface alterations (color change) and delamination at day 45. C) There was no sign of corrugation of the feedlines or water between the PaC layers indicating an intact passivation layer (i). The KiRi shanks were still standing (ii). D) SEM inspection at day 45 of the aging test, showing the delamination of a plain Au electrode (i) and an electrode coated with PEDOT:PSS (ii). The frontal (iii) and side view (iv) of the probe demonstrates that the shanks were still standing in an upright position (modified from [177]).

5.3.2. Mechanical stability in accelerated aging tests

During the annealing process, polymers undergo a transformation when subjected to elevated temperatures, resulting in the rearrangement of their molecular chains into more crystalline structures. This increased polymer chain mobility will also permit intertwining of the chains in adjacent layers, which may enhance adhesion in theory [218]. However, this process also affects the mechanical properties of the material. When the implant is situated within the body, particularly cables or elongated structures such as shanks are susceptible to micromotion and other irregular movements of the body, which can result in mechanical stress. Consequently, neural probe cables with varying numbers of electrode feedlines and subjected to varying annealing procedures will undergo an accelerated aging process to assess the longevity of the probes and to evaluate the impact of annealing on the adhesion of the probes. Tensile tests were conducted at specified intervals throughout the test period to evaluate the evolution of the mechanical properties of the neural probes in response to chronic implantation. The monitoring of the Young's modulus, stress, and strain at break provided insight into the ability of the flexible probes to maintain their flexibility and sustain consistent force and stretch throughout the course of testing. Moreover, microscope images (Keyence VK-X100, Germany) obtained at regular intervals throughout the test allowed for the visual detection of mechanical failures, including delamination and feedline erosion. The measurements were performed with the assistance of DAAD-internship student Kahlan Parker.

The samples were fabricated in accordance with the process depicted in Figure 5.9D, which included an annealing step at the final stage of the fabrication process. Thereby 10 µm thick, 1.5 mm wide and 25 mm long PaC stripes were produced comprising either 0, 32 or 128 feedlines (5 µm lines and spaces). The samples were subjected to either 160 ℃ or 200 ℃ annealing and then compared with an untreated control group. For the aging tests, eight samples were stored in airtight containers for each day of testing due to the destructive nature of the tensile test. The test was conducted at the outset of the trial and then repeated after two, four, six, eight weeks, and one year under accelerated aging conditions.

The tensile testing as detailed in section 3.3.2, facilitated the monitoring of the stress at fracture, strain at fracture, and Young's modulus throughout the aging test. The results of the aging test, which evaluated the mechanical properties and visual inspection of 10 µm thick PaC stripes with 32, 128, and without feedlines over time, are presented in Figure 5.12. The data set includes the Young's modulus, strain, and stress at break for unannealed, annealed at 160 ℃, and annealed at 200 ℃ samples, as measured at the specified time points during the aging test: 2, 4, 6, 8 weeks, and 1 year. The stability of the mechanical properties over time was verified by comparing the data against the control group, which was not subjected to aging, to ascertain whether any statistically significant differences existed. The stars in Figure 5.12A indicate instances where the statistical analysis yielded a p-value of less than 0.05 identified through the use of ANOVA and post-hoc pairwise t-tests with Bonferroni correction. Although some measurement points indicate a statistically significant change, such as strain at fracture in the annealed at 160 ℃ samples at weeks 2, 4, and 8, the trends were not sustained when inspected after one year. Therefore, over the course of one year, a discernible trend could not be identified in either of the sample groups (unannealed or annealed at 160 ℃ or 200 ℃) for either of the evaluated properties. Furthermore, it is evident that there is no significant difference between the feedline groups, suggesting that the feedlines do not significantly influence the mechanical properties. Upon optical examination of the samples (Figure 5.12B and Figure B.1), a discernible distinction was evident between the annealed and unannealed specimens. The samples that were not annealed (Figure 5.12B$_i$ and Figure 5.12B$_{ii}$, zoom-in) exhibited water ingress between the PaC sheets and feedline corrosion. The corrosion was observed to accumulate over the course of the aging test, becoming clearly

visible after two weeks. In contrast, the effects were only occasionally visible in the samples that were annealed at 160 °C (Figure 5.12B$_{iii,iv}$) and were not observed in the samples that were annealed at 200 °C (Figure 5.12B$_{v,vi}$). This demonstrates that the annealing process enhances the long-term stability of the layered structure while maintaining the mechanical properties to a considerable extent. This finding aligns with the observations reported in previous studies [196].

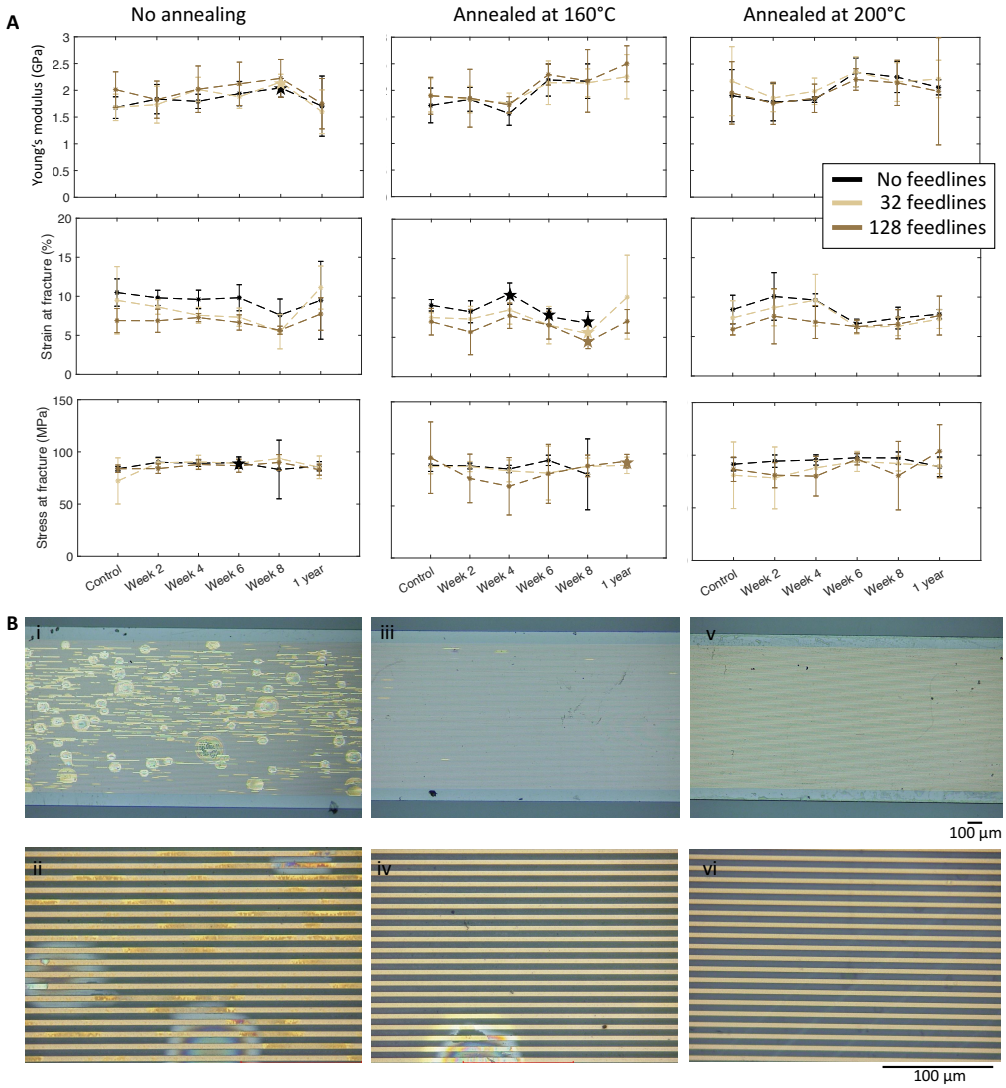

Figure 5.12.: Aging test results of the mechanical properties (A) and visual inspection (B) of 10 µm thick PaC stripes with 32, 128 and no feedlines after 1 year. A) The Young's modulus, strain and stress at break for unannealed, annealed at 160 °C and 200 °C samples are displayed for each measuring point during the aging test (control, after 2, 4, 6, 8, weeks and after 1 year). The values are displayed with mean ± standard deviation for N = 7 or 8 samples. Stars show when the statistical analysis using ANOVA and post-hoc pairwise t-tests with Bonferroni correction revealed a p-value < 0.05. B) The optical inspection of the samples after 1 year. Samples, which were not annealed (i and zoom-in ii) show water ingress between the PaC sheats and feedline corrosion. The effects were only occasionally visible in samples annealed at 160 °C (iii and iv), and were not observed in samples annealed at 200 °C (v and vi).

5.4. Summary and outlook

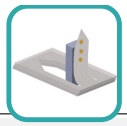

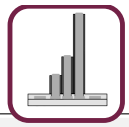

	KiRi	PiRi	Literature
Electrochemical performance	For electrodes with ø = 25 µm		
Impedance at 1 kHz	28.9 ± 9.9 kΩ (58.9 Ω/µm²)	30.3 ± 12.6 kΩ (~273 Ω/µm²)	127[a] - 336[b] Ω/µm²
CSC (mC/cm²)	6.9 ± 3.8	9.1 ± 1.5	2[c] – 9.6[d]
CIC (mC/cm²) anodic first pulse with T_{ph} = 500 ms	2.0 ± 0.9	2.5 ± 1.1	1.9[c] – 2.9[e]
Mechanical performance			
Insertion behavior	+ + +	+ +	
Bending stiffness	+ +	+ + +	Table A.3
Long-term stability			
Electrochemical stability	15 days	N/A	~ 30 days[f]
Mechanical stability	+ + +	N/A	

Figure 5.13.: Comparison of the electrochemical, mechanical and long-term performance of KiRi and PiRi neural implants and data from the literature a) [205] b) [208] c) [209] d) [208] e) [219] f) [220]).

The preceding sections presented an evaluation of the electrochemical and mechanical performance of the KiRi and PiRi neural implants.
The impedance of the large KiRi electrodes with an Ø= 25 µm is comparable to that of PiRi electrodes, with no statistically significant difference observed (28.9 ± 9.9 kΩ and 30.3 ± 12.6 kΩ, respectively). However, the standard deviation for the PiRi electrodes remains higher due to the indistinct nature of their surface area, which is a result of the sequential printing process and the individual electrodeposition of each pillar. Nevertheless, the low impedance levels indicate that high-quality signal recordings can be achieved [93].
The stimulation capabilities were assessed and compared by utilizing voltage transient measurements and CV to quantify the two major contributing factors to *in vivo* electrical stimulation performance, namely, CIC and CSC [209]. The PiRi electrodes exhibited slightly larger (approximately x1.3) CSC as well as CIC values in comparison to the KiRi electrodes. An increased electrode diameter allows for a greater current injection within the potential limits. Furthermore, CV responses for CSC measurements demonstrate larger current responses and larger hysteresis loop areas due to the increased electrode surface area [209]. This may have contributed to the elevated values observed in PiRi electrodes relative to those in KiRi electrodes. Another potential explanation is the discrepancy in the deposition methodology employed for the PEDOT:PSS layer, with chronoamperometry utilized for KiRi electrodes and CV for PiRi electrodes. Nevertheless, their comparable performance falls within a comparable range to values documented in the literature for PEDOT:PSS-coated microelectrodes [208][209][219]. It would be beneficial to investigate the impact of charge injection on the electrode surface over extended time periods through long-term pulse testing. Alternatively, IrOx could be considered as an electrode coating material. Despite the lower CIC of 15 mC/cm^2 in comparison to PEDOT:PSS, IrOx is widely employed in stimulating prosthetic devices due to its good biocompatibility and high resistance to corrosion [173][221].
It can be concluded that the KiRi and PiRi electrodes are suitable for the electrical stimulation of neural tissue. In the event that higher stimulating pulses are required for specific applications, "pulse engineering" may be employed. This refers to the application of asymmetric current pulses with the objective of optimizing the current limits [209]. It is essential to maintain charge balance when employing asymmetric pulses to prevent irreversible chemical reactions [80]. It is also noteworthy that while the outer layer of the material is typically engaged in charge transfer during stimulation, there is a tendency for CSC to overestimate the available charge [92].
In regard to the mechanical performance, the insertion behavior and bending stiffness - which

serves as an indicator for the probe's compliance in a chronic condition - were evaluated. It was found that longer PiRi probes could be inserted with a force of 0.5 mN, whereas KiRi shanks would buckle due to tissue dimpling when attempting to penetrate neural tissue at this force. Calculations indicate that cone-shaped pillars up to 1150 µm in length are feasible, whereas KiRi shanks would buckle when the length exceeds 530 µm. However, the results of the insertion tests conducted in agarose demonstrated that KiRi probes exhibited reduced dimpling and a higher probability of successful insertion in comparison to PiRi. Moreover, larger forces were recorded when using PiRi electrodes, despite their cross-sectional footprint being comparable (530 μm^2 for cone-shaped PiRi electrodes and 500 μm^2 for KiRi shanks). This discrepancy may be attributed to the shank configuration and the quantity of shanks or pillars, as well as their geometric characteristics. The KiRi shanks are equipped with a sharp tip of submicron width, which allows them to effectively pierce through neural tissue. In contrast, the PiRi electrodes feature a rounded electrode cap. Once within the neural tissue, the bending stiffness serves as an indicator of the probes' compliance. The lowest bending stiffness is observed in straight PiRi pillars, followed by KiRi shanks, multisite pillars, and cone-shaped pillars, which exhibit the highest bending stiffness. However, all designs exhibit lower values in comparison to state-of-the-art probes reported in the literature (see Figure 5.8).
Long-term stability tests were conducted using 2D MEA with Au electrodes and PaC-metal-PaC stripes to evaluate optimal 2D fabrication methods. In both cases, the annealed samples yielded the most favorable outcomes, exhibiting reduced delamination and water intrusion between the PaC sheets in comparison to the unannealed samples or samples treated with alternative methods, such as oxygen plasma or silane. Consequently, a reduction in feedline corrosion was observed, and the impedance of the electrodes in the electrochemical evaluation remained more constant over time, evaluated up to 30 days in accelerated aging, in comparison to the control and other methods employed. No discernible trend in mechanical property change was identified, neither in the annealed samples nor in the control group, even after a year of accelerated aging. At the one-year mark of the accelerated aging test, a thorough optical examination revealed a considerable degree of delamination, accompanied by subsequent water intrusion, corrosion, and feedline deterioration, in the unannealed (control) samples. In contrast, the samples that underwent annealing at 160 °C exhibited only minimal damage, while those that underwent annealing at 200 °C demonstrated a near absence of damage. This is a significant outcome when considering the use of these stripes as cable connections between electrodes and processing units in chronic recordings.
In the following step, KiRi samples comprising Au electrodes coated with PEDOT:PSS were subjected to an accelerated aging test. The shanks remained in an upright position for 45 days, as evidenced by the SEM inspection (see Figure 5.11), demonstrating the stability of the folding technique over time. Additionally, no water intrusion or delamination of PaC-PaC layer was observed. During thermoforming, the samples are subjected to a temperature of 160 °C, which is equal to the annealing process applied in the precedent test of the PaC-metal-PaC stripes. However, an evaluation of the electrochemical stability of the electrodes revealed, that the adhesion between the metal and PaC layer is insufficient. Shortly after 2 weeks, less than 50% of the electrodes were functioning during impedance testing. Optical inspection revealed delamination of the electrode metal layer (Au + PEDOT:PSS) as well as degradation of the PEDOT:PSS layer. A similar rapid decrease in functionality of Au electrodes coated with PEDOT:PSS has been observed in the literature during accelerated aging tests. Delamination of the metal layer from the PaC was also observed and attributed to the difference in Young's modulus of Au and PaC. In addition, they measured dissolved Au and PEDOT:PSS in the electrolyte, demonstrating corrosion [220].

In summary, the annealing process showed a significant improvement in PaC-PaC adhesion over time compared to the control group. However, there is still room for improvement in the adhesion of the metal to the PaC and the quality of the electrode coating. An additional Au elec-

trodeposition could be employed before the electrodeposition of PEDOT:PSS with the intention to improve the stability of the electrode material. Alternatively, IrOx as electrode coating shows good biocompatibility and corrosion resistance [222] and has been widely used in retinal implants due to its suitable CSC and CIC for efficient electrical stimulation [129][223]. In addition, IrOx could be combined with PEDOT:PSS coatings, which has been reported to survive over 110 days under accelerated aging conditions at 60 °C [224]. As an alternative, metal-free electrodes using spin-coated PEDOT:PSS could be used. It has been reported that spin-coated PEDOT:PSS improves stability by a factor of five compared to Au electrodes [220]. Using spin-coated PEDOT:PSS a transparent and metal-free implant can be fabricated that can be used in conjunction with imaging techniques for the examination of the brain. These include two-photon imaging, functional magnetic resonance imaging (fMRI), and positron-emission tomography (PET).

In addition to alternative electrode materials and coatings, PI should be further investigated as an alternative substrate material. While the long-term stability of PI is often reported in the literature, other studies suggest that it performs worse than PaC: In an accelerated aging test with 75 °C testing encapsulation material, PI was reported to last only 66 days in comparison to PaC with 117 days [225]. In addition, PI has no ISO certification [112]. Other alternatives could be a PDMS-based implant, which in addition has a lower Young's modulus and thereby offers a higher compliance [94].

It would be beneficial to evaluate the extent to which the results can be transferred to PiRi electrodes, where the same 2D fabrication process and similar materials were employed, in future studies. The adhesion of the 2PP pillars to the PaC layer may present an additional challenge and should be investigated in a long-term assessment.

An in-depth examination of long-term stability should consider not only elevated temperature as a potential accelerator of the aging process, but also the anticipated interactions with other possible accelerators, such as H_2O_2 and pH [92]. This should be taken into account in any forthcoming evaluations. However, should the objective of the analysis be to predict failure mechanisms, or time to failure, it is of the utmost importance to exercise caution when interpreting the results of such experiments. This is due to the functional connections between microelectrodes and neurons which are contingent upon intricate tissue integration, rendering it challenging to anticipate the combined impact of material aging and FBR *in vivo*. The composition and dynamics involved are complex, making it difficult to accurately predict the outcome [92].

However, the electrochemical and mechanical properties outlined in the aforementioned sections suggest that the PiRi and KiRi probes are effective devices for electrophysiological recordings from within neural tissue. Consequently, to substantiate these findings, the subsequent sections will present the tested applications.

6. Retinal applications

Considering the development of flexible 3D MEAs for retinal prostheses, the proof of concept started with the evaluation of the feasibility of recording electrophysiological activity in explanted retinas. First, the insertion of the 3D probes and recordings from different depths in the retina were tested and the insertion footprint was analyzed. To further confirm the physiological origin and behavior of the electrical activity recorded by the probes, light stimulation of the retina was performed. Furthermore, intraretinal recordings were performed in RCS retinas to test the possibility of using the 3D electrodes in degenerated retinas. Pharmacological treatment was performed to further analyze the physiological activity of a degenerated retina in the rat model. With the aim of an *in vivo* application, the surgical methods were established in a cadaveric setting. In addition, the electrical properties of the retina were further characterized using 2D MEAs. During these experiments, resistivity values were extracted and compared with resistivity measurements during the cadaveric surgeries to confirm successful implantation. Two types of cadaveric surgery were then tested: An open-sky procedure for an acute setting and a *pars-plana* implantation for a semi-chronic application.

This chapter is partly reproduced from the following publications:

- **M. Jung**, A. Willuweit, V. Rincón Montes. "Intraretinal Electrophysiology and Resistivity Profiles of WT and RCS Rat Retina". Sensors 2025, DOI: 10.3390/s25123765
- **M. Jung**, M. Kasavetov, N. Nruthyathi, J. Abu Shihada, S. Decke, L. Koschinski, F. Balcewicz, T. Lohmann, P. Walter, F. Müller, A. Offenhäusser, V. Rincón Montes. “Towards the in vivo validation of 3D retinal implants: an in vitro and cadaveric validation” (in preparation)
- J. Abu Shihada* and **M. Jung***, S. Decke, L. Koschinski, S. Musall, V. Rincón Montes, A. Offenhäusser. "Highly Customizable 3D Microelectrode Arrays for In Vitro and In Vivo Neuronal Tissue Recordings". Advanced Science 2024, DOI: 10.1002/advs.202305944 (**Equal contribution*)
- N. Nruthyathi, **M. Jung**, J. Wang, V. Rincón Montes, A. Offenhäusser, A. Willuweit, M. Müller. "Late emergence of pathological oscillatory activity in the retina of the Retinitis pigmentosa model RCS (Royal College of Surgeons) rat". PLoS One 2025, DOI: 10.1371/journal.pone.0324345

Experiments were conducted using the retina of mice and rats for *in vitro* trials and rats as well as rabbits for cadaveric trials, simulating the acute and semi-chronic implantation procedure. The dimensions of the eye and retina are summarized in table 6.1. Consequently, both types of 3D implants, KiRis and PiRis, were adapted to the application and design criteria for the retina, which is approximately 200 µm thick in all animal models (see table 6.1). Thus, for the KiRiRet design, a length of 225 µm was chosen to span the full thickness of the retina. Similarly, for the multisite PiRis, the height of the electrodes was adjusted to 80, 100, and 120 µm, and to 65 µm for single pillars. The aim was to have access to the ganglion cell layer for electrophysiological recordings by epiretinal placement of the electrodes. Taking the possibility of tissue dimpling and an uneven retinal surface into account, the dimensions of the 3D MEAs were chosen according to the thickness of the retinal layers.

Rats and mice are often the model of choice for medical device validation because they offer a number of advantages over other species. They reproduce rapidly, and their small size and

	Mice	Rats	Rabbits	Human
Ocular axial length (mm)	3.3[a]	5.6 - 6.3[a]	13.8 - 17.1[a]	newborn: 16-18, adult: 22-25[b]
Retinal thickness at the center (µm)	186.9[a]	192.7 - 220[a]	194.3[a]	at fovea rim: 320[c]

Table 6.1.: Ocular length and retinal thickness across different species. Data from a) [226], b) [227], c) [228]

adaptability make them easy to care for and to work with. Both species have been used in research for the last century, and several strains are now well characterized genetically and physiologically. Some strains develop diseases spontaneously, such as the retinal degeneration 10 (rd10) mouse model or RCS rat model of retinitis pigmentosa. In mice, genetic manipulation makes it possible to create mutant or transgenic strains, which in many cases are designed to closely imitate human diseases and pathologies. However, there are some cellular differences that result from species-specific adaptations to the environment and behavioral factors. For example, rodents are nocturnal and, therefore, their retina is rod-dominated [229]. The main differences between the rodent and human retina that should be considered when using rodents as models for retinal degeneration are the following:

- Retinal size: A clear distinction between the retinas of different species is the retinal size. The human retina is about 40 mm in diameter while that of a mouse is only about 5 mm [230].
- Color vision: Humans possess three types of cones, S-, M-, and L- cones, while rodents, like most mammals, possess two types of cones, S-cones (short wavelength detection cones, blue cones) and L/M-cones (medium wavelength detection cones, red-green cones) [229].
- Photoreceptor density gradients: In the human retina, photoreceptor density varies significantly across the retina. Cones dominate the central retina and rods dominate the peripheral retina. In rodents, on the other hand, rods and cones are evenly dispersed, with only slight gradients in density and no specialization in the fovea [230][231].
- Ganglion cells: Approximately 1 million ganglion cells in a human retina are concentrated in central retina, forming up to eight layers, decreasing to one layer in the periphery. Thus, ganglion cell density varies by a factor of 100 between the central and peripheral retina in humans. In contrast, ganglion cells are organized in a single layer throughout the rodent retina, and their density varies only by a factor of 4 [230].

However, the structure of the retinal layers, with the somas of the principal cell types (rods, cones, horizontal cells, bipolar cells, amacrine cells, Müller cells, and ganglion cells) arranged in three nuclear layers separated by two synaptic layers, is shared between humans and rodents. It is interesting to note that despite the gradient of photoreceptor density in humans, the central retina of the mouse actually exceeds that of the human macula with respect to the high density of photoreceptors. The rod/cone ratio is similar in humans and mice between 10° and 20°, which represents the more peripheral part of the macula in the human retina. Thus, a large central area of the mouse retina has some of the structural features that are thought to cause the macula to be more vulnerable to degeneration in the human retina [230]. However, despite the large number of (genetically engineered) models that have been developed, no model has yet reproduced all the features of human AMD [232].

6.1. Investigation on the electrophysiology and resistivity of healthy and RCS rat retina using 2D MEAs

Retinal prostheses have made the transition from the laboratory to the clinic and have restored partial vision to blind people affected by retinal degeneration. Despite this progress, the implants

had difficulty meeting patient expectations and CE-marked devices have been withdrawn from the market [131]. Consequently, ongoing research endeavors are directed towards enhancing the quality of visual perception. A fundamental element under investigation is modeling and simulating of retinal neural activation through electrical stimulation to comprehend spatial patterns [233][234][235][236]. Here, the electrical resistivity profile of the retina which changes throughout its layered structure determines the intraretinal current flow and potential distribution during electrical stimulation. The retinal resistivity profile is thus a critical factor in retinal prostheses design. A survey of the extant literature reveals that previous measurements of retinal resistivity were mostly limited to healthy retinas. This includes studies of the retinal resistivity profile of birds [237], frogs [238], chickens [239], rats [239], and mice [240]. Despite the existence of publications concerning the resistivity profile of diseased retina of mice, no study has yet been conducted on a diseased rat model.
Due to the above mentioned advantages and the superior size of the rat eye compared to that of a mouse, rats were chosen as the main animal model for retinal *in vivo* applications. To further characterize the electrical properties of the diseased rat retina, 2D MEAs were used to measure impedance at different retinal depths. The 2D MEA probes are illustrated in Figure A.2. The individual shanks containing four electrodes each had a length of 225 µm. The resistivity profiles of the retinal layers were then calculated from the impedance values. In parallel, electrophysiological recordings were performed at each z-step to correlate the spontaneous spiking activity and noise level with the resistivity values to provide further insight into the optimal position within the retina for electrical stimulation. Experiments were performed with RCS rats as a model for retinal degeneration (RD) and compared with measurements in WT animals.

6.1.1. From impedance measurements to resistivity values

The 2D MEA electrodes were analyzed in PBS by EIS as described in section 3.3.1 prior to the impedance measurements in Ames' medium and within the retina. The *in vitro* setup as described in section 3.4.1 was used as illustrated in Figure 6.1A. The retina was placed inside the perfusion chamber onto a PDMS pillow fixated with insect pins to allow the Ames' medium to reach the tissue from all sides. The penetrating electrodes were then inserted from the epiretinal site taking defined z-steps of 20 µm. The impedance was measured using a portable potentiostat (PalmSens4, PalmSens BV, NL). As previously reported in the literature [240][242], the electrode-tissue interface can be modeled with a modified Randles model. This model incorporates a double-layer capacitance, CE, which is represented by a CPE, a charge transfer resistance, R_E, a tissue/electrolyte resistance, R_Z, and a parallel parasitic capacitance C_P (Figure 6.1B). The values of the z-fit of the electrodes measured in electrolyte are given in Figure 6.1B. However, R_Z represents the sum of the resistance of the tissue and the electrode, and therefore undergoes changes at each z-depth due to the resistivity profile of the retina, when the electrode penetrates the tissue.
The PRF method was used to calculate the resistivity values from the impedance measurements. The method was described by Mercanzini et al. [243] and further analyzed by Weiland et al. highlighting the advantage of fast computation while estimating the resistivity with reasonable precision [242]. The methodology enables the identification of the frequency at which the impedance of the interface is most resistive, that is, where the phase φ_{PRF} is closest to zero degrees. Subsequently, the magnitude of the impedance at this phase $|Z_{PRF}|$ is registered. Figure 6.1C provides a schematic illustration of the PRF method. In order to convert the impedance measurements to resistivity values, the impedance was initially measured with the electrode immersed in the electrolyte, as well as the conductivity κ of the electrolyte, which was found to be 1.546 S/m for Ames' medium. The electrolyte resistance (R_E) was then extracted using the PRF method. The resistances were subsequently converted to resistivity in accordance with the cell constant c of

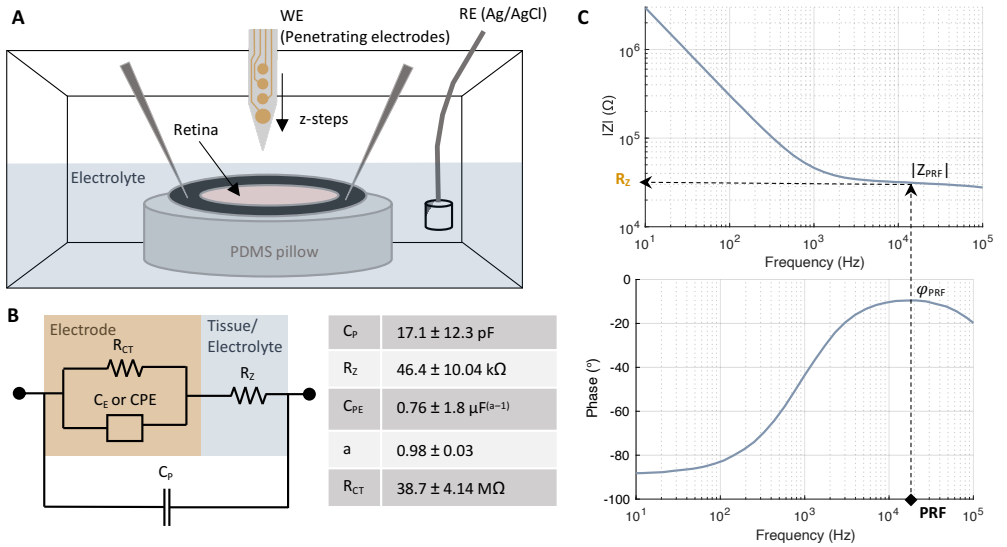

Figure 6.1.: Setup for the impedance and resistivity measurement of retinal tissue. A) The retina is placed into a perfusion chamber and fixated onto a PDMS pillow using insect pins and filter paper. The electrodes penetrate the retina from the epiretinal site. The impedance is measured using an Ag/AgCl reference electrode. B) The electrode-tissue interface model, employed for the purpose of characterizing the electrode and measuring tissue resistance is a modified Randles model. The model comprises a double layer capacitance C_E represented by a CPE, a charge transfer resistance R_E, a parallel parasitic capacitance C_P, and an resistance R_Z which is the sum of the tissue's and electrolyte's resistance. The values from the z-fit are displayed in the table and were in Ames' medium using N = 7 electrodes with a diameter of 25 µm. The goodness of fit (X^2/|Z|) was 7.62 ± 5.0. C) From the impedance measurements, the resistivity values are calculated using the PRF method which extracts the resistance $|Z_{PRF}|$ where the tissue is most resistive (φ_{PRF} closest to zero) (modified from [241]).

the electrode by

$$c = \kappa \cdot R_0. \tag{6.1}$$

Subsequently, the electrodes were inserted into the retinal tissue at a step size of 20 µm, with impedance measurements taken at each z-step. The resistance R_{Zi} was once more determined through the PRF method at each position Z_i. Given that the resistance of the tissue (R_T) is connected in series with the resistance of the electrolyte (R_E), the resistivity at the z-depths can be calculated by subtracting R_E and dividing by the cell constant

$$\rho_i = (R_{Zi} - R_E)/c. \tag{6.2}$$

6.1.2. Correlation of the resistivity profiles and electrophysiological activity

Electrophysiological and impedance measurements were taken at each z-depth within the retina. Figure 6.2A shows an example of electrophysiological measurements taken with one electrode at different intraretinal depths for WT and RCS retina. Initially, the probe is positioned in close proximity to the retinal surface via the use of a micromanipulator. At this stage (Z0), no evidence of spiking activity was observed. To circumvent the issue of tissue dimpling, a preliminary insertion of 100 µm is undertaken to penetrate the retina and gain access to position Z1, where small spikes are picked up with the electrode. This indicates that they are situated in close proximity to the ganglion cell layer. As the probe traverses the retinal tissue, the amplitude of the spikes increases with decreasing distance to the spiking ganglion cells. At a certain depth, the amplitude of the spikes again decreases (Z3 in 6.2A$_i$ and Z4 in 6.2A$_{ii}$), indicating that the probe has traveled past

the ganglion cell layer and is approaching the photoreceptor side.
Concurrently, impedance measurements were conducted at each z-location. An illustrative example from measurements in a WT retina can be found in Figure 6.2B. While the electrode remains within the electrolyte (in this case, Ames' medium), there is minimal change in impedance when the electrode position is altered. However, upon reaching position Z1, a notable change in the impedance measurement is typically observed. In comparison to the measurement conducted in the electrolyte, the magnitude of the impedance, $|Z_1|$, is consistently higher across the majority of frequencies. Meanwhile, the phase trace of the impedance exhibits a slight deviation. As the intraretinal depth increases, this pattern persists. Nevertheless, at a specific depth, designated as Z4 in Figure 6.2, the magnitude of the impedance begins to decline.

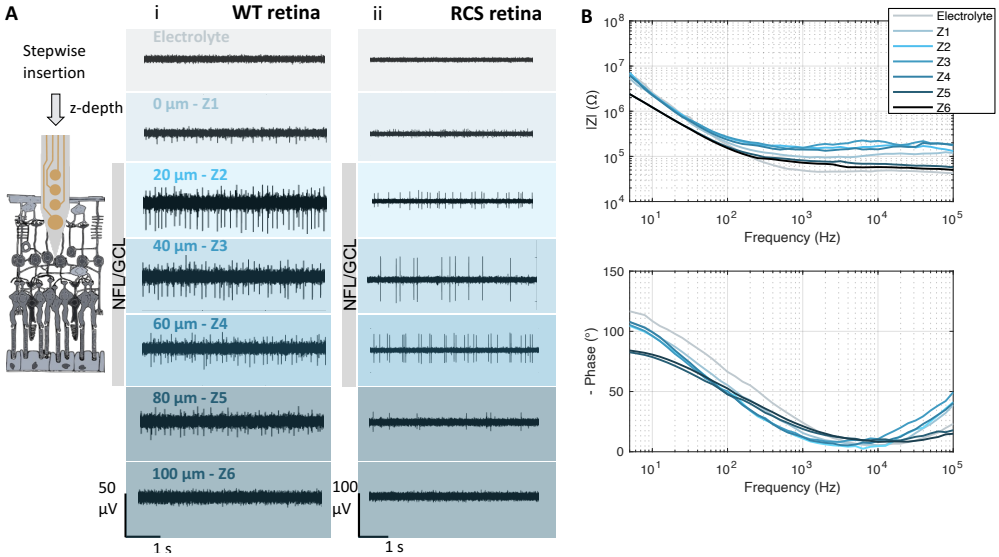

Figure 6.2.: Electrophysiological recordings and impedance measurements at different intraretinal depths. A) Electrophysiological recordings of WT (i) and RCS (ii) rat retina at different intraretinal positions Z_i. A step size of 20 µm was used and the data was bandpass filtered between 100 and 3000 Hz. B) Example of impedance measurements measured in a WT retina at different z-positions Z_i and in the electrolyte (modified from [241]).

As described in the previous section, from the impedance measurements the resistivity profiles were created for WT and RCS rats (Figure 6.3B). The resistivity profiles were aligned by their peaks and the average and standard deviation calculated. The alteration in resistivity values when penetrating the retina marks the probe's entry, with a threshold defined as 10 % from the initial baseline [240]. By this threshold the boundaries of the retina were defined. The RGC side is situated on the left of the graph and has been aligned for both groups. In contrast, the photoreceptor side is located towards the right side of the graph and differs between WT and RCS rats. From these boundaries, the thickness of the retina can be calculated, resulting in a value of 240 µm for WT and 120 µm for RCS rats, which is consistent with values found in the literature [244]. At the RGC side, the resistivity is 0.32 ± 0.27 Ωm for RCS and 0.59 ± 0.48 Ωm for WT. The resistivity profile shows an increase in resistivity until a peak of 1.76 ± 0.49 Ωm is reached for RCS (N = 12) and 2.89 ± 0.88 Ωm for WT retina (N = 12), respectively. From there, the resistivity profile decreases at the photoreceptor side.

From the electrophysiological data, patterns were identified that can be attributed to the resistivity profile (Figure 6.3C,D,E). The spiking activity increased upon reaching the ganglion cell layer and remained at a relatively constant level (Figure 6.3C). The increase is not homogeneous with high standard deviations, as this depends on the specific location and distance to the ganglion

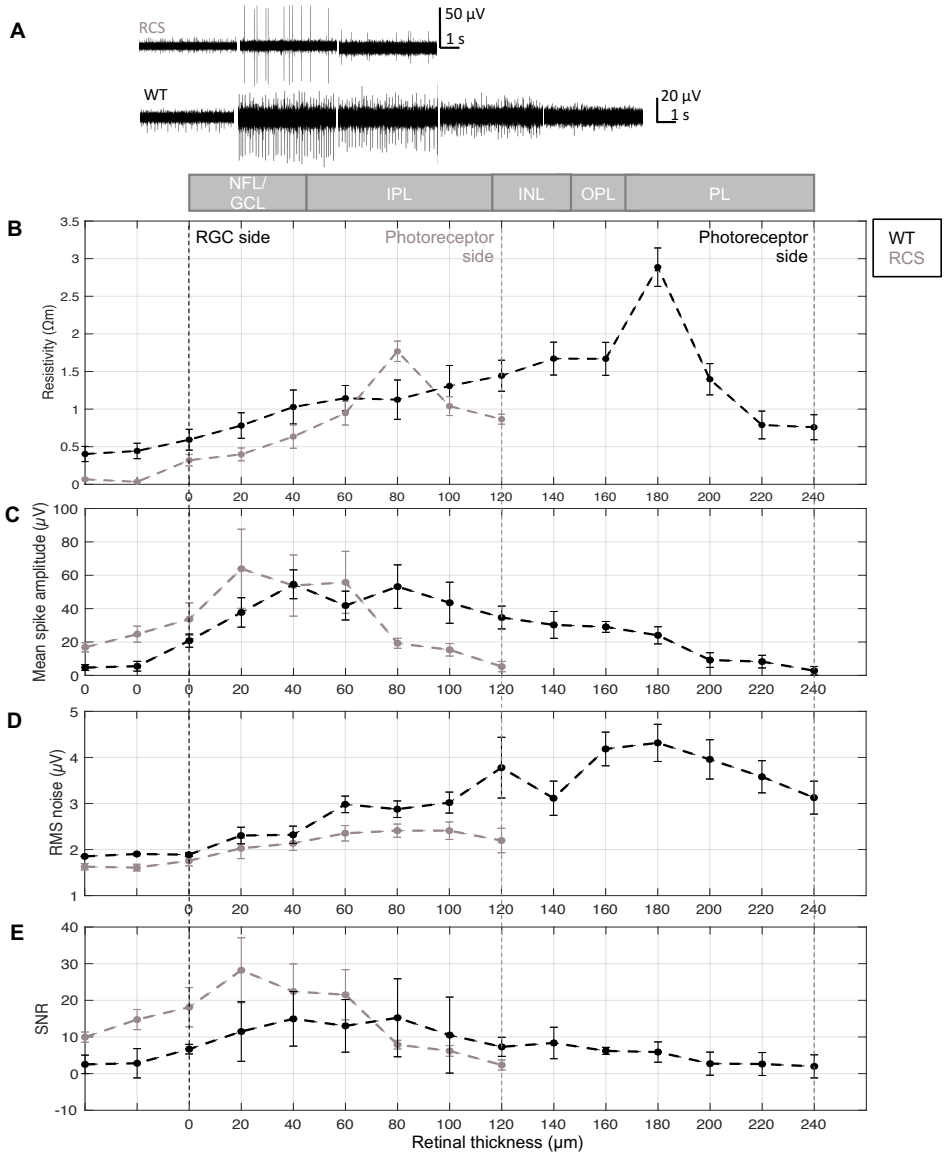

Figure 6.3.: Resistivity profile and electrophysiological activity of WT and RCS rats. A) Exemplary spiking activity (bandpass filtered signals) are given at a z-depth of 40, 80, 120, 160, and 200 µm for WT and RCS rats. B) The resistivity profile for WT and RCS rats (N = 12 (WT/RCS)) is shown according to the retinal depth. Spiking amplitude (C), RMS noise (D) and SNR (E) at each retinal depth (N = 6 each) (modified from [241]).

cells, which can vary from one recording to another. The spiking amplitudes of the RCS are observed to be lower in comparison to the WT recordings. This may also be attributed to the disease, as it is generally more challenging to capture active spiking cells. The RMS of the noise increases with increasing retinal depth until it decreases again (Figure 6.3D). A thorough examination of these profiles reveals a high degree of similarity between the resistivity profile of the WT and RCS rat models. In the WT model, the peak is reached at 180 µm and subsequently declines, in a man-

ner analogous to the resistivity profile. A similar trend is observed in the RCS rat model, where the peak is at 80 µm and subsequently declines. This finding aligns with the hypothesis that noise is influenced by the impedance of the electrode-tissue interface. As the SNR is derived from the ratio of the spiking amplitude and the RMS noise, it also increases upon reaching the ganglion cell layer and declines with rising RMS and falling spiking amplitude (Figure 6.3E). This profile is particularly noteworthy when considering recordings and stimulation using penetrating electrodes. In particular, the resistivity profile affects the current spread upon electrical stimulation and should be considered during simulations to estimate activation patterns.

6.1.3. Simulation of electrical stimulation of the retina using COMSOL

In order to gain a deeper understanding of the current spread upon electrical stimulation, taking into account the resistivity profile of the WT and RCS retina, simulations were conducted using the FEM software COMSOL Multiphysics.

COMSOL model descriptions

In order to analyze the electrical field upon current-controlled stimulation, a 2D AC/DC model was employed in COMSOL Multiphysics. The retinal thickness and resistivity profile were modeled using the results presented in section 6.1.1. Accordingly, a retinal thickness of 240 µm was selected for WT rats and 120 µm for RCS rats, respectively. An interpolation function was employed to define the resistivity values as a property when the material of the retina was specified. The 25 µm PEDOT:PSS electrode, with a conductivity of 101 S/cm [170] was positioned at a depth of 70 µm for both WT and RCS rats. This position is located within the inner retina, a region deemed to be an optimal location for electrical stimulation [245]. The stimulation pulse was implemented as a normal current density J_{stim} by

$$J_{stim} = I_{stim}/GSA \tag{6.3}$$

with the GSA of the electrode. To investigate how the electrical field spread changes depending on the stimulation pulse I_{stim}, a parameter sweep was performed, with values ranging from 0.5 to 15 µA with a step size of 0.5 µm. To evaluation if cell was activated at a specific location by the electric potential, a 10 µm long neuronal cell was considered. For this case, an electric field of approximately 3000 V/m is needed to depolarize the cell. This value will further be referred to as the electric field threshold (E_{th}), which is necessary to activate the tissue [223].

Results of the electrical stimulation

The results of the COMSOL simulation to analyze the electrical stimulation of WT and RCS rats with intraretinal probes are shown in Figure 6.4. As the stimulating current (I_{stim}) is increased, the strength of the electric field also rises. This is demonstrated in Figures 6.4A_i and 6.4B_i, which show the effects of I_{stim} equal to 3, 10 and 15 µA on both WT and RCS rats' retina. The dark red area represents E_{th}, indicating the portion of the retina where, in the event of a cell being present, activation would occur. As a consequence of the resistivity profile, the distribution of the spread is not uniform in z direction, for both, WT and RCS rats. Figure 6.4A_{ii} and 6.4A_{iii}, illustrate the evaluation of the electric field in a WT rat, according to the distance of the electrode in the x and z directions, respectively. Figure 6.4B_{ii} and 6.4B_{iii} present the same data set for RCS rats. The E_{th} of 3000 V/m is indicated in all four plots. It is evident that in x direction, E_{th} in RCS rats is reached with higher currents in comparison to WT rats. For instance, to stimulate a cell which is located 50 µm away from the electrode in x-direction, an I_{stim} of 7.5 µA is sufficient for WT, whereas 9 µA are required for RCS. This represents an increase of 21%. Similar observations are evident in the z-direction towards the deeper layers of the retina. For instance, when indirect stimulation of the

ganglion cells is desired, for example of the bipolar cells which are in the INL layer, the current required is 9.5 µA at a distance of 50 µm in RCS rats and only 6 µA in WT rats, thus an increase of 58%.

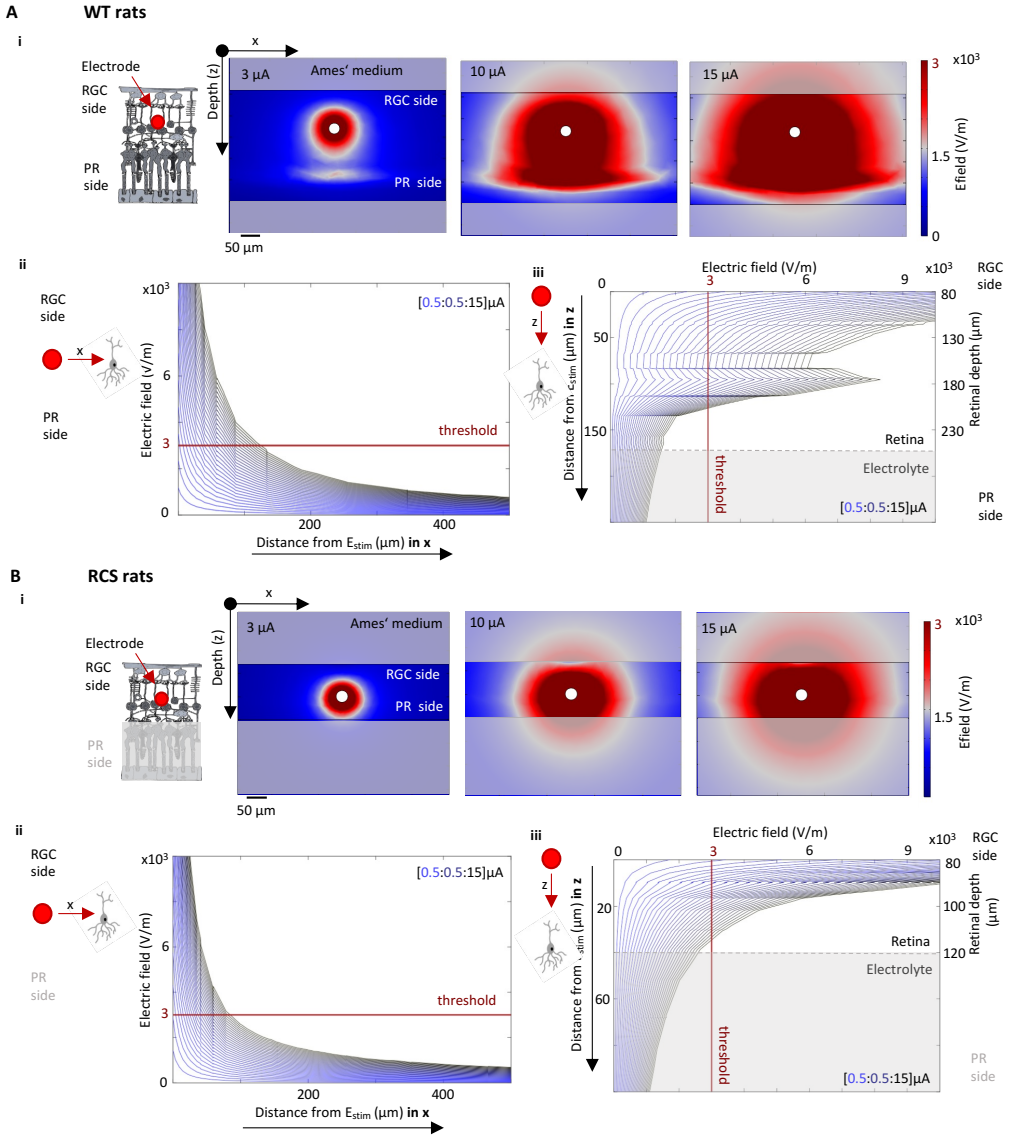

Figure 6.4.: Results of the simulation of electrical stimulation of WT (A) and RCS (B) retina. The electric field spread is evaluated for a range of stimulation pulses I_{stim}. The norm of the electric field for a I_{stim} of 3, 10 and 15 µA is shown in A_i and B_i for WT and RCS rats, respectively. The electric field depending on the distance to the stimulation electrode in x (ii) and z (iii) direction is shown for WT (A) and RCS (B) rats while varying I_{stim} from 0.5 to 15 µA with a step size of 0.5 µm (modified from [241]).

6.1.4. Discussion of the findings

The previously discussed data demonstrates that there are significant differences in the resistivity of the retinal layer between diseased and WT retinas in rats. The values observed in the WT retina are consistent with those previously reported in the literature [239]. The resistivity trace of the diseased rat model exhibits a high degree of similarity to that of a diseased mouse models retinal degeneration 1 (rd1) and rd10 [240]. The experiments were conducted on 10-month-old RCS rats, which are considered to be fully blind. This was tested during the electrophysiological experiments by optical stimulation, which yielded no response. Nevertheless, further recordings of the RCS at different ages would be beneficial in order to gain further insight into the timing of the change in resistivity and its development over time. Furthermore, it would be advantageous to evaluate alternative approaches for resistivity estimation, as noise can affect the accuracy of the PRF method, as illustrated by the relatively high standard deviations observed in the measurements. For example, the least squares method is thought to be more precise [242]. Furthermore, chronic *in vivo* implantation with penetrating implants often results in impedance changes due to foreign body reactions, which can lead to glial scar formation and device encapsulation [90]. It would be of interest to utilize this methodology with flexible BiMEA in chronic *in vivo* conditions to investigate the efficiency of stimulation in the context of changing electrode impedance.
In the context of penetrating retinal probes, the examination of resistivity traces in conjunction with electrophysiological measurements represents a valuable methodology for identifying the position of the electrode within the retina. The location can be identified from both the resistivity value and the electrophysiological recordings, for instance by calculating the RMS of the noise. In principle, this could be implemented as a closed-loop circuit, with the electrode position being automatically adjusted in accordance with the response upon electrical stimulation. By this, the optimal location for the electrical stimulation of retinal cells could be determined. Moreover, impedance and resistivity measurements serve as a valuable tool for evaluating the success of surgically placing the probe in the eye, particularly when testing surgical procedures on cadaveric animals.
The results of the COMSOL simulations demonstrate that the impact of resistivity alterations in the degenerated retina is a critical factor to be considered when developing a protocol for electrically stimulating retinal cells with intraretinal electrodes. This further underscores the necessity for a bidirectional communication approach in retinal prostheses, which enables the investigation of the diseased retinal network and the adjustment of electrical stimulation parameters in accordance with feedback from the cells, the electrical properties of the retina, and, consequently, the level of degeneration, which is subject to change in affected patients over time.

6.2. Retinal electrophysiological recordings using 3D neural implants

The objective was to develop an intraretinal application, whereby recordings could be made from the 3D retinal space of the various retinal layers. As previously stated, the KiRi and PiRi designs were aligned with the dimensions of a rodent's retina to span various retinal layers. Therefore, 3D kirigami intraretinal implants comprising 32 shanks of 225 µm height, as illustrated in Figure 4.6, were utilized. Each shank contained three or four electrodes (i.1, i.2, i.3, and i.4) with a vertical inter-electrode distance of 12 µm. In future applications, the objective is to simultaneously achieve electrical stimulation and recording with electrodes of the same diameter. For this reason, the diameter of the i.1 electrode was set at 25 µm, while the diameter of the i.2-4 electrodes was reduced to 15 µm. Moreover, in order to gain access to all three dimensions of the target tissue (including the surface), the KiRiRet incorporates surface electrodes for epiretinal coupling. The PiRi probes were utilized with either a multisite configuration or single pillars. The use of surface electrodes was not employed in this instance.

6.2.1. Insertion of 3D implants into the retina

Figure 6.5A illustrates the insertion of a KiRiRet probe into the retina, which was situated within a perfusion chamber and maintained in a continuously perfused solution of fresh Ames' medium (see Appendix C.1.1). Initially, the probe was positioned in close proximity to the retinal surface utilizing a micromanipulator (Figure 6.5A$_i$). Subsequently, an insertion rod was positioned in close proximity to the probe's surface utilizing a second micromanipulator (Figure 6.5A$_{ii}$). Then, the insertion rod was lowered in a stepwise manner at a velocity of 200 µm/s in accordance with a meticulously delineated insertion protocol, thereby ensuring minimal insertion-related damage until all shanks have penetrated the tissue (Figure 6.5A$_{iii}$).

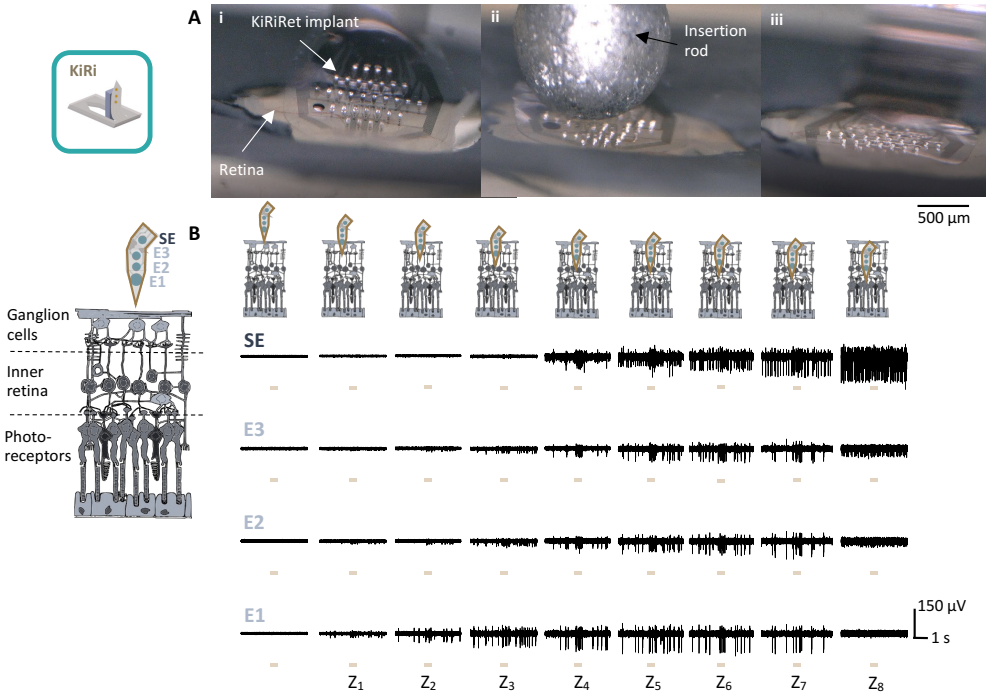

Figure 6.5.: Insertion of a KiRiRet probe into explanted rat retina. The insertion of a KiRiRet probe with shanks of 225 µm length. A) Images during the insertion: First the probe is placed close to the surface of the retina (i), then the insertion rod is used to press the implant towards the retina (ii) until the shanks fully penetrate the tissue (iii). After retracting the insertion rod, the shanks remain within the retina. B) The illustration depicts the measurements of a single shank comprising three electrodes (E1, E2, and E3) and a surface electrode (SE). The accompanying recordings illustrate the intraretinal placement of the KiRi probe following a stepwise insertion process (Z1-Z8). Initially, a large step of 100 µm was performed to reach Z1, followed by subsequent steps of 20 µm. The yellow bar indicates the time points of optical stimulations, which were done at each insertion step (modified from [197]).

The kirigami electrodes were positioned on the epiretinal side, in close proximity to the ganglion cells, which are known to express action potentials. Figure 6.5B illustrates the recording during the implantation of an exemplary shank and a surface electrode. In Figure 6.5A the electrode arrangement is illustrated and a microscopic picture of a KiRi probe penetrating the explanted retina is shown. When the probe was placed in close proximity to the surface, no electrophysiological activity was detected by the electrodes (see Figure 6.5B). Following the initial 100 µm insertion, the first electrode of the shank began to register spikes. This suggests that the initial insertion step was large enough to overcome tissue dimpling and penetrate the retina, allowing the electrode to reach a position in close proximity to the ganglion cell layer. Subsequently, the probe

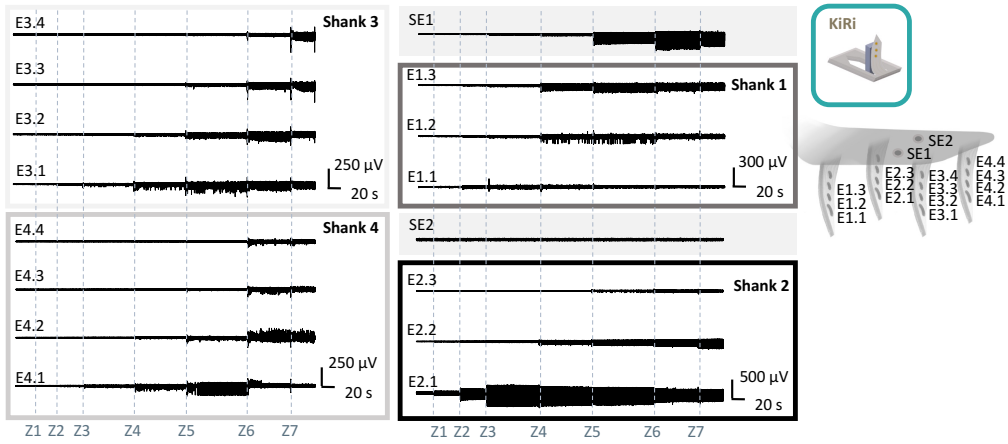

Figure 6.6.: 3D electrophysiological recordings during the insertion of a KiRiRet probe. This example shows an recording (bandpass filtered data) of 16 electrodes distributed on four shanks and two surface electrodes (SE1 and SE2), which capture spiking activity at different points in time. The insertion steps are indicated by dashed vertical lines (modified from [197]).

was inserted in a stepwise manner, with a movement of 20 µm. As the probe progressed deeper into the retinal tissue, the E2 and subsequently the E3 electrodes commenced detection of the activity, as they also reach the ganglion cell layer. Concurrently, the amplitude in E1 was observed to increase further, indicating that the probe was approaching the spiking cell. At a specific depth (Z4), all electrodes captured spiking activity, including the surface electrode. From Z4 to Z5, the amplitudes in all electrodes increased, indicating a reduction in distance to the spiking ganglion cell. Following another insertion step reaching position Z6, the amplitude in E1 was observed to be decreasing, thus indicating an increase in distance to the spiking ganglion cell. Subsequently, upon taking an additional step, the deepest electrodes traversed the ganglion cell layer, resulting in the observation of no longer discernible spiking activity from the background noise.
Similar spiking patterns were observed across the shanks of the 3D kirigami device (Figure 6.6). In this instance, the deepest electrodes of shank 2 (E2.1) picks up spiking activity one insertion step ahead of the other shanks. This might be attributed to the characteristic concarve surface of the retina. This findings underline further how monitoring the spiking activity is a useful tool for positioning the shanks and ensuring that all shanks are inserted at their full length.
This method allows for tight coupling between the neurons and the electrodes indicated by high peak-to-peak amplitudes of APs of up to 600 µV (Figure 6.7) with an SNR of 72, while the average SNR was 10.4 ± 9.5.

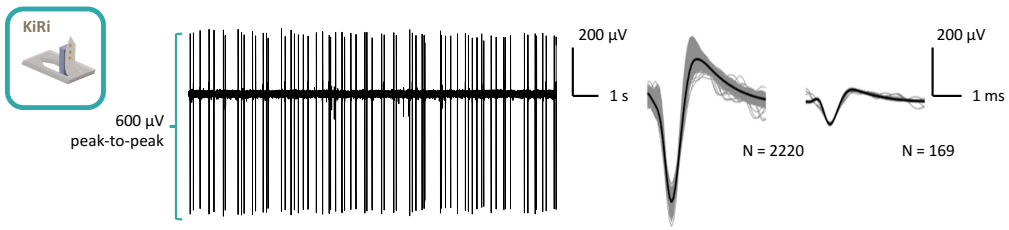

Figure 6.7.: High amplitudes of spiking activity measured with a KiRi probe. Peak-to-peak amplitudes of up to 600 µV with an SNR of up to 72 were measured in the retina using KiRi probes. In this figures the bandpass-filtered data is shown alongside the sorted spikes.

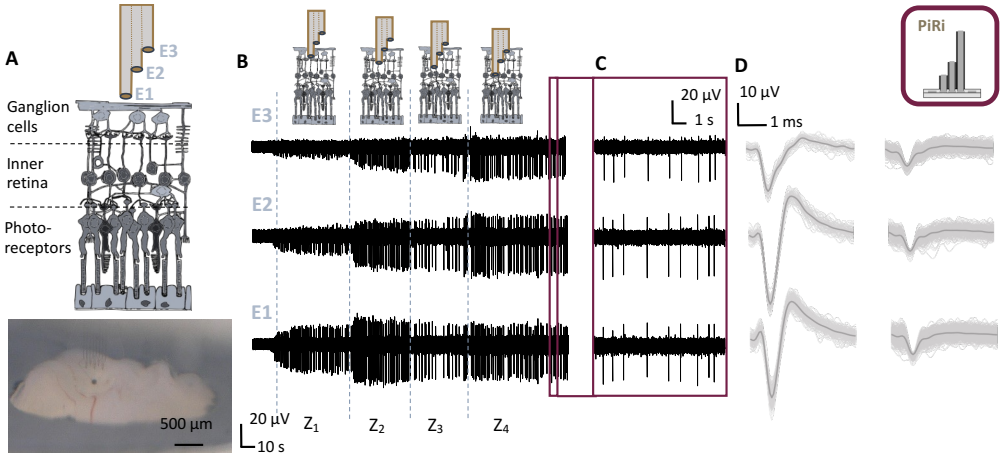

Figure 6.8.: Insertion of a multisite PiRi probe into explanted rat retina. The insertion of multisite pillars containing three electrodes with a height differential of 20 µm each is depicted (A) and a microscopic picture of a PiRi probe penetrating the explanted retina is shown. Recordings demonstrating the intraretinal placement of a multisite pillar subsequent to stepwise insertion (Z1-Z4) are provided (B). Additionally, recording sections at Z4 (C) and spike waveforms recorded from individual electrodes (D) within a single multisite pillar are shown (modified from [41]).

Similarly, a multisite PiRi probe was implemented and tested in order to gain access to the 3D intraretinal space. Figure 6.8A shows a schematic of the electrode arrangement as well as a microscopic picture of the PiRi probe penetrating the explanted retina. Figure 6.8B illustrates a recording example in which the insertion of the implant was conducted with an initial step size of 100 µm, followed by step sizes of 50 µm. Consequently, at the initial insertion stage (Z1) illustrated in Figure 6.8A, the lowest electrode (E1) penetrated the retinal ganglion cell layer (GCL), thereby enabling the recording of spontaneous activity. The second electrode (E2) recorded lower amplitude spikes as it was situated further away from the ganglion cells, potentially at the retinal surface. No spiking activity was observed at the third electrode (E3), as its location was not yet close enough to capture the electrophysiological signal. Following a second insertion step (Z2), an increase in spike amplitude was observed in both the E1 and E2 electrodes, while the E3 electrode also began to capture spiking activity. Upon further insertion into the retina (Z3 and Z4), a decrease in spiking activity amplitude was observed in E1, while a slight increase was noted in E2 and E3. This confirmed that these electrodes have also penetrated the GCL. Consequently, at Z4, E2 was in closest proximity to a spiking cell, exhibiting the highest amplitude spikes. Peak amplitudes of up to 80 µV, an average SNR of 9.5 ± 6.3, and a maximum SNR of 25.2 were captured.
The recordings obtained during the implantation of KiRi and PiRi electrodes demonstrate the high degree of precision with which the method enables the positioning of the electrodes within the tissue. This enables the optimization of neural measurements from disparate regions of the tissue, as well as the identification of the optimal location for the subsequent application of electrical stimulation. A closer examination of individual spikes reveals that the same units in the neural column are being followed by the electrodes within one shank (KiRi) or multisite pillar (PiRi). This is evidenced by the minimal conduction delay of 0.5 to 1 ms observed in all channels, which captures the same waveforms with varying amplitudes (see example in Figure 6.8B,C,D). These results align with those of previous studies that employed two-dimensional (2D) multisite and penetrating intraretinal electrodes in retinal models [78][155]. This application demonstrates the capacity for neural recording, specifically tracking the same neuronal column at varying depths. Additionally, this methodological approach can facilitate identification of the optimal locations for both recording and electrical stimulation of neural activity, which is a critical consideration for future retinal

prosthetic devices.

6.2.2. Optical stimulation of healthy retinas

The KiRi and PiRi implants facilitated the recording of clear physiological responses when the retina explant was stimulated with light. Typical waveforms in the low-frequency range (less than 100 Hz), designated as LFP (large field potentials), and a change in the firing rate of the spiking activity of retinal ganglion cells were observed to occur in conjunction with optical stimulation.

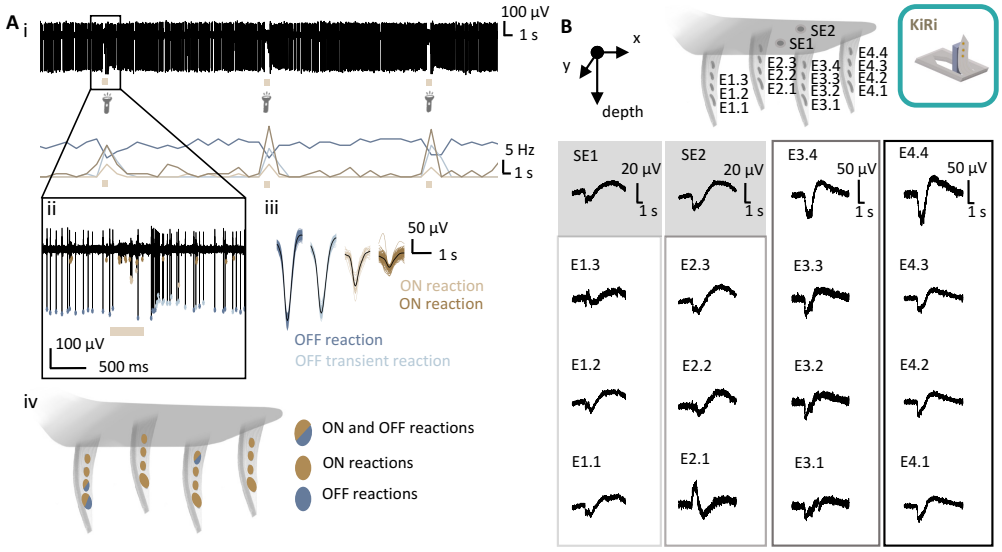

Figure 6.9.: Optical stimulation of explanted retina recorded with a KiRiRet implant. A) The bandpass-filtered signal and firing rates upon light stimulation using a 500 ms long light pulse every 15 s are illustrated in (i). In (ii), a zoom-in is provided to show the OFF as well as the ON reactions captured with individual electrodes. In (iii), the spikes are sorted to provide further insight into the type of recorded reaction, which differs in the 3D intraretinal space (iv). B) The 3D map of LFPs upon light stimulation after low-pass filtering and averaging the responses is presented (modified from [197]).

The spike sorting of the trace following optical stimulation of a dark-adapted retina demonstrates that a single electrode can capture multiple ON and OFF pathways (Figure 6.9A$_i$, and zoom-in in A$_{ii}$), revealed by spike sorting (Figure 6.9A$_{iii}$). ON pathways are activated when light is switched on, while OFF pathways are activated when light is switched off (see section 2.1.3). Furthermore, the ON and OFF reactions can be classified with greater specificity. For instance, an OFF transient reaction is defined by an increase in firing rate for a brief time interval following the illumination's deactivation. A 3D map was constructed by analyzing the optical stimulation responses of the recording electrodes, which demonstrates the locations where ON and OFF reactions were observed (Figure 6.9A$_{iv}$). In this example predominantly ON reactions were observed, with the presence of OFF reactions in some electrodes that were situated on the same shank. This illustrates the intricate nature of the retinal neural tissue and emphasizes the importance of a comprehensive examination of the retinal network.
Moreover, LFP recordings were made at the onset of illumination, displaying waveform morphology similar to that observed in ERG recordings. These comprise the summed activity of retinal neurons and reflect photoreceptor and bipolar cell function. This observation was also reported in previous studies utilizing 2D intraretinal probes [155]. In this instance, the typical a- and b-waves of

an ERG exhibit a change in polarity when the electrodes are situated in close proximity to the photoreceptor layer within the retina. The same behavior was observed with the kirigami electrodes (see Figure 6.9B). The two epiretinal surface electrodes, SE1 and SE2, exhibit a smaller amplitude for the a-wave in comparison to the b-wave. In general, the electrode situated in closest proximity to the ganglion cells, such as E2.4 or E3.3, exhibits the highest amplitudes, whereas electrodes positioned deeper within the tissue, at a greater distance from the ganglion cells, demonstrate comparatively lower amplitudes, such as 2.3 or 3.2. Upon reaching deeper layers, in closer proximity to the photoreceptors, a shift in polarity of the a- and b-waves is typically observed, as evidenced by E2.1. Although the electrodes in all shanks are horizontally aligned, the retina does not have an even surface, particularly when prepared for *in vitro* recordings. Consequently, electrodes of different shanks at the same horizontal location may be located at different depths within the retina. The analysis of spiking activity and LFPs represents a valuable approach for determining the position of the electrodes within the retina.

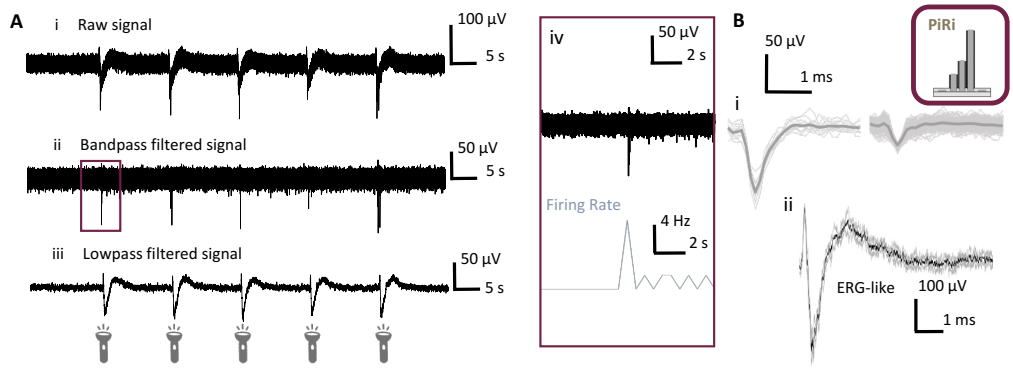

Figure 6.10.: Optical stimulation of explanted retina recorded with a PiRi implant with straight pillars. The use of straight PiRi pillars for *in vitro* retinal recordings allows for the capture of raw electrical signals (A_i), spiking activity (bandpass filtered signal) (A_{ii}), and local field potentials (lowpass filtered signal) (A_{iii}) captured upon optical stimulation. Individual optical responses were observed, and it was found that the firing rate (blue trace) of the spiking signal (black trace) increased upon optical stimulation (A_{iv}). In B), distinct neural waveforms corresponding to the spikes of the ON-pathway are demonstrated (i). Furthermore, averaged ERG-like waveforms (ii) were recorded following four to five stimuli representing the summed activity of the retina (modified from [41]).

A comparable investigation was conducted with PiRis as illustrated in Figure 6.10A. The firing rate was observed to increase in response to optical stimulation. This suggests that the recording electrodes were positioned in close proximity to tonic ON-ganglion cells, which exhibited a sustained spiking response during light stimulation. The LFPs (Figure 6.10B$_{ii}$), were also comparable to the reported waveforms of ERGs from intraretinal recordings in explanted mouse retinas [155]. In contrast to the recordings obtained with the KiRiRet implant, a change of polarity was not observed with the PiRi electrodes. This is due to the shorter length of the electrodes, which do not reach the deeper retinal layers. However, the biphasic waveform of somatic spikes in the retina extracted from the bandpass-filtered signal (Figure 6.10B$_i$) indicates a deep insertion into the retinal ganglion cell layer [246].

6.2.3. Electrophysiological recordings from degenerated retinas

Following the death of the photoreceptors, the retina initiates a remodeling process. As previously outlined in section 6.1, this results in alterations to the properties of the retinal network. In the case of rd1 and rd10 mice, there have been comprehensive investigations into the intrinsic neuronal oscillations that were observed during electrophysiological recordings. In the widely utilized

mouse model of retinal degeneration, rd1, the loss of photoreceptors results in the emergence of rhythmic electrical activity within the remaining retinal network, exhibiting frequencies of approximately 10-16 Hz [247]. In contrast, in rd10 models, oscillatory activity occurs at frequencies of 3-7 Hz [247]. The rd10 model, exhibits delayed onset and slowed progression of the degenerative process, rendering this strain of mice a superior model for studying human retinitis pigmentosa. The efficacy of electrical stimulation was found to be diminished in comparison to WT retinas in the rd10 model. In instances where oscillations disappeared spontaneously or were terminated through pharmacological intervention, stimulation efficiency demonstrated an increase to levels that were comparable to those observed in WT animals [248]. It is therefore of paramount importance to ascertain the origin and occurrence of these oscillations in degenerated models, as they have the potential to significantly impair the performance of a retinal implant.
As RCS rats possess an enlarged retina, which is more suitable for testing larger (3D) probes, they are increasingly being used as a diseased model to test for the development of retinal prostheses. The results of section 6.1 indicate a comparable alteration in resistance to that observed in the rd1 and rd10 mouse models. Consequently, it may be hypothesized that the retina will exhibit characteristic electrophysiological behavior in the form of spontaneous rhythmic activity. As oscillations might interfere with the performance of a retinal implant, it is important to know, whether they are a common feature of retinal degeneration models. This hypothesis was tested using 3D probes, KiRis and PiRis.

Investigation of oscillations

In the RCS rats, LFPs, which reflect changes in the extracellular ion concentration that accompany the firing of neurons, were present in the form of oscillatory rhythmic activity, similarly to what was observed in rd1 and rd10 mice. Oscillations in the LFPs were observed regularly in RCS retinas, but were never recorded from WT retinas under the same experimental conditions. The oscillations exhibited an irregular occurrence pattern, comparable to that previously documented in diseased mice [247]. As the rats aged and the disease progressed, the number of observed oscillations increased. Figure 6.11 depicts the oscillations using penetrating KiRi electrodes, which were utilized to record for a longer duration (3 min) to facilitate a comprehensive analysis of the behavior and occurrence of these oscillations. In rats of three months of age, oscillations are observed on an occasional basis, with an average of 0.6 oscillations occurring in five-second windows. In rats of six months of age, the occurrence of oscillations is observed to increase, with an average of 1.9 oscillations noted in five-second windows. In the case of a 19-month-old rat, the number of oscillations rises to 3.9 in a five-second window.

It would be of great interest to investigate which layer of the retina the oscillations are predominantly recorded in using penetrating electrodes, as this could provide insight into their origin. Initially, a comparison was conducted between surface and penetrating electrodes utilizing the KiRiRet probe. As illustrated in Figure 6.12, which depicts the raw and LFP data in addition to the spectrogram of a 19-month-old RCS rat, a notable distinction between the surface and penetrating probes was observed. The surface electrode demonstrated a lower capture rate of oscillations compared to the penetrating electrode. Furthermore, the spectrogram indicated that the majority of frequencies below 5 Hz contributed to the oscillations.

This is also demonstrated by the fast Fourier transformation (FFT) of the recorded traces. This was analyzed in Figure 6.13 using 3-, 6-, and 19-month-old RCS rats. It is evident that in all ages, there is a shift in the FFT highest peak when comparing the surface with the penetrating electrodes. In the 3-month-old rat, there were nearly no oscillations and peaks. The FFT was highest at approximately 1 Hz, which may also be indicative of low-frequency noise. Conversely, in traces exhibiting discernible oscillations, the peak in the FFT was observed at around 2.5 Hz in surface electrodes, shifting to approximately 2 Hz in penetrating electrodes, where oscillations

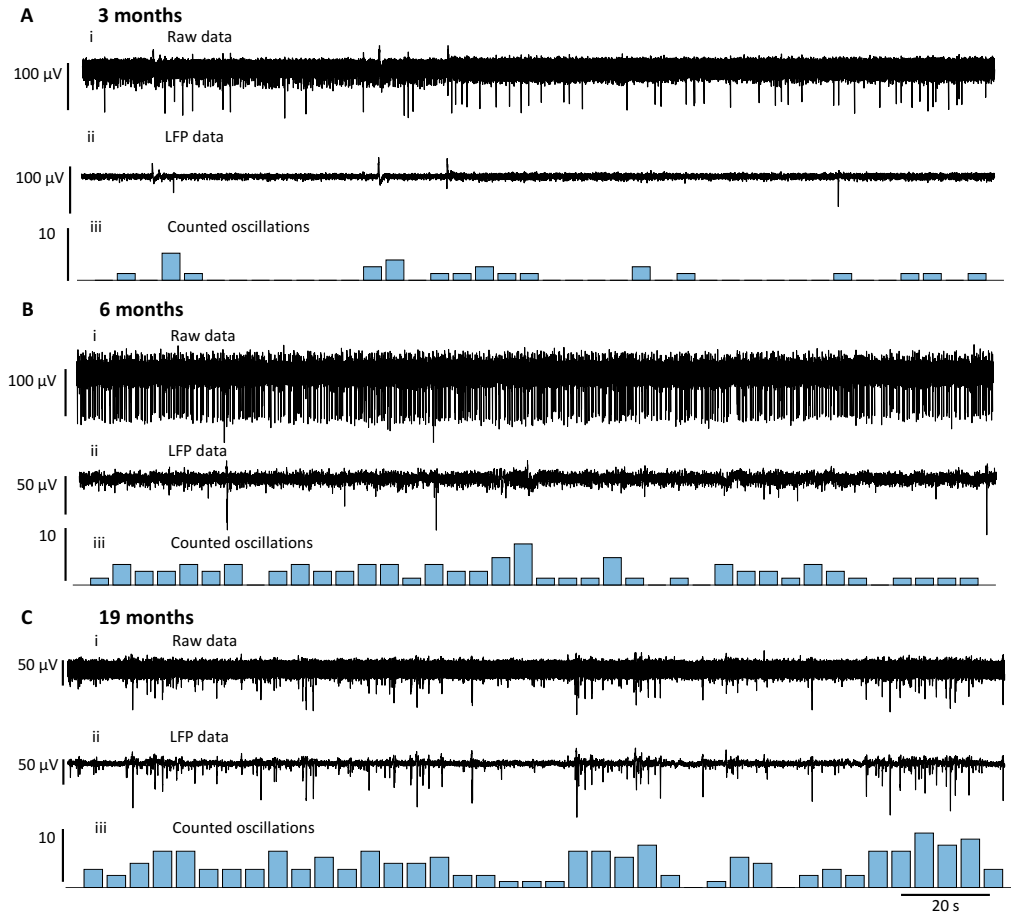

Figure 6.11.: Occurence of oscillations in RCS rats. Raw data (i), LFP data (ii) and counted oscillations (iii) in 5 s long time windows for 3 months (A), 6 months (B), and 19 months(C) months old RCS rats (modified from [249]).

were captured with higher amplitude. Similar observations were made in rd10 mice [156].

As the characteristics of the oscillations were observed to differ within the different retinal depths, as evidenced by the analysis of the frequency components, in the next step, the spread of oscillations was investigated using the 3D nature of the PiRi and KiRi probes. As the used PiRi electrodes have a height of 65 µm, they were supposed to be positioned in the IPL layer, in proximity to the GCL. With a PiRi-iM probe, an area of around 270 x 220 µm is covered by the electrode array at one single z-plane. In Figure 6.14A, the raw data and LFPs are shown which were recorded in the retina of a 19-month-old rat. Typically, the low-frequency deflections are phase-locked with spiking activity (Figure 6.14B). Interestingly, some oscillations expressed a similar shape in several electrodes which might indicate that the rhythmic activity was triggered at one side of the retina and travels to another area. This is further supported by the analysis of the cross-correlation which shows that the data of E4 and E8, which are neighboring electrodes with a distance of 56 µm are highly correlated (Figure 6.14C, other electrodes in Figure C.2A). The waveforms were observed to travel between the pillars with velocities of 3 to 6 ms. This is similar to what was observed in rd10 mice (3 mm/s [247]) and rd1 mice (8 mm/s [250])

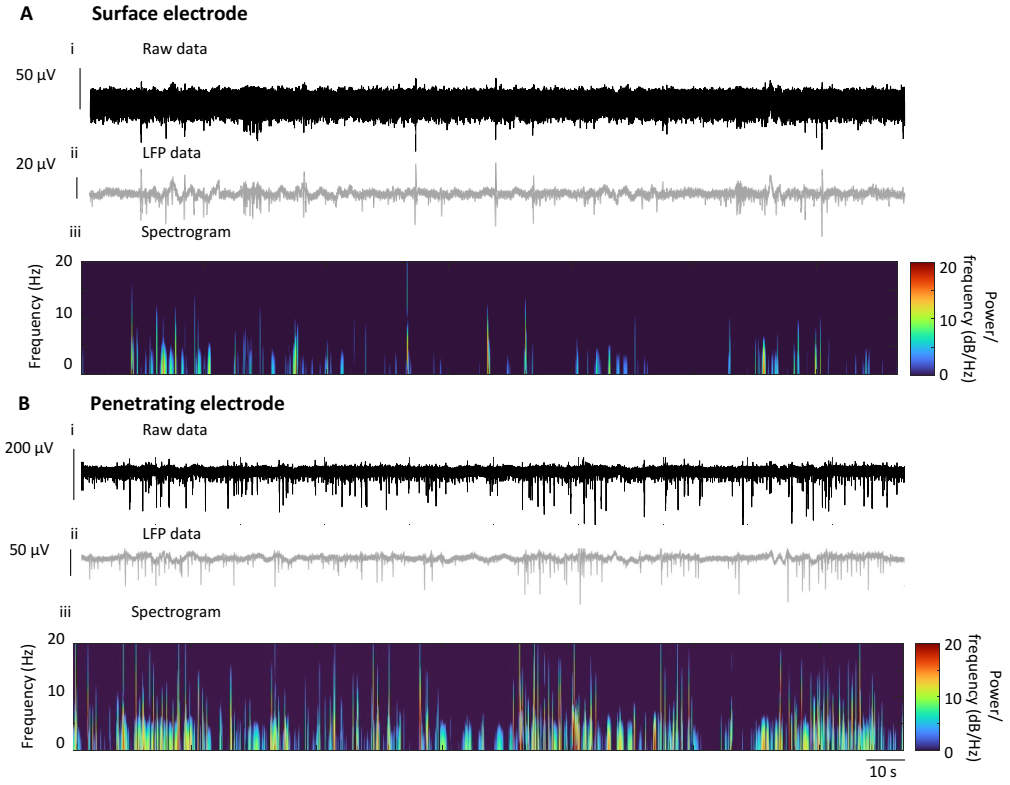

Figure 6.12.: Oscillations in RCS rats recorded with a surface *versus* a penetrating KiRi electrode. Raw data (i), LFP data (ii) after low-pass filtering and spectrogram of recordings from a retina of a 19-month-old RCS rat using a surface (A) and penetrating (B) KiRi electrode.

The KiRi electrodes allowed to additionally investigate how the oscillations differ in all three dimensions of the retina while covering a z-depth of 100 µm and x - y area of 170 x 270 µm with 16 connected electrodes (Figure 6.15). In a manner consistent with the observations made with PiRi electrodes, the deflections exhibited a phase-locked relationship with the occurrence of spiking activity (Figure 6.15A$_i$). However, this assertion is largely applicable to electrodes positioned in close proximity to or within the GCL, such as E1.3 and E1.2 in this particular instance. In contrast, E1.1 is inserted deeper into the retina, likely located within the OPL, and while no spiking activity is recorded, oscillations are still captured. As illustrated in Figure 6.15B, similar waveforms were encountered with a phase shift of 1 - 4 ms of the local minima between neighboring shanks, which would correspond to velocities of 3 to 12 mm/s. The KiRi implant is equipped with surface electrodes, a feature that facilitates the comparison of surface recordings with those obtained from deeper retinal layers. The data of the surface electrode SE1 exhibits a high degree of correlation with the data of penetrating electrodes in more superficial layers of neighboring shanks (e.g., E1.3, E2.4, see Figure 6.15B and all electrodes in Figure C.2B). This correlation extends to the other surface electrode SE2. In contrast, it does not demonstrate a correlation with electrodes in deeper retinal layers, such as E1.1. Indeed, electrode E1.1 exhibits a correlation only with data from electrodes of the same shank and with another deep-inserted electrode (E3.1). Conversely, when examining the cross-correlation of E4.4, which is likely situated in proximity to the GCL, there is a high correlation to the electrode in the neighboring shank 1. This phenomenon is also observed

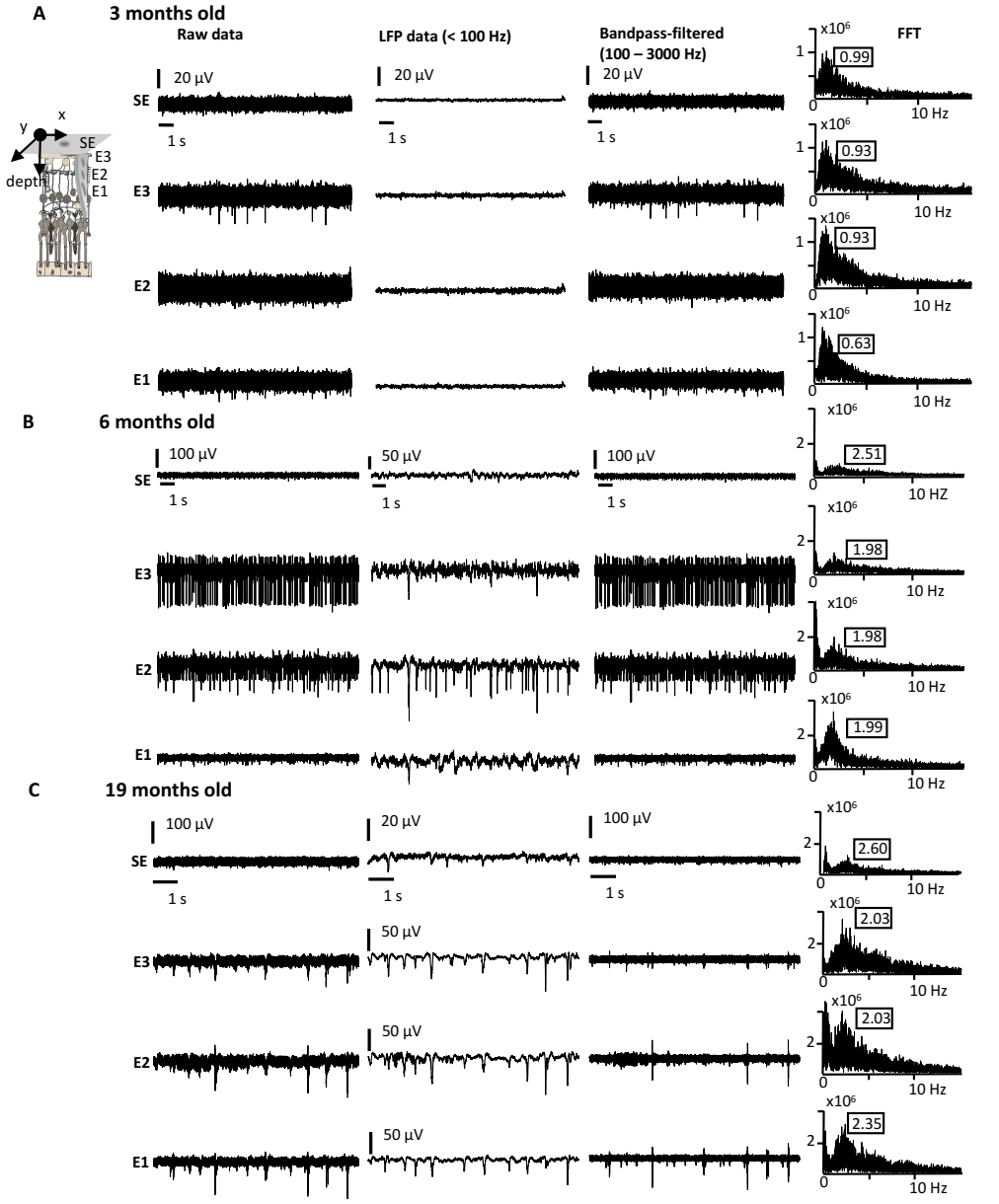

Figure 6.13.: FFT during oscillations in RCS retina changes with the depth. In this image the raw, lowpass-filtered data (LFPs) and bandpass-filtered data are presented alongside the FFT for 3 (A), 6 (B) and 19 (C) old RCS rats (modified from [249]).

in the IPL, where electrodes in a comparable position to the PiRi electrodes (E4.3, E4.2, E3.3, as depicted in Figure C.2B) exhibit a similar trend. The cross-correlation analysis reveals that retinal oscillations exhibit both diffusion and containment within specific regions across the retinal 3D space.

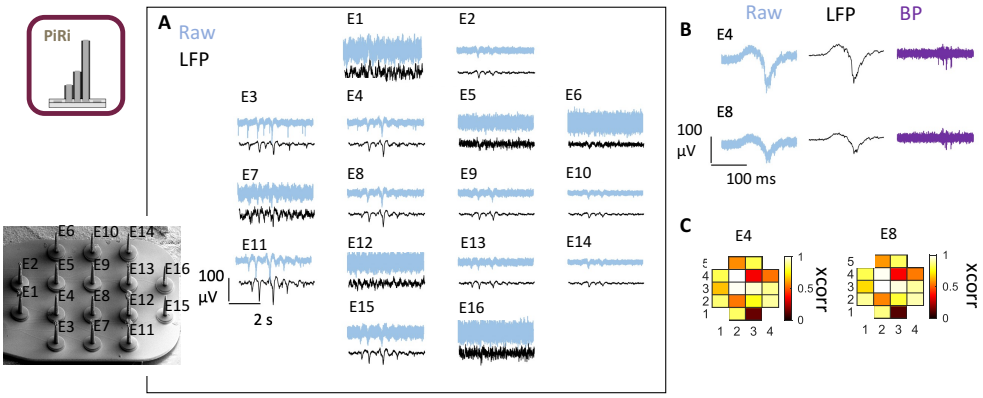

Figure 6.14.: Oscillations in RCS rat retina recorded with a PiRi probe. A) Recordings using a PiRi electrode (raw data (blue) and LFP data < 100 Hz (black). B) A closer look at E4 and E8 show that the deflections are phase-locked with spiking activity (violet). C) A crosscorrelation analysis (LFP data) revealed that the electrodes are highly correlated (modified from [197]).

The multisite design of the KiRis facilitates the acquisition of enhanced information regarding the propagation of oscillations across the retina. This enhanced information content enables a more profound understanding of the disparities in oscillation spread between the deeper retinal layers, such as the OPL or photoreceptor layer, and the more superficial layers, including the GCL and the IPL. This finding underscores the utility of KiRis as a valuable instrument for discerning variations in oscillatory propagation.

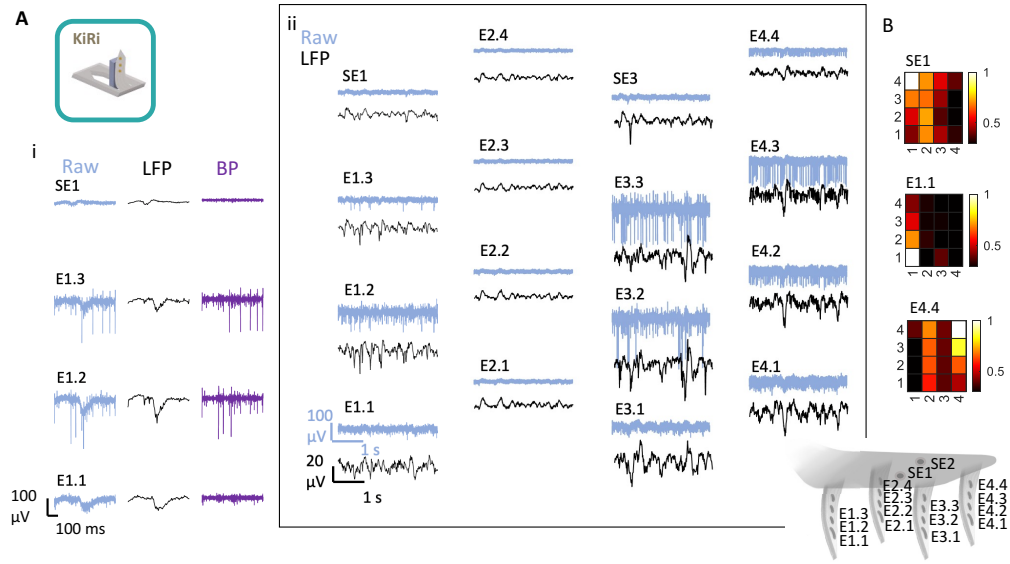

Figure 6.15.: Oscillations in RCS rat retina recorded with a KiRi probe. A) The deflections are phase-locked with spiking activity (i), when the electrode is positioned in close proximity to the ganglion cell layer. The raw (blue) and LFP (black) data shows that oscillations are recorded with surface as well as penetrating electrodes (ii). B) Crosscorrelations of the LFP data of SE1, E1.1 and E1.4 with all other electrodes (modified from [197]).

Origin of the oscillations

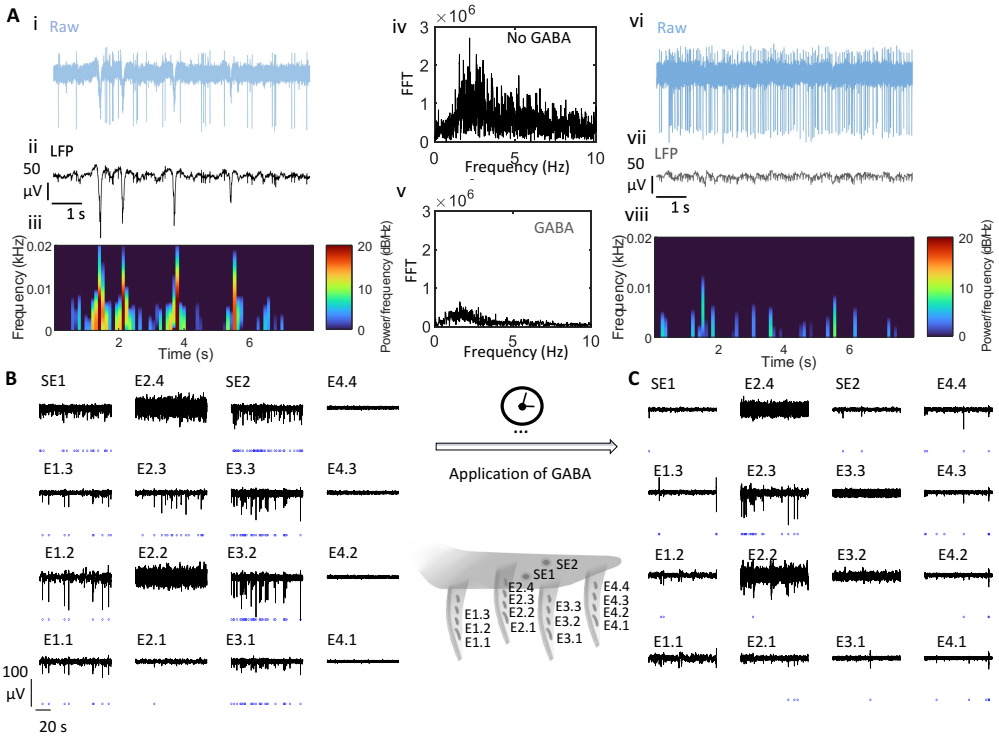

Figure 6.16.: Abolishing oscillations using GABA. A) Raw (i), LFP (ii) and spectrogram (iii) as well as FFT (iv) before the application of GABA. Raw (vi), LFP (vii) and spectrogram (viii) after applying GABA for 1.5 hours. Electrophysiological activity before (B) and after (C) the application of GABA recorded with a KiRiRet implant. The lowpass-filtered data < 100 Hz are shown and the deflections are marked with blue circles (modified from [197]).

Subsequently, 500 µM of GABA was administered to observe its impact on the rhythmic activity. Figure 6.16A illustrates an exemplary recording employing a KiRi probe, in which oscillations are detected prior to the administration of GABA (Figure 6.16A$_i$ raw data and 6.16A$_{ii}$ LFP data). In the spectrogram, low-frequency components manifest with high power at each oscillatory deflection. This phenomenon is analogous to the observations made in the FFT, which also exhibited a peak at 2.2 Hz (other electrodes in Figure C.2D). Following a period of embedding in GABA that extended for approximately 90 minutes, a marked reduction in the occurrence of oscillations was observed. The deflections nearly completely vanished and no rhythmic behavior was observed anymore as evidenced in Figure 6.16B,C. This decline culminated in the absence of rhythmic behavior, as demonstrated in Figure 6.16A$_{vi-viii}$, and the FFT peak (Figure 6.16A$_{vi-viii}$) is significantly less pronounced. Figure C.1 illustrates the duration of GABA application required to affect the rhythmic activity, as well as the progressive reduction in recorded deflections over time. Thus, in a manner analogous to the rd10 retina [247][248], the presence of GABA resulted in the absence of recorded oscillations. The origin of the oscillations has been the subject of debate in several academic works. One hypothesis posits that the electrical coupling between cone ON-bipolar cells and AII amacrine cells, facilitated by gap junctions, plays a role in the generation of these oscillations. It has been demonstrated that oscillations only occur when the membrane potential of the AII amacrine cells is within the range necessary to open their voltage-activated sodium channels. Subsequently, the oscillatory activity was conveyed via bipolar cells [251][252].

In contrast, Yee et al. put forth the hypothesis that an oscillator in amacrine cells serves as the source of rhythmic activity [253]. The inhibitory transmitters GABA abolish oscillations in RCS retina, which is in agreement with both aforementioned hypotheses. In the first hypothesis, the effect of GABA is to hyperpolarize the membrane potential of the AII, thereby reducing the likelihood of sodium channels becoming activated. In the amacrine cell model, GABA reduces the rhythmic input from amacrine cells [249].

6.3. Insertion footprint of kirigami and 3D printed neural probes

The proof-of-concept for flexible KiRis and PiRis for intraretinal applications *in vitro* was established. Subsequently, the performance of both devices was evaluated according to their insertion footprint. KiRi probes with 32 shanks of length 225 µm and an inter-shank distance of 50 µm or 100 µm were tested. Thus, they will be designated as KiRi-i50 and KiRi-i100. The PiRis are designed with multisite pillars at a distance of 80 µm between pillars and with pillar heights of 80, 100, and 120 µm, hence the designation PiRi-Multi. Moreover, straight pillars with a height of 65 µm and inter-pillar distances of 16, 56, 106 and 150 µm were tested and subsequently labelled PiRi-iS, PiRi-iM, PiRi-iL and PiRi-iXL, respectively (see Figure 4.16 and 4.17). For the KiRis-i100, insertion speeds v_{in} of 200, 1000 and 4000 µm/s were tested, in accordance with the protocol outlined in section 3.4.1. Thus, an insertion speed v_{in} that resulted in the least damage was selected for the next experiments. Two to three insertions were conducted for each device, yielding a total of 24 retinal samples using in total eight TN-L15 mice.
The insertion impact of the 3D devices was evaluated in accordance with the methodology in section 3.4.1. The acute insertion footprint of the devices was quantified based on the insertion trauma area ITA, defined as the insertion hole area encompassing the dead cells within and surrounding the borders of the insertion site; and the number of dead cells within each ITA.

Acute insertion footprint of kirigami implants

In order to evaluate the insertion footprint of different KiRi devices, a comparison was conducted between the KiRi-i50 and KiRi-i100. In Figure 6.17A$_i$ and 6.17C$_i$, the ITA of each shank of the KiRi-i50 and KiRi-i100 probes are indicated by white dashed lines in the whole-mount images of TN-L15 retina with stained dead cells (red). In order to gain a more complete picture of the location, depth of the dead cells and cross-section retina, 3D projections were used in conjunction with the whole-mount images. The ITA for both the KiRi-i50 and KiRi-i100 is relatively small, with a mean of 1097 ± 407 µm² and 943 ± 329 µm², respectively. This is only about double the size of the cross-section of a KiRi shank. Despite the slight reduction in ITA size observed for the KiRi-i100 samples in comparison to the KiRi-i50 samples, no statistically significant difference was identified. In the cross-sectional view of the insertion areas (Figure 6.17A$_{ii,iii}$ and 6.17C$_{ii,iii}$), it can be observed that dead cells are present beyond the ganglion cell layers, indicating a deep intraretinal insertion for both cases. The number of dead cell within the ITA was quantified for both devices. Examples with a larger amount of dead cells were selected for illustration in Figure 6.17A$_{ii,iii}$ and 6.17C$_{ii,iii}$ in order to more clearly demonstrate the depth of the insertion. The mean number of dead cells within the ITA for KiRi-i50 and KiRi-i100 was found to be 1.2 ± 1.0 and 0.9 ± 0.9, respectively. These values did not indicate any statistically significant difference. Furthermore, it is important to note that some dead cells are dislodged from the retina and transported with the shanks upon extraction, ultimately accumulating on the surface of the retina, as for instance observed in Figure 6.17C$_{iii}$.
The insertion speed (v_{in}) was evaluated using the KiRi-i100 in order to ascertain its effect on the insertion impact. The probes were inserted with an v_{in} of either 1000 or 4000 µm/s. The ITAs are indicated by white dashed lines in the whole-mount images of TN-L15 retina with stained dead cells in Figure 6.17B$_i$ and 6.17D$_i$, respectively. In comparison to the data presented in Figure 6.17B$_i$ where a v_{in} of 200 µm/s was employed, it is evident that the larger ITA and higher amount of dead cells are a consequence of the KiRi-i100 probes being inserted at higher velocities. At a speed of 1000 µm/s, ITAs were found to possess a size of 1389 ± 706 µm^2 containing 1.3 ± 1.5 dead cells. Therefore, the ITA is markedly increased by 32% in comparison to the lower v_{ii} of 200 µm/s (see Figure 6.17E). At a v_{ii} of 4000 µm/s, the acute insertion impact is even more pronounced with an ITA of 2393 ± 1429 containing 3.8 ± 3.6 dead cells. In this instance, the ITA

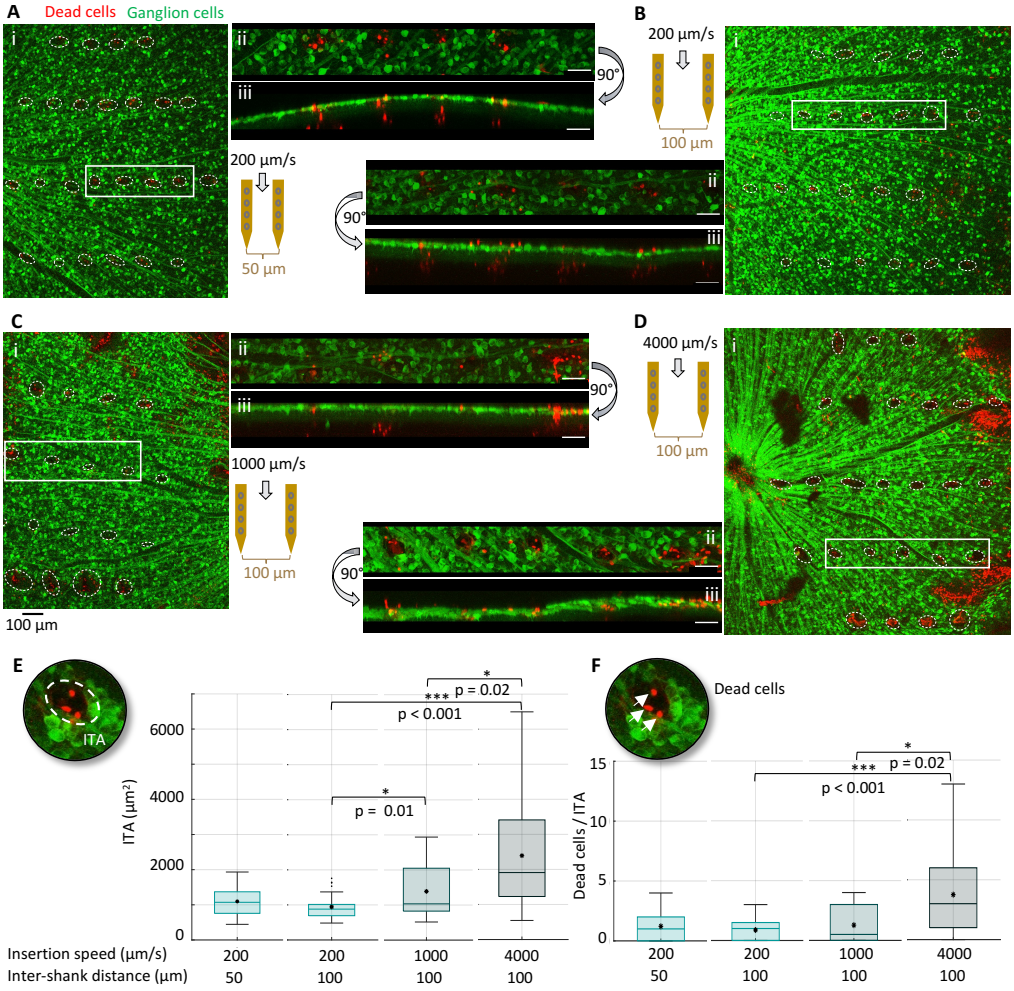

Figure 6.17.: Insertion impact of KiRi probes upon different insertion speeds. The insertion of KiRi-i50 (A) and KiRi-i100 (B) implants was performed using an insertion speeds v_{in} of 200 µm/s. In addition, for the KiRi-i100 device, v_{in} of 1000 (C) and 4000 µm/s (D) were evaluated to analyze the impact of v_{in} on the acute insertion damage. Whole-mount images with ITAs marked with white dashed circles (i) as well as zoom-ins into the white area (ii) and the cross-section (iii) after rotating the 3D images by 90° are shown. The ITA of KiRi-i50 and KiRi-i100 (D) as well as the number of dead cells within each ITA was evaluated (E) and illustrated by box plots. The mean values are indicated with black stars inside the box plots. Statistical analysis was conducted using pairwise unpaired t-test with Bonferroni correction(* for $p < 0.05$, ** for $p < 0.01$, *** for $p < 0.001$, N = 27, 31, 18, 45 for KiRi-i50, KiRi-i100 at v_{in} of 200, 1000, and 4000 µm/s respectively) (modified from [197]).

increased by a factor of 1.5 and the number of dead cells increased by nearly a factor of 4 in comparison to a v_{ii} of 200 µm/s. This represents a highly significant change (see Figure 6.17E and 6.17F).

Additional stainings of the RGC, amacrine and photoreceptor cells were conducted to ascertain the depth of insertion according to section 3.4.1 (see Figure 6.18). Here, the size of the ITA was 403 ± 155 µm² and 454 ± 152 µm² for the KiRi-i100 and KiRi-i50, respectively. 1.3 ± 1.1 dead cells were identified within the ITA by a KiRi-i100 probe and 1.6 ± 1.4 for the KiRi-50 probes, respectively. The differences, especially in the site of the ITA, are mainly due to the additional

staining of the RGC with green fluorescent protein (GFP), which allowed for better identification of the ITAs due to the enhanced fluorescence of the RGC layer. In the 3D images (6.18A$_{ii,iii}$ and 6.18B$_{ii,iii}$), both the KiRi-i100 and KiRi-i50 designs exhibited the presence of dead cells along the z-axis of the ITAs. Additionally, within the photoreceptor layer, some dead cells were observed, which suggests that the KiRi shanks were successfully inserted and that they penetrated the entire retina.

This analysis aimed to evaluate the influence of the insertion speed (v$_{in}$) and the inter-shank distance of the KiRi shank with respect to the acute insertion impact. In conclusion, the absence of a statistically significant difference between the ITA and dead cell count of the KiRi-i50 and KiRi-i100 probes indicates that the inter-shank distance does not exert a considerable influence on insertion damage. This implies that the inter-shank distance could be further reduced with the objective of placing the shanks in closer proximity, thus creating an implant with an even higher electrode density. Nevertheless, it is possible that this may eventually have an impact when the shanks are positioned in closer proximity. It is therefore recommended that further investigation be conducted with more densely packed shanks. The selected low v$_{in}$ demonstrated a significant impact on improving the acute insertion damage, findings that align with those of other researchers in the field [254]. In contrast, other research groups have proposed that higher insertion speeds are beneficial for (flexible) neural implants [156][255]. This indicates that insertion damage may not be exclusively attributable to the v$_{in}$, but rather should be considered in conjunction with the employed insertion protocol and the specific type of flexible probes. In addition, it should be considered that when evaluating the whole mount images regarding the dead cell count, they could be obstructed by blood vessels or other cells, as marked with the white arrow in Figure 6.18A$_{ii,iii}$ and Figure 6.18B$_{ii,iii}$. Thus, the number of dead cells might be underestimated.

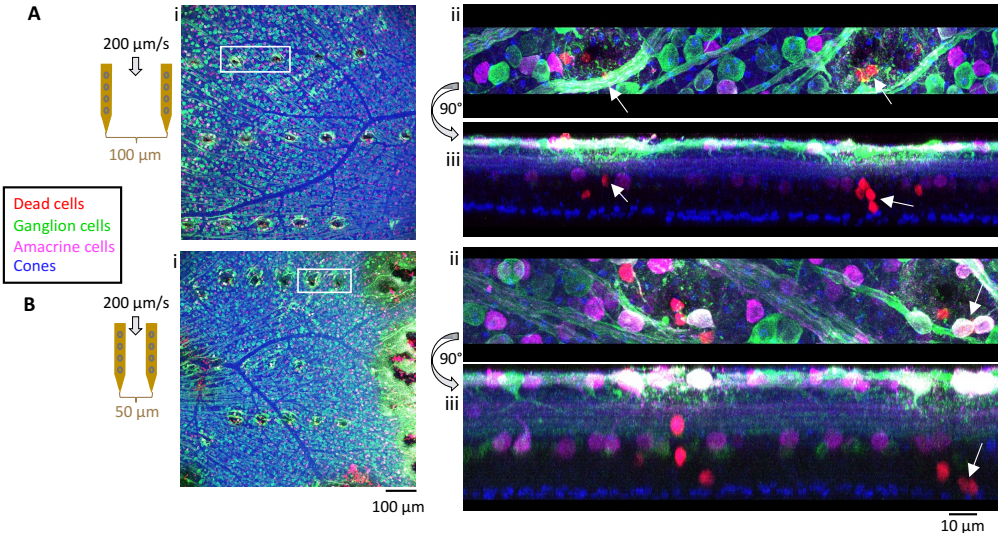

Figure 6.18.: Histological analysis of the retina after inserting KiRi probes. Whole-mount images (i) and 3D images (top-view ii, side-view iii) of a stained retina after inserting a KiRi-i100 (A) and a KiRi-i50 (B) probe. Dead cells are stained in red, amacrine cells in pink, and photoreceptor cones in blue. Ganglion cells appear in green (modified from [197]).

6.3.1. Acute insertion footprint of 3D printed implants

When analyzing the stained dead cells and fluorescence of the ganglion cells, identifying the ITA was difficult for the PiRi devices with straight pillars (PiRi-iS, PiRi-iM, PiRi-iL, PiRi-iXL). In contrast

to the KiRi, clear holes from the penetrating pillars could not be identified in the green channel which shows the ganglion cells. But, dead cells were found in the insertion area after the insertion of each PiRi probe as marked in Figure 6.19. The location of the dead cells matched the geometric placement of the pillars.

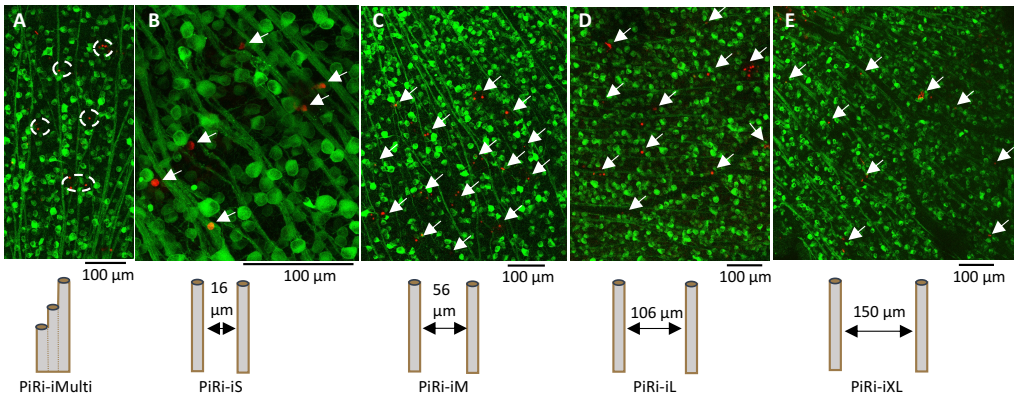

Figure 6.19.: Whole-mount images of stained dead cells in TN-L15 mice after the insertion of PiRi probes. The dead cells are indicated with white arrows after the insertion of a PiRi-iMulti (A), a PiRi-iS (B), a PiRi-iM (C), a PiRi-iL (D) and a PiRi-iXL (E) probe. Dead cells are shown in red and retinal ganglion cells in green.

Due to the difficulty in identifying the insertion sites, an additional staining of the retinal tissue was performed (see section 3.4.1). The antibodies Cal and PEA were used to stain amacrine cells and photoreceptors, respectively. In addition, GFP was used to enhance the fluorescence of the ganglion cells. After that, it was possible to evaluate the ITA as well as the dead cells for the different PiRi designs (Figure 6.21). For the multisite design, the ITA has a size of 576 ± 240 μm^2, which is 2.3 times the cross-section of a multisite pillar. Dead cells were found close to the photoreceptor layer as evidenced in Figure 6.20A_{iii}, which is in accordance with the multisite pillar length of 120 µm. The mean ITA of PiRi-iS, PiRi-iL and PiRi-iXl designs were evaluated. With 595 ± 346 μm^2 the PiRi-iS implant express the highest ITA followed by the PiRi-iL implant with 417 ± 212 μm^2 and lastly the PiRi-iXL implant with 389 ± 272 μm^2. Even though the PiRi-iS has the largest ITA, there was no statistical significant difference found between all four designs. In contrast, comparing the amount of dead cells within the ITA, the PiRi-iMulti design showed the highest number with 2.3 ± 2 dead cells, followed by the PiRi-iL design with 0.9 ± 0.9 and the PiRi-iXL design with 0.7 ± 0.6. For the PiRi-iS design, the amount of dead cells couldn't be evaluated due to bleaching of some slices. Even though there is a statistical significant difference ($p < 0.05$) found between the PiRi-iMulti and the PiRi-iL as well as the PiRi-iXL design in terms of the amount of dead cells, it should be considered that the PiRi-iMulti design has three electrodes within one multisite pillar, while the PiRi-iL and PiRi-iXL are single pillar designs. Thus, when the amount of dead cells was evaluated for each electrode, there were 0.8 ± 0.7 dead cells per electrode found inserting the PiRi-iMulti design, which is comparable with the other two. The 3D analysis and cross-section view of the stained retina showed that the dead cells were sometimes found close to the surface. This is mostly true for the PiRi-iS configuration (Figure 6.20B_{iii}) and might indicate an unsuccessful insertion due to tissue dimpling. In contrast, the dead cells in the PiRi-iL and PiRi-iXL insertions were found in close proximity to the ganglion layer (Figure 6.20C_{iii} and 6.20D_{iii}, respectively). This is consistent with the pillar length of 65 µm.

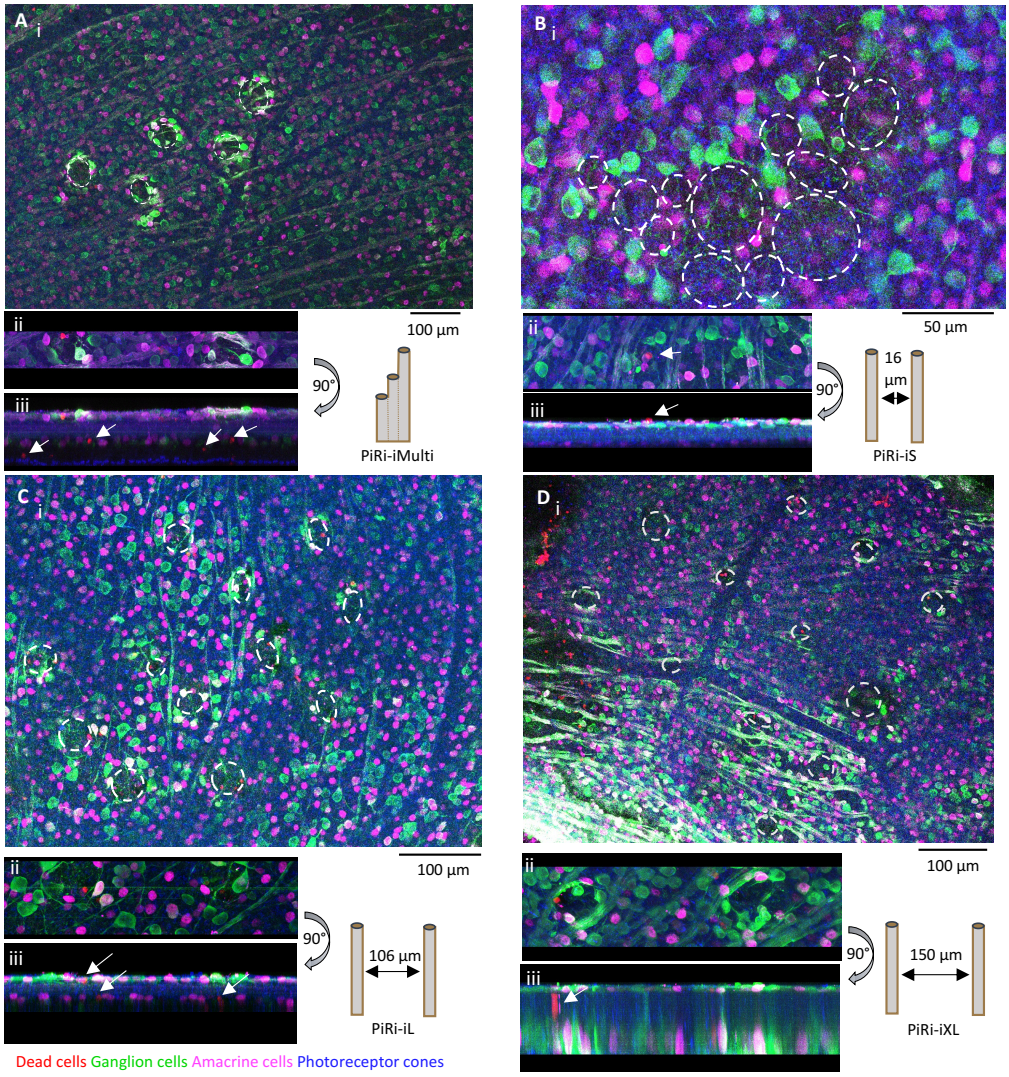

Figure 6.20.: Histological analysis of the retina after inserting PiRi probes. Whole-mount images (i) and 3D images (top-view ii, side-view iii) of a stained retina after inserting a PiRi-iMulti (A), a PiRi-iS (B), a PiRi-iL (C) and a PiRi-iXL (D) probe. Dead cells are stained in red, amacrine cells in pink, and photoreceptor cones in blue. Ganglion cells appear in green (modified from [197]).

6.3.2. Comparison of the acute insertion footprint of kirigami and 3D printed implants

A comparative analysis of the acute insertion footprints of KiRis and PiRis was conducted using images stained with EthD-1, GFP, Cal, and PEA. The results revealed that the ITA of KiRis and PiRis is similar in absolute numbers, with a significant difference ($p < 0.5$) only observed between PiRi-iL and KiRi-i50 probes (Figure 6.22A). When the ITA is divided by the cross-sectional areas of the specific designs, the value for the KiRis is observed to be lower in comparison to the PiRis, with a statistically significant difference ($p < 0.001$) being expressed in all cases (Figure 6.22C).

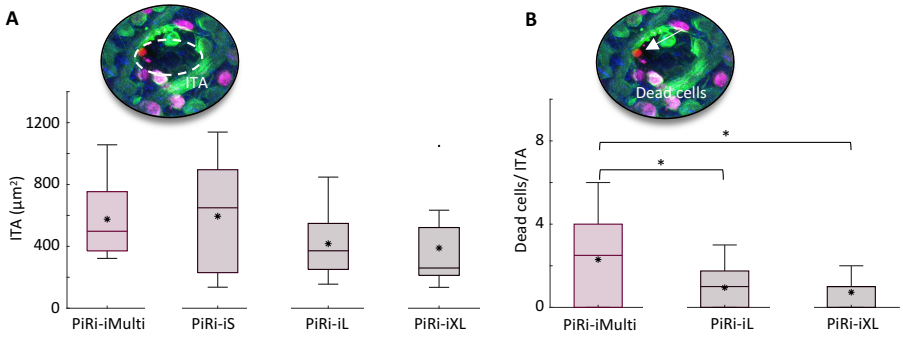

Figure 6.21.: Evaluation of the histological analysis retina samples penetrated with PiRi probes. ITA (A) and dead cell (B) count from the acute insertion footprint comparing various PiRi designs and testing the statistically significant difference between all of them using an unpaired t-test with Bonferroni correction (* $p < 0.05$, ** $p < 0.01$, *** $p < 0.001$, N = 10, 11, 11, 19 for PiRi-iMulti, PiRi-iS, PiRi-iL, and PiRi-iXL, respectively) (modified from [197]).

In contrast, no significant difference was observed in the number of dead cells between the KiRi and PiRi probes, as demonstrated in Figure 6.22B. However, upon dividing the total number of dead cells within an ITA by the number of electrodes included in the corresponding design, the PiRi exhibited a greater number of dead cells in comparison to the KiRi (Figure 6.22D).
In summary, the PiRi demonstrated a greater acute insertion impact in comparison to the KiRis, as evidenced by a larger ITA (divided by the cross-section of the electrode) and a higher density of dead cells per electrode. These results are particularly noteworthy when considering the geometric characteristics of the KiRi and PiRi designs. Specifically, the cross-sectional area of a straight PiRi pillar is approximately 4.5 times smaller than that of a KiRi shank, and the multisite design is 2 times smaller. However, the Young's modulus should also be considered, and it is lower for the KiRis (4.73 vs. 1.7 GPa). Additionally, the KiRis are characterized by a sharp tip, while the PiRis possess a more rounded geometry, which could potentially result in a less seamless insertion. Furthermore, during the insertion tests in agarose, more buckling was observed in the trials with PiRis, which could also have a negative impact on the ITA and number of dead cells.
It is also important to note that the insertion depth varied between the KiRis and PiRis, as illustrated in the 3D plots. The length of the pillar was 65 µm, with the objective of targeting the electrodes in the ganglion cell layer for direct stimulation and electrophysiological recordings. This is approximately 3.5 times smaller than the length of the KiRi shank, which was 225 µm and incorporates multiple electrodes for capturing electrophysiological activity across multiple retinal depths. Consequently, the individual pillars of the PiRi do not penetrate the retina as deeply as a KiRi shank, and dead cells were found in more superficial layers, such as the ganglion cell layer. It should be noted that, in some instances, dead cells were obscured by blood vessels or other cells, potentially influencing the total number of dead cells. Given that the biological samples were explanted, some of the dead cells may have corresponded to cells that died during the preparation of the tissue. Nevertheless, only dead cells aligning with the intraretinal insertion holes were included in the study.

6.3.3. Success of insertion

The success of the insertion was evaluated during the staining experiments, as all probe designs were employed during those experiments under the same conditions. The reliability of the extraction of insertion success is contingent upon the nature of the experiment, which in this case involved a single insertion per retina slice. In contrast, in other experiments, multiple insertions were performed into the same slice, which could potentially impact the recording due to an in-

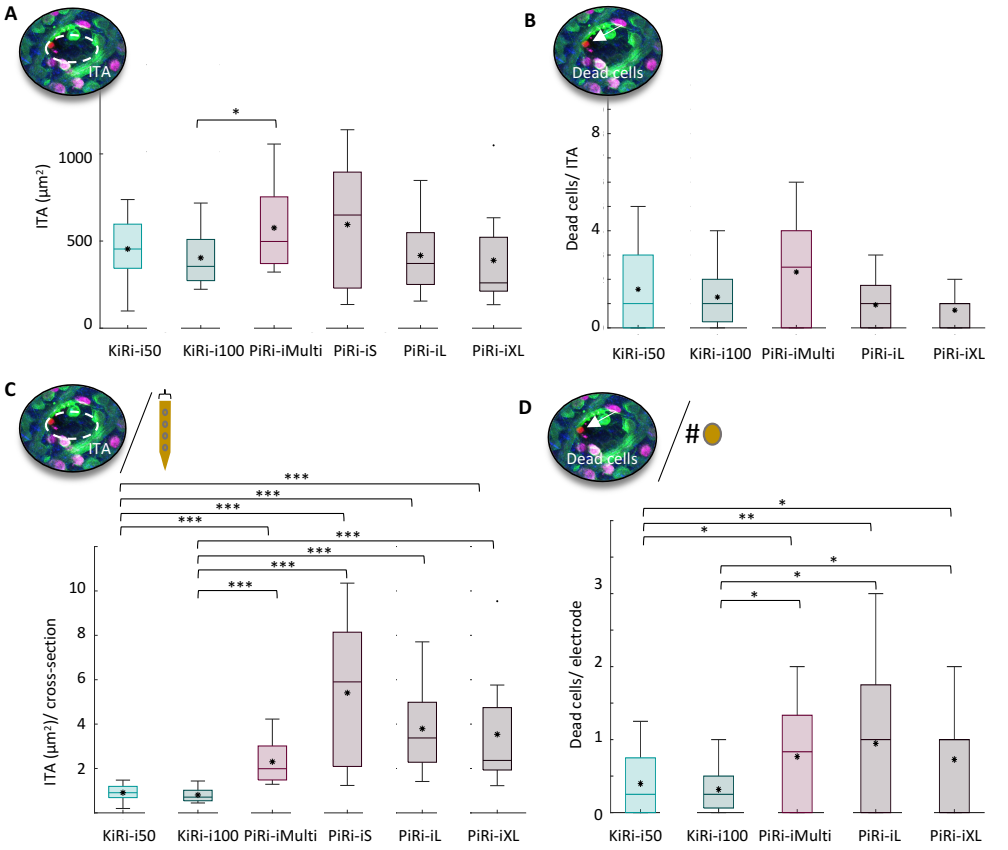

Figure 6.22.: Evaluation of the histological analysis of retina samples penetrated with PiRi probes. ITA averaged over each shank/ pillar of the KiRi and PiRi designs (A) and devided by the cross-section of the corresponding design (C). Dead cell count within each ITA (B) and per electrode (D) of the acute insertion footprint comparing various PiRi with KiRi designs. The statistical significance was tested between the KiRis and PiRis using an unpaired t-test with Bonferroni correction (* $p < 0.05$, ** $p < 0.01$, *** $p < 0.001$, N = 15, 34, 10, 11, 11, 19, for KiRi-i50, KiRi-i100, PiRi-iMulti, PiRi-iS, PiRi-iL, and PiRi-iXL, respectively) (modified from [197]).

creased number of dead cells. Additionally, the retina was observed to be healthy and, in general, more readily captured spikes in healthy tissue, which is less degenerated than in the case of the RCS rat. Figure 6.23A compares the success of insertion when different insertion speeds (v_{in}) were tested using the KiRi-i100 probes. The highest success rate for insertion was observed at a speed of 200 µm/s, with approximately 90% success compared to the use of v_{in} values of 1000 µm/s and 4000 µm/s. In these instances, the insertion success was as low as 50% or even only 37%, respectively. This finding aligns with the observed increase in dead cells and elevated ITA associated with higher insertion speeds. Furthermore, the success rate of KiRi and PiRi probes correlates with the analyzed ITA when evaluated based on the cross-sectional area (see Figure 6.23B). Notably, the KiRi probes and the PiRi-iMulti probe demonstrated higher success rates compared to the single pillar PiRi probes. The PiRi-iS probe showed the lowest insertion success, which is consistent with the previous findings of the stained images, that not all pillars penetrated the retina successfully (see Figure 6.20B).

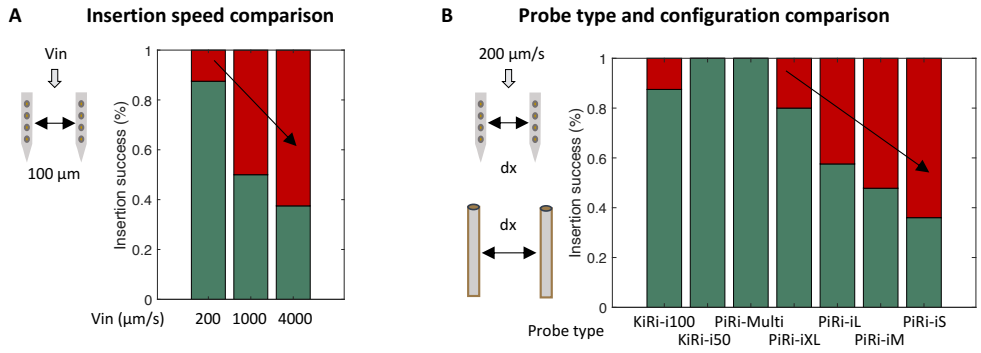

Figure 6.23.: Insertion success of KiRi and PiRi implants. The success rate of the insertion was evaluated for different insertion speeds with KiRi-i100 probes (A) and during experiments examining the acute insertion footprint of different designs of KiRi and PiRi implants (B). The data were normalized by the total number of inserted KiRi shanks or PiRi pillars for each design. Successful insertions are illustrated in green, while unsuccessful insertion attempts are represented in red (modified from [197]).

6.4. Towards *in vivo* applications: Cadaveric tests

Prior to *in vivo* experiments, surgical methods for implantation of 3D MEAs from the epiretinal surface of the retina must be established and tested in cadaveric eyes. As in *in vitro* experiments, the vitreous must be removed (vitrectomy) to allow retinal recordings. For acute *in vivo* experiments, an open-sky approach was chosen, whereas for semichronic applications, a *pars-plana* vitrectomy and implantation of the 3D implants was desired. Cadaveric experiments were either conducted using the facilities in Jülich or at the Department of Ophthalmology, RWTH University Hospital. The cadaveric surgeries were performed with the help of a retinal surgeon, Dr. med. Tibor Lohmann (RWTH Aachen University Hospital). Being the standard approach for vitrectomy, the *pars-plana* vitrectomy offers numerous advantages, including a small incision in the globe and, consequently, the potential to maintain constant intraocular pressure [256]. Conversely, the open-sky procedure results in the complete exposure of the intraocular contents to atmospheric pressure, resulting in the risk of edematous swelling and reduction of static stability [257]. The latter can be mitigated using a Flieringa ring [256]. However, for small animals, such as rodents, adapted ring sizes are not commercially available. Opposed to the elevated risks associated with the open-sky surgery, there are notable advantages. These include enhanced accessibility for surgical instruments to the operative site, the capacity to rapidly transition between instruments and modify their positioning and a better visibility. The surgical field is directly observed through a microscope, facilitating greater accessibility and visibility of anterior fundus structures compared to the closed method [256].

6.4.1. Acute retinal application with open-sky surgery

Open-sky surgical procedure

Prior to the open-sky surgery, the cadaver's head was fixed to the sterile, covered surgical table in a rotated position. A corneal incision was initially performed using a paracentesis (MVR Angled 23G-D) (Figure 6.24A). Subsequently, curved scissors (e.g., Castroviejo corneal scissors, Geuder AG, Reutlingen, Germany) were employed for the removal of the cornea. A complete 360° incision was made, and the corneal tissue was removed. Damaging of the iris must be avoided, as this would have resulted in hemorrhage under *in vivo* conditions, and possibly damage to lens or lens capsule. Subsequently, a lensectomy was performed using the fishhook technique. To

achieve this, a 26G x 1/2" cannula was bent at the tip and inserted into the lens from the anterior lenticular pole. Subsequently, the lens could be elevated and removed (Figure 6.24B). In most cases, the vitreous body was attached to the posterior lenticular capsule, and was thus simultaneously removed. Residual vitreous body was then dislodged and removed. For this step, the use of tweezers (Geuder AG, Reutlingen, Germany) was preferred over the use of a syringe to avoid retinal surface damage induced by uncontrolled vacuum. This is supported by findings in the literature [256]. Subsequently, a saline solution was applied with the objective of preventing retinal detachment (Figure 6.24C). Perfluocarbon liquid (F-Decalin, Fluoron GmbH, Ulm, Germany, 1.93 g/cm^3, 0.08/0.10 µS/cm) is denser than water and effectively stabilizes the choroido-retinal complex. However, it is non-conductive. Therefore, prior to the insertion of a 3D implant, the medium must be exchanged for Polysol (Polytech Domilens, 500/K - 15.93 /16.1 µS/cm). To maintain the visual field for insertion, the eyelids were secured with tape. The cadaver was then transferred from the surgical table to the Faraday cage. The open-sky surgeries were conducted on both WT and diseased animals (RCS rats). Figures 6.24D and 6.24E present the postoperative appearance of a WT and RCS eye, respectively, following open-sky surgery, demonstrating the anterior segment incision site for implant insertion. Subsequently, the 3D implants were inserted through the aforementioned corneal aperture (schematic in 6.24F$_i$ and microscopic picture of an inserted KiRi probe in 6.24F$_{ii}$) with the objective of positioning them in close proximity to the epiretinal surface. This was achieved through careful navigation, taking advantage of the distinctive blood vessels that delineate the retina from the underlying choroid.

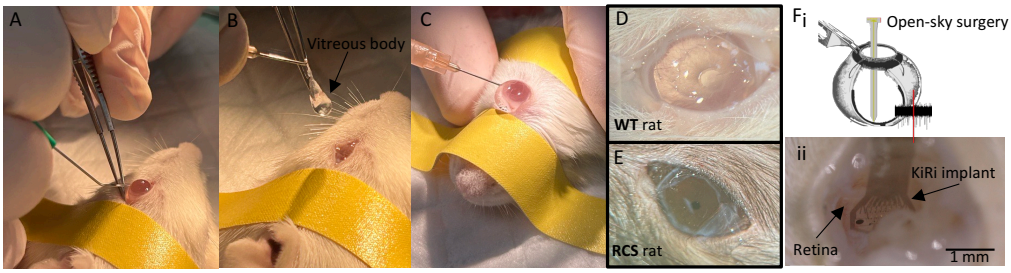

Figure 6.24.: Open-sky surgery for 3D MEA implantation. A) To remove the cornea, an incision was made using a paracentesis knife prior to a 360° dissection of the cornea. B) The lensectomy was performed using a fishhook technique. The vitreous and anterior segment fluids adhered to the lens and were partly removed along with it. C) The eye was filled with saline solution to prevent retinal detachment. The open-sky surgeries were performed with WT (D) and RCS rats (E). Subsequently, the 3D implants were inserted through the small corneal openings (schematic in F$_i$ and microscopic picture of an inserted KiRi probe in F$_{ii}$) with the objective of positioning them in close proximity to the retina (modified from [197]).

Nevertheless, the open-sky surgery presented a number of challenges. The collapse of the eyeball was observed subsequent to the surgical removal of the ocular contents. Prior to conducting open-sky surgeries on rats, the procedure was first tested on a rabbit obtained from a local abattoir, which serves as a larger animal model. To prevent the eyeball from collapsing, a Flieringa ring with a diameter of 12 mm was attached approximately 1 mm distal to the corneal limb. The ring was then sutured onto the eye at four points (12, 3, 6, and 9 o'clock) using a 6-0 Prolene suture (Figure 6.25A$_i$). The relatively large eye of the rabbit (comparable in size to that of a child) permitted the placement of a 23G trocar for saline medium infusion, in a distal and posterior position relative to the Flieringa ring. However, for small animals, such as rodents, the suturing of Flieringa rings is not a viable option. In one attempt, a customized Flieringa ring with a diameter of 6 mm was attached to the eyeball (Figure 6.25A$_{ii}$). However, this procedure did not offer sufficient advantages to justify its implementation. A further challenge was retinal detachment. This phenomenon is often encountered in post-mortem examinations [258]. It was observed in WT as well as RCS rats (Figure 6.25B$_i$ and Figure 6.25B$_{ii}$, respectively, indicated by black and white arrows). However,

further investigation is necessary to ascertain whether retinal detachment would also occur in living animals. Another challenge encountered during the insertion of the 3D implants was limited vision. This was particularly evident in the pigmented RCS eye in comparison to the albino WT eye (Figure 6.25C$_i$ and Figure 6.25C$_{ii}$, respectively). The limited vision proved to be a significant challenge when the insertion rod obstructed the field of view. This was particularly evident when the implant was inserted aiming for the center of the retina (Figure 6.25C$_{ii}$). Conversely, when the shanks of the implant were placed close to the peripheral retina (Figure 6.25D$_i$, black arrow), the shanks were clearly visible prior to insertion and were then observed to penetrate into the retina (Figure 6.25D$_{ii}$, black arrow) using the insertion rod to push the implant. It is recommended that the size of the flexible cable and the shank holder of the KiRi implants be reduced in order to facilitate their passage through the corneal incision. Enhancing the vision could be achieved by utilizing a more flexible microscope and vertically aligning the visual axis with the anatomical axis, or by improving the light source. Another potential solution would be to employ an endoscope. It is also noteworthy that prior to the surgical procedure, the animal's head had been rotated. For the purpose of conducting experiments with living animals, it is therefore essential that the head is fixated in a rotating stereotactic frame to facilitate this procedure. With the objective of conducting experiments with living animals, the results of this experiment should be taken into consideration.

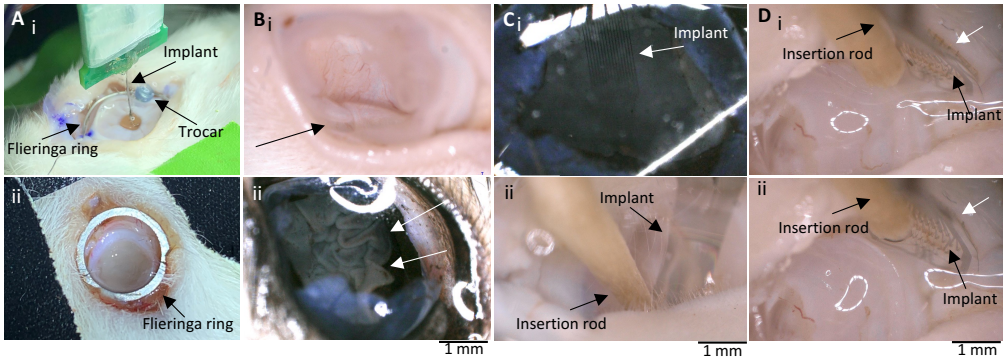

Figure 6.25.: Challenges of open-sky surgery for 3D MEA implantation. A) The utilization of a Flieringa ring to inhibit eyeball collapse was found to be feasible for larger animal models, such as rabbits (i), but presented a considerable challenge when attempting to attach it in rats (ii). B) Retinal detachment was observed in WT as well as in RCS rats. C) Visual obstruction occurred during the insertion process, particularly in the pigmented eyes of RCS rats due to limited light sources (i) and when the insertion rod obstructed the view (ii). D) Conversely, when the implant was inserted into the peripheral retina, it was possible to monitor the positions of the shanks prior to insertion (i) and when they were penetrating the retina (ii) (modified from [197]).

Impedance measurements (Comparison of 2D *in vitro* with 3D cadaveric measurements)

While *in vitro* experiments may provide insight into the location of electrodes within the retina, such as through the observation of the polarity of the LFPs upon light stimulation or the analysis of noise levels or spiking amplitudes, as detailed in section 6.1.1, there is no feedback available when experiments are conducted with cadaveric tissue. However, when developing surgical techniques, it is crucial to ascertain whether the insertion was successful. Consequently, during the cadaveric validation of the open-sky surgical approach, the impedance of the electrodes was measured at varying intraretinal depths, and the resistivity of the retinal tissue at each position was calculated as described in section 6.1.1. These values were then compared with the results from *in vitro* resistivity measurements (section 6.1.1) to provide insights into the success of the 3D implant insertion. The experiments were conducted using RCS rats and the results are presented in Figure 6.26. This figure illustrates that the resistivity trace for both KiRis and PiRis is comparable

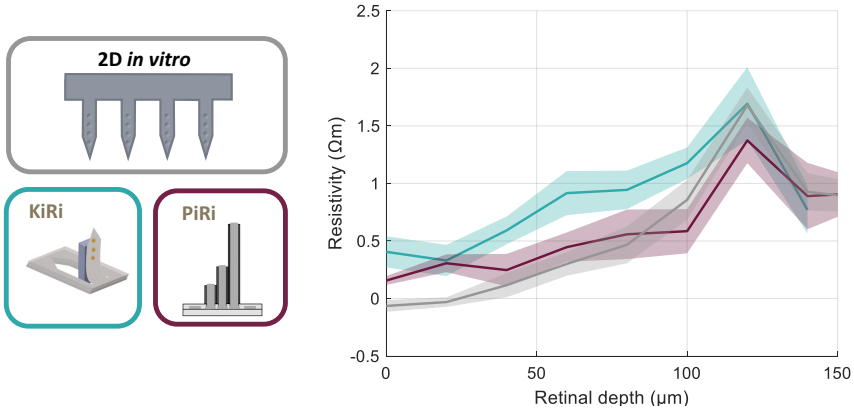

Figure 6.26.: Resistivity of the retina measured *in vitro* and during cadaveric Open-sky surgical trials with KiRis and PiRis (modified from [197]).

to the *in vitro* measurements obtained with 2D probes. Similarly, the resistivity increased as the probes began to penetrate the retinal tissue, reaching a peak of 1.69 ± 0.58 for KiRis (N = 9) and 1.37 ± 0.65 for PiRis (N = 11), which is in a similar range as the peak in the resistivity profile measured with the 2D BiMEAs during *in vitro* recordings. Thereafter, the resistivity decreased as the probe approached the photoreceptor layer. These findings demonstrate that even during challenging open-sky insertion and with restricted visibility due to the optics, a successful insertion was achieved.

6.4.2. Semi-chronic application: *Pars-plana* implantation

In order to establish a *pars-plana* implantation procedure for semi-chronic recordings with 3D implants, cadaveric rabbits obtained from a local abattoir were used. For this purpose, KiRi implants were fabricated containing flaps for handling (Figure 6.27A). As the shank holder of the PiRis possess enough space, an additional probe design with flaps was not needed. The *pars-plana* vitrectomy was performed similarly to the implantation of the VLARS epiretinal implant [259]. For the insertion of the 3D implants, the 3D-PLAPS insertion device was used [260].

To facilitate access to the surgical site, the eyelids were retracted laterally with the aid of blepharostats. First, a lensectomy was conducted via a corneal incision using a standard phacoemulsification technique (Ruck Ophthalmologische Systeme, Eschweiler, Germany). For *pars-plana* vitrectomy, three 23-gauge scleral incisions were made for the purpose of facilitating infusion, the placement of the light source, and the introduction of vitreoretinal surgical instruments (Figure 6.27B). For the infusion, buffered saline solution (BSS, Alcon, Fort Worth, USA) was used. To facilitate the insertion of the implants into the anterior chamber, the 3D-PLAPS implantation device was positioned and sutured into an enlarged corneal opening (Figure 6.27C). Subsequently, the 3D implants were advanced through the channel and maneuvered with the assistance of surgical forceps (Geuder AG, Heidelberg, Germany) (Figure 6.27D). To facilitate retinal attachment and ensure the secure positioning of the 3D implants at the posterior pole, perfluocarbon liquid (F-Decalin, Fluoron GmbH, Ulm, Germany, 1.93 g/cm^3, 0.08/0.10 µS/cm) was injected into the eye. The position of the 3D implants within the eye could be adjusted using vitreoretinal surgical forceps (Geuder AG, Heidelberg, Germany). Subsequently, observation of the implants through the cornea demonstrated that they had been successfully inserted through the implantation device (Figure 6.27E,F). While PaC is transparent, the KiRi implant was clearly identified due to its higher

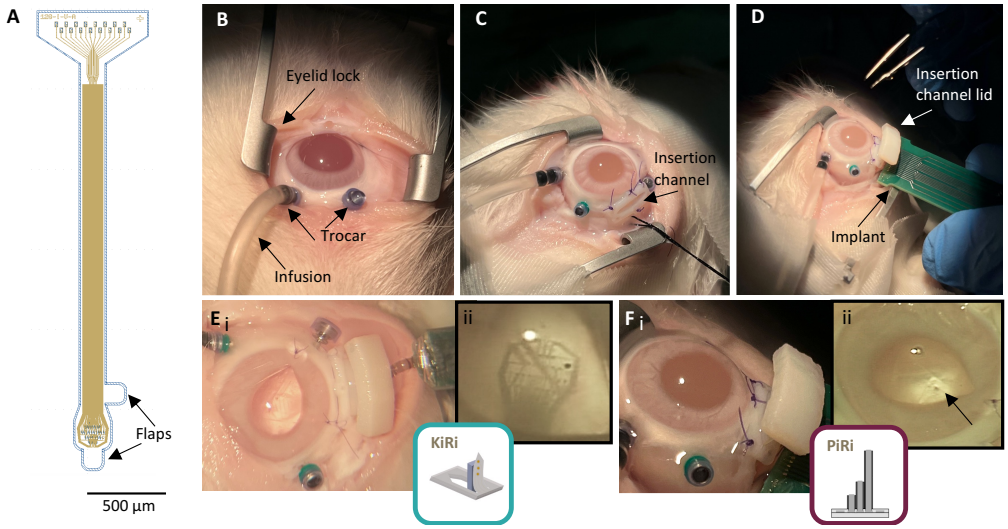

Figure 6.27.: ***Pars-plana*** **implantation of 3D MEA in cadaveric rabbit eyes.** A) An adapted probe design with flaps was utilized, facilitating handling during surgery. B) The implementation of an eyelid lock was done to improve access to the surgical site. Three 20-gauge scleral incisions were created for the purposes of infusion, the placement of the light source, and the introduction of vitreous surgical instruments. C) The insertion channel (3D-PLAPS device [260]) was introduced through a corneal incision and sutured. D) The 3D implants were then inserted into the eye via the insertion channel and maneuvered within the eye using surgical tools. Following the positioning of the implants, they were visible through the cornea (KiRi in E_i and zoom-in E_{ii}, and PiRi in F_i and zoom-in F_{ii}, black arrow pointing at the reference electrode) (modified from [197]).

metal content (Figure 6.27E_{ii}). This was more challenging for the PiRi implants, which contain fewer feedlines, and thus the reference electrode of the PiRi implant is indicated in Figure 6.27F_{ii} by a black arrow.

During the *pars-plana* implantation, difficulties were encountered with the trocar system, which exhibited a tendency to become dislodged when subjected to the forces exerted by surgical instruments. In further experiments, an approach without trocars should be tested. Another challenge was encountered during the implantation procedure. The implants were manually inserted and subsequently secured to the lateral aspect of the rabbit head with adhesive tape. Subsequently, the position within the eye was adjusted using tweezers. However, impedance measurements could not be taken due to difficulties in establishing a connection between the measurement system and the probes. This should be done in future implantations to confirm the insertion. Nevertheless, the implantation through the insertion device was feasible. It would be beneficial to improve the setup for upcoming experiments. It is necessary to utilize a holder for the implants. Furthermore, the integration of a micromanipulator could facilitate precise implant movement. Additionally, a system for connecting the potentiostat to the probes for impedance measurements is essential. Furthermore, there is a need to determine whether retinal tacks are necessary for implant fixation or whether the penetrating shanks are sufficient for this purpose.

6.5. Summary and outlook

The employment of KiRi and PiRi electrodes during *in vitro* retinal recordings was successfully accomplished. Their capacity to record 3D activity provided insights into the underlying functionality of retinal degeneration, offering a comparative advantage over 2D surface MEAs. An investigation into the pathological oscillations exhibited by RCS rats is of considerable value in the development

of retinal prostheses. This is due to the fact that such oscillations have been shown to impede the efficacy of electrical stimulation, a phenomenon that has also been observed in the rd10 mouse model [78][248].
The resistivity measurements facilitated enhanced intraretinal guidance during the implantation of 3D intraretinal probes. Given the flexible nature of the implant and the viscoelastic properties of the retina, the step sizes do not directly correspond to the insertion depths. This is due to the fact that the tissue is subject to dimpling during the insertion process. As demonstrated in section 6.1.1, the intraretinal positioning can be guided by the electrical activity recorded by the electrodes, as well as by the resistivity of the retinal layers. This methodology was utilized during the cadaveric trials. The insertion of KiRis and PiRis was successfully completed during cadaveric trials of open-sky, as evidenced by the resistivity measurements. In order to proceed with subsequent trials, it is imperative to enhance the quality of the light source and the illumination of the surgical site. Furthermore, it may be advantageous to reduce the dimensions of the KiRi implant, thereby facilitating its insertion through the corneal cavity. In subsequent trials, it would be advantageous to conduct resistivity measurements during *pars-plana* implantation. Moreover, it would be advantageous to ascertain whether implantation can be performed without 3D PLAPS, with the objective of closing the eye for chronic implantation over an extended period.
Next, the influence of the KiRi and PiRi insertion was evaluated. The results demonstrated that the total number of dead cells was comparable in both cases. Nevertheless, the relative ITA with regards to the cross-section of the probes as well as the dead cells per electrode were higher for the PiRis. This leads to the conclusion that eventually, upscaling and increasing the channel count may prove to be a more feasible option for the KiRis.
It can thus be concluded that the 3D electrodes provide a valuable tool for advancing the understanding of the retina, which is of great importance for the development of functional visual prostheses.
To further investigate these findings, the implementation of a bidirectional stimulation strategy should be considered in future studies. In previous works, an intraretinal bidirectional communication strategy was developed, which couples electrically with the inside of the retina [78][155][156]. This strategy demonstrated the feasibility of simultaneous recording and stimulation the retina using 2D intraretinal implants. It is thus urged that 3D neural probes (encompassing both penetrating and surface electrodes) be subjected to testing during electrical stimulation and 3D recordings, with a view to further analyzing the current spread upon stimulation and the spread of electrophysiological response.
The analysis of the performance of the KiRi and PiRi electrodes, in comparison with existing literature on electrical stimulation, demonstrated that electrodes coated with PEDOT:PSS are capable of delivering sufficient pulses to stimulate intraretinally [156][245][261][262]. Nevertheless, it is necessary to ascertain whether the CIC measured intraretinally remains sufficiently high, as it was observed to be reduced, for example, by approximately 20% using implanted IrOx electrodes [156].
During electrical stimulation of the retina, it is differentiated between network and direct response: Indirect stimulation of ganglion cells is achieved by stimulating bipolar cells that in turn activate postsynaptic ganglion cells. The rationale for using indirect stimulation is that the stimulus will be processed and refined by the remaining retinal circuitry to produce a more natural ganglion cell output [262]. However, the success of stimulation of the ganglion cells might depend on the state of retinal degeneration. While for network stimulation, the stimulation threshold was observed to increase with the state of degeneration in the mouse model [156][263], the ganglion cells remained directly excitable [264]. In light of the remodeling process of the retina in response to photoreceptor death and the increased stimulation threshold, direct stimulation of the ganglion cells may prove to be a more viable approach. Asymmetric pulses or alternative waveforms such as sinusoidal stimulation, as well as deep learning algorithms were recently employed to

find optical stimulation parameters enhancing the efficiency and selectivity of electrical stimulation [265][266][267][268][269]. It is recommended that these techniques be utilized and investigated with KiRi and PiRi electrodes. It is essential to conduct further investigations that consider not only the explanted retina and measure the response of the retinal network, but also to investigate the visual pathway from the retina to the brain. This can only be achieved during *in vivo* trials. Therefore, during acute *in vivo* settings, the objective should be to evoke potentials in the retina using electrical stimulation and map the neuronal activity recorded in the cortex (Figure 6.28). This will necessitate two surgeries: An open-sky surgery to implant 3D KiRis or PiRis for electrical stimulation of the retina and a subsequent craniotomy to implant µECoGs for electrophysiological recordings in the cortex (as previously demonstrated in [66]).

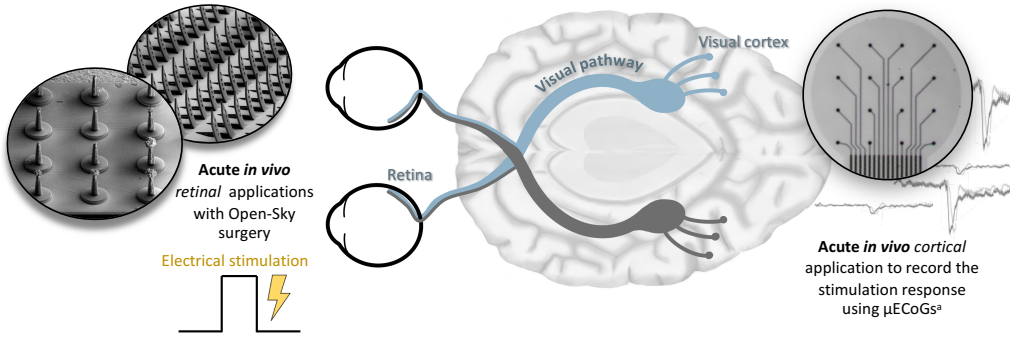

Figure 6.28.: From the retina to the brain. Stimulation of the retina using KiRis or PiRis and recording the stimulation response, which traveled via the visual pathway to the visual cortex, using µECoGs (image (a) from [66]).

7. Cortical applications

This chapter aims to demonstrate the impact of 3D neural probes on understanding pathological and healthy activity across a variety of CNS regions and to highlight their versatility in capturing neural dynamics at differing spatial scales. To this end, the use of flexible KiRis and PiRis for cortical applications will be presented.
In recent decades, the mouse has become a prominent model organism in the field of brain research. The utilization of a mouse model is advantageous for several reasons. The brain is reduced in size, the cortex is characterized by a smooth surface, and a range of sophisticated genetic instruments can be employed to analyze connectivity and manipulate activity in cortical circuits. In addition, there is a close evolutionary similarity with humans in terms of ion channels, synaptic receptors, and other crucial molecular elements of the brain. Consequently, a number of studies have demonstrated that the fundamental response properties observed in humans are also present in the mouse. With regard to the visual cortex, the existence of essential characteristics of the human visual network - including functional specialization, the segmentation of sensory information into parallel processing streams, and evidence of active vision - in the mouse underscores its potential as a model of early visual processing [270][271].
However, the existence of analogous similarities at the level of cortical neuronal circuits is still under investigation. In their study, Loomba et al. compared the synaptic connectivity of mouse and human/macaque cortex, concluding that the principal cells of the cerebral cortex (pyramidal neurons) exhibited a comparable inhibitory-to-excitatory input balance between the species. Despite the significantly larger size of human cells compared to mouse counterparts, human cells do not receive more synapses. A notable distinction in network complexity was identified, characterized by an expansion of the interneuron-to-interneuron network in humans, accounting for nearly an order of magnitude more connections compared to mice [270]. Hodge et al. utilized single-nucleus ribonucleid acid (RNA) sequencing analysis to conduct a systematic investigation of cell types in the human and mouse cortex. Their findings revealed discrepancies between human and mouse cell types, including alterations in proportions, laminar distributions, gene expression, and morphology. These variations are likely to impact microcircuit function [272]. These studies underscore the necessity to analyze the human brain in conjunction with that of model organisms to avert failures in translation studies. The extent to which the system shares structural and functional principles with higher-order mammals determines the usefulness of the mouse model.
Thus, in this study, *in vitro* models of epilepsy were investigated using human brain slices, to demonstrate the impact of 3D neural probes on understanding pathological activity. Additionally, *in vivo* studies were performed in mouse models to highlight the ability of 3D neural probes to capture neural activity at the neuronal level under different conditions. Responses to somatosensory and visual stimuli were recorded in acute *in vivo* conditions in the anesthetized and awake brains of mice, respectively.
This chapter is partly reproduced from the following publications:

- **M. Jung**, J. Abu Shihada, S. Decke, L. Koschinski, P. S. Graff, S. Maruri Pazmino, A. Höllig, H. Koch, S. Musall, A. Offenhäusser, V. Rincón Montes. "Flexible 3D *Kirigami* Probes for In Vitro and In Vivo Neural Applications". Advanced Materials 2025, DOI: 10.1002/adma.202418524

- J. Abu Shihada* and **M. Jung***, S. Decke, L. Koschinski, S. Musall, V. Rincón Montes, A. Offenhäusser. "Highly Customizable 3D Microelectrode Arrays for In Vitro and In Vivo Neu-

ronal Tissue Recordings". Advanced Science 2024, DOI: 10.1002/advs.202305944 (**Equal contribution*)

7.1. *In vitro* human brain slices

Epilepsy research has traditionally relied on intracranial EEG, which is recorded from the surface of the brain with widely spaced electrodes. To enhance the precision of seizure localization, researchers have employed stereoelectroencephalography (sEEG) implanting high-density neural probes in deeper layers of the brain [273], or µECoGs [20][58]. A comprehensive 3D map of brain regions linked to epilepsy could enhance surgical efficacy and facilitate the identification of neurostimulation targets. However, the aforementioned state-of-the-art techniques lack the capacity to access the 3D space of neural tissue. In contrast, 3D implants possess this capability. By capturing the intricacies of neural tissue, these implants may advance the diagnosis and treatment of pathological behaviors and eventually enhance the quality of life for affected patients.

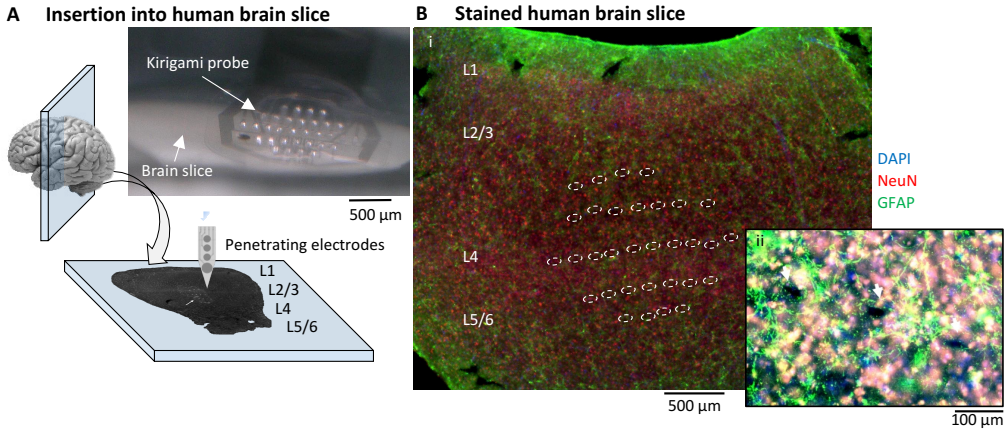

Figure 7.1.: Insertion of a KiRi probe into a human brain slice. A) Insertion of a kirigami probe into a human brain slice inside a perfusion chamber with constant inflow and outflow of aCSF. The brain slice is submerged in aCSF and is supported by a doughnut-shaped filter paper and fixed on a PDMS supporting pillow with insect pins, while the KiRi probe is inserted perpendicular to the tissue. B) Immunohistological staining for NeuN (red), GFAP (green) and DAPI (blue) showing the insertion sites of a KiRi probe (modified from [177]).

The acute and cultured brain slices were obtained from recessed access cortical tissue of patients with epilepsy or tumor at the University Hospital Aachen (Uniklinik Aachen) as described in section 3.4.1. Due to their thickness of 250 - 300 µm, which is similar to the retina, KiRiRet probes with a length of 225 µm and straight PiRi probes with a length of 65 µm were employed.
Human brain slices were embedded in aCSF and placed in a perfusion chamber of the *in vitro* setup, as previously described in section 3.4.1 and shown in Figure 7.1A. The 3D probes were inserted using the same protocol as that employed for the explanted retina. This involved first positioning the device on the surface of the brain slice using a micromanipulator. This was followed by the application of gentle downward pressure by a metal rod attached to a second micromanipulator. The probe was inserted in a manner that allowed individual KiRi shanks or PiRi pillars to span multiple cortical layers. The placement was validated in two samples via immunohistochemical staining, as described in section 3.4.1, which revealed the position of the shanks across layers 2/3 to 5/6 of the cortex (see Figure 7.1B). This configuration enabled the acquisition of neural activity data at varying tissue depths and layers.

7.1.1. Stimulation with high potassium

The objective of the preliminary experiment was to substantiate that the electrical signals recorded by the electrodes represented genuine neural activity. To this end, spontaneous activity was initially recorded and then a physiological response was induced through the elevation of the K^+ concentration of the aCSF from 3 mM to 20 mM. This concentration has been demonstrated to elicit a depolarization block [157]. The latter was observed shortly after adjusting the K^+ concentration to 20 mM, as evidenced by a pronounced increase in spiking activity, accompanied by larger spike amplitudes and higher firing rates (Figure 7.2A). Using KiRi probes it was observed that the increase in firing is not a local event but rather spread throughout the brain slice as the signal was recorded with different shanks (Figure 7.2B). It was observed, that the start of the depolarization block did not occur at the same time across the shanks, but rather with a time-shift of several seconds, while the firing rate and amplitudes of the spikes were also varying. Similar observations were done with PiRi probes as shown in Figure C.3.

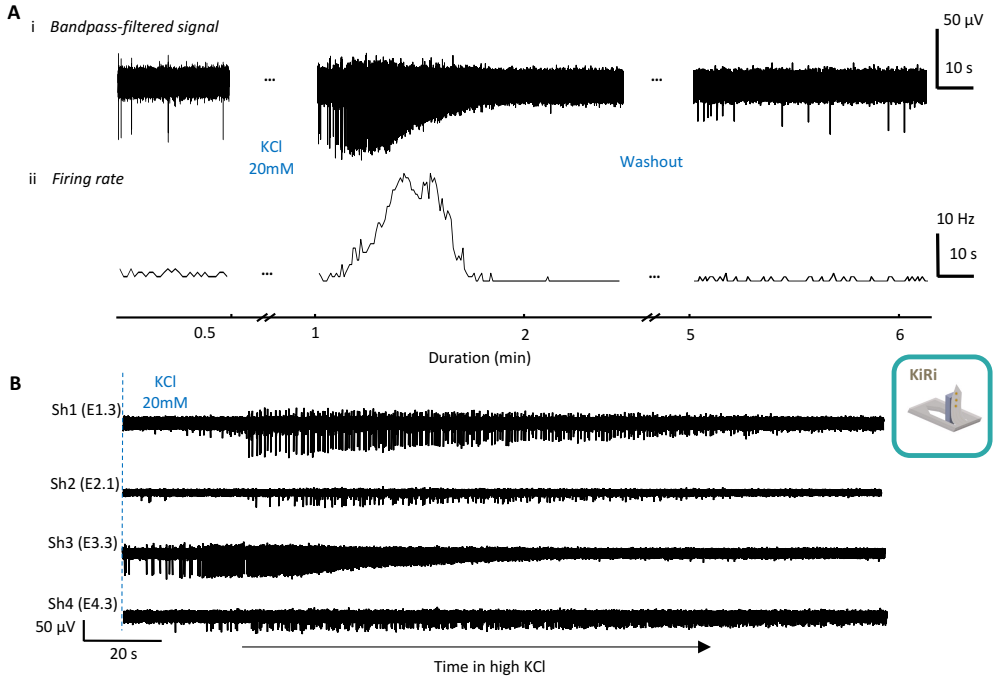

Figure 7.2.: Inducing a depolarization block with modified aCSF (high KCl). A) Example of a human brain slice response to treatment with a high extracellular potassium concentration of 20 mM measured with KiRi probes. Bandpass-filtered data (i) and the firing rate along the complete recording (bin size = 1 ms) (ii), show that the cells reach a depolarization block under the treatment and go back to baseline activity after washout (modified from [177]). B) The depolarization block was observed to occur at different time points across the shanks.

7.1.2. Inducing seizure-like activity

As has been previously reported by other researchers, SLEs can be triggered by pharmacological manipulation [182]. An SLE is defined by three key characteristics: a sudden and transient alteration in neural activity that is distinct from the background activity, a temporal and spectral evolution of discharges, and a return to baseline activity [58][274]. During SLEs, ictal discharges are observed, with increased spectral power in a frequency range from 1 to 100 Hz, HFO in the

250 to 350 Hz range, and increased MUA above 300 Hz. Given the thickness of the explanted human brain slices, which ranged from 250 to 300 µm, the KiRiRet probes with a shank length of 225 µm, which contain both penetrating and surface electrodes, were employed for the purpose of electrophysiological recordings. PiRi electrodes were not used during this study.

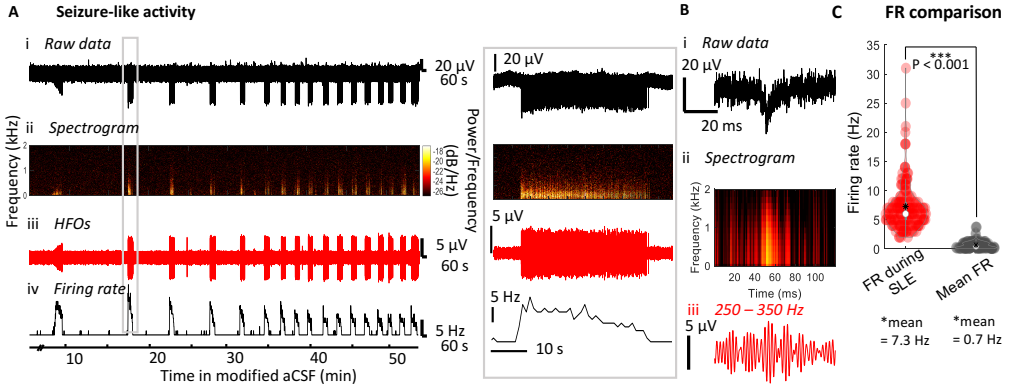

Figure 7.3.: Seizure-like activity in a human brain slice. A) Electrophysiological activity upon treatment with modified aCSF (8 mM K^+ and 0.25 mM Mg^{2+}), raw data (i), spectrogram (ii), HFOs filtered at 250 – 350 Hz (iii), and firing rate traces (iv). B) Illustrative examples of an ictal-like discharge, comprising raw data (i), a spectrogram (ii), and filtered HFOs (iii). C) A comparison of the firing rates during SLEs and those averaged over the entire trace revealed a statistically significant difference ($p < 0.001$, using a paired t-test with N = 153 SLEs) (modified from [177]).

In a second series of experiments, the propagation of epileptic activity within six human brain slices was investigated by modulating the extracellular ion concentration to elicit epileptic activity patterns. In accordance with the methodology outlined by Pallud et al. [182], the aCSF medium was modified by increasing the K^+ concentration to 8 mM and reducing the Mg^{2+} concentration to 0.25 mM. Following the introduction of the modified aCSF medium, the occurrence of SLEs was observed. Figure 7.4A of the accompanying document illustrates a data trace from one electrode. In addition to the elevated firing rates, low-frequency discharges and HFOs were observed during the SLEs. Figure 7.4B illustrates a close-up of one of the IDs during SLEs. The recorded electrophysiological signals were predominantly attributed to frequencies below 1 kHz, as evidenced by the increased spectral power. The duration of SLEs was determined by a sustained increase in the firing rate of spiking activity, which exceeded the baseline firing rate (evaluated by the median) and ranged from 100 to 3000 Hz. The mean firing rate during a SLE was 7.8 ± 5.2 Hz, which was significantly higher than the overall mean firing rate of 0.7 ± 0.7 Hz (Figure 7.4C). SLEs were observed in five out of six slices from three different patients. The mean duration of an increased firing rate during SLEs was 51.4 seconds, with a standard deviation of 73.5 seconds (N = 88 SLEs). These events occurred repeatedly, with intervals averaging 144.2 ± 170 s. The initial inter-SLE periods were as long as 809 s, but decreased over time to as short as 6 s (see Figure 7.3). The observation of SLEs commenced after an average of 33.7 ± 13.7 min of perfusing the modified aCSF across six slices. A summary of the observed features indicates that the change in activity upon modified aCSF exhibited characteristics of epileptic activity that matched the temporal and spectral characteristics described in earlier studies [182].

Utilizing the spatial arrangement of electrodes within the KiRi probe, a comparison was conducted between the recorded data from surface and penetrating electrodes. This analysis revealed the presence of ictal-like discharges that were detected by electrodes located inside the neural slice, thereby enabling the identification of the onset of SLEs within shanks. Figure 7.4A illustrates a representative recording and Figure 7.4B shows the change of firing rate of each electrode during the complete recording, which reveals that SLEs occur at different time points in each

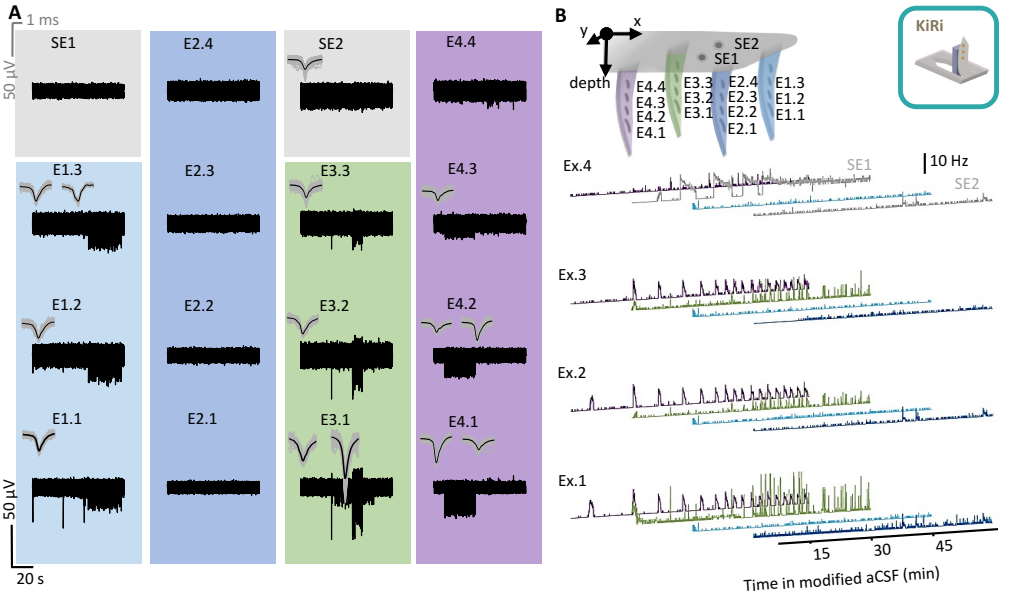

Figure 7.4.: Seizure-like activity in human brain slice recorded with KiRis. A) Exemplary snapshot of a recording trace where unsynchronized SLEs were observed in the electrodes of shank 1, 2, 4 indicated by the increase in spiking activity. B) 3D map of firing rate upon treatment with modified aCSF. The electrodes of four shanks (dark blue, light blue, green, violet) and the surface electrodes (grey) each capture SLEs at different time points (modified from [177]).

shank as revealed by the change of spiking activity. In Figure 7.4A, the onset of an SLE in shank 4 (pink column) occurred at approximately 160 µm (centered on a 25 µm diameter recording electrode) below the surface electrode. The spread of the SLE was observed to occur vertically over a distance of approximately 60 µm, based on the center-to-center distance between E4.1 and E4.3. This provides further evidence of the ability of penetrating 3D kirigami MEAs to detect SLEs within the tissue parenchyma that would otherwise be undetected by surface electrodes. Spike detection and sorting of the bandpass-filtered data demonstrated the capacity to record the spiking activity of various neurons, including MUA and SUA, with a maximum SNR of 200 (average of 6 ± 3.2) with average maximum spike amplitudes of 82.6 ± 9.2 µV. Additionally, each penetrating shank was capable of capturing up to two distinct units during an SLE, with additional units identified outside of these events (see Figure 7.4A and Figure C.5 for further details).
Moreover, as demonstrated by analyzing the cross-correlation of the traces captured by the different electrodes, SLEs captured across individual shanks separated by 100 µm and 300 µm in the x and y axes, respectively, were observed to be independent (see Figure C.4A). In contrast, cross-correlation of electrodes within the same shank, such as shank 4 (see Figure C.4B$_i$), exhibited a high degree of correlation, whereas the cross-correlation with electrodes on neighboring shanks was low. Similarly, the surface electrode SE2 was not significantly correlated with any of the electrodes on the penetrating shanks, nor with the other surface electrode SE1 (see Figure C.4B$_{ii}$). These findings indicate that the epileptic events captured were confined to individual shanks rather than spreading across all cortical layers. This activity pattern was observed in all the recorded slices, indicating the presence of independent local networks across shanks.
Therefore, the data obtained from the 3D kirigami MEAs substantiates the occurrence of distinctive SLEs at varying time points within human brain slices. 3D recordings permitted the capture of independent SLEs by neighboring shanks, thereby underscoring the complexity of such activity.

These findings highlight the necessity of investigating neural behavior not only with 2D MEAs on the brain surface but also through 3D sampling. It is notable that the slicing procedure has the potential to damage cells at the surface of the slices. In comparison to planar MEA systems, the penetrating KiRi probes offer a notable advantage due to their incorporation of both surface and penetrating electrodes. This configuration permits the documentation of neural activity not only on the surface of the tissue but also within the slice parenchyma and throughout the tissue volume. The deployment of 3D kirigami MEAs in human brain slices facilitates a more comprehensive understanding of pathological activity patterns, enabling the localization of SLE onset, the tracking of its spread through localized networks, and the observation of neural activity from other local networks.

7.2. *In vivo* cortical experiments

In addition to *in vitro* applications, 3D MEAs are promising tools for *in vivo* brain recording, especially in the cortex. The design and electrode density of both probes can be flexibly adapted to the spatial layout of different brain regions, which allows for customized applications that require observing the spread of neural activity across different cortical layers and brain areas. Such cross-layer and cross-regional recordings could be of great value for various clinical applications. The KiRi and PiRi implants were both implanted in the somatosensory cortex of mice, and stimulation experiments were conducted on anesthetized animals. Additionally, KiRi probes were implanted into the visual cortex of mice, and visual stimulation experiments were performed on awake animals.

7.2.1. Surgical approach and insertion of 3D implants into the cortex

Widefield imaging prior to the surgery

The objective of the *in vivo* experiments was to create 3D recordings by placing the electrodes in multiple cortical layers and across brain regions. Accordingly, prior to the surgical procedure and electrode implantation, wide-field imaging was conducted via the cleared intact skull. The mice were transgenic animals that expressed the calcium indicator GCaMP6s in all excitatory neurons, thus enabling the measurement of alterations in neural activity via alterations in fluorescence intensity during wide-field imaging [275]. This approach facilitated the identification of the optimal implantation site prior to surgery. Thus, the mice were placed into a custom-built setup, as detailed in section 3.4.2. The hind and forepaw were stimulated using the custom-built stimulator. The spread of the stimulus was thereby visualized, and the areas for implantation in the somatosensory cortex were selected.

Subsequently, the somatosensory hindlimb area exhibited the most robust average neural response to brief mechanical stimuli applied to the left hindlimb in the presence of isoflurane anesthesia (N = 50 trials). To identify the precise location for probe placement, a high-resolution vessel image (Figure 7.5A) was utilized. To obtain a 3D recording from multiple cortical regions *in vivo*, the shanks of the probe were placed within the somatosensory hindlimb region, with the border of the widefield response serving as a guide. In comparison to the averaged hindlimb stimulation response (Figure 7.5B$_{i,ii}$), the averaged forelimb stimulation response (Figure 7.5C$_{i,ii}$) was observed to be overall weaker in the widefield imaging.

Surgery for acute recordings and tactile stimulation

During the surgical procedure the anesthetized mice were placed in a stereotactic frame with their body temperature monitored and maintained at 37 °C using a heating pad. Anesthesia was induced with 1–5% isoflurane (Figure 7.6A). Following an initial incision, the skin covering the skull was carefully elevated and displaced laterally. In order to facilitate low-noise signal recordings, a reference pin was positioned on the cerebellum. A head bar was then fixed on the mouse head using dental cement (Figure 7.6B). Subsequently, a craniotomy of approximately 4 mm in diameter was conducted on the left or right hemisphere. This was achieved by utilizing a biopsy punch to delineate the precise location and an orthopedic drill (Eickemeyer, Germany) to create an opening in the skull (Figure 7.6C). The skull was then removed with great care using tweezers, after which the brain was exposed (Figure 7.6D,E). Following this, the exposed dura was treated and rinsed with PBS. Subsequently, an initial incision was made at the edge of the craniotomy window. This was followed by a dural incision, which was performed with a hooked needle in order to gain access to the cortex.

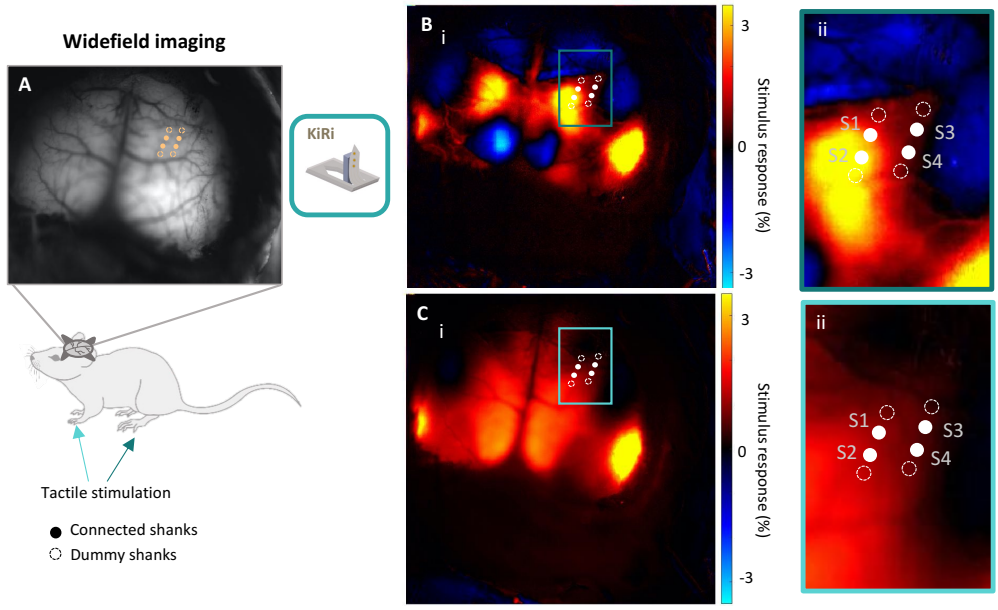

Figure 7.5.: Widefield imaging of the mouse cortex prior to KiRi implantation. To identify the optimal positioning of the shanks across different brain regions, widefield imaging was employed to ascertain cortical responses to tactile stimulation. A high-resolution vessel image was obtained to ascertain the probe location. Upon stimulation of the limbs, widefield images were captured. The images in B_i and B_{ii} illustrate the stimulation of the hind paw, while those in C_i and C_{ii} illustrate the stimulation of the fore paw (modified from [177]).

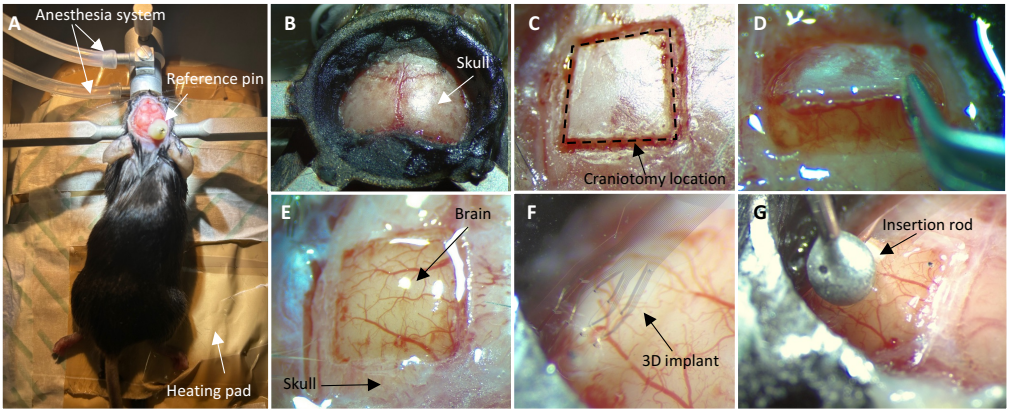

Figure 7.6.: Surgical procedure for *in vivo* cortical applications with mice. (A) The mice were placed on a heating pad and anesthetized via isoflurane. A reference pin was affixed to the cerebellum. B) A head bar was attached to the skull prior to commencing the craniotomy. The location of the craniotomy was initially marked using a biopsy punch (C), then meticulously drilled and the skull was removed using tweezers (D) to expose the brain (E). Subsequently, the 3D implants were placed with precision using a micromanipulator, and an insertion rod was employed to insert the implants into the neural tissue (F) (modified from [177]).

Insertion of 3D penetrating implants

The 3D probes were placed with precision on the desired position of the dried cortex using a 3-axis micromanipulator (MTM-3, World Precision Instruments, Germany) (Figure 7.6F). A metal rod,

fixed on a second micromanipulator (uMp4, Sensapex), was employed to facilitate penetration of the tissue by the implant. The insertion into the cortex was conducted with incremental step sizes of 100 - 250 µm and a velocity of 200 - 4000 µm/s. The insertion of 3D implants into the cortex of mice was assessed via visual inspection, electrophysiological recordings of spiking activity and tissue stainings.
Prior to and subsequent to the insertion of the KiRi and PiRi probes into the cortex of mice, a visual inspection was conducted using an optical microscope (Figure 7.7). This served to provide an initial assessment of the success of the implantation procedure. Therefore, particular attention was paid to the positioning of the shanks and pillars. When the KiRi and PiRi probes were placed on the surface of the exposed cortex, the shanks and pillars were clearly visible (Figure 7.7A). Conversely, when they were inserted, neither the KiRi shanks nor the PiRi pillars were visible, indicating that they had been successfully positioned within the neural tissue (Figure 7.7B).

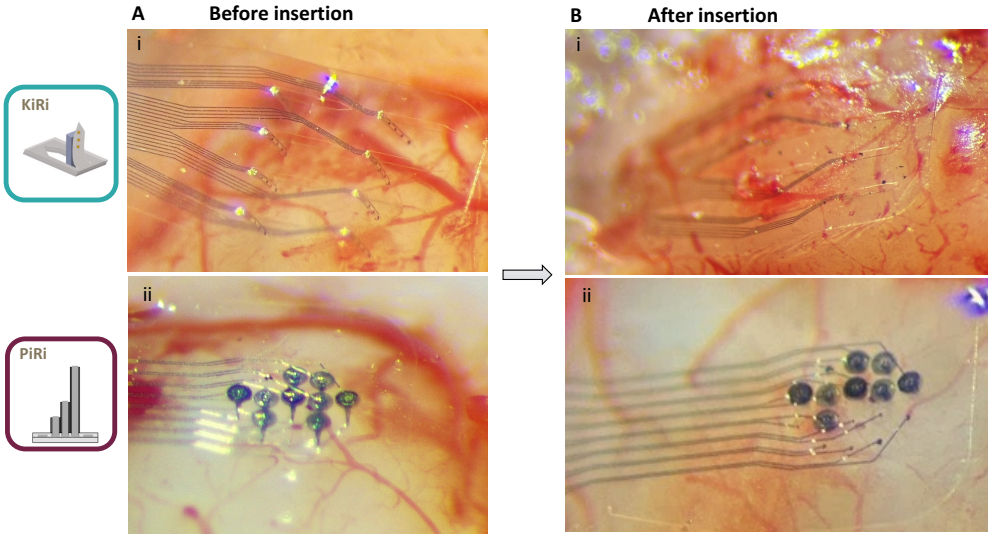

Figure 7.7.: Optical inspection prior to (A) and subsequent to (B) the insertion of KiRi and PiRi probes into the cortex of mice. A) Following the removal of the dura mater, the KiRi (i) and PiRi (ii) probes were positioned on the surface of the cortex. The shanks and pillars are clearly discernible on the exposed cortical surface. B) Using a micromanipulator, they were precisely inserted into the cortex. At this point, neither the KiRi shanks (i) nor the PiRi pillars (ii) are visible, as they have been successfully positioned within the neural tissue.

Figure 7.8 provides an illustrative example of the recorded signals with respect to the time point of insertion of a PiRi implant. To differentiate between the spiking activity of individual neurons and the low-frequency LFP signals, the raw signal was filtered for high- and low-frequency bands (Figure 7.8A$_{i-iii}$). Immediately post-insertion, high-amplitude spiking activity reaching approximately 200 µV was observed. The firing rates and amplitudes of these spikes exhibited a high initial value, which subsequently decreased. Concurrently, low-frequency activity remained largely unaltered. This evidence indicates that the pillars were capable of traversing the cortex without causing any substantial disruption to the neural tissue or the ongoing activity patterns. Furthermore, it suggests that they can be employed to effectively record spiking activity from cortical neurons. Following the retraction of the insertion rod, the 3D implants remained securely embedded within the tissue while simultaneously capturing the spontaneous spiking activity of individual cortical neurons from multiple electrodes (Figure 7.8B). Spike sorting revealed that each electrode recorded the activity of multiple neurons simultaneously, including multi-unit recordings (Figure 7.8B$_i$, orange spikes, Figure 7.8B$_{iii}$ pink spikes) as well as potential individual neurons (green spikes in Figure

7.8B$_{i-iii}$).
Comparable observations were made during the insertion of a KiRi probe monitoring the intraoperative recording of electrophysical signals of the brain, ensuring the precise positioning and penetration of all shanks within the cortex. An illustration of the occurrence of spiking activity immediately following insertion is provided in Figure 7.9, where two insertion steps of 100 µm were performed after the placement of the insertion rod. In addition, Figure C.6 shows an example recording of eight shanks with four electrodes each during insertion. The insertion of a KiRi implant into the cortex was accompanied by an increase in the amplitude of spiking activity after the first seconds after insertions (Figure 7.9B, C.6B) or by a notable sudden increase in electrical activity (Figure 7.9C, C.6C). In addition, the electrodes began to capture spikes when the insertion rod was positioned on top of the shanks and slightly lowered. After a short resting period, during which tissue relaxation occurred, activity returned to its baseline state as spiking activity was captured by the majority of the electrodes (Figure C.6D).
These observations demonstrate that after insertion, physiological spontaneous activity was captured, using PiRi as well as KiRi electrodes.

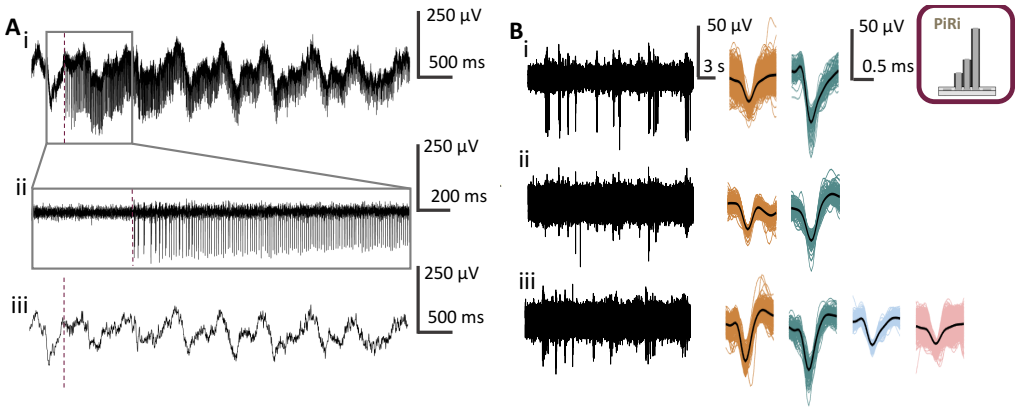

Figure 7.8.: Insertion of a PiRi probe into the somatosensory cortex of a mouse. A) Recording example at the time of insertion, showing the raw (i), as well as spiking activity in the high- (300 to 3000 Hz, ii) and LFPs in the low-frequency (up to 300 Hz, iii) range. The red line in (i), (ii) and (iii) indicates the time stamp of insertion where spiking activity was observed immediately whereas the low-frequency activity was largely unperturbed. B) Example of simultaneous recordings from 3 electrodes (i), (ii) and (iii) with sorted waveforms from multi-unit and potential single-unit recordings (modified from [41]).

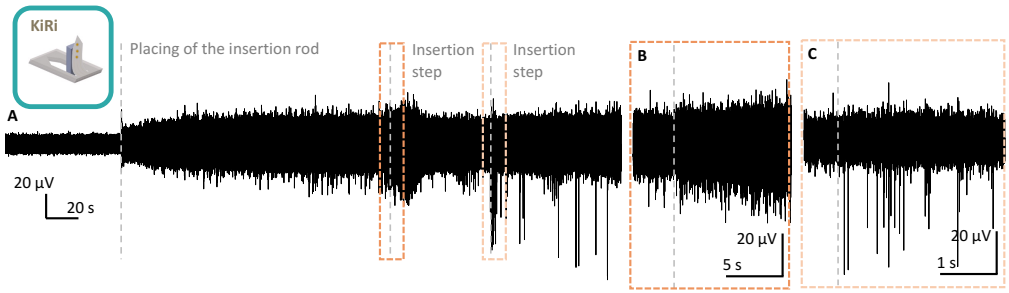

Figure 7.9.: Spiking activity during the insertion of a KiRi implant into the cortex. Recordings from one example electrode, which started capturing spikes when the insertion rod was placed on top of the shanks and slightly lowered. Two subsequent insertion steps of 100 µm were performed which led to either an increase in spiking amplitude during the first seconds after insertion (i) or a short bursting activity directly after the insertion (ii) (modified from [177]).

Histological analysis with fluorescently labeled pillars and shanks once more demonstrated the successful insertion of the implants into the cortex and their penetration to the superficial cortical layers 2/3. For this, prior to insertion, PiRi pillars and KiRi shanks were coated with the fluorescent dye DiD (DiD V22887, ThermoFisher, USA) dissolved in ethanol. Figures 7.10A,C show examples of a coated PiRi and KiRi probe, respectively. Following implant extraction, the brains of the mice were vertically sliced and stained as described in 3.4.2. The images 7.10B and 7.10C depict exemplary brain slices from an implanted mouse, displaying fluorescently labeled electrode tracts within the somatosensory cortex. The blue channel demonstrates fluorescence resulting from DAPI staining of all cell nuclei, which is utilized to visualize the diverse structural elements of the brain. The red channel presents a false-color image of infrared fluorescence, which is a consequence of coating the electrode pillars with the fluorescent dye DiD. For the PiRis, a magnification of the region in which the electrode has been implanted reveals the presence of fluorescence from two distinct electrode tracts, which is illustrated by dashed outlines (7.10B$_{ii}$). In a similar manner, the insertion site of KiRi shanks could be traced, as illustrated in Figure 7.10D$_{ii}$. This finding serves as a confirmation that the complete shanks, with a length of 500 µm, had been successfully inserted reaching layer 2/3 of the somatosensory cortex.

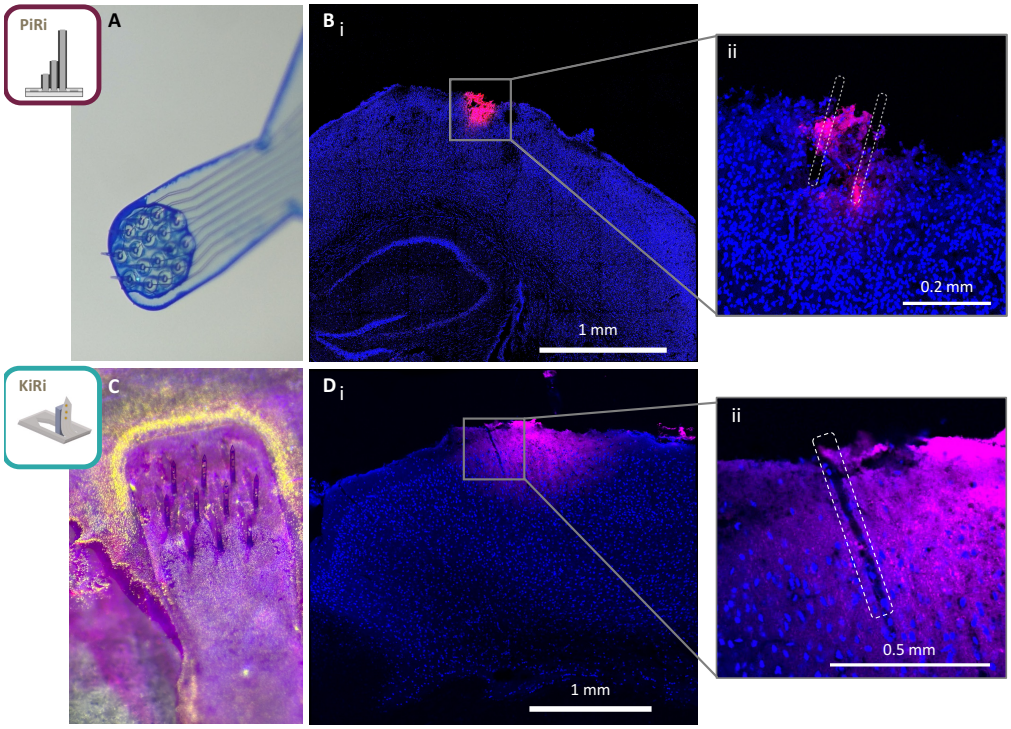

Figure 7.10.: Histology of brain slices post explantation of PiRi and KiRi electrodes. Prior to insertion, the PiRi pillars (A) and KiRi shanks (C) were coated with the fluorescent dye DiD. DAPI staining of all cell nuclei was conducted, resulting in a blue coloration. A false-color image of infrared fluorescence, produced by coating the electrode pillars with the fluorescent dye DiD, is demonstrated using the red channel. B) The image illustrates an exemplary brain slice from an implanted mouse following a PiRi implant extraction, exhibiting fluorescently labeled electrode tracts within the somatosensory cortex. A magnification of the region of the brain in which the implant has been placed reveals the presence of fluorescence from two electrode tracts (indicated by dashed outlines) (ii) (modified from [41]) D) Similarly, the implantation site of KiRi shanks could be traced in the slices post explantation.

7.2.2. Tactile stimulation and recordings from the somatosensory cortex

Following the implantation of both PiRi and KiRi, a series of tactile stimulation experiments were conducted.

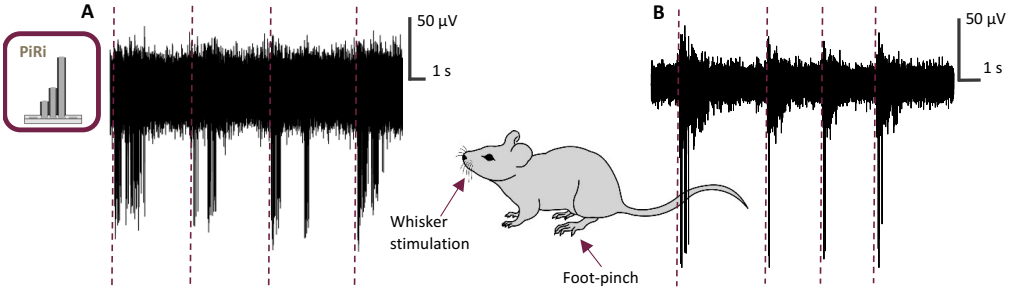

Figure 7.11.: Example recording from a PiRi electrode upon tactile stimulation. Band-pass filtered data upon a periodic whisker stimulation every 5 s (A) and foot-pinch stimulation every 3 s (B) (modified from [41]).

Prior to the surgical procedure, no widefield imaging of the cortex of the mice was conducted for the PiRis. Nevertheless, it was demonstrated that tactile stimulation led to an increase in spiking activity recorded with the PiRi electrodes. Thus, in order to induce neural responses to sensory stimulation, a periodic stimulation regimen was employed, comprising two mild air puffs delivered to the facial whiskers at 5-second intervals (Figure 7.11A) and a similar regimen of foot-pinches (Figure 7.11B). Figure 7.11 shows examples of the respective spiking activity acquired upon band-pass filtering the data (100 - 3000 Hz). The sensory stimulation resulted in clear neural responses in the pillar electrodes, in the form of bursting spikes that exhibited a correlation with the time stamps of stimulation. This outcome serves to confirm that the array is indeed capable of capturing functional responses from cortical neurons.
For the KiRis, the goal was to extract 3D neural activity maps in the cortex, a process enabled by the implant's multisite architecture. To accomplish this, both the low-frequency LFPs (below 100 Hz) and high-frequency spiking activity (100 to 3000 Hz) underwent independent analysis (Figure 7.12, and Figure C.8). Upon hind paw stimulation, neural responses to tactile stimulation were visible in the LFPs (Figure 7.12A), exhibiting notable variations across the cortical locations of each shank. For each electrode, the mean LFP response to tactile stimulation was calculated. Figure 7.12A$_i$ depicts the averaged peak-to-peak values, while Figure 7.12A$_{ii}$ illustrates the averaged LFP during the initial second of stimulation for each electrode. It is apparent that certain electrodes exhibit a distinct peak at the onset of stimulation. In the electrodes of Sh2 and E1.2 on Sh1, the peak is negative, whereas in the remaining electrodes, it is positive. The peak-to-peak amplitudes of the aforementioned peaks, representing the neural response to tactile stimulation, were markedly stronger in the two shanks (Sh1 and Sh2) within the hindlimb region of the somatosensory cortex than in the more lateral shanks (Sh3 and Sh4) placed outside the hindlimb region. These results are in accordance with those obtained through widefield imaging (see Figure 7.5A). The electrodes in Sh2 demonstrated the most robust electrophysiological response, which corroborates the findings of the widefield imaging, which identified this region as the most responsive. The strongest response was observed in electrode E2.2, which is situated at a depth of 300 µm, exhibiting an average potential of 28 µV. In comparison, electrode E4.1 on the neighboring shank Sh4 only yielded an average potential of 5.6 µV. Furthermore, the analysis of the cross-correlation between the electrodes indicated the presence of robust interactions across electrodes within the same cortical depth and region. This finding is demonstrated by the elevated correlation observed between Sh1 and Sh2 within the hindlimb region, as well as between Sh3 and Sh4 outside the hindlimb region (Figure 7.12A$_{iii}$ and Figure C.7).

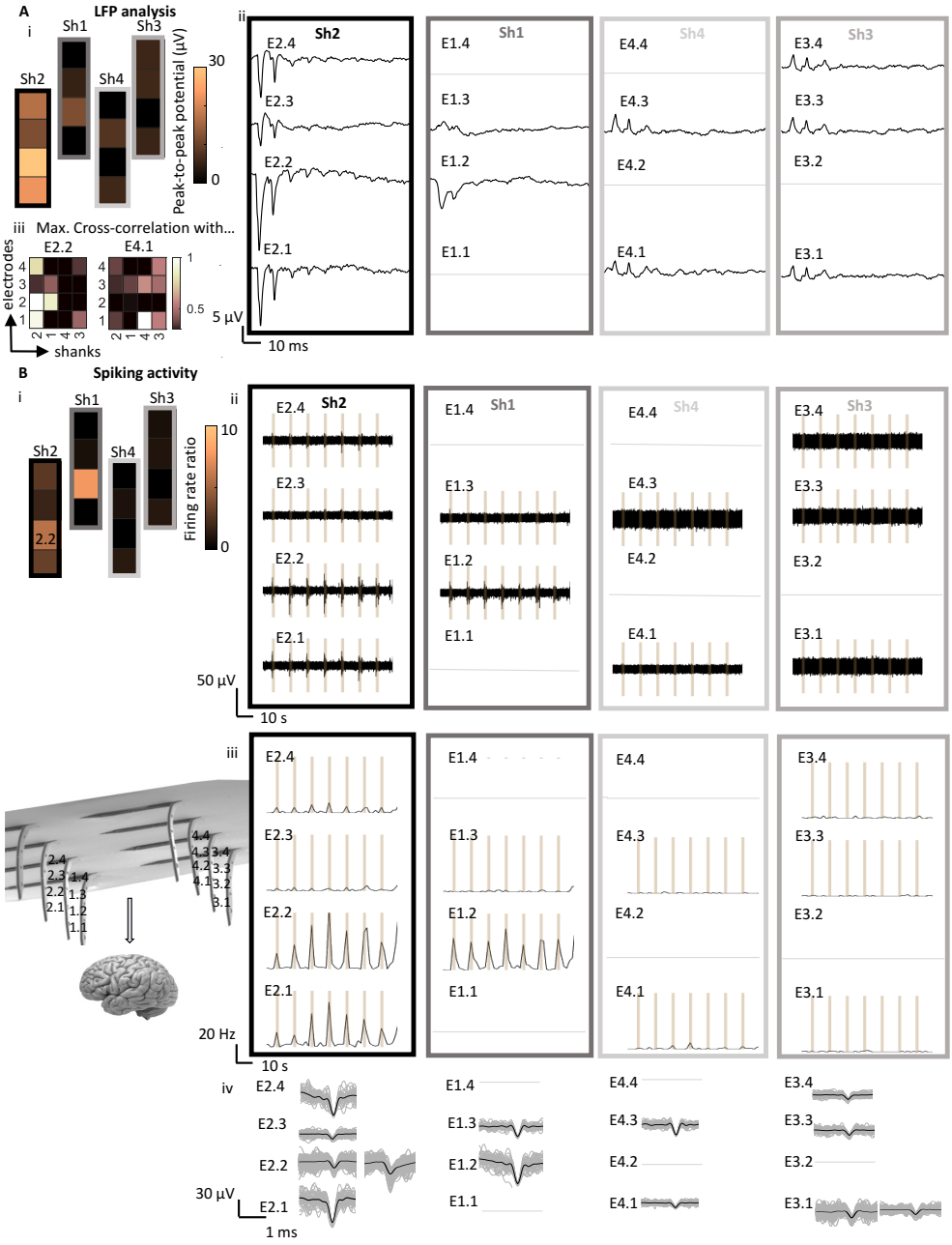

Figure 7.12.: Recording from S1 using KiRis during tactile stimulation of the hand limb. A) Averaged LFPs during the initial second of tactile stimulation demonstrate the spatial activity distribution contingent on the depth (z) and x-y electrode location (ii). The peak-to-peak potentials were derived from the averaged LFPs over 50 trials (i). The heatmaps of (iii) show the maximal cross-correlation of E2.2 and E4.1 with all other electrodes. B) The firing activity demonstrates a corresponding increase in response to the stimulation (brown bars). Therefore, the mean changes (firing rate ratio during versus before stimulation) in spiking activity are also dependent on the position of the electrodes (i). Figure B$_{ii}$ depicts an example of band-pass filtered data from electrode E2.2, which demonstrates a strong correlation between spiking activity and stimulation (brown bars). Figure B$_{iii}$ illustrates the computed firing rate traces derived from the band-pass filtered data for all electrodes during the tactile stimulation (brown bars). The grey lines indicate electrodes that are not functional (modified from [177]).

The analysis of the band-pass filtered signals (100 to 3000 Hz) to isolate neural spiking activity yielded comparable results with respect to the distribution of electrophysiological activity. During the stimulation period, an increase in firing rates was observed in electrodes in proximity to neuronal units that exhibited the greatest response to tactile stimulation. Figure 7.12B$_i$ illustrates an example of the band-pass filtered signal in E1.2. To analyze the spread of activity, the firing rate traces (Figure 7.12B$_{ii}$) and the firing rate ratio (amount of spikes during *versus* before the stimulus, Figure 7.12B$_{iii}$) were calculated. This revealed a high firing rate ratio for Sh1 and Sh2, whereas less change in firing rates was observed in Sh3 and Sh4. It is evident that in Sh2 and E1.2 of Sh1, the peaks of the firing rate traces are correlated with the stimulation onset (Figure 7.12B$_{iii}$). Notably, the electrodes E1.2, E2.2, and E2.1 exhibited a pronounced stimulus-induced alteration in firing rates, reaching a firing ratio of up to 2.5. In contrast, the firing rate ratio in Sh3 and Sh4 was 1.0 and 1.3, respectively, indicating that the stimulation had no or only a minimal effect (averaged with all electrodes on the respective shank). This finding is, similarly to the LFPs, consistent with the results of the widefield imaging. In general, spiking activity is more readily discernible in deeper cortical layers, as cortical layer 1 at the surface of the cortex is predominantly composed of axons. Consequently, while high-amplitude LFPs were captured with all four electrodes of Sh1, high spiking activity was predominantly captured with deeper implanted electrodes, such as E1.2, E2.2, and E2.1.
With respect to the stimulation of the forelimb, the implantation region exhibits diminished response amplitudes in comparison to the hind paw stimulation during widefield imaging (see Figure 7.5). Nevertheless, a distinction can be made between Sh1 and Sh2, which are situated in the region that exhibits greater responsiveness, and Sh3 and Sh4, which are located in the region that demonstrates lesser responsiveness. This phenomenon is similarly evident in the electrophysiological data (Figure C.8). The highest peak-to-peak amplitudes of LFPs were observed in E2.2, with a value of 12.4 µV, and in E1.2, with 12.5 µV. In contrast, the lowest values were observed in E4.1 and E3.1, with a value of 2.9 µV for each. In comparison to the hind limb stimulation, the peak-to-peak amplitudes were lower, and this time no clear peak was observed at the beginning of the stimulation (Figure C.8A). Similarly, the highest level of spiking activity was observed in Sh1, with E1.2 exhibiting a firing ratio of 2.5. However, the neural activity exhibited lower amplitudes and less correlation with the stimulation period in comparison to the hind paw stimulation. This phenomenon can be observed in the recording of E2.2 upon fore paw stimulation (Figure C.8B) in contrast to E2.2 upon hind paw stimulation (Figure 7.12B$_{ii,iii}$). In conclusion, the propagation of neural activity was markedly less pronounced when stimulation is applied to the hind paw. This is evidenced by the electrophysiological data, LFP recordings, and spiking activity, as well as by the widefield imaging. Nevertheless, this provides further evidence of the consistency between the electrophysiological recordings acquired using the KiRi electrodes and the neural activity obtained via widefield imaging.
The findings of this experiment illustrate the capacity of the multisite kirigami electrodes to construct a 3D map of the underlying neural tissue, thereby facilitating a more comprehensive examination of the spatial dependency of signal distribution in the somatosensory cortex. Furthermore, the results evidenced the electrodes' capability to withstand implantation *in vivo*, where they are subjected to insertion forces and micromotions resulting from the animal's respiration and cardiac activity.

7.2.3. Visual stimulations in awake mice and recordings from the visual cortex

To further illustrate the utility of recording from cortical regions using 3D probes, KiRi implants were implanted into V1 in a chronic preparation with awake mice. This involved recordings made in awake mice upon recovery on the day of implantation and histological analysis one-month post-implantation. The objective was to record neural responses to diverse visual stimuli across varying

depths and cortical regions to elucidate the characteristics of sensory neural responses in the awake brain. In addition, the FBR was analyzed after one-month implantation.

Surgical extension for chronic implantation

Following the surgical method illustrated in Figure 7.6 and the insertion of a KiRi implant, a glass window was affixed to the implant (Figure 7.13A) using gentle pressure and the assistance of the insertion rod. Subsequently, the implant was secured with dental cement to the skull and PCB (Figure 7.13B$_i$). This allowed for stabilization of the implant in the cortex while its position could be monitored through the glass window (Figure 7.13B$_{ii}$). For this chronic application, the front-end connector of the implant was customized for a total form factor of 21 x 11.5 x 7.5 mm and a weight of 1.6 g, ensuring a small and lightweight design that could be carried by the mouse (Figure 7.13C).

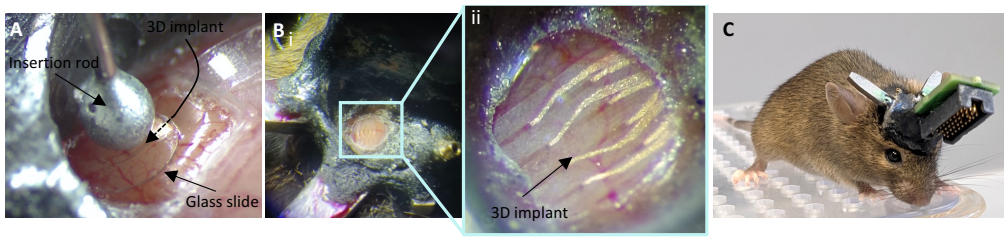

Figure 7.13.: Extension of the surgical procedure for chronic *in vivo* applications. A) A glass window was affixed to the 3D implant with the assistance of the insertion rod. B) Dental cement was applied to the skull and PCB to facilitate a stable fixation of the front-end connector (i), while the glass window enables optical monitoring of the implant (ii). C) The front-end connector was sufficiently lightweight and compact to be carried by awake mice (modified from [177]).

Visual stimulation with awake mice

To ascertain the location of the visual cortical areas prior to implantation, wide-field imaging was employed once more for retinotopic mapping and the identification of the primary cortex and several higher visual areas (Figure 7.14B, blue and red regions). To this end, mice were placed in an experimental setup (Figure 7.14A) comprising a running wheel and a monitor displaying visual stimuli that covered the visual field of the right eye, contralateral to the implanted cortical hemisphere. The neural responses to visual stimulation observed through widefield imaging were found to align with the expected location of visual areas (white outlines in 7.14B). Consequently, the KiRiCor probes (Figure 7.14C) were inserted in accordance with the procedure detailed in the preceding section, to encompass V1 and multiple higher visual areas.

Subsequently, the response of distinct cortical areas and layers to two forms of visual stimulation was examined: a basic moving grating and a complex texture (Figure 7.14A$_{ii}$ and 7.14A$_{iii}$, respectively). By examining the LFP responses in two adjacent shanks (Sh1 and Sh2), it became evident that there were notable discrepancies in the mean stimulus responses across the electrodes at distinct depth and locations (Figure 7.14D). Electrodes E1.1 and E2.1, situated in the deeper cortical layers 2/3, demonstrated a more pronounced visual response than the superficial electrodes E.13 and E2.4 in layer 1. This discrepancy in the response was especially evident in V1 (shank Sh2), whereas in the more medial anterior cortex (area AM, shank Sh1), the responses were more uniform across different depths. This observation was subsequently validated by the presence of spike responses alongside the LFPs, exhibiting an average SNR of 4.9 ± 0.5. In instances where the responses were more pronounced, the SNR could reach up to 17, as evidenced by the electrodes positioned in deeper layers (see Figure C.9). Furthermore, while both

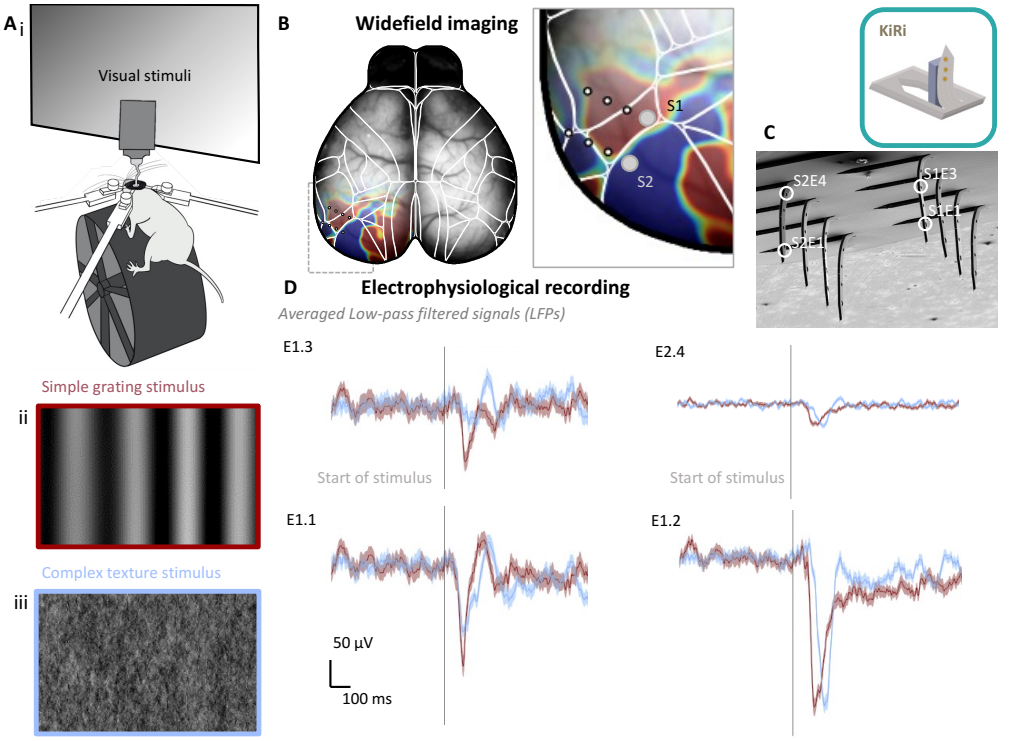

Figure 7.14.: Widefield imaging and recordings of electrophysiological activity in V1 upon visual stimulation. A) The awake mice were placed inside the setup (i) and exposed to simple grading (ii) and complex texture (iii) stimuli. B) Widefield imaging was used to determine the active cortical areas upon visual stimulation. Visually evoked fluorescence changes were measured. After inserting the KiRi shanks (C), visually evoked averaged LFP responses were measured in shank 1 and 2 (D) (modified from [177]).

gratings and texture stimuli evoked robust neural responses in V1 (Sh2), visual responses in Sh1 were comparatively weaker and more selective for gratings over texture stimuli, particularly in the superficial electrode E1.3 (red versus blue traces in 7.14D). A noteworthy finding was a shift in the response latency to visual stimuli in area V1 (Sh2) in the presence of textures, which exhibited a longer delay than gratings. This is likely attributed to the increased complexity of the texture stimulus, necessitating more extensive neural processing within the visual system [276].
In conclusion, these findings reveal significant disparities in the neurophysiological processing of complex visual stimuli across cortical depth and regional brain areas. This evidence substantiates the utility of KiRi probes for chronic electrophysiological recordings in the awake, non-anesthetized brain. Despite the attempts to reduce the weight of the front-end connector, the interface between the flexible array and the printed circuit board of the front-end failed one day after implantation, which hindered the realization of long-term chronic recordings. However, awake recordings could be conducted following the recovery of the subjects on the day of implantation, and additional insights of FBRs were investigated through histological examination of the tissue one-month post-implantation.

7.2.4. Post-explantation study

Four weeks following implantation, the KiRiCor probes were explanted, after which immunohistochemical analysis was conducted on the implanted brain tissue (Figures 7.15 and 7.16) and an

optical inspection was performed on the explanted electrodes (Figure 5.7C).
Horizontal sections of the cortex with a thickness of 20 µm were stained for mature neurons (NeuN, red), cell nuclei (DAPI, blue), astrocytes (GFAP, gray), and microglia (Iba-1, green). Figure 7.10 shows a brain slice where the insertion holes of each of the eight shanks are clearly discernible from the surrounding tissue. The implantation footprint of the shanks was discernible as small lesions (dark holes), which are referred to as small ROIs. Furthermore, the slices demonstrated FBR in tissue regions in close proximity to the aforementioned small ROIs (Figure 7.16A, indicated by white circles). The FBR was evident as alterations in the surrounding tissue (large ROI, with small lesions (small ROIs) typically situated at the midpoint and on occasion off-center within the affected regions (Figure 7.16A, indicated by gray circles). The footprint of the insertion, which encompassed multiple instances of individual shanks, could be tracked at depths reaching up to 260 micrometers. The mean area of the small ROIs, which was 478 ± 380 µm² (N = 24), is consistent with the dimensions of the shanks. The mean size of the affected regions (large ROIs) exhibiting an FBR was found to be 7467 ± 373 µm² (N = 56 large ROIs across 11 slices), which is approximately 15 times larger than the cross-sectional area of the shanks (500 µm²). The relative size of the affected region was consistent with the range of observed FBR in studies employing flexible single-shank polymer devices (large ROIs approximately 7 - 39 times the cross-section of the shank [109]). However, in these investigations, stiff shuttles were employed to facilitate implantation, resulting in larger footprints (small ROIs approximately 2 to 8 times the cross-section of the shank [99][109]) in comparison to the findings here.

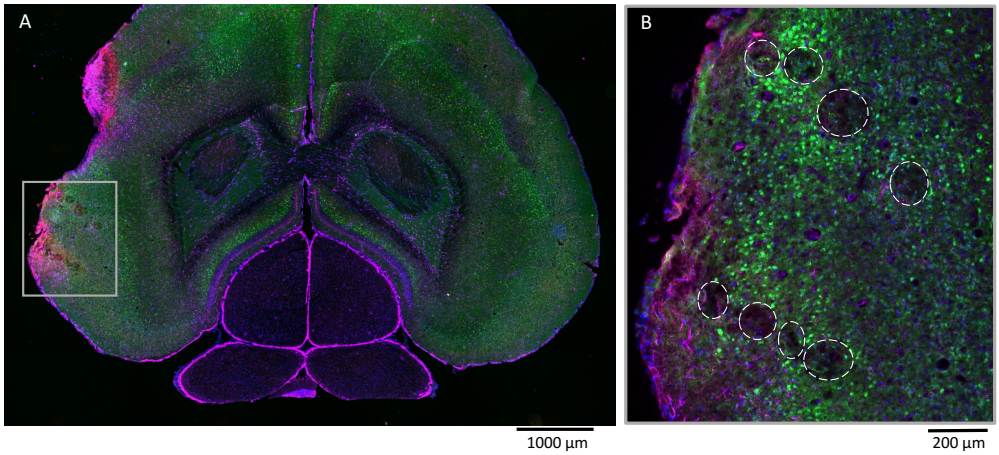

Figure 7.15.: Stained brain slice after four-week implantation with a KiRiCor probe. A) Overview of the complete brain slice. B) Zoom-in on the insertion area showing the eight areas affected by the insertion of each of the eight shanks of the KRiCor probe (modified from [177]).

A comprehensive examination of the larger ROIs across various depth levels revealed a tendency for the implantation footprint to increase at the boundary between layers 1 and 2/3 (see 7.16B,C). Within layers 2/3, FBRs exhibited a decrease in intensity until they were no longer discernible from the surrounding tissue at Z13 (260 µm, Figure 7.16B$_i$). In contrast, the small lesions were only present until position Z10, which corresponds to an insertion depth of approximately 200 µm (Figure 7.16B$_{ii}$). This can be attributed to the fact that the shanks exhibit a diminished cross-sectional area towards the tip, which results in a smaller footprint in the deeper layers.
A reduction in the number of astrocytes in the vicinity of the insertion site (small ROIs) was observed in the deep cortical layers and in the larger ROIs, as evidenced by the relative fluorescence intensity (Figure 7.16C), in a manner consistent with the findings of previous studies [153]. In

contrast, no nuclei or neurons were observed in proximity to the implantation site (Figure 7.16C). Similar observations have been documented in other studies [211]. The expression of the GCaMP indicator in excitatory neurons of the genetically modified mice, which also appear green, interfered with the ability to reliably analyze Iba-1 staining.
It is important to note, however, that the slicing process may not have been perfectly perpendicular to the insertion direction. Achieving perfect alignment during the insertion process is a challenging procedure. It is, therefore, possible that the total insertion depth may have been underestimated and that the size of the ROIs may have been overestimated when the slices were not cut perpendicular to the shank length. Furthermore, the pulling during implant retrieval caused irregularly shaped insertion holes, which resulted in considerable variability in the measured footprint areas (both large and small ROIs). Consequently, it is likely that the assessment of FBRs is overestimated due to both the retraction of the implants and the slicing process.
Nevertheless, upon retrieval of the implant, the shanks of the probe were observed to remain accurately folded (see Figure 5.7B). Additionally, SEM inspection of the electrodes revealed no evidence of delamination, with the exception of the expected minor adsorption of biological matter (Figure 5.7C). While this might indicate the long-term stability of the kirigami folding and electrodes of the shanks, electrode failure cannot be completely ruled out due to the failed packaging and therefore missing impedance measurements throughout the implantation period. Nevertheless, the collective findings of these experiments illustrate the capacity of 3D kirigami probes to obtain recordings from various depths and brain regions within living neural tissue, thereby facilitating a comprehensive examination of neural response patterns. Furthermore, although stable packaging is required for further tests, the results substantiate the resilience of kirigami implants to acute and chronic implantation *in vivo*, while the accumulation of astrocytes as an indicator of FBR was minimal, particularly in the deeper layers of the cortex.

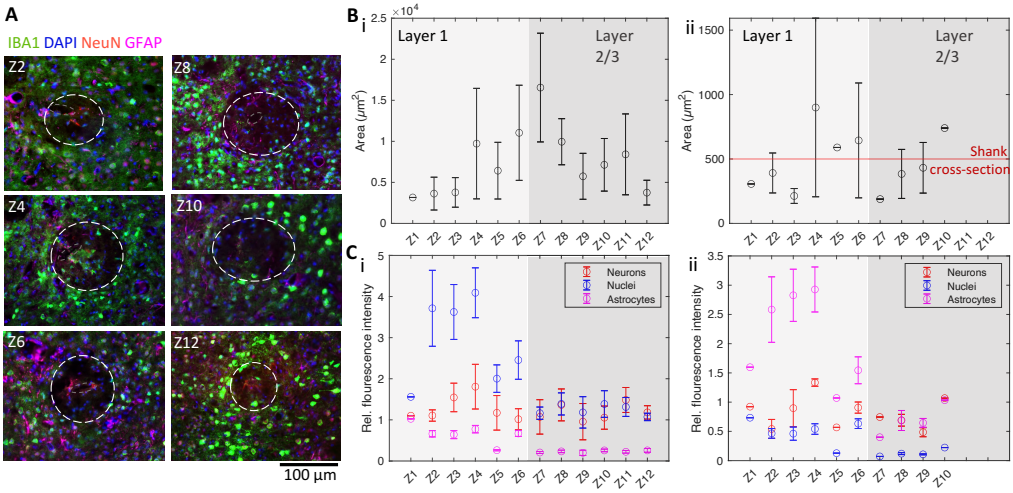

Figure 7.16.: Analysis of the histology after four-week implantation. A) illustrates the tracking of a single hole through varying depths, with the ROIs (white) and small ROIs (gray) marked with dashed circles. The implantation lesions (small ROI) are observed to align with the dimensions of the shanks (gray circle surrounding the 50 µm wide hole) and the implantation locations of the shanks. B) The dimensions of the large (i) and small (ii) regions of interest (ROIs) at each cortical depth. C) An examination of the relative fluorescence intensity of each channel for the large (i) and small (ii) ROIs (modified from [177]).

7.3. Summary and outlook

This chapter presents the manner in which the 3D KiRi and PiRi MEAs facilitate the capture of spatial dependencies in electrophysiological activity patterns in both *in vitro* and *in vivo* cortical applications. Further investigation is required to elucidate the complex mechanisms underlying cortical function, particularly in the context of degenerative or pathological processes such as epilepsy. Such knowledge is vital for the development of more efficacious diagnostic tools and treatments. It is, therefore, evident that a 3D MEA with the capability of high spatial and temporal resolution is an extremely beneficial tool for the efficient mapping of electrophysiological activity throughout the 3D neural space. However, the most sophisticated 3D neural implants are either merely recording devices that capture data from specific x–y planes at designated z-depths within the neural tissue, as observed in Utah arrays [24], or they are y–z neural threads that must be implanted in succession to create a comprehensive 3D mapping of the cortex [31][32]. In contrast, both 3D devices of this study, the KiRis and PiRis, were implanted in a single step without the use of an insertion shuttle. This approach has the advantage of shortening the overall implantation and surgical periods while facilitating post-implantation monitoring of the implantation sites.
The use of KiRis with penetrating and surface electrodes was successfully demonstrated in human brain slices *in vitro*, including electrophysiological recordings while inducing SLEs by modified aCSF. This approach was employed to examine the spatial origin and spread of these events throughout the tissue. The SLEs recorded in this study exhibited characteristics similar to those observed in previous studies. Additionally, the 3D sampling demonstrated that SLEs occurred in discrete local networks across cortical layers. To illustrate the efficacy of the 3D MEAs for volumetric neural recordings *in vivo*, they were utilized in the somatosensory and visual cortex of mice. These sites were selected due to their crucial involvement in sensory restoration processes, such as those related to touch or vision. The objective was to demonstrate how spatial-dependent activity can be captured upon tactile and visual stimulation, thereby exposing possible stimulation target sites for sensory restoration. In the somatosensory cortex, 3D electrophysiological activity was successfully recorded, as evidenced by the spatial-dependent LFP amplitudes and firing rates of individual neurons in response to hind limb stimulation. For the KiRis, the differences in activity between neighboring shanks also accurately reflected their respective position in somatosensory subregions. Furthermore, clear differences were observed across cortical layers in individual shanks.
Similarly, recordings in the visual cortex of awake mice demonstrated a distinct spatial dependency upon different cortical layers using the KiRi implants. Moreover, the responses demonstrated variability across visual areas in accordance with the complexity of the stimulus. Following a four-week period of implantation, a comprehensive examination was conducted on the electrodes and the implantation site. Immunohistochemical analysis of the tissue demonstrated that the cross-sectional footprint was consistent with the dimensions of the kirigami shanks. It is noteworthy that an accumulation of astrocytes was observed exclusively in layer 1, in close proximity to the cortical surface and the insertion site. This indicates that the insertion impact was minimal, likely due to the flexible and biocompatible characteristics of the kirigami implant. However, during the initial chronic trials, a considerable number of broken electrodes were observed during the surgical procedure, which was most likely due to an unstable connection with the PCB. Therefore, a smaller connector should be utilized, which necessitates less sealing and could potentially reduce the likelihood of broken connections. However, a thorough optical inspection of the folded kirigami shanks revealed no evidence of unfolding or delamination of the electrode material, thus substantiating the hypothesis that the flexible 3D microelectrode array structure maintains long-term stability.
Thus, further experimentation is necessary to draw statistically significant conclusions regarding the long-term stability of 3D implants for long-term electrophysiological recordings in the cortex. Similarly, further investigation of FBR over time is necessary, considering both KiRi and PiRi elec-

trodes. A study should be conducted to compare the insertion and implantation impact of both 3D approaches using optimized histological methods. In this scenario, it would be advantageous to closely monitor the interaction between the shank/pillars and neural tissue. Rather than extracting the implant, it would be more beneficial to slice the brain along with the implant. This approach would facilitate the analysis of the probe-tissue interface in terms of FBR, such as the accumulation of astrocytes and neural death in the vicinity of the implants. The next step could be to implant longer shanks or pillars to reach deeper cortical layers and increase our knowledge of cell behavior across the cortical dimensions. However, the fabrication of such devices is more complex, and their insertion is challenging, as previously discussed in section 5.4.
Nonetheless, the experiments demonstrated the capacity of the 3D electrodes to accurately record electrophysiological activity. This capability is evidenced by the discernibility of dependencies between depths and locations in these preliminary trials.

8. Conclusion

This work presents two novel approaches for the rapid and reliable fabrication of 3D penetrating neural implants. In the initial approach, the PiRis, 2PP was utilized to print hollow pillars onto flexible MEAs. These pillars served as templates to direct the electrochemical deposition of conductive materials, including Au and PEDOT:PSS, facilitating the growth of 2D electrodes into the third dimension. The innovation of this process, when compared to other approaches previously documented in the literature [117][151], lies in the concept of utilizing hollow pillars instead of solid pillars. Therefore, the hollow pillars produced in a single photolithography step serve two purposes: to direct the electrochemical deposition and to passivate the conductive materials. Consequently, the number of fabrication steps required to modify a planar MEA substrate into a 3D MEA is reduced, as only two post-processing steps are necessary to create a conductive pillar: the printing of a hollow pillar, which serves as a template for the subsequent electrodeposition of the conductive material.
The second approach is that of scalable kirigami implants. The simultaneous folding of up to 128 shanks was achieved through the use of matched-die forming, resulting in the creation of a flexible 3D MEA with both penetrating and surface electrodes. The dimensions and electrode counts of the kirigami MEAs - with a maximum shank length of 1000 µm and a minimal inter-shank spacing of 50 µm - exceed those of existing approaches for flexible 3D neural implants. Although the fabrication process remains manual, implants can be produced rapidly and reliably with a high yield. The KiRi folding technique employs a matched die compression process, rendering it suitable for serial manufacturing.
A multitude of design configurations were examined for potential utilization in a spectrum of neural tissue applications ranging from *in vitro* retina and human brain slices to *in vivo* cortical applications in mice. Due to the intricate nature of neural networks, particularly in diseased models, 3D recording platforms are of vital importance for the capture of electrophysiological activity patterns across layers and regions of the brain. With the overarching objective of advancing our understanding of, and ultimately treating, neurological disorders such as epilepsy and loss of sensory functions, the versatile 3D MEAs presented in this work provide a valuable tool for future research. Nevertheless, the applications have thus far been confined to electrophysiological recordings under diverse forms of stimulation, including optical and pharmaceutical stimulation of explanted WT and RCS retinas, as well as pharmaceutical stimulation in explanted human brain slices, and visual and tactile stimulation during *in vivo* implantation in the cortex. The bidirectional stimulation strategy, which employs electrical stimulation to stimulate the remaining diseased network with the objective of restoring vision by providing artificial sensing, has yet to be explored in the context of degenerated retina using 3D implants. However the performance of both the KiRi and PiRi implants, as well as their *in vitro* and cadaveric validation, has been completed, thus rendering the implants ready for initial trials utilizing electrical stimulation of the retina.
Nevertheless, further improvements should be considered to advance the performance of the KiRi and PiRi neural probes and overcome the on-going challenges as summarized in Figure 8.1:

- **Long-term stability and FBR upon chronic implantation** Alternative substrates, such as PI, should be investigated, as well as alternative electrode material for KiRi electrodes, such as spin-coated PEDOT:PSS to improve the long-term stability. The use of only transparent and flexible polymeric materials provides additional benefits. The long-term stability investigation of PiRi electrodes is pending. During chronic implantations, the FBR should be thoroughly investigated in the retina and cortex.

- **Fabrication and insertion of longer shanks/pillars** In addition to the fabrication challenges, the insertion process may necessitate the utilization of a stiff shuttle device or a resolvable brace.
- **High-density implants** In order to effectively restore sensory functions and map complex neural activity in the brain, it is imperative to utilize thousands of channels. Microfabrication of high-density implants poses significant challenges, and connecting all channels using a small, portable, wireless connector is equally demanding. Furthermore, processing a large volume of data in a limited time frame and storage capacity represents an additional challenge.

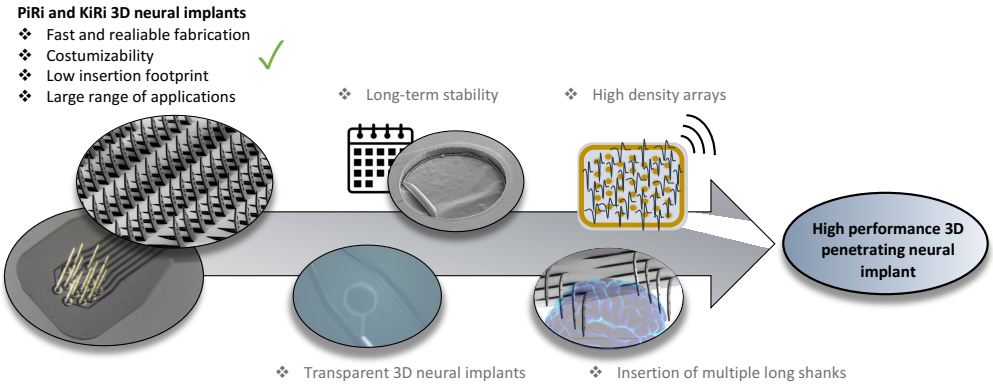

Figure 8.1.: Outlook. The fabrication process of the customizable KiRi and PiRi implants is both rapid and reliable. Both types of neural probes possess a low insertion footprint and are suitable for a broad range of applications. However, further research is necessary to assess their long-term stability and FBR upon implantation during chronic trials. Investigations should be made on how to build a fully transparent, wireless and high-density probe. Another ongoing challenge is the development and insertion of long shanks/pillars.

Finally, as in this work a comparison of PiRi and KiRi electrodes was conducted, it is essential to offer a concluding remark. Both electrodes possess a rapid, reliable, and customizable fabrication process; however, scalability is only possible for KiRis. Their electrochemical performance, including impedance, CSC and CIC, is comparable and competitive with state-of-the-art technology. Furthermore, the mechanical properties, such as bending stiffness, exceed those of all other known 3D devices. Both devices demonstrated the capacity to capture electrophysiological activity, ranging from spiking activity to LFPs, during *in vitro* and *in vivo* trials utilizing diverse neural tissue types. However, a higher insertion success rate with KiRis was revealed during *in vitro* trials. With regard to the insertion footprint, the absolute footprint in terms of dead cell count and ITA did not demonstrate significant differences between the probes. However, when the number of electrodes inserted was taken into consideration, the KiRis probe exhibited a lower value. A comprehensive evaluation of the long-term stability and FBR upon implantation of both approaches is necessary to determine the optimal method for chronic use.
The selection of the 3D approach is contingent upon the underlying application. In cases necessitating multisite design, KiRis stand out as a superior option. The principle of employing more electrodes on a shank using a high-density approach is applicable to KiRis without increasing the cross-section of the shank. In contrast, the multisite design of PiRis is constrained and invariably scales with the cross-section. Conversely, for model structures of minimal size and fragility, such as organoids, PiRis emerges as the optimal solution. The utilization of thin pillars in organoids is less prone to compromising the integrity of the delicate cell structure when compared to the use of KiRis. Additionally, the versatility of substrates for PiRis is a notable advantage. The implemen-

tation of long-term recording systems for organoids might be facilitated by employing PiRis on stiff MEAs, wherein organoids are positioned on top and can grow around the pillars.
In conclusion, both devices, KiRis and PiRis are highly effective tools capable of facilitating large-scale electrical sampling in complex neural tissues. The efficacy of these devices in promoting tissue integration, thereby facilitating advanced analysis of neural disorders and disease models, has been demonstrated. In scenarios where high spatial resolution is of paramount importance, these devices offer a valuable solution.

Acknowledgments

I am deeply grateful to my family, friends, and all of my colleagues at the IBI-3 Institute. Their help and support throughout my research project and writing process was absolutely essential to bringing this project to life. I am especially grateful to the following people.

- **Prof. Dr. Andreas Offenhäusser**, thank you so much for giving me the opportunity to be part of this special institute, IBI-3. This experience has been such a unique opportunity that has enriched my personal and professional growth and career. Your guidance, constant support, and insightful conversations, both scientific and non-scientific, have been instrumental in helping me navigate and thrive in my PhD journey.
- **Prof. Dr. Sven Ingebrandt**, I really appreciate all of our discussions at the TAC meetings, seminars at the RWTH, and RTG events, and the input from your side regarding my project. Thank you for being my second supervisor.
- **Dr. Viviana Rincón Montes** thank you for being my daily supervisor at the FZJ and leading the *in vivo* neuroelectronics group. Thank you for introducing me to the incredible world of retinal implants. I am so grateful for all the knowledge you have shared and the ongoing support you have given me over the years. Thanks for your input and all the enlightening discussions we had!
- Thank you **Prof. Dr. med. Peter Walter** for your input regarding retinal surgeries, for sharing your knowledge and experience. Special thanks for being the spokesperson of the RTG and for being so dedicated to the interdisciplinary research group. And to all the other members of the **InnoRetVision RTG**, thank you as well! I am so grateful to have been a part of this research group, where I learned so much from different disciplines. I am incredibly thankful for all the enlightening discussions we had during the Full-Day meetings, Journal Club, and Retreats. Thank you so much for your valuable input!
- **Prof. Dr. Simon Musall** thank you for all the great input you have given me, for making the cortical *in vivo* trials with 3D probes possible, and for all your support during the data processing.
- A huge thanks to all of **my colleagues from the *in vivo* neuroelectronics group** for your support and all the challenges we have overcome together, especially those related to fabrication. I was happy to be part of such an amazing team! Special thanks to **Lina** for being part of this journey from the beginning to the end. Thanks for introducing me to the cleanroom when I first started at FZJ, for all the conferences we attended together and for your constant support, especially through all the challenges we faced over the last few years. Thank you so much, **Erkan**, for being the greatest office buddy, for always willing to lend a helping hand, and for your always honest feedback. **Simon D.**, thank you so much for all your great input from a mechanical engineering point of view, your help, and your support. **Sofiia**, thank you for your help in the Ephys lab and for being patient with me when the experiment had to be done in the dark, and for always making me laugh with your fun weekly memes! Thank you, **Martin**, for taking over the kirigami project and for keeping up with the work. I am so happy to know it is in such good hands. **Alejandra** and **Alwin**, you were such great master's students, and **Kahlan** and **Kelsey**, you were both such excellent interns. I am

grateful to have had the opportunity to supervise you. Thank you all so much for your hard work and support.

- I am incredibly grateful to **Jamal** for collaborating with me and showing what amazing things you can accomplish when you work together as a team! Thank you for all the creative ideas we have tried together and all the laughs we have shared.
- Thanks to all **current and former IBI-3 members** for creating such a welcoming and interdisciplinary working environment!
- **Tibor** and **Frederic**, thank you for your hard work and dedication during the retina surgical trials. I had a great time working with you as an interdisciplinary team. Our scientific and non-scientific conversations were a real joy, and our experimental trials, though occasionally running long and late, were always a time of fun.
- Thank you **Nruthyathi** for your hard work during our retinal experiments and for being so patient during our long sessions at the confocal microscope. Thank you **Prof. Dr. Frank Müller** for your insights on the retina and your biological perspective. Thank you **Antje** and **Jing** for providing the RCS rats.
- Thank you **Vanessa**, **Dirk** and **Francesca** for all the discussions and your input during the seminars. You always made yourselves available for any questions, and your willingness to help were truly appreciated!
- **Michael**, **Marko**, **Regina**, **Elke**, thank you for all your help with the cleanroom, the SEM, the PaC machine, and **Michael**, for always solving problems related to the Carbogen bottle! Thank you **Sven** for your support with the NanoScribe and lithography-related problems and last-minute design conversions. Special thanks to the **HNF team** for all the support and fabrication-related discussions.
- **Tina**, you were always there to help, whether it was answering questions, sorting out orders, or just having a friendly chat that made my day so much better. IBI-3 wouldn't be the same without you. Thank you!
- Thank you **Norbert**, **Nadine** and the rest of the electronic workshop for your help regarding PCBs and other electronic components. Thanks to the **IBI-IT** team for tackling all software problems. Thanks to the mechanical workshop for your technical support. Thanks to **Susanne** and **Zita** for your contributions regarding the organizational matters of IBI-3.
- Thank you **Colin**, **Jamal**, **Justus**, **Mateo**, **Lina**, **Simon D.**, **Erkan**, **Kevin**, **Cole**, **Sergio** for the fun we had during our discussion at lunch, social events and the winter school. Thank you **Jamal** for teaching me how to cross-country ski! Special thanks to **Lina**, **Erkan**, **Simon D.** and **Jamal** for cheering me up after a tough day in the lab.
- A huge thank you to all my **friends** for all the support you have given me over the years. You have always had my back and been there for me through thick and thin, and I can't thank you enough!
- A very special thanks to my amazing **parents** and **grant-parents** for creating such a welcoming and supportive home! Your unending support, motivation, and guidance have been instrumental in shaping my life. Thank you for always encouraging me to be curious, creative and determined. I would certainly not be where I am today without you.
- Thank you so much, **Pascal**, for being such an incredible partner and for showing me this every day through your unconditional and loving encouragement and support.

Bibliography

[1] Jaimie D Steinmetz et al. “Global, Regional, and National Burden of Disorders Affecting the Nervous System, 1990–2021: A Systematic Analysis for the Global Burden of Disease Study 2021”. In: *The Lancet Neurology* 23.4 (Apr. 2024), pp. 344–381. ISSN: 14744422. DOI: 10.1016/S1474-4422(24)00038-3. URL: https://linkinghub.elsevier.com/retrieve/pii/S1474442224000383 (visited on 08/20/2024).

[2] Aklima Akter Lima et al. “A Comprehensive Survey on the Detection, Classification, and Challenges of Neurological Disorders”. In: *Biology* 11.3 (Mar. 18, 2022), p. 469. ISSN: 2079-7737. DOI: 10.3390/biology11030469. URL: https://www.mdpi.com/2079-7737/11/3/469 (visited on 09/25/2024).

[3] World Health Organization and Disease Control Priorities Project. “Disease Control Priorities Related to Mental, Neurological, Developmental and Substance Abuse Disorders”. In: *Disease control priorities in developing countries. 2nd ed* (2006). ISSN: 924156332X. URL: https://iris.who.int/handle/10665/43565 (visited on 09/25/2024).

[4] Kathryn Rimmer, Hiral Shah, and Kiran Thakur. “Expanding Medicines for Neurologic Disorders on the WHO Model List”. In: *Neurology* 88.10 (Mar. 7, 2017). ISSN: 0028-3878, 1526-632X. DOI: 10.1212/WNL.0000000000003691. URL: https://www.neurology.org/doi/10.1212/WNL.0000000000003691 (visited on 09/25/2024).

[5] Olivia Brancatisano, Amee Baird, and William Forde Thompson. “Why Is Music Therapeutic for Neurological Disorders? The Therapeutic Music Capacities Model”. In: *Neuroscience & Biobehavioral Reviews* 112 (May 2020), pp. 600–615. ISSN: 01497634. DOI: 10.1016/j.neubiorev.2020.02.008. URL: https://linkinghub.elsevier.com/retrieve/pii/S014976341930243X (visited on 09/25/2024).

[6] Massimo S. Fiandaca et al. “Advancing Gene Therapies, Methods, and Technologies for Parkinson’s Disease and Other Neurological Disorders”. In: *Neurologia i Neurochirurgia Polska* 54.3 (June 30, 2020), pp. 220–231. ISSN: 1897-4260, 0028-3843. DOI: 10.5603/PJNNS.a2020.0046. URL: https://journals.viamedica.pl/neurologia_neurochirurgia_polska/article/view/68420 (visited on 09/25/2024).

[7] Anna Andrzejewska et al. “Mesenchymal Stem Cells for Neurological Disorders”. In: *Advanced Science* 8.7 (Apr. 2021), p. 2002944. ISSN: 2198-3844, 2198-3844. DOI: 10.1002/advs.202002944. URL: https://onlinelibrary.wiley.com/doi/10.1002/advs.202002944 (visited on 09/25/2024).

[8] Chang-Geng Song et al. “Stem Cells: A Promising Candidate to Treat Neurological Disorders”. In: *Neural Regeneration Research* 13.7 (2018), p. 1294. ISSN: 1673-5374. DOI: 10.4103/1673-5374.235085. URL: https://journals.lww.com/10.4103/1673-5374.235085 (visited on 09/25/2024).

[9] Abdul Waris et al. “Applications of Various Types of Nanomaterials for the Treatment of Neurological Disorders”. In: *Nanomaterials* 12.13 (June 22, 2022), p. 2140. ISSN: 2079-4991. DOI: 10.3390/nano12132140. URL: https://www.mdpi.com/2079-4991/12/13/2140 (visited on 09/25/2024).

[10] Ulrich G. Hofmann and Thomas Stieglitz. “Why Some BCI Should Still Be Called BMI”. In: *Nature Communications* 15.1 (July 23, 2024), p. 6207. ISSN: 2041-1723. DOI: 10.1038/s41467-024-50603-7. URL: https://www.nature.com/articles/s41467-024-50603-7 (visited on 09/25/2024).

[11] Fan-Gang Zeng. “Celebrating the One Millionth Cochlear Implant”. In: *JASA Express Letters* 2.7 (July 1, 2022), p. 077201. ISSN: 2691-1191. DOI: 10.1121/10.0012825. URL: https://pubs.aip.org/jel/article/2/7/077201/2844572/Celebrating-the-one-millionth-cochlear-implanta (visited on 09/25/2024).

[12] Jose Antonio Camacho-Conde et al. “Brain Stimulation: A Therapeutic Approach for the Treatment of Neurological Disorders”. In: *CNS Neuroscience & Therapeutics* 28.1 (Jan. 2022), pp. 5–18. ISSN: 1755-5930, 1755-5949. DOI: 10.1111/cns.13769. URL: https://onlinelibrary.wiley.com/doi/10.1111/cns.13769 (visited on 09/25/2024).

[13] Nasser Zangiabadi et al. “Deep Brain Stimulation and Drug-Resistant Epilepsy: A Review of the Literature”. In: *Frontiers in Neurology* 10 (June 6, 2019), p. 601. ISSN: 1664-2295. DOI: 10.3389/fneur.2019.00601. URL: https://www.frontiersin.org/article/10.3389/fneur.2019.00601/full (visited on 09/26/2024).

[14] Viviana Gradinaru et al. “Optical Deconstruction of Parkinsonian Neural Circuitry”. In: *Science* 324.5925 (Apr. 17, 2009), pp. 354–359. ISSN: 0036-8075, 1095-9203. DOI: 10.1126/science.1167093. URL: https://www.science.org/doi/10.1126/science.1167093 (visited on 09/26/2024).

[15] Henri Lorach et al. “Walking Naturally after Spinal Cord Injury Using a Brain–Spine Interface”. In: *Nature* 618.7963 (June 1, 2023), pp. 126–133. ISSN: 0028-0836, 1476-4687. DOI: 10.1038/s41586-023-06094-5. URL: https://www.nature.com/articles/s41586-023-06094-5 (visited on 09/25/2024).

[16] Jasmina Cehajic-Kapetanovic et al. “Bioengineering Strategies for Restoring Vision”. In: *Nature Biomedical Engineering* 7.4 (Jan. 31, 2022), pp. 387–404. ISSN: 2157-846X. DOI: 10.1038/s41551-021-00836-4. URL: https://www.nature.com/articles/s41551-021-00836-4 (visited on 09/25/2024).

[17] Gerwin Schalk et al. “Translation of Neurotechnologies”. In: *Nature Reviews Bioengineering* 2.8 (May 31, 2024), pp. 637–652. ISSN: 2731-6092. DOI: 10.1038/s44222-024-00185-2. URL: https://www.nature.com/articles/s44222-024-00185-2 (visited on 09/25/2024).

[18] A. Tanwar et al. “A Review on Microelectrode Array Fabrication Techniques and Their Applications”. In: *Materials Today Chemistry* 26 (Dec. 2022), p. 101153. ISSN: 24685194. DOI: 10.1016/j.mtchem.2022.101153. URL: https://linkinghub.elsevier.com/retrieve/pii/S2468519422003822 (visited on 09/26/2024).

[19] Dongyang Yi et al. “Design, Fabrication, and Implantation of Invasive Microelectrode Arrays as in Vivo Brain Machine Interfaces: A Comprehensive Review”. In: *Journal of Manufacturing Processes* 126 (Sept. 2024), pp. 185–207. ISSN: 15266125. DOI: 10.1016/j.jmapro.2024.07.100. URL: https://linkinghub.elsevier.com/retrieve/pii/S152661252400759X (visited on 08/13/2024).

[20] Catherine A. Schevon et al. “Microphysiology of Epileptiform Activity in Human Neocortex”. In: *Journal of Clinical Neurophysiology* 25.6 (Dec. 2008), pp. 321–330. ISSN: 0736-0258. DOI: 10.1097/WNP.0b013e31818e8010. URL: https://journals.lww.com/00004691-200812000-00001 (visited on 08/20/2024).

[21] Mark S. Humayun et al. “Interim Results from the International Trial of Second Sight’s Visual Prosthesis”. In: *Ophthalmology* 119.4 (Apr. 2012), pp. 779–788. ISSN: 01616420. DOI: 10.1016/j.ophtha.2011.09.028. URL: https://linkinghub.elsevier.com/retrieve/pii/S0161642011008840 (visited on 01/14/2025).

[22] Ettore Beghi. “The Epidemiology of Epilepsy”. In: *Neuroepidemiology* 54.2 (2020), pp. 185–191. ISSN: 0251-5350, 1423-0208. DOI: 10.1159/000503831. URL: https://karger.com/NED/article/doi/10.1159/000503831 (visited on 08/20/2024).

[23] Lauren N. Ayton et al. “An Update on Retinal Prostheses”. In: *Clinical Neurophysiology* 131.6 (June 2020), pp. 1383–1398. ISSN: 13882457. DOI: 10.1016/j.clinph.2019.11.029. URL: https://linkinghub.elsevier.com/retrieve/pii/S1388245719313264 (visited on 07/03/2024).

[24] P.K. Campbell et al. “A Silicon-Based, Three-Dimensional Neural Interface: Manufacturing Processes for an Intracortical Electrode Array”. In: *IEEE Transactions on Biomedical Engineering* 38.8 (Aug./1991), pp. 758–768. ISSN: 00189294. DOI: 10.1109/10.83588. URL: http://ieeexplore.ieee.org/document/83588/ (visited on 07/16/2024).

[25] Kensall D. Wise, James B. Angell, and Arnold Starr. “An Integrated-Circuit Approach to Extracellular Microelectrodes”. In: *IEEE Transactions on Biomedical Engineering* BME-17.3 (July 1970), pp. 238–247. ISSN: 0018-9294, 1558-2531. DOI: 10.1109/TBME.1970.4502738. URL: http://ieeexplore.ieee.org/document/4502738/ (visited on 07/17/2024).

[26] K.D. Wise et al. “Wireless Implantable Microsystems: High-Density Electronic Interfaces to the Nervous System”. In: *Proceedings of the IEEE* 92.1 (Jan. 2004), pp. 76–97. ISSN: 0018-9219. DOI: 10.1109/JPROC.2003.820544. URL: http://ieeexplore.ieee.org/document/1258173/ (visited on 07/16/2024).

[27] Hyogeun Shin et al. “3D High-Density Microelectrode Array with Optical Stimulation and Drug Delivery for Investigating Neural Circuit Dynamics”. In: *Nature Communications* 12.1 (Jan. 21, 2021), p. 492. ISSN: 2041-1723. DOI: 10.1038/s41467-020-20763-3. URL: https://www.nature.com/articles/s41467-020-20763-3 (visited on 09/26/2024).

[28] Gustavo Rios et al. “Nanofabricated Neural Probes for Dense 3-D Recordings of Brain Activity”. In: *Nano Letters* 16.11 (Nov. 9, 2016), pp. 6857–6862. ISSN: 1530-6984, 1530-6992. DOI: 10.1021/acs.nanolett.6b02673. URL: https://pubs.acs.org/doi/10.1021/acs.nanolett.6b02673 (visited on 07/16/2024).

[29] Cristin G. Welle et al. “Longitudinal Neural and Vascular Structural Dynamics Produced by Chronic Microelectrode Implantation”. In: *Biomaterials* 238 (Apr. 2020), p. 119831. ISSN: 01429612. DOI: 10.1016/j.biomaterials.2020.119831. URL: https://linkinghub.elsevier.com/retrieve/pii/S0142961220300776 (visited on 07/17/2024).

[30] Paras R Patel et al. “Utah Array Characterization and Histological Analysis of a Multi-Year Implant in Non-Human Primate Motor and Sensory Cortices”. In: *Journal of Neural Engineering* 20.1 (Feb. 1, 2023), p. 014001. ISSN: 1741-2560, 1741-2552. DOI: 10.1088/1741-2552/acab86. URL: https://iopscience.iop.org/article/10.1088/1741-2552/acab86 (visited on 07/17/2024).

[31] Elon Musk and Neuralink. “An Integrated Brain-Machine Interface Platform With Thousands of Channels”. In: *Journal of Medical Internet Research* 21.10 (Oct. 31, 2019), e16194. ISSN: 1438-8871. DOI: 10.2196/16194. URL: http://www.jmir.org/2019/10/e16194/ (visited on 07/16/2024).

[32] Xiao Yang et al. “Bioinspired Neuron-like Electronics”. In: *Nature Materials* 18.5 (May 2019), pp. 510–517. ISSN: 1476-1122, 1476-4660. DOI: 10.1038/s41563-019-0292-9. URL: https://www.nature.com/articles/s41563-019-0292-9 (visited on 07/16/2024).

[33] Ming Yuan Cheng et al. “Three-Dimensional Flexible Polyimide Based Probe Array with Stiffness Improvement by Using Biodegradable Polymer”. In: *Advanced Materials Research* 651 (Jan. 2013), pp. 517–522. ISSN: 1662-8985. DOI: 10.4028/www.scientific.net/AMR.651.517. URL: https://www.scientific.net/AMR.651.517 (visited on 08/09/2024).

[34] Shoji Takeuchi et al. “3D Flexible Multichannel Neural Probe Array”. In: *Journal of Micromechanics and Microengineering* 14.1 (Jan. 1, 2004), pp. 104–107. ISSN: 0960-1317, 1361-6439. DOI: 10.1088/0960-1317/14/1/014. URL: https://iopscience.iop.org/article/10.1088/0960-1317/14/1/014 (visited on 07/17/2024).

[35] W. Sim et al. “Theoretical and Experimental Studies on the Parylene Diaphragms for Microdevices”. In: *Microsystem Technologies* 11.1 (Jan. 2005), pp. 11–15. ISSN: 0946-7076, 1432-1858. DOI: 10.1007/s00542-003-0342-7. URL: http://link.springer.com/10.1007/s00542-003-0342-7 (visited on 09/13/2024).

[36] David A. Soscia et al. “A Flexible 3-Dimensional Microelectrode Array for *in Vitro* Brain Models”. In: *Lab on a Chip* 20.5 (2020), pp. 901–911. ISSN: 1473-0197, 1473-0189. DOI: 10.1039/C9LC01148J. URL: https://xlink.rsc.org/?DOI=C9LC01148J (visited on 07/17/2024).

[37] Ju Young Lee et al. “Foldable Three Dimensional Neural Electrode Arrays for Simultaneous Brain Interfacing of Cortical Surface and Intracortical Multilayers”. In: *npj Flexible Electronics* 6.1 (Oct. 27, 2022), p. 86. ISSN: 2397-4621. DOI: 10.1038/s41528-022-00219-y. URL: https://www.nature.com/articles/s41528-022-00219-y (visited on 07/17/2024).

[38] Chang-Hsiao Chen et al. “A Three-Dimensional Flexible Microprobe Array for Neural Recording Assembled through Electrostatic Actuation”. In: *Lab on a Chip* 11.9 (2011), p. 1647. ISSN: 1473-0197, 1473-0189. DOI: 10.1039/c0lc00718h. URL: https://xlink.rsc.org/?DOI=c0lc00718h (visited on 09/26/2024).

[39] Alexander K. Nguyen and Roger J. Narayan. “Two-Photon Polymerization for Biological Applications”. In: *Materials Today* 20.6 (July 2017), pp. 314–322. ISSN: 13697021. DOI: 10.1016/j.mattod.2017.06.004. URL: https://linkinghub.elsevier.com/retrieve/pii/S1369702117303917 (visited on 09/26/2024).

[40] Zahra Faraji Rad, Philip D. Prewett, and Graham J. Davies. “High-Resolution Two-Photon Polymerization: The Most Versatile Technique for the Fabrication of Microneedle Arrays”. In: *Microsystems & Nanoengineering* 7.1 (Sept. 3, 2021), p. 71. ISSN: 2055-7434. DOI: 10.1038/s41378-021-00298-3. URL: https://www.nature.com/articles/s41378-021-00298-3 (visited on 09/26/2024).

[41] J. Abu Shihada et al. “Highly Customizable 3D Microelectrode Arrays for In Vitro and In Vivo Neuronal Tissue Recordings”. In: *Advanced Science* 11.13 (Apr. 2024), p. 2305944. ISSN: 2198-3844, 2198-3844. DOI: nru. URL: https://onlinelibrary.wiley.com/doi/10.1002/advs.202305944 (visited on 07/02/2024).

[42] Mark F. Bear, Barry W. Connors, and Michael A. Paradiso. *Neuroscience: Exploring the Brain*. Fourth edition. Philadelphia: Wolters Kluwer, 2016. 975 pp. ISBN: 978-0-7817-7817-6.

[43] Eric R. Kandel et al., eds. *Principles of Neural Science*. 5th ed. New York: McGraw-Hill, 2013. ISBN: 978-1-283-65624-5.

[44] Paul Johns. “Electrical Signalling in Neurons”. In: *Clinical Neuroscience*. Elsevier, 2014, pp. 71–80. ISBN: 978-0-443-10321-6. DOI: 10.1016/B978-0-443-10321-6.00006-0. URL: https://linkinghub.elsevier.com/retrieve/pii/B9780443103216000060 (visited on 07/23/2024).

[45] Walter F. Boron and Emile L. Boulpaep, eds. *Medical Physiology*. Third edition. Philadelphia, PA: Elsevier, 2017. 1297 pp. ISBN: 978-1-4557-4377-3 978-0-323-42796-8 978-0-323-31973-7.

[46] Anne M. Gilroy et al., eds. *Atlas of Anatomy*. Third edition. New York: Thieme, 2016. ISBN: 978-1-62623-252-5.

[47] Frank H. Netter. *Atlas of Human Anatomy*. Seventh edition. Philadelphia, PA: Elsevier, 2019. ISBN: 978-0-323-39322-5.

[48] Tomomi Ichinose and Samar Habib. "On and off Signaling Pathways in the Retina and the Visual System". In: *Frontiers in Ophthalmology* 2 (Aug. 26, 2022), p. 989002. ISSN: 2674-0826. DOI: 10.3389/fopht.2022.989002. URL: https://www.frontiersin.org/articles/10.3389/fopht.2022.989002/full (visited on 07/05/2024).

[49] Leo Peichl. "Retinal Ganglion Cells". In: *Encyclopedia of Neuroscience*. Ed. by Marc D. Binder, Nobutaka Hirokawa, and Uwe Windhorst. Berlin, Heidelberg: Springer Berlin Heidelberg, 2009, pp. 3507–3513. ISBN: 978-3-540-23735-8 978-3-540-29678-2. DOI: 10.1007/978-3-540-29678-2_5106. URL: https://link.springer.com/10.1007/978-3-540-29678-2_5106 (visited on 07/15/2024).

[50] T.A. Münch. "Information Processing: Ganglion Cells". In: *Encyclopedia of the Eye*. Elsevier, 2010, pp. 355–362. ISBN: 978-0-12-374203-2. DOI: 10.1016/B978-0-12-374203-2.00198-6. URL: https://linkinghub.elsevier.com/retrieve/pii/B9780123742032001986 (visited on 07/05/2024).

[51] Rainer Goebel, Lars Muckli, and Dae-Shik Kim. "Visual System". In: *The Human Nervous System*. Elsevier, 2012, pp. 1301–1327. ISBN: 978-0-12-374236-0. DOI: 10.1016/B978-0-12-374236-0.10037-9. URL: https://linkinghub.elsevier.com/retrieve/pii/B9780123742360100379 (visited on 07/15/2024).

[52] Bryan W. Jones, Robert E. Marc, and Carl B. Watt. "Retinal Remodeling and Visual Prosthetics". In: *Visual Prosthetics*. Ed. by Gislin Dagnelie. Boston, MA: Springer US, 2011, pp. 59–75. ISBN: 978-1-4419-0753-0 978-1-4419-0754-7. DOI: 10.1007/978-1-4419-0754-7_3. URL: https://link.springer.com/10.1007/978-1-4419-0754-7_3 (visited on 08/20/2024).

[53] Madhurima Chaudhuri et al. "Age-Related Macular Degeneration: An Exponentially Emerging Imminent Threat of Visual Impairment and Irreversible Blindness". In: *Cureus* (May 29, 2023). ISSN: 2168-8184. DOI: 10.7759/cureus.39624. URL: https://www.cureus.com/articles/159274-age-related-macular-degeneration-an-exponentially-emerging-imminent-threat-of-visual-impairment-and-irreversible-blindness (visited on 08/20/2024).

[54] Geneva: World Health Organization. *World Report on Vision*. 2019.

[55] Nancy Cross et al. "Retinitis Pigmentosa: Burden of Disease and Current Unmet Needs". In: *Clinical Ophthalmology* Volume 16 (June 2022), pp. 1993–2010. ISSN: 1177-5483. DOI: 10.2147/OPTH.S365486. URL: https://www.dovepress.com/retinitis-pigmentosa-burden-of-disease-and-current-unmet-needs-peer-reviewed-fulltext-article-OPTH (visited on 08/20/2024).

[56] World Health Organization. *Epilepsy: A Public Health Imperative*. Geneva: World Health Organization, 2019. 146 pp. ISBN: 978-92-4-151593-1. URL: https://iris.who.int/handle/10665/325293 (visited on 08/20/2024).

[57] Thomas J. Foutz and Michael Wong. “Brain Stimulation Treatments in Epilepsy: Basic Mechanisms and Clinical Advances”. In: *Biomedical Journal* 45.1 (Feb. 2022), pp. 27–37. ISSN: 23194170. DOI: 10.1016/j.bj.2021.08.010. URL: https://linkinghub.elsevier.com/retrieve/pii/S2319417021001104 (visited on 08/20/2024).

[58] James Sun et al. “Intraoperative Microseizure Detection Using a High-Density Micro-Electrocorticography Electrode Array”. In: *Brain Communications* 4.3 (May 2, 2022), fcac122. ISSN: 2632-1297. DOI: 10.1093/braincomms/fcac122. URL: https://academic.oup.com/braincomms/article/doi/10.1093/braincomms/fcac122/6593922 (visited on 08/20/2024).

[59] Renxin Wang, Huaiqiang Yu, and Zhihong Li. “Microelectrode Array”. In: *Micro Electro Mechanical Systems*. Ed. by Qing-An Huang. Singapore: Springer Singapore, 2018, pp. 1379–1411. ISBN: 978-981-10-5944-5 978-981-10-5945-2. DOI: 10.1007/978-981-10-5945-2_41. URL: http://link.springer.com/10.1007/978-981-10-5945-2_41 (visited on 08/06/2024).

[60] Marie Engelene J. Obien et al. “Revealing Neuronal Function through Microelectrode Array Recordings”. In: *Frontiers in Neuroscience* 8 (Jan. 6, 2015). ISSN: 1662-453X. DOI: 10.3389/fnins.2014.00423. URL: http://journal.frontiersin.org/article/10.3389/fnins.2014.00423/abstract (visited on 08/07/2024).

[61] Qing-An Huang, ed. *Micro Electro Mechanical Systems*. Micro/Nano Technologies. Singapore: Springer Singapore, 2018. ISBN: 978-981-10-5944-5 978-981-10-5945-2. DOI: 10.1007/978-981-10-5945-2. URL: http://link.springer.com/10.1007/978-981-10-5945-2 (visited on 08/06/2024).

[62] Kailyn A. Ramirez et al. “An Update on Visual Prosthesis”. In: *International Journal of Retina and Vitreous* 9.1 (Nov. 23, 2023), p. 73. ISSN: 2056-9920. DOI: 10.1186/s40942-023-00498-1. URL: https://journalretinavitreous.biomedcentral.com/articles/10.1186/s40942-023-00498-1 (visited on 09/27/2024).

[63] Johannes B Erhardt et al. “Should Patients with Brain Implants Undergo MRI?” In: *Journal of Neural Engineering* 15.4 (Aug. 1, 2018), p. 041002. ISSN: 1741-2560, 1741-2552. DOI: 10.1088/1741-2552/aab4e4. URL: https://iopscience.iop.org/article/10.1088/1741-2552/aab4e4 (visited on 09/01/2025).

[64] Michele Bianchi et al. “Poly(3,4-ethylenedioxythiophene)-Based Neural Interfaces for Recording and Stimulation: Fundamental Aspects and In Vivo Applications”. In: *Advanced Science* 9.12 (Apr. 2022), p. 2104701. ISSN: 2198-3844, 2198-3844. DOI: 10.1002/advs.202104701. URL: https://onlinelibrary.wiley.com/doi/10.1002/advs.202104701 (visited on 09/01/2025).

[65] Thomas Niederhoffer, Anne Vanhoestenberghe, and Henry T Lancashire. “Methods of Poly(3,4)-Ethylenedioxithiophene (PEDOT) Electrodeposition on Metal Electrodes for Neural Stimulation and Recording”. In: *Journal of Neural Engineering* 20.1 (Feb. 1, 2023), p. 011002. ISSN: 1741-2560, 1741-2552. DOI: 10.1088/1741-2552/acb084. URL: https://iopscience.iop.org/article/10.1088/1741-2552/acb084 (visited on 09/27/2024).

[66] Lina Koschinski et al. “Validation of Transparent and Flexible Neural Implants for Simultaneous Electrophysiology, Functional Imaging, and Optogenetics”. In: *Journal of Materials Chemistry B* 11.40 (2023), pp. 9639–9657. ISSN: 2050-750X, 2050-7518. DOI: 10.1039/D3TB01191G. URL: https://xlink.rsc.org/?DOI=D3TB01191G (visited on 10/22/2024).

[67] Ece Boran et al. “High-Density ECoG Improves the Detection of High Frequency Oscillations That Predict Seizure Outcome”. In: *Clinical Neurophysiology* 130.10 (Oct. 2019), pp. 1882–1888. ISSN: 1388-2457. DOI: 10.1016/j.clinph.2019.07.008. URL: https://linkinghub.elsevier.com/retrieve/pii/S1388245719311526 (visited on 01/14/2025).

[68] Lukas Hiendlmeier et al. “4D-Printed Soft and Stretchable Self-Folding Cuff Electrodes for Small-Nerve Interfacing”. In: *Advanced Materials* 35.12 (Mar. 2023), p. 2210206. ISSN: 0935-9648, 1521-4095. DOI: 10.1002/adma.202210206. URL: https://onlinelibrary.wiley.com/doi/10.1002/adma.202210206 (visited on 01/14/2025).

[69] Alejandro Carnicer-Lombarte et al. “Ultraconformable Cuff Implants for Long-Term Bidirectional Interfacing of Peripheral Nerves at Sub-Nerve Resolutions”. In: *Nature Communications* 15.1 (Aug. 30, 2024), p. 7523. ISSN: 2041-1723. DOI: 10.1038/s41467-024-51988-1. URL: https://www.nature.com/articles/s41467-024-51988-1 (visited on 01/14/2025).

[70] Valentina Paggi et al. “A Soft, Scalable and Adaptable Multi-Contact Cuff Electrode for Targeted Peripheral Nerve Modulation”. In: *Bioelectronic Medicine* 10.1 (Feb. 14, 2024), p. 6. ISSN: 2332-8886. DOI: 10.1186/s42234-023-00137-y. URL: https://bioelecmed.biomedcentral.com/articles/10.1186/s42234-023-00137-y (visited on 01/14/2025).

[71] Konlin Shen et al. “Translational Opportunities and Challenges of Invasive Electrodes for Neural Interfaces”. In: *Nature Biomedical Engineering* 7.4 (Apr. 20, 2023), pp. 424–442. ISSN: 2157-846X. DOI: 10.1038/s41551-023-01021-5. URL: https://www.nature.com/articles/s41551-023-01021-5 (visited on 07/03/2024).

[72] Eve McGlynn et al. “The Future of Neuroscience: Flexible and Wireless Implantable Neural Electronics”. In: *Advanced Science* 8.10 (May 2021), p. 2002693. ISSN: 2198-3844, 2198-3844. DOI: 10.1002/advs.202002693. URL: https://onlinelibrary.wiley.com/doi/10.1002/advs.202002693 (visited on 08/06/2024).

[73] Daniel R. Merrill, Marom Bikson, and John G.R. Jefferys. “Electrical Stimulation of Excitable Tissue: Design of Efficacious and Safe Protocols”. In: *Journal of Neuroscience Methods* 141.2 (Feb. 2005), pp. 171–198. ISSN: 01650270. DOI: 10.1016/j.jneumeth.2004.10.020. URL: https://linkinghub.elsevier.com/retrieve/pii/S0165027004003826 (visited on 08/06/2024).

[74] Zbigniew Stojek. “The Electrical Double Layer and Its Structure”. In: *Electroanalytical Methods*. Ed. by Fritz Scholz et al. Berlin, Heidelberg: Springer Berlin Heidelberg, 2010, pp. 3–9. ISBN: 978-3-642-02914-1 978-3-642-02915-8. DOI: 10.1007/978-3-642-02915-8_1. URL: http://link.springer.com/10.1007/978-3-642-02915-8_1 (visited on 08/06/2024).

[75] Aditi Ray and James D. Weiland. “Structures, Materials, and Processes at the Electrode-to-Tissue Interface”. In: *Visual Prosthetics*. Ed. by Gislin Dagnelie. Boston, MA: Springer US, 2011, pp. 113–135. ISBN: 978-1-4419-0753-0 978-1-4419-0754-7. DOI: 10.1007/978-1-4419-0754-7_6. URL: https://link.springer.com/10.1007/978-1-4419-0754-7_6 (visited on 07/16/2024).

[76] Paolo Massobrio, Giuseppe Massobrio, and Sergio Martinoia. “Interfacing Cultured Neurons to Microtransducers Arrays: A Review of the Neuro-Electronic Junction Models”. In: *Frontiers in Neuroscience* 10 (June 21, 2016). ISSN: 1662-453X. DOI: 10.3389/fnins.2016.00282. URL: http://journal.frontiersin.org/Article/10.3389/fnins.2016.00282/abstract (visited on 08/06/2024).

[77] Micha E. Spira and Aviad Hai. “Multi-Electrode Array Technologies for Neuroscience and Cardiology”. In: *Nature Nanotechnology* 8.2 (Feb. 2013), pp. 83–94. ISSN: 1748-3387, 1748-3395. DOI: 10.1038/nnano.2012.265. URL: https://www.nature.com/articles/nnano.2012.265 (visited on 08/07/2024).

[78] Viviana Rincón Montes et al. “Toward a Bidirectional Communication Between Retinal Cells and a Prosthetic Device – A Proof of Concept”. In: *Frontiers in Neuroscience* 13 (Apr. 30, 2019), p. 367. ISSN: 1662-453X. DOI: 10.3389/fnins.2019.00367. URL: https://www.frontiersin.org/article/10.3389/fnins.2019.00367/full (visited on 08/26/2024).

[79] Bartosz Teleńczuk and Alain Destexhe. “Local Field Potential, Relationship to Unit Activity”. In: *Encyclopedia of Computational Neuroscience*. Ed. by Dieter Jaeger and Ranu Jung. New York, NY: Springer New York, 2014, pp. 1–6. ISBN: 978-1-4614-7320-6. DOI: 10.1007/978-1-4614-7320-6_543-1. URL: https://link.springer.com/10.1007/978-1-4614-7320-6_543-1 (visited on 08/07/2024).

[80] David T. Brocker and Warren M. Grill. “Principles of Electrical Stimulation of Neural Tissue”. In: *Handbook of Clinical Neurology*. Vol. 116. Elsevier, 2013, pp. 3–18. ISBN: 978-0-444-53497-2. DOI: 10.1016/B978-0-444-53497-2.00001-2. URL: https://linkinghub.elsevier.com/retrieve/pii/B9780444534972000012 (visited on 08/07/2024).

[81] Andrew M. Geller, Catherine M. Osborne, and Robert L. Peiffer. “The ERG, EOG, and VEP in Rats”. In: *Ocular Toxicology*. Ed. by Ingo Weisse et al. Boston, MA: Springer US, 1995, pp. 7–25. ISBN: 978-1-4613-5769-8 978-1-4615-1887-7. DOI: 10.1007/978-1-4615-1887-7_2. URL: http://link.springer.com/10.1007/978-1-4615-1887-7_2 (visited on 02/10/2025).

[82] Lawrence H. Pinto et al. “Interpretation of the Mouse Electroretinogram”. In: *Documenta Ophthalmologica* 115.3 (Oct. 30, 2007), pp. 127–136. ISSN: 0012-4486, 1573-2622. DOI: 10.1007/s10633-007-9064-y. URL: http://link.springer.com/10.1007/s10633-007-9064-y (visited on 02/10/2025).

[83] Ido Perlman. “The Electroretinogram: ERG”. In: *Webvision: The Organization of the Retina and Visual System*. Ed. by Helga Kolb et al. Salt Lake City (UT): University of Utah Health Sciences Center, 1995. pmid: 21413407. URL: http://www.ncbi.nlm.nih.gov/books/NBK11554/ (visited on 02/10/2025).

[84] Rüdiger Land et al. “32-Channel Mouse EEG: Visual Evoked Potentials”. In: *Journal of Neuroscience Methods* 325 (Sept. 2019), p. 108316. ISSN: 01650270. DOI: 10.1016/j.jneumeth.2019.108316. URL: https://linkinghub.elsevier.com/retrieve/pii/S0165027019301748 (visited on 02/18/2025).

[85] Jonas Duun-Henriksen et al. “EEG Signal Quality of a Subcutaneous Recording System Compared to Standard Surface Electrodes”. In: *Journal of Sensors* 2015 (2015), pp. 1–9. ISSN: 1687-725X, 1687-7268. DOI: 10.1155/2015/341208. URL: http://www.hindawi.com/journals/js/2015/341208/ (visited on 02/18/2025).

[86] Jorma O. Ollikainen et al. “Effects of Electrode Properties on EEG Measurements and a Related Inverse Problem”. In: *Medical Engineering & Physics* 22.8 (Oct. 2000), pp. 535–545. ISSN: 13504533. DOI: 10.1016/S1350-4533(00)00070-9. URL: https://linkinghub.elsevier.com/retrieve/pii/S1350453300000709 (visited on 02/18/2025).

[87] Michael S. Beauchamp et al. “Dynamic Stimulation of Visual Cortex Produces Form Vision in Sighted and Blind Humans”. In: *Cell* 181.4 (May 2020), 774–783.e5. ISSN: 00928674. DOI: 10.1016/j.cell.2020.04.033. URL: https://linkinghub.elsevier.com/retrieve/pii/S0092867420304967 (visited on 07/03/2024).

[88] Héctor Acarón Ledesma et al. “An Atlas of Nano-Enabled Neural Interfaces”. In: *Nature Nanotechnology* 14.7 (July 2019), pp. 645–657. ISSN: 1748-3387, 1748-3395. DOI: 10.1038/s41565-019-0487-x. URL: https://www.nature.com/articles/s41565-019-0487-x (visited on 08/08/2024).

[89] James A. Frank, Marc-Joseph Antonini, and Polina Anikeeva. “Next-Generation Interfaces for Studying Neural Function”. In: *Nature Biotechnology* 37.9 (Sept. 2019), pp. 1013–1023. ISSN: 1087-0156, 1546-1696. DOI: 10.1038/s41587-019-0198-8. URL: https://www.nature.com/articles/s41587-019-0198-8 (visited on 08/08/2024).

[90] Stéphanie P. Lacour, Grégoire Courtine, and Jochen Guck. “Materials and Technologies for Soft Implantable Neuroprostheses”. In: *Nature Reviews Materials* 1.10 (Sept. 27, 2016), p. 16063. ISSN: 2058-8437. DOI: 10.1038/natrevmats.2016.63. URL: https://www.nature.com/articles/natrevmats201663 (visited on 08/08/2024).

[91] Qi Zeng and Zhaoling Huang. “Challenges and Opportunities of Implantable Neural Interfaces: From Material, Electrochemical and Biological Perspectives”. In: *Advanced Functional Materials* 33.32 (Aug. 2023), p. 2301223. ISSN: 1616-301X, 1616-3028. DOI: 10.1002/adfm.202301223. URL: https://onlinelibrary.wiley.com/doi/10.1002/adfm.202301223 (visited on 08/07/2024).

[92] Christian Boehler et al. “Tutorial: Guidelines for Standardized Performance Tests for Electrodes Intended for Neural Interfaces and Bioelectronics”. In: *Nature Protocols* 15.11 (Nov. 2020), pp. 3557–3578. ISSN: 1754-2189, 1750-2799. DOI: 10.1038/s41596-020-0389-2. URL: https://www.nature.com/articles/s41596-020-0389-2 (visited on 08/08/2024).

[93] Christopher M. Lewis et al. “Recording Quality Is Systematically Related to Electrode Impedance”. In: *Advanced Healthcare Materials* (Feb. 23, 2024), p. 2303401. ISSN: 2192-2640, 2192-2659. DOI: 10.1002/adhm.202303401. URL: https://onlinelibrary.wiley.com/doi/10.1002/adhm.202303401 (visited on 08/08/2024).

[94] Aziliz Lecomte, Emeline Descamps, and Christian Bergaud. “A Review on Mechanical Considerations for Chronically-Implanted Neural Probes”. In: *Journal of Neural Engineering* 15.3 (June 1, 2018), p. 031001. ISSN: 1741-2560, 1741-2552. DOI: 10.1088/1741-2552/aa8b4f. URL: https://iopscience.iop.org/article/10.1088/1741-2552/aa8b4f (visited on 08/09/2024).

[95] C S Bjornsson et al. “Effects of Insertion Conditions on Tissue Strain and Vascular Damage during Neuroprosthetic Device Insertion”. In: *Journal of Neural Engineering* 3.3 (Sept. 1, 2006), pp. 196–207. ISSN: 1741-2560, 1741-2552. DOI: 10.1088/1741-2560/3/3/002. URL: https://iopscience.iop.org/article/10.1088/1741-2560/3/3/002 (visited on 08/09/2024).

[96] Arati Sridharan and Jit Muthuswamy. “Quantitative Assessment of the Mechanical Properties of the Neural Interface”. In: *Handbook of Neuroengineering*. Ed. by Nitish V. Thakor. Singapore: Springer Singapore, 2021, pp. 1–47. ISBN: 9789811528484. DOI: 10.1007/978-981-15-2848-4_4-1. URL: https://link.springer.com/10.1007/978-981-15-2848-4_4-1 (visited on 08/09/2024).

[97] Hannah R Joo et al. “A Microfabricated, 3D-sharpened Silicon Shuttle for Insertion of Flexible Electrode Arrays through Dura Mater into Brain”. In: *Journal of Neural Engineering* 16.6 (Dec. 1, 2019), p. 066021. ISSN: 1741-2560, 1741-2552. DOI: 10.1088/1741-2552/ab2b2e. URL: https://iopscience.iop.org/article/10.1088/1741-2552/ab2b2e (visited on 08/09/2024).

[98] Zhengtuo Zhao et al. “Parallel, Minimally-Invasive Implantation of Ultra-Flexible Neural Electrode Arrays”. In: *Journal of Neural Engineering* 16.3 (June 1, 2019), p. 035001. ISSN: 1741-2560, 1741-2552. DOI: 10.1088/1741-2552/ab05b6. URL: https://iopscience.iop.org/article/10.1088/1741-2552/ab05b6 (visited on 08/09/2024).

[99] Sagnik Middya et al. “Multishank Thin-Film Neural Probes and Implantation System for High-Resolution Neural Recording Applications”. In: *Advanced Electronic Materials* 9.9 (Sept. 2023), p. 2200883. ISSN: 2199-160X, 2199-160X. DOI: 10.1002/aelm.202200883. URL: https://onlinelibrary.wiley.com/doi/10.1002/aelm.202200883 (visited on 08/09/2024).

[100] Timothy L Hanson et al. *The "Sewing Machine" for Minimally Invasive Neural Recording*. Mar. 14, 2019. URL: http://biorxiv.org/lookup/doi/10.1101/578542 (visited on 08/09/2024). Pre-published.

[101] Yu Zhou et al. "A Mosquito Mouthpart-like Bionic Neural Probe". In: *Microsystems & Nanoengineering* 9.1 (July 12, 2023), p. 88. ISSN: 2055-7434. DOI: 10.1038/s41378-023-00565-5. URL: https://www.nature.com/articles/s41378-023-00565-5 (visited on 08/09/2024).

[102] Kagithiri Srikantharajah et al. "Minimally-Invasive Insertion Strategy and in Vivo Evaluation of Multi-Shank Flexible Intracortical Probes". In: *Scientific Reports* 11.1 (Sept. 23, 2021), p. 18920. ISSN: 2045-2322. DOI: 10.1038/s41598-021-97940-x. URL: https://www.nature.com/articles/s41598-021-97940-x (visited on 08/09/2024).

[103] Seongjun Park et al. "Adaptive and Multifunctional Hydrogel Hybrid Probes for Long-Term Sensing and Modulation of Neural Activity". In: *Nature Communications* 12.1 (June 8, 2021), p. 3435. ISSN: 2041-1723. DOI: 10.1038/s41467-021-23802-9. URL: https://www.nature.com/articles/s41467-021-23802-9 (visited on 08/09/2024).

[104] Fei He et al. "Ultraflexible Neural Electrodes for Long-Lasting Intracortical Recording". In: *iScience* 23.8 (Aug. 2020), p. 101387. ISSN: 25890042. DOI: 10.1016/j.isci.2020.101387. URL: https://linkinghub.elsevier.com/retrieve/pii/S2589004220305757 (visited on 08/09/2024).

[105] James C Barrese, Juan Aceros, and John P Donoghue. "Scanning Electron Microscopy of Chronically Implanted Intracortical Microelectrode Arrays in Non-Human Primates". In: *Journal of Neural Engineering* 13.2 (Apr. 1, 2016), p. 026003. ISSN: 1741-2560, 1741-2552. DOI: 10.1088/1741-2560/13/2/026003. URL: https://iopscience.iop.org/article/10.1088/1741-2560/13/2/026003 (visited on 09/18/2024).

[106] J.D. Weiland and D.J. Anderson. "Chronic Neural Stimulation with Thin-Film, Iridium Oxide Electrodes". In: *IEEE Transactions on Biomedical Engineering* 47.7 (July 2000), pp. 911–918. ISSN: 00189294. DOI: 10.1109/10.846685. URL: http://ieeexplore.ieee.org/document/846685/ (visited on 09/18/2024).

[107] János A Perge et al. "Intra-Day Signal Instabilities Affect Decoding Performance in an Intracortical Neural Interface System". In: *Journal of Neural Engineering* 10.3 (June 1, 2013), p. 036004. ISSN: 1741-2560, 1741-2552. DOI: 10.1088/1741-2560/10/3/036004. URL: https://iopscience.iop.org/article/10.1088/1741-2560/10/3/036004 (visited on 09/18/2024).

[108] Hsin-Yi Lai et al. "Design, Simulation and Experimental Validation of a Novel Flexible Neural Probe for Deep Brain Stimulation and Multichannel Recording". In: *Journal of Neural Engineering* 9.3 (June 1, 2012), p. 036001. ISSN: 1741-2560, 1741-2552. DOI: 10.1088/1741-2560/9/3/036001. URL: https://iopscience.iop.org/article/10.1088/1741-2560/9/3/036001 (visited on 09/18/2024).

[109] Maria Vomero et al. "On the Longevity of Flexible Neural Interfaces: Establishing Biostability of Polyimide-Based Intracortical Implants". In: *Biomaterials* 281 (Feb. 2022), p. 121372. ISSN: 01429612. DOI: 10.1016/j.biomaterials.2022.121372. URL: https://linkinghub.elsevier.com/retrieve/pii/S0142961222000114 (visited on 09/18/2024).

[110] Tian-Ming Fu et al. "Stable Long-Term Chronic Brain Mapping at the Single-Neuron Level". In: *Nature Methods* 13.10 (Oct. 2016), pp. 875–882. ISSN: 1548-7091, 1548-7105. DOI: 10.1038/nmeth.3969. URL: https://www.nature.com/articles/nmeth.3969 (visited on 09/18/2024).

[111] Ryan Caldwell et al. “Characterization of Parylene-C Degradation Mechanisms: In Vitro Reactive Accelerated Aging Model Compared to Multiyear in Vivo Implantation”. In: *Biomaterials* 232 (Feb. 2020), p. 119731. ISSN: 01429612. DOI: 10.1016/j.biomaterials.2019.119731. URL: https://linkinghub.elsevier.com/retrieve/pii/S014296121930849X (visited on 09/18/2024).

[112] Poppy Oldroyd and George G Malliaras. “Achieving Long-Term Stability of Thin-Film Electrodes for Neurostimulation”. In: *Acta Biomaterialia* 139 (Feb. 2022), pp. 65–81. ISSN: 17427061. DOI: 10.1016/j.actbio.2021.05.004. URL: https://linkinghub.elsevier.com/retrieve/pii/S1742706121003056 (visited on 09/18/2024).

[113] Seung-Jae Kim et al. “Electrophysiological Mapping of Cat Primary Auditory Cortex with Multielectrode Arrays”. In: *Annals of Biomedical Engineering* 34.2 (Feb. 2006), pp. 300–309. ISSN: 0090-6964, 1573-9686. DOI: 10.1007/s10439-005-9037-9. URL: http://link.springer.com/10.1007/s10439-005-9037-9 (visited on 07/16/2024).

[114] Leroy Grob et al. “Inkjet-Printed and Electroplated 3D Electrodes for Recording Extracellular Signals in Cell Culture”. In: *Sensors* 21.12 (June 9, 2021), p. 3981. ISSN: 1424-8220. DOI: 10.3390/s21123981. URL: https://www.mdpi.com/1424-8220/21/12/3981 (visited on 07/16/2024).

[115] Amin Sandoughsaz Zardini et al. *Sea of Electrodes Array (SEA): Extremely Dense and High-Count Silicon-Based Electrode Array Technology for High-Resolution High-Bandwidth Interfacing with 3D Neural Structures*. Jan. 26, 2021. URL: http://biorxiv.org/lookup/doi/10.1101/2021.01.24.427975 (visited on 07/16/2024). Pre-published.

[116] Sang Heon Lee et al. “Scalable Thousand Channel Penetrating Microneedle Arrays on Flex for Multimodal and Large Area Coverage BrainMachine Interfaces”. In: *Advanced Functional Materials* 32.25 (June 2022), p. 2112045. ISSN: 1616-301X, 1616-3028. DOI: 10.1002/adfm.202112045. URL: https://onlinelibrary.wiley.com/doi/10.1002/adfm.202112045 (visited on 07/16/2024).

[117] Morgan A. Brown et al. “Direct Laser Writing of 3D Electrodes on Flexible Substrates”. In: *Nature Communications* 14.1 (June 17, 2023), p. 3610. ISSN: 2041-1723. DOI: 10.1038/s41467-023-39152-7. URL: https://www.nature.com/articles/s41467-023-39152-7 (visited on 07/16/2024).

[118] Jason E. Chung et al. “High-Density, Long-Lasting, and Multi-region Electrophysiological Recordings Using Polymer Electrode Arrays”. In: *Neuron* 101.1 (Jan. 2019), 21–31.e5. ISSN: 08966273. DOI: 10.1016/j.neuron.2018.11.002. URL: https://linkinghub.elsevier.com/retrieve/pii/S0896627318309930 (visited on 07/17/2024).

[119] Richard A Normann. “Technology Insight: Future Neuroprosthetic Therapies for Disorders of the Nervous System”. In: *Nature Clinical Practice Neurology* 3.8 (Aug. 2007), pp. 444–452. ISSN: 1745-834X, 1745-8358. DOI: 10.1038/ncpneuro0556. URL: https://www.nature.com/articles/ncpneuro0556 (visited on 09/27/2024).

[120] Matthew A. Hopcroft, William D. Nix, and Thomas W. Kenny. “What Is the Young’s Modulus of Silicon?” In: *Journal of Microelectromechanical Systems* 19.2 (Apr. 2010), pp. 229–238. ISSN: 1057-7157, 1941-0158. DOI: 10.1109/jmems.2009.2039697. URL: http://ieeexplore.ieee.org/document/5430873/ (visited on 01/14/2025).

[121] Nicholas F. Nolta, Michael B. Christensen, and Patrick A. Tresco. “Advanced Age Is Not a Barrier to Chronic Intracortical Single-Unit Recording in Rat Cortex”. In: *Frontiers in Neuroscience* 18 (May 15, 2024), p. 1389556. ISSN: 1662-453X. DOI: 10.3389/fnins.2024.1389556. URL: https://www.frontiersin.org/articles/10.3389/fnins.2024.1389556/full (visited on 07/17/2024).

[122] Neuralink and Elon Musk. “Neuralink Clinical Trial (PRIME Study: Precise Robotically Implanted Brain-Computer Interface)”. In: ().

[123] Gurbir S. Grewal and Nicole Creola Kelly. *Request for Investigation of Neuralink Corp. and Its Chief Executive Officer Elon Musk for Securities Fraud*. Letter. Sept. 20, 2023.

[124] Kyoseung Sim et al. “Curvy Surface Conformal Ultra-Thin Transfer Printed Si Optoelectronic Penetrating Microprobe Arrays”. In: *npj Flexible Electronics* 2.1 (Jan. 18, 2018), p. 2. ISSN: 2397-4621. DOI: 10.1038/s41528-017-0015-8. URL: https://www.nature.com/articles/s41528-017-0015-8 (visited on 11/04/2024).

[125] Eduardo Fernandez. “Development of Visual Neuroprostheses: Trends and Challenges”. In: *Bioelectronic Medicine* 4.1 (Dec. 2018). ISSN: 2332-8886. DOI: 10.1186/s42234-018-0013-8. URL: https://bioelecmed.biomedcentral.com/articles/10.1186/s42234-018-0013-8 (visited on 01/14/2025).

[126] Ivan Tochitsky and Richard H Kramer. “Optopharmacological Tools for Restoring Visual Function in Degenerative Retinal Diseases”. In: *Current Opinion in Neurobiology* 34 (Oct. 2015), pp. 74–78. ISSN: 09594388. DOI: 10.1016/j.conb.2015.01.018. URL: https://linkinghub.elsevier.com/retrieve/pii/S0959438815000276 (visited on 07/03/2024).

[127] Deniz Dalkara et al. “Let There Be Light: Gene and Cell Therapy for Blindness”. In: *Human Gene Therapy* 27.2 (Feb. 2016), pp. 134–147. ISSN: 1043-0342, 1557-7422. DOI: 10.1089/hum.2015.147. URL: http://www.liebertpub.com/doi/10.1089/hum.2015.147 (visited on 07/03/2024).

[128] Edward Bloch, Yvonne Luo, and Lyndon Da Cruz. “Advances in Retinal Prosthesis Systems”. In: *Therapeutic Advances in Ophthalmology* 11 (Jan. 2019), p. 251584141881750. ISSN: 2515-8414, 2515-8414. DOI: 10.1177/2515841418817501. URL: http://journals.sagepub.com/doi/10.1177/2515841418817501 (visited on 07/03/2024).

[129] Gernot Roessler et al. “Implantation and Explantation of a Wireless Epiretinal Retina Implant Device: Observations during the EPIRET3 Prospective Clinical Trial”. In: *Investigative Opthalmology & Visual Science* 50.6 (June 1, 2009), p. 3003. ISSN: 1552-5783. DOI: 10.1167/iovs.08-2752. URL: http://iovs.arvojournals.org/article.aspx?doi=10.1167/iovs.08-2752 (visited on 07/03/2024).

[130] Katrin Gekeler et al. “Implantation, Removal and Replacement of Subretinal Electronic Implants for Restoration of Vision in Patients with Retinitis Pigmentosa”. In: *Current Opinion in Ophthalmology* 29.3 (May 2018), pp. 239–247. ISSN: 1040-8738. DOI: 10.1097/ICU.0000000000000467. URL: https://journals.lww.com/00055735-201805000-00009 (visited on 07/03/2024).

[131] Daniel Palanker. “Electronic Retinal Prostheses”. In: *Cold Spring Harbor Perspectives in Medicine* 13.8 (Aug. 2023), a041525. ISSN: 2157-1422. DOI: 10.1101/cshperspect.a041525. URL: http://perspectivesinmedicine.cshlp.org/lookup/doi/10.1101/cshperspect.a041525 (visited on 07/03/2024).

[132] Matthew A. Petoe et al. “A Second-Generation (44-Channel) Suprachoroidal Retinal Prosthesis: Interim Clinical Trial Results”. In: *Translational Vision Science & Technology* 10.10 (Sept. 28, 2021), p. 12. ISSN: 2164-2591. DOI: 10.1167/tvst.10.10.12. URL: https://tvst.arvojournals.org/article.aspx?articleid=2777940 (visited on 08/19/2024).

[133] Eberhart Zrenner. “Visual Prosthesis, Subretinal Devices”. In: *Encyclopedia of Computational Neuroscience*. Ed. by Dieter Jaeger and Ranu Jung. New York, NY: Springer New York, 2022, pp. 3618–3623. ISBN: 978-1-07-161004-6 978-1-07-161006-0. DOI: 10.1007/978-1-0716-1006-0_667. URL: https://link.springer.com/10.1007/978-1-0716-1006-0_667 (visited on 03/13/2025).

[134] H Christiaan Stronks and Gislin Dagnelie. “The Functional Performance of the Argus II Retinal Prosthesis”. In: *Expert Review of Medical Devices* 11.1 (Jan. 2014), pp. 23–30. ISSN: 1743-4440, 1745-2422. DOI: 10.1586/17434440.2014.862494. URL: http://www.tandfonline.com/doi/full/10.1586/17434440.2014.862494 (visited on 07/03/2024).

[135] Ralf Hornig et al. “Pixium Vision: First Clinical Results and Innovative Developments”. In: *Artificial Vision*. Ed. by Veit Peter Gabel. Cham: Springer International Publishing, 2017, pp. 99–113. ISBN: 978-3-319-41874-2 978-3-319-41876-6. DOI: 10.1007/978-3-319-41876-6_8. URL: http://link.springer.com/10.1007/978-3-319-41876-6_8 (visited on 07/03/2024).

[136] Mahiul M.K. Muqit et al. “Six-Month Safety and Efficacy of the Intelligent Retinal Implant System II Device in Retinitis Pigmentosa”. In: *Ophthalmology* 126.4 (Apr. 2019), pp. 637–639. ISSN: 01616420. DOI: 10.1016/j.ophtha.2018.11.010. URL: https://linkinghub.elsevier.com/retrieve/pii/S016164201832685X (visited on 07/03/2024).

[137] Peter Walter. “A Fully Intraocular Approach for a Bi-Directional Retinal Prosthesis”. In: *Artificial Vision*. Ed. by Veit Peter Gabel. Cham: Springer International Publishing, 2017, pp. 151–161. ISBN: 978-3-319-41874-2 978-3-319-41876-6. DOI: 10.1007/978-3-319-41876-6_12. URL: http://link.springer.com/10.1007/978-3-319-41876-6_12 (visited on 07/03/2024).

[138] P. Walter. “Zukünftige Entwicklungen bei implantierbaren Netzhautprothesen”. In: *Klinische Monatsblätter für Augenheilkunde* 233.11 (Sept. 19, 2016), pp. 1238–1243. ISSN: 0023-2165, 1439-3999. DOI: 10.1055/s-0042-115411. URL: http://www.thieme-connect.de/DOI/DOI?10.1055/s-0042-115411 (visited on 07/03/2024).

[139] Florian Waschkowski et al. “Development of Very Large Electrode Arrays for Epiretinal Stimulation (VLARS)”. In: *BioMedical Engineering OnLine* 13.1 (Dec. 2014), p. 11. ISSN: 1475-925X. DOI: 10.1186/1475-925X-13-11. URL: https://biomedical-engineering-online.biomedcentral.com/articles/10.1186/1475-925X-13-11 (visited on 07/03/2024).

[140] Leonid Yanovitch, Dorit Raz-Prag, and Yael Hanein. *A New High-Resolution Three-Dimensional Retinal Implant:* System Design and Preliminary Human Results. Sept. 17, 2022. URL: http://biorxiv.org/lookup/doi/10.1101/2022.09.14.507901 (visited on 07/03/2024). Pre-published.

[141] Shawn K. Kelly and Joseph Rizzo. “The Boston Retinal Implant”. In: *Artificial Vision*. Ed. by Veit Peter Gabel. Cham: Springer International Publishing, 2017, pp. 85–97. ISBN: 978-3-319-41874-2 978-3-319-41876-6. DOI: 10.1007/978-3-319-41876-6_7. URL: http://link.springer.com/10.1007/978-3-319-41876-6_7 (visited on 07/03/2024).

[142] Katarina Stingl et al. “Artificial Vision with Wirelessly Powered Subretinal Electronic Implant Alpha-IMS”. In: *Proceedings of the Royal Society B: Biological Sciences* 280.1757 (Apr. 22, 2013), p. 20130077. ISSN: 0962-8452, 1471-2954. DOI: 10.1098/rspb.2013.0077. URL: https://royalsocietypublishing.org/doi/10.1098/rspb.2013.0077 (visited on 07/03/2024).

[143] Katarina Stingl et al. “Subretinal Visual Implant Alpha IMS – Clinical Trial Interim Report”. In: *Vision Research* 111 (June 2015), pp. 149–160. ISSN: 00426989. DOI: 10.1016/j.visres.2015.03.001. URL: https://linkinghub.elsevier.com/retrieve/pii/S0042698915000784 (visited on 07/03/2024).

[144] Daniel Palanker et al. “Photovoltaic Restoration of Central Vision in Atrophic Age-Related Macular Degeneration”. In: *Ophthalmology* 127.8 (Aug. 2020), pp. 1097–1104. ISSN: 01616420. DOI: 10.1016/j.ophtha.2020.02.024. URL: https://linkinghub.elsevier.com/retrieve/pii/S0161642020301895 (visited on 07/03/2024).

[145] D. Palanker et al. “Simultaneous Perception of Prosthetic and Natural Vision in AMD Patients”. In: *Nature Communications* 13.1 (Jan. 26, 2022), p. 513. ISSN: 2041-1723. DOI: 10.1038/s41467-022-28125-x. URL: https://www.nature.com/articles/s41467-022-28125-x (visited on 07/03/2024).

[146] Matthew A. Petoe et al. “A Second-Generation (44-Channel) Suprachoroidal Retinal Prosthesis: A Single-Arm Clinical Trial of Feasibility”. In: *Ophthalmology Science* (May 2024), p. 100525. ISSN: 26669145. DOI: 10.1016/j.xops.2024.100525. URL: https://linkinghub.elsevier.com/retrieve/pii/S2666914524000617 (visited on 07/03/2024).

[147] Takashi Fujikado. “Retinal Prosthesis by Suprachoroidal-Transretinal Stimulation (STS), Japanese Approach”. In: *Artificial Vision*. Ed. by Veit Peter Gabel. Cham: Springer International Publishing, 2017, pp. 139–150. ISBN: 978-3-319-41874-2 978-3-319-41876-6. DOI: 10.1007/978-3-319-41876-6_11. URL: http://link.springer.com/10.1007/978-3-319-41876-6_11 (visited on 07/03/2024).

[148] Laura Ferlauto et al. “Design and Validation of a Foldable and Photovoltaic Wide-Field Epiretinal Prosthesis”. In: *Nature Communications* 9.1 (Mar. 8, 2018), p. 992. ISSN: 2041-1723. DOI: 10.1038/s41467-018-03386-7. URL: https://www.nature.com/articles/s41467-018-03386-7 (visited on 07/03/2024).

[149] Paola Vagni et al. “POLYRETINA Restores Light Responses in Vivo in Blind Göttingen Minipigs”. In: *Nature Communications* 13.1 (June 27, 2022), p. 3678. ISSN: 2041-1723. DOI: 10.1038/s41467-022-31180-z. URL: https://www.nature.com/articles/s41467-022-31180-z (visited on 07/03/2024).

[150] Moosa Zaidi et al. “Inferring Light Responses of Primate Retinal Ganglion Cells Using Intrinsic Electrical Signatures”. In: *Journal of Neural Engineering* 20.4 (Aug. 1, 2023), p. 045001. ISSN: 1741-2560, 1741-2552. DOI: 10.1088/1741-2552/ace657. URL: https://iopscience.iop.org/article/10.1088/1741-2552/ace657 (visited on 07/03/2024).

[151] Pingyu Wang et al. *Direct-Print Three-Dimensional Electrodes for Large-Scale, High-Density, and Customizable Neural Interfaces*. June 2, 2023. URL: http://biorxiv.org/lookup/doi/10.1101/2023.05.30.542925 (visited on 07/03/2024). Pre-published.

[152] Won Gi Chung et al. “Liquid-Metal-Based Three-Dimensional Microelectrode Arrays Integrated with Implantable Ultrathin Retinal Prosthesis for Vision Restoration”. In: *Nature Nanotechnology* 19.5 (May 2024), pp. 688–697. ISSN: 1748-3387, 1748-3395. DOI: 10.1038/s41565-023-01587-w. URL: https://www.nature.com/articles/s41565-023-01587-w (visited on 07/03/2024).

[153] Kevin Joseph et al. “Transcriptional Characterization of the Glial Response Due to Chronic Neural Implantation of Flexible Microprobes”. In: *Biomaterials* 279 (Dec. 2021), p. 121230. ISSN: 01429612. DOI: 10.1016/j.biomaterials.2021.121230. URL: https://linkinghub.elsevier.com/retrieve/pii/S0142961221005871 (visited on 08/13/2024).

[154] Dries Kil et al. “Dextran as a Resorbable Coating Material for Flexible Neural Probes”. In: *Micromachines* 10.1 (Jan. 17, 2019), p. 61. ISSN: 2072-666X. DOI: 10.3390/mi10010061. URL: https://www.mdpi.com/2072-666X/10/1/61 (visited on 08/13/2024).

[155] V. Rincón Montes et al. “Development and in Vitro Validation of Flexible Intraretinal Probes”. In: *Scientific Reports* 10.1 (Nov. 16, 2020), p. 19836. ISSN: 2045-2322. DOI: 10.1038/s41598-020-76582-5. URL: https://www.nature.com/articles/s41598-020-76582-5 (visited on 08/18/2024).

[156] Viviana Rincón Montes. *Development, Characterization, and Application of Intraretinal Implants*. Vol. RWTH Aachen University. RWTH Aachen University, 2021, pages 1 Online-Ressource : Illustrationen, Diagramme. DOI: 10.18154/RWTH-2021-06382. URL: https://publications.rwth-aachen.de/record/821875 (visited on 08/26/2024).

[157] Kagithiri Srikantharajah. *Development, Characterization, and Application of Compliant Intracortical Implants*. Vol. RWTH Aachen University. RWTH Aachen University, 2021, pages 1 Online-Ressource (155, xvii Seiten) : Illustrationen, Diagramme. DOI: 10.18154/RWTH-2021-11377. URL: https://publications.rwth-aachen.de/record/836520 (visited on 08/26/2024).

[158] Ahuva Weltman, James Yoo, and Ellis Meng. "Flexible, Penetrating Brain Probes Enabled by Advances in Polymer Microfabrication". In: *Micromachines* 7.10 (Oct. 4, 2016), p. 180. ISSN: 2072-666X. DOI: 10.3390/mi7100180. URL: https://www.mdpi.com/2072-666X/7/10/180 (visited on 08/14/2024).

[159] B J Kim et al. "Formation of Three-Dimensional Parylene C Structures via Thermoforming". In: *Journal of Micromechanics and Microengineering* 24.6 (June 1, 2014), p. 065003. ISSN: 0960-1317, 1361-6439. DOI: 10.1088/0960-1317/24/6/065003. URL: https://iopscience.iop.org/article/10.1088/0960-1317/24/6/065003 (visited on 08/15/2024).

[160] "Effect of Thermal and Deposition Processes on Surface Morphology, Crystallinity, and Adhesion of Parylene-C". In: *Sensors and Materials* (2008), p. 87. ISSN: 0914-4935. DOI: 10.18494/SAM.2008.515. URL: http://myukk.org/SM2017/article.php?ss=515 (visited on 09/02/2024).

[161] Christina Hassler, Tim Boretius, and Thomas Stieglitz. "Polymers for Neural Implants". In: *Journal of Polymer Science Part B: Polymer Physics* 49.1 (Jan. 2011), pp. 18–33. ISSN: 0887-6266, 1099-0488. DOI: 10.1002/polb.22169. URL: https://onlinelibrary.wiley.com/doi/10.1002/polb.22169 (visited on 08/14/2024).

[162] Specialty Coating Systems. *PDS 2010 LABCOTERTM 2 Parylene Deposition System Operator's Manual*.

[163] Ellis Meng. *Biomedical Microsystems*. Boca Raton: CRC, 2011. 392 pp. ISBN: 978-1-4200-5122-3.

[164] MicroChemicals GmbH. *Photolithography- Basics of Microstructuring*.

[165] Heidelberg Instruments. *MLA 150, The Advanced Maskless Aligner - Brochure*.

[166] Seán O'Halloran et al. "Two-Photon Polymerization: Fundamentals, Materials, and Chemical Modification Strategies". In: *Advanced Science* 10.7 (Mar. 2023), p. 2204072. ISSN: 2198-3844, 2198-3844. DOI: 10.1002/advs.202204072. URL: https://onlinelibrary.wiley.com/doi/10.1002/advs.202204072 (visited on 09/26/2024).

[167] Kwang-Sup Lee et al. "Advances in 3D Nano/Microfabrication Using Two-Photon Initiated Polymerization". In: *Progress in Polymer Science* 33.6 (June 2008), pp. 631–681. ISSN: 00796700. DOI: 10.1016/j.progpolymsci.2008.01.001. URL: https://linkinghub.elsevier.com/retrieve/pii/S0079670008000130 (visited on 09/26/2024).

[168] Bijoy Bhattacharyya. "Design and Developments of Microtools". In: *Electrochemical Micromachining for Nanofabrication, MEMS and Nanotechnology*. Elsevier, 2015, pp. 101–122. ISBN: 978-0-323-32737-4. DOI: 10.1016/B978-0-323-32737-4.00006-2. URL: https://linkinghub.elsevier.com/retrieve/pii/B9780323327374000062 (visited on 09/27/2024).

[169] M. Bagheri Hariri, A. Dolati, and R. Siavash Moakhar. “The Potentiostatic Electrodeposition of Gold Nanowire/Nanotube in $HAuCl_4$ Solutions Based on the Model of Recessed Cylindrical Ultramicroelectrode Array”. In: *Journal of The Electrochemical Society* 160.6 (2013), pp. D279–D288. ISSN: 0013-4651, 1945-7111. DOI: 10.1149/2.141306jes. URL: https://iopscience.iop.org/article/10.1149/2.141306jes (visited on 09/27/2024).

[170] Hajar Mousavi et al. “Kinetics and Physicochemical Characteristics of Electrodeposited PEDOT:PSS Thin Film Growth”. In: *Advanced Electronic Materials* 9.9 (Sept. 2023), p. 2201282. ISSN: 2199-160X, 2199-160X. DOI: 10.1002/aelm.202201282. URL: https://onlinelibrary.wiley.com/doi/10.1002/aelm.202201282 (visited on 09/27/2024).

[171] Michael Mierzejewski et al. “The Noise and Impedance of Microelectrodes”. In: *Journal of Neural Engineering* 17.5 (Oct. 1, 2020), p. 052001. ISSN: 1741-2560, 1741-2552. DOI: 10.1088/1741-2552/abb3b4. URL: https://iopscience.iop.org/article/10.1088/1741-2552/abb3b4 (visited on 09/11/2024).

[172] Steven M. Kaplan. *Wiley Electrical and Electronics Engineering Dictionary*. [Piscataway, NJ?], Hoboken, N.J.: IEEE Press ; Wiley-Interscience, 2004. ISBN: 978-1-61583-854-7.

[173] Stuart F. Cogan. “Neural Stimulation and Recording Electrodes”. In: *Annual Review of Biomedical Engineering* 10.1 (Aug. 1, 2008), pp. 275–309. ISSN: 1523-9829, 1545-4274. DOI: 10.1146/annurev.bioeng.10.061807.160518. URL: https://www.annualreviews.org/doi/10.1146/annurev.bioeng.10.061807.160518 (visited on 08/18/2024).

[174] Justyna Lipus and Katarzyna Krukiewicz. “Challenges and Limitations of Using Charge Storage Capacity to Assess Capacitance of Biomedical Electrodes”. In: *Measurement* 191 (Mar. 2022), p. 110822. ISSN: 02632241. DOI: 10.1016/j.measurement.2022.110822. URL: https://linkinghub.elsevier.com/retrieve/pii/S026322412200118X (visited on 08/18/2024).

[175] John Case, Henry Chilver Chilver, and C. T. F. Ross. *Strength of Materials and Structures*. 4th ed. London ; New York: Arnold, 1999. 706 pp. ISBN: 978-0-340-71920-6.

[176] Specialty Coating Systems. *SCS PARYLENE PROPERTIES High Performance Conformal Coatings*. 2018.

[177] Marie Jung et al. “Flexible 3D *Kirigami* Probes for In Vitro and In Vivo Neural Applications”. In: *Advanced Materials* (Apr. 14, 2025), p. 2418524. ISSN: 0935-9648, 1521-4095. DOI: 10.1002/adma.202418524. URL: https://advanced.onlinelibrary.wiley.com/doi/10.1002/adma.202418524 (visited on 06/12/2025).

[178] Multi Channel Systems MCS GmbH. *ME2100-System, User Manual*. July 13, 2022.

[179] Pavel Měřička et al. “Cell Viability Assessment Using Fluorescence Vital Dyes and Confocal Microscopy in Evaluating Freezing and Thawing Protocols Used in Cryopreservation of Allogeneic Venous Grafts”. In: *International Journal of Molecular Sciences* 22.19 (Sept. 30, 2021), p. 10653. ISSN: 1422-0067. DOI: 10.3390/ijms221910653. URL: https://www.mdpi.com/1422-0067/22/19/10653 (visited on 10/24/2024).

[180] Johannes Schindelin et al. “Fiji: An Open-Source Platform for Biological-Image Analysis”. In: *Nature Methods* 9.7 (July 2012), pp. 676–682. ISSN: 1548-7091, 1548-7105. DOI: 10.1038/nmeth.2019. URL: https://www.nature.com/articles/nmeth.2019 (visited on 10/24/2024).

[181] Aniella Bak et al. “Human Organotypic Brain Slice Cultures: A Detailed and Improved Protocol for Preparation and Long-Term Maintenance”. In: *Journal of Neuroscience Methods* 404 (Apr. 2024), p. 110055. ISSN: 01650270. DOI: 10.1016/j.jneumeth.2023.110055. URL: https://linkinghub.elsevier.com/retrieve/pii/S0165027023002741 (visited on 08/19/2024).

[182] Johan Pallud et al. “Cortical GABAergic Excitation Contributes to Epileptic Activities around Human Glioma”. In: *Science Translational Medicine* 6.244 (July 9, 2014), 244ra89. ISSN: 1946-6242. DOI: 10.1126/scitranslmed.3008065. pmid: 25009229.

[183] Joao Couto. *Labcams*. URL: https://github.com/jcouto/labcams.

[184] Talia N. Lerner et al. “Intact-Brain Analyses Reveal Distinct Information Carried by SNc Dopamine Subcircuits”. In: *Cell* 162.3 (July 2015), pp. 635–647. ISSN: 00928674. DOI: 10.1016/j.cell.2015.07.014. URL: https://linkinghub.elsevier.com/retrieve/pii/S009286741500851X (visited on 02/10/2025).

[185] Marina E. Garrett et al. “Topography and Areal Organization of Mouse Visual Cortex”. In: *The Journal of Neuroscience* 34.37 (Sept. 10, 2014), pp. 12587–12600. ISSN: 0270-6474, 1529-2401. DOI: 10.1523/JNEUROSCI.1124-14.2014. URL: https://www.jneurosci.org/lookup/doi/10.1523/JNEUROSCI.1124-14.2014 (visited on 02/10/2025).

[186] Quanxin Wang et al. “The Allen Mouse Brain Common Coordinate Framework: A 3D Reference Atlas”. In: *Cell* 181.4 (May 2020), 936–953.e20. ISSN: 00928674. DOI: 10.1016/j.cell.2020.04.007. URL: https://linkinghub.elsevier.com/retrieve/pii/S0092867420304025 (visited on 02/10/2025).

[187] James H. Marshel et al. “Functional Specialization of Seven Mouse Visual Cortical Areas”. In: *Neuron* 72.6 (Dec. 2011), pp. 1040–1054. ISSN: 08966273. DOI: 10.1016/j.neuron.2011.12.004. URL: https://linkinghub.elsevier.com/retrieve/pii/S0896627311010464 (visited on 02/10/2025).

[188] Armin Walter. *McsMatlabDataTools*. GitHub, 2024. URL: https://github.com/multichannelsystems/McsMatlabDataTools/releases/tag/1.3.1.

[189] D. N. Hill, S. B. Mehta, and D. Kleinfeld. “Quality Metrics to Accompany Spike Sorting of Extracellular Signals”. In: *Journal of Neuroscience* 31.24 (June 15, 2011), pp. 8699–8705. ISSN: 0270-6474, 1529-2401. DOI: 10.1523/jneurosci.0971-11.2011. URL: https://www.jneurosci.org/lookup/doi/10.1523/JNEUROSCI.0971-11.2011 (visited on 01/14/2025).

[190] Viviana Rincón Montes et al. “Patent Application: Herstellung Dreidimensional Strukturierter Elektrodenlagen, Insbesondere Im Kirigami-Prinzip”. German pat. 102023102257.1.

[191] Jamal Abu Shihada et al. “Patent Application: Herstellung Dreidimensionaler Elektroden Mittels Schablonengestützter Elektrochemischer Abscheidung 102023102460.4, Filed on February 1, 2023.” Pat. 102023102460.4.

[192] Jamal Abu Shihada. “3D Scaffolds with Integrated Electrodes for Neuronal Cell Culture”. RWTH Aachen University, 2024, pages vii, 163 Seiten : Illustrationen. DOI: 10.18154/RWTH-2024-05678. URL: https://publications.rwth-aachen.de/record/987468 (visited on 08/26/2024).

[193] Wolfgang Albrecht, Juergen Moers, and Bernd Hermanns. “HNF - Helmholtz Nano Facility”. In: *Journal of large-scale research facilities JLSRF* 3 (May 22, 2017), A112. ISSN: 2364-091X. DOI: 10.17815/jlsrf-3-158. URL: https://jlsrf.org/index.php/lsf/article/view/158 (visited on 08/26/2024).

[194] Aziliz Lecomte et al. “Deep Plasma Etching of Parylene C Patterns for Biomedical Applications”. In: *Microelectronic Engineering* 177 (June 2017), pp. 70–73. ISSN: 01679317. DOI: 10.1016/j.mee.2017.02.012. URL: https://linkinghub.elsevier.com/retrieve/pii/S0167931717300680 (visited on 08/29/2024).

[195] Jae-Han Kim et al. “Tensile Testing of Ultra-Thin Films on Water Surface”. In: *Nature Communications* 4.1 (Oct. 2, 2013), p. 2520. ISSN: 2041-1723. DOI: 10.1038/ncomms3520. URL: https://www.nature.com/articles/ncomms3520 (visited on 09/10/2024).

[196] Rene Patrick Von Metzen and Thomas Stieglitz. “The Effects of Annealing on Mechanical, Chemical, and Physical Properties and Structural Stability of Parylene C”. In: *Biomedical Microdevices* 15.5 (Oct. 2013), pp. 727–735. ISSN: 1387-2176, 1572-8781. DOI: 10.1007/s10544-013-9758-8. URL: http://link.springer.com/10.1007/s10544-013-9758-8 (visited on 09/03/2024).

[197] Marie Jung et al. “Towards the in Vivo Validation of 3D Retinal Implants: An in Vitro and Cadaveric Validation”. In: *in preparation* ().

[198] Amedeo Ruggiero et al. “Two-Photon Polymerization Lithography Enabling the Fabrication of PEDOT:PSS 3D Structures for Bioelectronic Applications”. In: *Chemical Communications* 58.70 (2022), pp. 9790–9793. ISSN: 1359-7345, 1364-548X. DOI: 10.1039/D2CC03152C. URL: https://xlink.rsc.org/?DOI=D2CC03152C (visited on 09/05/2024).

[199] Julia Purtov et al. “Improved Development Procedure to Enhance the Stability of Microstructures Created by Two-Photon Polymerization”. In: *Microelectronic Engineering* 194 (July 2018), pp. 45–50. ISSN: 01679317. DOI: 10.1016/j.mee.2018.03.009. URL: https://linkinghub.elsevier.com/retrieve/pii/S0167931718301205 (visited on 09/06/2024).

[200] P.A Kralchevsky et al. “Capillary Meniscus Interaction between Colloidal Particles Attached to a Liquid—Fluid Interface”. In: *Journal of Colloid and Interface Science* 151.1 (June 1992), pp. 79–94. ISSN: 00219797. DOI: 10.1016/0021-9797(92)90239-I. URL: https://linkinghub.elsevier.com/retrieve/pii/002197979290239I (visited on 09/06/2024).

[201] Stefania Carapezzi, Gabriele Boschetto, and Aida Todri-Sanial. “Capillary-Force-Driven Self-Assembly of Carbon Nanotubes: From *Ab Initio* Calculations to Modeling of Self-Assembly”. In: *Nanoscale Advances* 4.19 (2022), pp. 4131–4137. ISSN: 2516-0230. DOI: 10.1039/D2NA00295G. URL: https://xlink.rsc.org/?DOI=D2NA00295G (visited on 09/06/2024).

[202] Jiumeng Zhang et al. “Digital Light Processing Based Three-dimensional Printing for Medical Applications”. In: *International Journal of Bioprinting* 6.1 (Nov. 28, 2019), p. 242. ISSN: 2424-7723, 2424-8002. DOI: 10.18063/ijb.v6i1.242. URL: https://accscience.com/journal/IJB/6/1/10.18063/ijb.v6i1.242 (visited on 09/10/2024).

[203] Qi Ge et al. “Projection Micro Stereolithography Based 3D Printing and Its Applications”. In: *International Journal of Extreme Manufacturing* 2.2 (June 1, 2020), p. 022004. ISSN: 2631-8644, 2631-7990. DOI: 10.1088/2631-7990/ab8d9a. URL: https://iopscience.iop.org/article/10.1088/2631-7990/ab8d9a (visited on 09/10/2024).

[204] Kee Scholten and Ellis Meng. “Electron-Beam Lithography for Polymer bioMEMS with Submicron Features”. In: *Microsystems & Nanoengineering* 2.1 (Nov. 7, 2016), p. 16053. ISSN: 2055-7434. DOI: 10.1038/micronano.2016.53. URL: https://www.nature.com/articles/micronano201653 (visited on 11/06/2024).

[205] Adam Wang et al. “Impedance Characterization and Modeling of Subcellular to Micro-sized Electrodes with Varying Materials and PEDOT:PSS Coating for Bioelectrical Interfaces”. In: *ACS Applied Electronic Materials* 3.12 (Dec. 28, 2021), pp. 5226–5239. ISSN: 2637-6113, 2637-6113. DOI: 10.1021/acsaelm.1c00687. URL: https://pubs.acs.org/doi/10.1021/acsaelm.1c00687 (visited on 09/11/2024).

[206] Eleni Stavrinidou et al. “A Physical Interpretation of Impedance at Conducting Polymer/Electrolyte Junctions”. In: *AIP Advances* 4.1 (Jan. 1, 2014), p. 017127. ISSN: 2158-3226. DOI: 10.1063/1.4863297. URL: https://pubs.aip.org/adv/article/4/1/017127/20586/A-physical-interpretation-of-impedance-at (visited on 09/11/2024).

[207] Gerwin Dijk, Hermanus J. Ruigrok, and Rodney P. O’Connor. “Influence of PEDOT:PSS Coating Thickness on the Performance of Stimulation Electrodes”. In: *Advanced Materials Interfaces* 7.16 (Aug. 2020), p. 2000675. ISSN: 2196-7350, 2196-7350. DOI: 10.1002/admi.202000675. URL: https://onlinelibrary.wiley.com/doi/10.1002/admi.202000675 (visited on 09/11/2024).

[208] Zhanhong Jeff Du et al. “Poly(3,4-Ethylenedioxythiophene)-Ionic Liquid Coating Improves Neural Recording and Stimulation Functionality of MEAs”. In: *Journal of Materials Chemistry C* 3.25 (2015), pp. 6515–6524. ISSN: 2050-7526, 2050-7534. DOI: 10.1039/C5TC00145E. URL: https://xlink.rsc.org/?DOI=C5TC00145E (visited on 10/01/2024).

[209] Mehran Ganji et al. “Scaling Effects on the Electrochemical Performance of Poly(3,4-ethylenedioxythiophene (PEDOT), Au, and Pt for Electrocorticography Recording”. In: *Advanced Functional Materials* 27.42 (Nov. 2017), p. 1703018. ISSN: 1616-301X, 1616-3028. DOI: 10.1002/adfm.201703018. URL: https://onlinelibrary.wiley.com/doi/10.1002/adfm.201703018 (visited on 09/11/2024).

[210] Neda Haj Hosseini et al. “Comparative Study on the Insertion Behavior of Cerebral Microprobes”. In: *2007 29th Annual International Conference of the IEEE Engineering in Medicine and Biology Society*. 29th Annual International Conference of the IEEE EMBS. Vol. 2488. Lyon: IEEE, Aug. 2007, pp. 4711–4714. DOI: 10.1109/iembs.2007.4353391. URL: http://ieeexplore.ieee.org/document/4353391/ (visited on 09/17/2024).

[211] M. Welkenhuysen et al. “Effect of Insertion Speed on Tissue Response and Insertion Mechanics of a Chronically Implanted Silicon-Based Neural Probe”. In: *IEEE Transactions on Biomedical Engineering* 58.11 (Nov. 2011), pp. 3250–3259. ISSN: 0018-9294, 1558-2531. DOI: 10.1109/tbme.2011.2166963. URL: http://ieeexplore.ieee.org/document/6008631/ (visited on 09/17/2024).

[212] Christina Hassler et al. “Characterization of Parylene C as an Encapsulation Material for Implanted Neural Prostheses”. In: *Journal of Biomedical Materials Research Part B: Applied Biomaterials* 93B.1 (Apr. 2010), pp. 266–274. ISSN: 1552-4973, 1552-4981. DOI: 10.1002/jbm.b.31584. URL: https://onlinelibrary.wiley.com/doi/10.1002/jbm.b.31584 (visited on 09/19/2024).

[213] Dani Zeniieh et al. “Effect of Plasma Treatments and Plasma- P Olymerized Films on the Adhesion of Parylene- C to Substrates”. In: *Plasma Processes and Polymers* 10.12 (Dec. 2013), pp. 1081–1089. ISSN: 1612-8850, 1612-8869. DOI: 10.1002/ppap.201300045. URL: https://onlinelibrary.wiley.com/doi/10.1002/ppap.201300045 (visited on 09/19/2024).

[214] Curtis D. Lee and Ellis Meng. “Mechanical Properties of Thin-Film Parylene–Metal–Parylene Devices”. In: *Frontiers in Mechanical Engineering* 1 (Sept. 8, 2015). ISSN: 2297-3079. DOI: 10.3389/fmech.2015.00010. URL: http://journal.frontiersin.org/Article/10.3389/fmech.2015.00010/abstract (visited on 09/19/2024).

[215] V. Radun et al. “Evaluation of Adhesion Promoters for Parylene C on Gold Metallization”. In: *Current Directions in Biomedical Engineering* 1.1 (Sept. 1, 2015), pp. 493–497. ISSN: 2364-5504. DOI: 10.1515/cdbme-2015-0118. URL: https://www.degruyter.com/document/doi/10.1515/cdbme-2015-0118/html (visited on 09/19/2024).

[216] Seonho Seok, HyungDal Park, and Jinseok Kim. “Characterization and Analysis of Metal Adhesion to Parylene Polymer Substrate Using Scotch Tape Test for Peripheral Neural Probe”. In: *Micromachines* 11.6 (June 22, 2020), p. 605. ISSN: 2072-666X. DOI: 10.3390/mi11060605. URL: https://www.mdpi.com/2072-666X/11/6/605 (visited on 09/19/2024).

[217] Dion Khodagholy et al. “Highly Conformable Conducting Polymer Electrodes for In Vivo Recordings”. In: *Advanced Materials* 23.36 (Sept. 22, 2011). ISSN: 0935-9648, 1521-4095. DOI: 10.1002/adma.201102378. URL: https://onlinelibrary.wiley.com/doi/10.1002/adma.201102378 (visited on 09/19/2024).

[218] Nathan Jackson et al. “Crystallinity and Mechanical Effects from Annealing Parylene Thin Films”. In: *Thin Solid Films* 603 (Mar. 2016), pp. 371–376. ISSN: 00406090. DOI: 10.1016/j.tsf.2016.02.047. URL: https://linkinghub.elsevier.com/retrieve/pii/S0040609016001462 (visited on 09/20/2024).

[219] Subramaniam Venkatraman et al. “In Vitro and In Vivo Evaluation of PEDOT Microelectrodes for Neural Stimulation and Recording”. In: *IEEE Transactions on Neural Systems and Rehabilitation Engineering* 19.3 (June 2011), pp. 307–316. ISSN: 1534-4320, 1558-0210. DOI: 10.1109/TNSRE.2011.2109399. URL: https://ieeexplore.ieee.org/document/5705581/ (visited on 10/01/2024).

[220] Poppy Oldroyd, Johannes Gurke, and George G. Malliaras. “Stability of Thin Film Neuromodulation Electrodes under Accelerated Aging Conditions”. In: *Advanced Functional Materials* 33.1 (Jan. 2023), p. 2208881. ISSN: 1616-301X, 1616-3028. DOI: 10.1002/adfm.202208881. URL: https://onlinelibrary.wiley.com/doi/10.1002/adfm.202208881 (visited on 10/02/2024).

[221] Stuart F. Cogan et al. “Sputtered Iridium Oxide Films for Neural Stimulation Electrodes”. In: *Journal of Biomedical Materials Research Part B: Applied Biomaterials* 89B.2 (May 2009), pp. 353–361. ISSN: 1552-4973, 1552-4981. DOI: 10.1002/jbm.b.31223. URL: https://onlinelibrary.wiley.com/doi/10.1002/jbm.b.31223 (visited on 10/22/2024).

[222] Nuan Chen et al. “Neural Interfaces Engineered via Micro- and Nanostructured Coatings”. In: *Nano Today* 14 (June 2017), pp. 59–83. ISSN: 17480132. DOI: 10.1016/j.nantod.2017.04.007. URL: https://linkinghub.elsevier.com/retrieve/pii/S174801321730018X (visited on 10/02/2024).

[223] Daniel Palanker et al. “Design of a High-Resolution Optoelectronic Retinal Prosthesis”. In: *Journal of Neural Engineering* 2.1 (Mar. 1, 2005), S105–S120. ISSN: 1741-2560, 1741-2552. DOI: 10.1088/1741-2560/2/1/012. URL: https://iopscience.iop.org/article/10.1088/1741-2560/2/1/012 (visited on 10/02/2024).

[224] Christian Boehler et al. “Long-Term Stable Adhesion for Conducting Polymers in Biomedical Applications: IrOx and Nanostructured Platinum Solve the Chronic Challenge”. In: *ACS Applied Materials & Interfaces* 9.1 (Jan. 11, 2017), pp. 189–197. ISSN: 1944-8244, 1944-8252. DOI: 10.1021/acsami.6b13468. URL: https://pubs.acs.org/doi/10.1021/acsami.6b13468 (visited on 10/02/2024).

[225] Seung Woo Lee et al. “Monolithic Encapsulation of Implantable Neuroprosthetic Devices Using Liquid Crystal Polymers”. In: *IEEE Transactions on Biomedical Engineering* 58.8 (Aug. 2011), pp. 2255–2263. ISSN: 0018-9294, 1558-2531. DOI: 10.1109/TBME.2011.2136341. URL: http://ieeexplore.ieee.org/document/5741833/ (visited on 10/23/2024).

[226] Brian C. Gilger, ed. *Ocular Pharmacology and Toxicology*. Methods in Pharmacology and Toxicology. Totowa, NJ: Humana Press, 2014. ISBN: 978-1-62703-744-0 978-1-62703-745-7. DOI: 10.1007/978-1-62703-745-7. URL: https://link.springer.com/10.1007/978-1-62703-745-7 (visited on 10/10/2024).

[227] Veena Bhardwaj. "Axial Length, Anterior Chamber Depth-A Study in Different Age Groups and Refractive Errors". In: *JOURNAL OF CLINICAL AND DIAGNOSTIC RESEARCH* (2013). ISSN: 2249782X. DOI: 10.7860/JCDR/2013/7015.3473. URL: http://www.jcdr.net/article_fulltext.asp?issn=0973-709x&year=2013&volume=7&issue=10&page=2211&issn=0973-709x&id=3473 (visited on 10/10/2024).

[228] Helga Kolb et al., eds. *Webvision: The Organization of the Retina and Visual System*. Salt Lake City (UT): University of Utah Health Sciences Center, 1995. pmid: 21413389. URL: http://www.ncbi.nlm.nih.gov/books/NBK11530/ (visited on 10/10/2024).

[229] Caridad Galindo-Romero et al. "The Retina of the Lab Rat: Focus on Retinal Ganglion Cells and Photoreceptors". In: *Frontiers in Neuroanatomy* 16 (Sept. 23, 2022), p. 994890. ISSN: 1662-5129. DOI: 10.3389/fnana.2022.994890. URL: https://www.frontiersin.org/articles/10.3389/fnana.2022.994890/full (visited on 10/10/2024).

[230] Ulrike Grünert and Paul R. Martin. "Cell Types and Cell Circuits in Human and Non-Human Primate Retina". In: *Progress in Retinal and Eye Research* 78 (Sept. 2020), p. 100844. ISSN: 13509462. DOI: 10.1016/j.preteyeres.2020.100844. URL: https://linkinghub.elsevier.com/retrieve/pii/S1350946220300161 (visited on 10/10/2024).

[231] Stefanie Volland et al. "A Comparison of Some Organizational Characteristics of the Mouse Central Retina and the Human Macula". In: *PLOS ONE* 10.4 (Apr. 29, 2015). Ed. by Tiansen Li, e0125631. ISSN: 1932-6203. DOI: 10.1371/journal.pone.0125631. URL: https://dx.plos.org/10.1371/journal.pone.0125631 (visited on 10/10/2024).

[232] Mark E. Pennesi, Martha Neuringer, and Robert J. Courtney. "Animal Models of Age Related Macular Degeneration". In: *Molecular Aspects of Medicine* 33.4 (Aug. 2012), pp. 487–509. ISSN: 00982997. DOI: 10.1016/j.mam.2012.06.003. URL: https://linkinghub.elsevier.com/retrieve/pii/S0098299712000635 (visited on 10/10/2024).

[233] Harsha Kasi et al. "Simulation of Epiretinal Prostheses - Evaluation of Geometrical Factors Affecting Stimulation Thresholds". In: *Journal of NeuroEngineering and Rehabilitation* 8.1 (2011), p. 44. ISSN: 1743-0003. DOI: 10.1186/1743-0003-8-44. URL: http://jneuroengrehab.biomedcentral.com/articles/10.1186/1743-0003-8-44 (visited on 10/10/2024).

[234] Abdulrahman Alqahtani et al. "Optimizing Stimulation Strategies for Retinal Electrical Stimulation: A Modelling Study". In: *2019 41st Annual International Conference of the IEEE Engineering in Medicine and Biology Society (EMBC)*. 2019 41st Annual International Conference of the IEEE Engineering in Medicine & Biology Society (EMBC). Berlin, Germany: IEEE, July 2019, pp. 2872–2875. ISBN: 978-1-5386-1311-5. DOI: 10.1109/EMBC.2019.8856918. URL: https://ieeexplore.ieee.org/document/8856918/ (visited on 10/10/2024).

[235] Gita Khalili Moghaddam et al. "Performance Optimization of Current Focusing and Virtual Electrode Strategies in Retinal Implants". In: *Computer Methods and Programs in Biomedicine* 117.2 (Nov. 2014), pp. 334–342. ISSN: 01692607. DOI: 10.1016/j.cmpb.2014.06.012. URL: https://linkinghub.elsevier.com/retrieve/pii/S0169260714002466 (visited on 10/10/2024).

[236] Shiwei Zheng et al. “Influence of Retinal Degeneration Stages on RGC Threshold under Epiretinal Electrical Stimulation: A Modeling Study”. In: *Journal of Physics: Conference Series* 1827.1 (Mar. 1, 2021), p. 012016. ISSN: 1742-6588, 1742-6596. DOI: 10.1088/1742-6596/1827/1/012016. URL: https://iopscience.iop.org/article/10.1088/1742-6596/1827/1/012016 (visited on 10/10/2024).

[237] T E Ogden and H Ito. “Avian Retina. II. An Evaluation of Retinal Electrical Anisotropy.” In: *Journal of Neurophysiology* 34.3 (May 1971), pp. 367–373. ISSN: 0022-3077, 1522-1598. DOI: 10.1152/jn.1971.34.3.367. URL: https://www.physiology.org/doi/10.1152/jn.1971.34.3.367 (visited on 10/10/2024).

[238] G. S. Brindley. “The Passive Electrical Properties of the Frog’s Retina, Choroid and Sclera for Radial Fields and Currents”. In: *The Journal of Physiology* 134.2 (Nov. 28, 1956), pp. 339–352. ISSN: 0022-3751, 1469-7793. DOI: 10.1113/jphysiol.1956.sp005647. URL: https://physoc.onlinelibrary.wiley.com/doi/10.1113/jphysiol.1956.sp005647 (visited on 10/10/2024).

[239] Harsha Kasi et al. “Direct Localised Measurement of Electrical Resistivity Profile in Rat and Embryonic Chick Retinas Using a Microprobe”. In: *Journal of Electrical Bioimpedance* 1.1 (Dec. 31, 2010), pp. 84–92. ISSN: 1891-5469. DOI: 10.5617/jeb.149. URL: https://www.sciendo.com/article/10.5617/jeb.149 (visited on 10/10/2024).

[240] Boshuo Wang and James D. Weiland. “Resistivity Profiles of Wild-Type, Rd1, and Rd10 Mouse Retina”. In: *2015 37th Annual International Conference of the IEEE Engineering in Medicine and Biology Society (EMBC)*. 2015 37th Annual International Conference of the IEEE Engineering in Medicine and Biology Society (EMBC). Milan: IEEE, Aug. 2015, pp. 1650–1653. ISBN: 978-1-4244-9271-8. DOI: 10.1109/EMBC.2015.7318692. URL: http://ieeexplore.ieee.org/document/7318692/ (visited on 10/10/2024).

[241] Marie Jung, Antje Willuweit, and Viviana Rincón Montes. “Intraretinal Electrophysiology and Resistivity Profiles of WT and RCS Rat Retina”. In: *Sensors* 25.12 (June 16, 2025), p. 3765. ISSN: 1424-8220. DOI: 10.3390/s25123765. URL: https://www.mdpi.com/1424-8220/25/12/3765 (visited on 08/20/2025).

[242] Boshuo Wang and James D. Weiland. “Analysis of the Peak Resistance Frequency Method”. In: *IEEE Transactions on Biomedical Engineering* 63.10 (Oct. 2016), pp. 2086–2094. ISSN: 0018-9294, 1558-2531. DOI: 10.1109/TBME.2015.2510335. URL: http://ieeexplore.ieee.org/document/7360118/ (visited on 10/10/2024).

[243] A. Mercanzini et al. “*In Vivo* Electrical Impedance Spectroscopy of Tissue Reaction to Microelectrode Arrays”. In: *IEEE Transactions on Biomedical Engineering* 56.7 (July 2009), pp. 1909–1918. ISSN: 0018-9294, 1558-2531. DOI: 10.1109/TBME.2009.2018457. URL: http://ieeexplore.ieee.org/document/4812076/ (visited on 10/10/2024).

[244] Renee C. Ryals et al. “Long-Term Characterization of Retinal Degeneration in Royal College of Surgeons Rats Using Spectral-Domain Optical Coherence Tomography”. In: *Investigative Opthalmology & Visual Science* 58.3 (Mar. 2, 2017), p. 1378. ISSN: 1552-5783. DOI: 10.1167/iovs.16-20363. URL: http://iovs.arvojournals.org/article.aspx?doi=10.1167/iovs.16-20363 (visited on 01/14/2025).

[245] David Boinagrov et al. “Selectivity of Direct and Network-Mediated Stimulation of the Retinal Ganglion Cells with Epi-, Sub- and Intraretinal Electrodes”. In: *Journal of Neural Engineering* 11.2 (Apr. 1, 2014), p. 026008. ISSN: 1741-2560, 1741-2552. DOI: 10.1088/1741-2560/11/2/026008. URL: https://iopscience.iop.org/article/10.1088/1741-2560/11/2/026008 (visited on 10/22/2024).

[246] Ronen Segev et al. “Recording Spikes from a Large Fraction of the Ganglion Cells in a Retinal Patch”. In: *Nature Neuroscience* 7.10 (Oct. 2004), pp. 1155–1162. ISSN: 1097-6256, 1546-1726. DOI: 10.1038/nn1323. URL: https://www.nature.com/articles/nn1323 (visited on 10/21/2024).

[247] Sonia Biswas et al. “Pharmacological Analysis of Intrinsic Neuronal Oscillations in Rd10 Retina”. In: *PLoS ONE* 9.6 (June 11, 2014). Ed. by Erica Lucy Fletcher, e99075. ISSN: 1932-6203. DOI: 10.1371/journal.pone.0099075. URL: https://dx.plos.org/10.1371/journal.pone.0099075 (visited on 11/04/2024).

[248] Jana Gehlen et al. “Blockade of Retinal Oscillations by Benzodiazepines Improves Efficiency of Electrical Stimulation in the Mouse Model of RP, *Rd10*”. In: *Investigative Opthalmology & Visual Science* 61.13 (Nov. 30, 2020), p. 37. ISSN: 1552-5783. DOI: 10.1167/iovs.61.13.37. URL: https://iovs.arvojournals.org/article.aspx?articleid=2772002 (visited on 11/04/2024).

[249] Nruthyathi et al. “Late Emergence of Pathological Oscillatory Activity in the Retina of the Retinitis Pigmentosa Model RCS (Royal College of Surgeons) Rat”. In: *PLOS One* 20.5 (May 27, 2025). Ed. by Gerrit Hilgen, e0324345. ISSN: 1932-6203. DOI: 10.1371/journal.pone.0324345. URL: https://dx.plos.org/10.1371/journal.pone.0324345 (visited on 06/06/2025).

[250] Jacob Menzler and Günther Zeck. “Network Oscillations in Rod-Degenerated Mouse Retinas”. In: *The Journal of Neuroscience* 31.6 (Feb. 9, 2011), pp. 2280–2291. ISSN: 0270-6474, 1529-2401. DOI: 10.1523/jneurosci.4238-10.2011. URL: https://www.jneurosci.org/lookup/doi/10.1523/JNEUROSCI.4238-10.2011 (visited on 01/14/2025).

[251] Stuart Trenholm et al. “Intrinsic Oscillatory Activity Arising within the Electrically Coupled AII Amacrine–ON Cone Bipolar Cell Network Is Driven by Voltage-gated Na^+ Channels”. In: *The Journal of Physiology* 590.10 (May 15, 2012), pp. 2501–2517. ISSN: 0022-3751, 1469-7793. DOI: 10.1113/jphysiol.2011.225060. URL: https://physoc.onlinelibrary.wiley.com/doi/10.1113/jphysiol.2011.225060 (visited on 11/04/2024).

[252] Hannah Choi et al. “Intrinsic Bursting of AII Amacrine Cells Underlies Oscillations in the Rd1 Mouse Retina”. In: *Journal of Neurophysiology* 112.6 (Sept. 15, 2014), pp. 1491–1504. ISSN: 0022-3077, 1522-1598. DOI: 10.1152/jn.00437.2014. URL: https://www.physiology.org/doi/10.1152/jn.00437.2014 (visited on 11/04/2024).

[253] Christopher W. Yee, Abduqodir H. Toychiev, and Botir T. Sagdullaev. “Network Deficiency Exacerbates Impairment in a Mouse Model of Retinal Degeneration”. In: *Frontiers in Systems Neuroscience* 6 (2012). ISSN: 1662-5137. DOI: 10.3389/fnsys.2012.00008. URL: http://journal.frontiersin.org/article/10.3389/fnsys.2012.00008/abstract (visited on 11/04/2024).

[254] Richárd Fiáth et al. “Slow Insertion of Silicon Probes Improves the Quality of Acute Neuronal Recordings”. In: *Scientific Reports* 9.1 (Jan. 14, 2019). ISSN: 2045-2322. DOI: 10.1038/s41598-018-36816-z. URL: https://www.nature.com/articles/s41598-018-36816-z (visited on 01/14/2025).

[255] Ingrid N McNamara et al. “Electrode Sharpness and Insertion Speed Reduce Tissue Damage near High-Density Penetrating Arrays”. In: *Journal of Neural Engineering* 21.2 (Apr. 1, 2024), p. 026030. ISSN: 1741-2560, 1741-2552. DOI: 10.1088/1741-2552/ad36e1. URL: https://iopscience.iop.org/article/10.1088/1741-2552/ad36e1 (visited on 01/14/2025).

[256] Charles L. Schepens. “Clinical and Research Aspects of Subtotal Open-Sky Vitrectomy”. In: *American Journal of Ophthalmology* 91.2 (Feb. 1981), pp. 143–171. ISSN: 00029394. DOI: 10.1016/0002-9394(81)90168-9. URL: https://linkinghub.elsevier.com/retrieve/pii/0002939481901689 (visited on 10/09/2024).

[257] “The Relationship Between Anthropometric Z-Score Measurements and Ocular Structures in Turkish Children”. In: *romanian journal of ophthalmology* 67.4 (Dec. 15, 2023). ISSN: 24574325, 25012533. DOI: 10.22336/rjo.2023.60. URL: https://rjo.ro/the-relationship-between-anthropometric-z-score-measurements-and-ocular-structures-in-turkish-children/ (visited on 10/09/2024).

[258] John Finnie et al. “Temporal Sequence of Post-Mortem Autolysis in the Mouse Retina”. In: *Journal of Comparative Pathology* 187 (Aug. 2021), pp. 17–26. ISSN: 00219975. DOI: 10.1016/j.jcpa.2021.06.006. URL: https://linkinghub.elsevier.com/retrieve/pii/S0021997521000839 (visited on 03/08/2025).

[259] Tibor Karl Lohmann et al. “The Very Large Electrode Array for Retinal Stimulation (VLARS)—A Concept Study”. In: *Journal of Neural Engineering* 16.6 (Dec. 1, 2019), p. 066031. ISSN: 1741-2560, 1741-2552. DOI: 10.1088/1741-2552/ab4113. URL: https://iopscience.iop.org/article/10.1088/1741-2552/ab4113 (visited on 10/09/2024).

[260] Frederic Kuba Balcewicz et al. “Design, Fabrication, and Surgical Testing of the 3D-Printed Large-Array Port-System for the Implantation of Large Epiretinal Stimulators”. In: *Translational Vision Science & Technology* 14.2 (Feb. 5, 2025), p. 8. ISSN: 2164-2591. DOI: 10.1167/tvst.14.2.8. URL: https://tvst.arvojournals.org/article.aspx?articleid=2802546 (visited on 03/08/2025).

[261] David Boinagrov et al. “Upper Threshold of Extracellular Neural Stimulation”. In: *Journal of Neurophysiology* 108.12 (Dec. 15, 2012), pp. 3233–3238. ISSN: 0022-3077, 1522-1598. DOI: 10.1152/jn.01058.2011. URL: https://www.physiology.org/doi/10.1152/jn.01058.2011 (visited on 10/22/2024).

[262] James D. Weiland, Steven T. Walston, and Mark S. Humayun. “Electrical Stimulation of the Retina to Produce Artificial Vision”. In: *Annual Review of Vision Science* 2.1 (Oct. 14, 2016), pp. 273–294. ISSN: 2374-4642, 2374-4650. DOI: 10.1146/annurev-vision-111815-114425. URL: https://www.annualreviews.org/doi/10.1146/annurev-vision-111815-114425 (visited on 10/22/2024).

[263] Ralph J. Jensen and Joseph F. Rizzo. “Activation of Retinal Ganglion Cells in Wild-Type and Rd1 Mice through Electrical Stimulation of the Retinal Neural Network”. In: *Vision Research* 48.14 (June 2008), pp. 1562–1568. ISSN: 00426989. DOI: 10.1016/j.visres.2008.04.016. URL: https://linkinghub.elsevier.com/retrieve/pii/S0042698908002277 (visited on 10/22/2024).

[264] Chris Sekirnjak et al. “Loss of Responses to Visual But Not Electrical Stimulation in Ganglion Cells of Rats With Severe Photoreceptor Degeneration”. In: *Journal of Neurophysiology* 102.6 (Dec. 2009), pp. 3260–3269. ISSN: 0022-3077, 1522-1598. DOI: 10.1152/jn.00663.2009. URL: https://www.physiology.org/doi/10.1152/jn.00663.2009 (visited on 10/22/2024).

[265] Philipp Löhler et al. “A Cell-Type Selective Stimulation and Recording System for Retinal Ganglion Cells”. In: *IEEE Transactions on Biomedical Circuits and Systems* 18.3 (June 2024), pp. 498–510. ISSN: 1932-4545, 1940-9990. DOI: 10.1109/TBCAS.2023.3342465. URL: https://ieeexplore.ieee.org/document/10360310/ (visited on 10/23/2024).

[266] Dorsa Haji Ghaffari et al. “Real-Time Optimization of Retinal Ganglion Cell Spatial Activity in Response to Epiretinal Stimulation”. In: *IEEE Transactions on Neural Systems and Rehabilitation Engineering* 29 (2021), pp. 2733–2741. ISSN: 1534-4320, 1558-0210. DOI: 10.1109/TNSRE.2021.3138297. URL: https://ieeexplore.ieee.org/document/9662355/ (visited on 10/23/2024).

[267] Javad Paknahad, Mark Humayun, and Gianluca Lazzi. “Selective Activation of Retinal Ganglion Cell Subtypes Through Targeted Electrical Stimulation Parameters”. In: *IEEE Transactions on Neural Systems and Rehabilitation Engineering* 30 (2022), pp. 350–359. ISSN: 1534-4320, 1558-0210. DOI: 10.1109/TNSRE.2022.3149967. URL: https://ieeexplore.ieee.org/document/9706498/ (visited on 10/23/2024).

[268] Yao-Chuan Chang et al. “Stimulation Strategies for Selective Activation of Retinal Ganglion Cell Soma and Threshold Reduction”. In: *Journal of Neural Engineering* 16.2 (Apr. 1, 2019), p. 026017. ISSN: 1741-2560, 1741-2552. DOI: 10.1088/1741-2552/aaf92b. URL: https://iopscience.iop.org/article/10.1088/1741-2552/aaf92b (visited on 10/23/2024).

[269] Daniel K. Freeman et al. “Selective Activation of Neuronal Targets With Sinusoidal Electric Stimulation”. In: *Journal of Neurophysiology* 104.5 (Nov. 2010), pp. 2778–2791. ISSN: 0022-3077, 1522-1598. DOI: 10.1152/jn.00551.2010. URL: https://www.physiology.org/doi/10.1152/jn.00551.2010 (visited on 10/23/2024).

[270] Sahil Loomba et al. “Connectomic Comparison of Mouse and Human Cortex”. In: *Science* 377.6602 (July 8, 2022), eabo0924. ISSN: 0036-8075, 1095-9203. DOI: 10.1126/science.abo0924. URL: https://www.science.org/doi/10.1126/science.abo0924 (visited on 02/03/2025).

[271] Steffen Katzner and Sarah Weigelt. “Visual Cortical Networks: Of Mice and Men”. In: *Current Opinion in Neurobiology* 23.2 (Apr. 2013), pp. 202–206. ISSN: 09594388. DOI: 10.1016/j.conb.2013.01.019. URL: https://linkinghub.elsevier.com/retrieve/pii/S0959438813000354 (visited on 02/03/2025).

[272] Rebecca D. Hodge et al. “Conserved Cell Types with Divergent Features in Human versus Mouse Cortex”. In: *Nature* 573.7772 (Sept. 5, 2019), pp. 61–68. ISSN: 0028-0836, 1476-4687. DOI: 10.1038/s41586-019-1506-7. URL: https://www.nature.com/articles/s41586-019-1506-7 (visited on 02/03/2025).

[273] James J. Jun et al. “Fully Integrated Silicon Probes for High-Density Recording of Neural Activity”. In: *Nature* 551.7679 (Nov. 9, 2017), pp. 232–236. ISSN: 0028-0836, 1476-4687. DOI: 10.1038/nature24636. URL: https://www.nature.com/articles/nature24636 (visited on 01/14/2025).

[274] Matt Stead et al. “Microseizures and the Spatiotemporal Scales of Human Partial Epilepsy”. In: *Brain* 133.9 (Sept. 2010), pp. 2789–2797. ISSN: 1460-2156, 0006-8950. DOI: 10.1093/brain/awq190. URL: https://academic.oup.com/brain/article-lookup/doi/10.1093/brain/awq190 (visited on 11/05/2024).

[275] M.T. Valley et al. *Separation of Hemodynamic Signals from GCaMP Fluorescence Measured with Widefield Imaging*. May 10, 2019. URL: http://biorxiv.org/lookup/doi/10.1101/634923 (visited on 10/07/2024). Pre-published.

[276] Elisabeta Balla et al. *Broadband Visual Stimuli Improve Neuronal Representation and Sensory Perception*. May 3, 2023. URL: http://biorxiv.org/lookup/doi/10.1101/2023.05.03.539238 (visited on 10/08/2024). Pre-published.

[277] A. I. Cowan and R. L. Martin. “Simultaneous Measurement of pH and Membrane Potential in Rat Dorsal Vagal Motoneurons during Normoxia and Hypoxia: A Comparison in Bicarbonate and HEPES Buffers”. In: *Journal of Neurophysiology* 74.6 (Dec. 1, 1995), pp. 2713–2721. ISSN: 0022-3077, 1522-1598. DOI: 10.1152/jn.1995.74.6.2713. URL: https://www.physiology.org/doi/10.1152/jn.1995.74.6.2713 (visited on 01/20/2025).

List of Figures

List of Tables

A. Appendix: Fabrication of 2D and 3D implants

A.1. Detailed microfabrication process parameters for 2D flexible BiMEA probes

A.1.1. Parylene-C substrate deposition

- Machine: PDS 2010 LABCOATER 2
- Process parameter: PLA1 15, SP 25, PhA1 160, rest: default, no micro-90, no silane
- 6 g dimer for a thickness of 3 µm

A.1.2. Metallization

1. Surface activation: Machine TePl Gigabatch 360, O_2 plasma, flow 80 sccm, power 50 W, time 2 min, use of Faraday cage
2. Surface preparation: Dehydration at 150 °C for 5 min. Let the wafer cool down to room temperature
3. Spin-coating: 5 ml of LOR3B at 3000 rpm 500 rpm/s for 30 s
4. Soft-bake: 150 °C, 5 min on hot plate
5. Spin-coating: 4 ml of AZnLOF2020 at 3000 rpm, 500 rpm/s, 30 s
6. Soft-bake: 110 °C, 1 min on hot plate
7. Exposure: Süss MA8/BA8 (MA4), dose 40 mJ/cm^2, soft contact
8. Post-exposure bake: 110 °C, 2 min on hot plate
9. Development: stir on wafer holder in AZ MIF326 for $\approx$ 35 s, then rinse in water cascade, spin-dry
10. Metal layer deposition: Machine Balzer PLS 570 (e-beam assisted evaporation), Ar sputtering, recipe 3 (100 V, 7 A, 1 min), Ti/Au/Ti layer, thickness 20/100/10 nm, deposition rate 0.1/0.5/0.1 nm/s
11. Lift-off: Immerse wafer in acetone for 2-3 h, remove metal residues with a pipette, rinse with fresh acetone if necessary, rinse in isopropanol
12. LOR3B removal: In AZ 326 MIF for 5 min, then water cascade, spin-dry

A.1.3. Passivation layer

Deposition of a second PaC layer which serves as passivation. Typically with a thickness of 3 µm, deposited as described before.

A.1.4. Shape and openings

First the etch mask was structured, then RIE was performed in two consecutive steps: PaC etch (Table A.1) followed by Ti etch at the electrode sites (Table A.2).
Etch mask:

1. Surface activation: Machine TePl Gigabatch 360, O_2 plasma, flow 80 sccm, power 50 W, time 2 min, use of Faraday cage
2. Surface preparation: Dehydration at 150 °C for 5 min. Let the wafer cool down to room temperature
3. Spin-coating: ≈ 5 ml of AZ10XT at 2400 rpm, 200 rpm/s, spin-time 60 s
4. Soft-bake: 110 °C, 1:20 min on hot plate
5. Spin-coating: ≈ 5 ml of AZ10XT at 2100 rpm, 200 rpm/s, spin-time 60 s
6. Soft-bake: 110 °C, 2:40 min on hot plate
7. Exposure: Süss MA8/BA8 (MA4), dose 1900 mJ/cm^2, soft contact
8. Development: Stir on wafer holder in AZ400K for 6 to 7 min, then rinse in water cascade, spin-dry
9. PaC etch: Use of RIE recipe in Table A.1 for 6 min and subsequently in one-minute intervals after wafer inspection
10. Ti etch: Use of RIE recipe in Table A.2 for 1:15 min
11. Resist stripping: In two bath of AZ100 remover for 10 min each, using ultrasound power of 5 in the first step, then rinse 3x for 2 min in IPA

Machine		Oxford PL 100 / ICP (RIE-7)
	Helium stable	
Strike Pressure		0.020
Gases	***O2 (sccm)***	36
	CF4 (sccm)	4
He backing pressure (mbar)		8
He backing flow (sccm)		20
	O2/CF isotropic	
RF power (W)		50
ICP Power (W)		500
Gases	***O2 (sccm)***	36
	CF4 (sccm)	4
Cryo Temp (°C)		10
APC pressure (mbar)		0.007
Strike pressure		0.03
He backing pressure (mbar)		8
He backing flow (sccm)		20
DC Bias minimum (V)		2
Etch rate	***PaC (nm/min)***	800

Table A.1.: RIE recipe for PaC etch

Machine		Oxford PL 100 / ICP (RIE-7)
RF power (W)		150
ICP Power (W)		-
Gases	***O2 (sccm)***	20
	Ar (sccm)	20
Cryo Temp (℃)		10
Strike pressure		0.04
He backing pressure (mbar)		10
He backing flow (sccm)		20
Etch rate	***Ti (nm/min)***	6.6-10

Table A.2.: RIE recipe for Ti etch

A.2. Detailed microfabrication process parameters for 2D MEAs for PiRis and KiRis

The following runsheet described the process parameters of the fabrication of the 2D MEAs for PiRi and KiRi implants in detail.

A.2.1. Parylene-C substrate deposition

- Machine: PDS 2010 LABCOATER 2
- Process parameter: PLA1 15, SP 25, PhA1 160, rest: default, no micro-90, no silane
- 10 g dimer for a thickness of 5 µm

A.2.2. Metallization

1. Surface preparation: Dehydration at 150 ℃ for 5 min. Let the wafer cool down to room temperature
2. Spin-coating: 3.5 ml of LNR003 at 4000 rpm, 500 rpm/s, 45 s
3. Soft-bake: 120 ℃, 2 min on hot plate
4. Exposure: Machine MLA150, dose 320 mJ/cm^2, defoc 2, CDB 800
5. Post-exposure bake: 100℃, 1:30 min on hot plate
6. Development: stir on wafer holder in AZ MIF326 for 1:30 min, then rinse in water cascade, spin-dry
7. Metal layer deposition: Machine Balzer PLS 570 (e-beam assisted evaporation), no Ar sputtering, W-liner, Ti/Au/Ti layer, thickness 20/100/10 nm, deposition rate 0.1/0.5/0.1 nm/s
8. Lift-off: Immerse wafer in acetone for 2-3 h, remove metal residues with a pipette, rinse with fresh acetone if necessary, rinse in isopropanol

A.2.3. Passivation layer

Deposition of a second PaC layer which serves as passivation. Typically with a thickness of 5 µm, deposited as described before.

A.2.4. Shape and openings

First the etch mask was structured, then RIE was performed in two consecutive steps.
Etch mask:

1. Surface preparation: Dehydration at 150 ℃ for 5 min. Let the wafer cool down to room temperature
2. Spin-coating: 5 ml of AZ12XT at 1000 rpm, 200 rpm/s, spin-time 180 s
3. Soft-bake: 110 ℃, 4 min on hot plate
4. Exposure: Machine MLA150, dose 350 mJ/cm^2, defoc 2, CDB -800
5. Post-exposure bake: 90℃, 1 min on hot plate
6. Development: Stir on wafer holder in AZ MIF326 for 2 min, then rinse in water cascade, spin-dry
7. PaC etch: Use of RIE recipe in Table A.1 for 12 min and subsequently in one-minute intervals after wafer inspection
8. Ti etch: Use of RIE recipe in Table A.2 for 1:15 min
9. Resist stripping: In two bath of AZ100 remover for 10 min each, using ultrsound power of 5 in the first step, then rinse 3x for 2 min in IPA

A.3. Implant designs

For the initial aging tests 2D cortical probes comprising a single shank with 16 electrodes was used. The design is shown in Figure A.1. For retinal applications, initial tests were performed using 2D BiMEA probes (Figure A.2). These were also used for the characterization of the electrical properties of the retina as described in section 6.1.1. In order to meet the requirements of different applications with kirigami implants, several KiRiRet and KiRiCor designs were employed. The flexible cable length was adjusted depending on the currently used setup; for example a length of 1.5 or 2 cm was used in the *in vitro* setup, or 1 cm for *in vivo* trials with the KiRiCor implant. The KiRiRet implant was designed with either 32 x 225 µm long shanks with a spacing of 100 (Figure A.3A$_i$) or 50 µm (Figure A.3A$_{ii}$) or with 128 shanks with 100 µm inter-shanks distance (Figure A.3A$_{iii}$). For the KiRiCor implant, variations with four (Figure A.3B$_i$), eight (Figure A.3B$_{ii}$) or ten 500 µm long shanks were fabricated (Figure A.3B$_{iii}$), while the former was not used during animal experiments. The designs could also include surface electrodes (ECoG electrodes) (Figure A.3B$_{iv}$). The design incorporating 30 shanks measuring 1000 µm in length (Figure A.3B$_v$), failed to be folded successfully, as discussed in section 4.2.5.

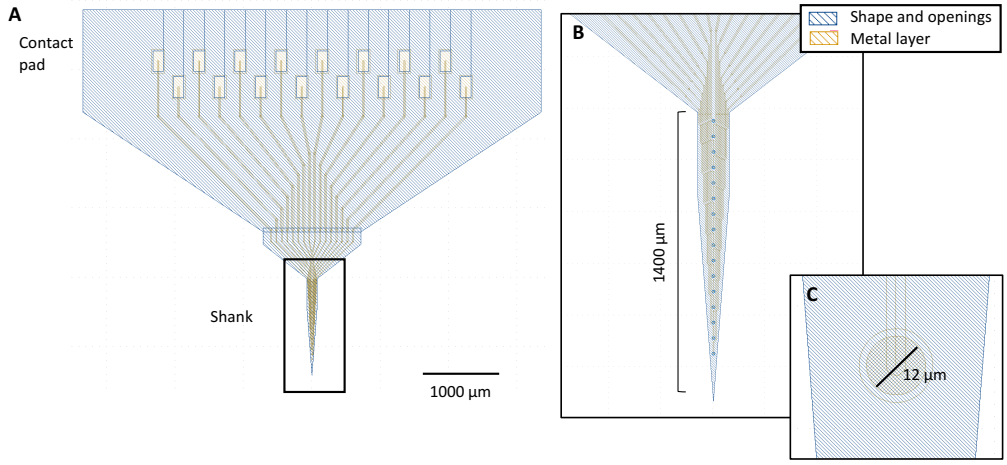

Figure A.1.: Design of the 16-channel probe used in the electrochemical accelerated aging test. A) The probe consists of a contact pad area for PCB connection and a single shank (B) with a length of 1400 µm comprising 16 electrodes with a diameter of 12 µm (C).

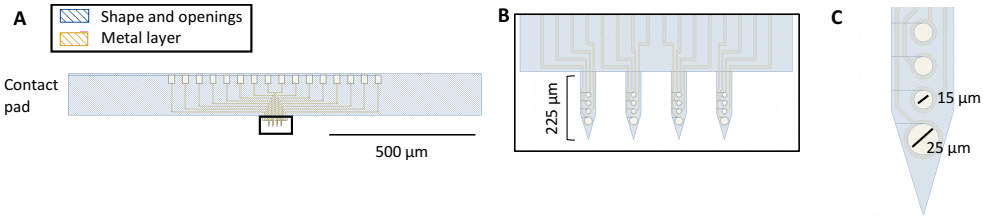

Figure A.2.: 2D BiMEA design for the characterization of the retinal tissue.

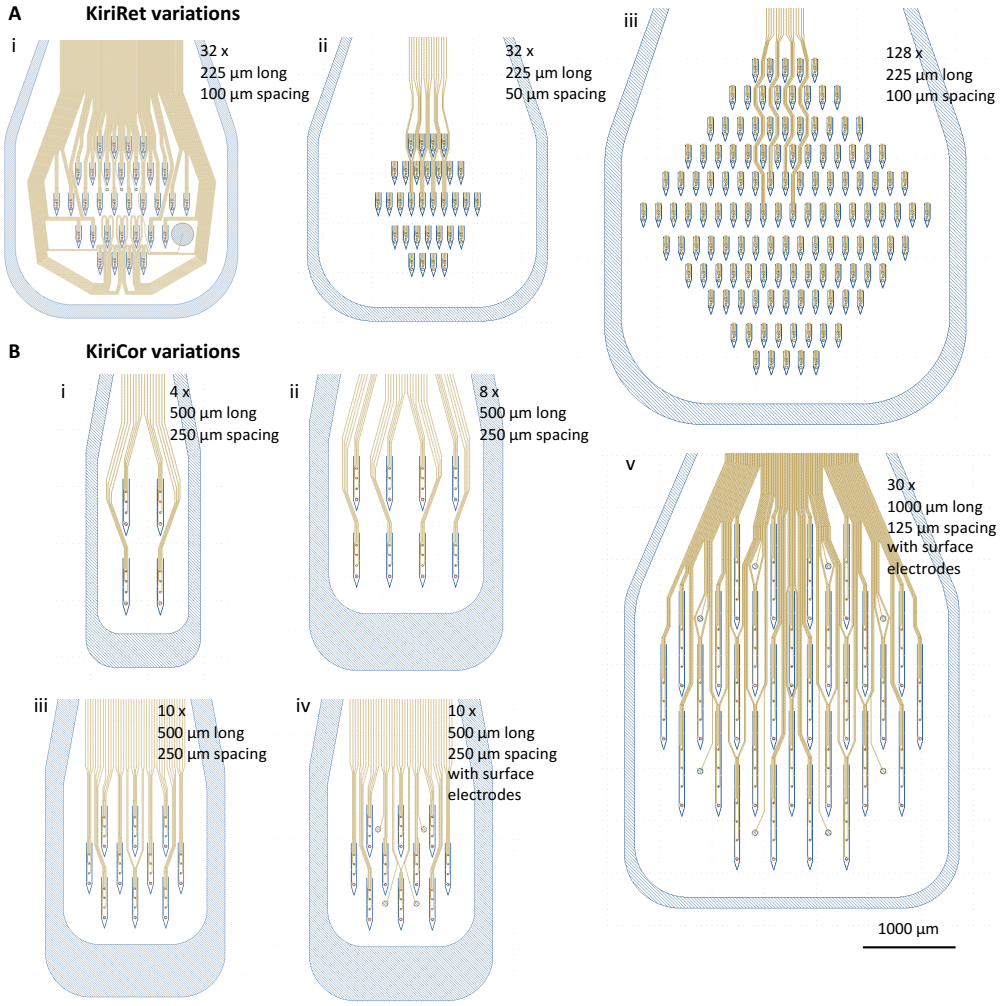

Figure A.3.: Kirigami design variations. A) KiRiRet variations reaching from 32 x 225 µm long shanks with 100 µm (i) or 50 µm spacing (ii). Up to 512 electrodes distributed equally over 128 shanks were achieved (iii). B) KiRiCor variations reaching from 4 (i), 8 (ii) to 10 (iii) x 500 µm long shanks with 250 µm spacing. The designs also included surface electrodes if desired (iv). A probe with 30 x 1000 µm long shanks was tested, but the folding was not entirely successful.

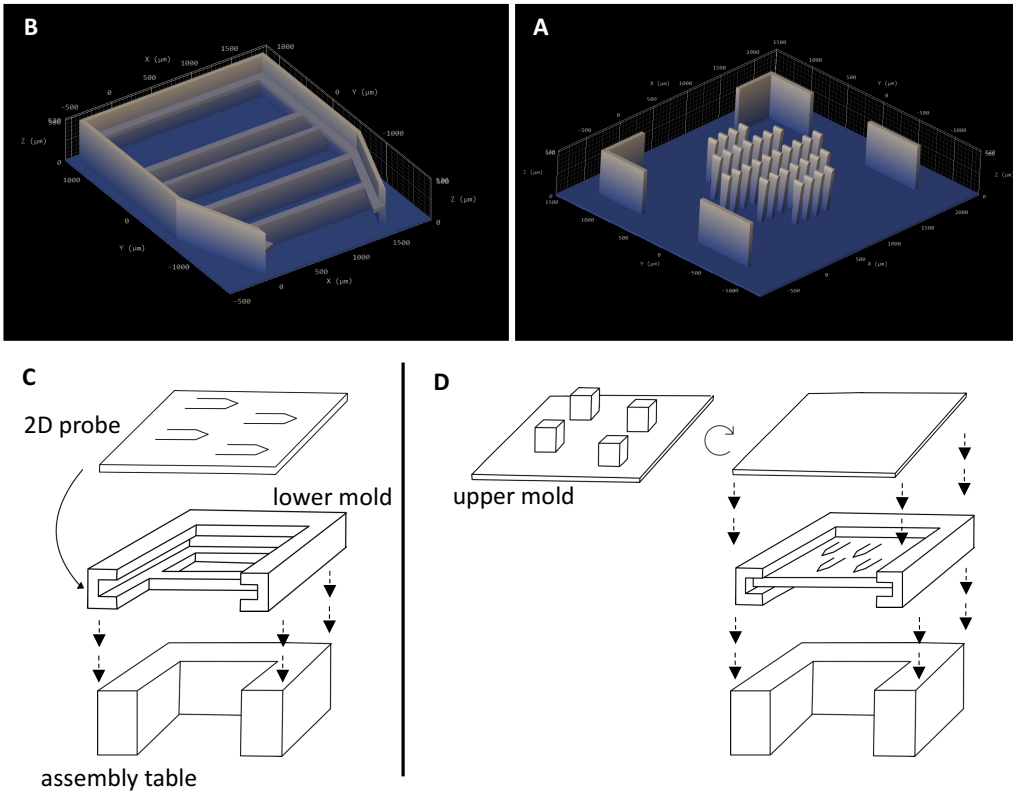

Figure A.4.: Upside-down approach for the folding of kirigami implants. An alternative folding method also uses an upper mold (A) and a lower mold (B). Here, the flexible probe is placed on the lower mold which has protruding etches to hold the probe in place (C). Then the upper mold, which contains the blogs, is turned upside down and approaches the 2D probe from the top to fold all the shanks at the same time (D).

B. Appendix: Implant characterization

KiRi	Anodic first		Cathodic first		**PiRi**	Anodic first		Cathodic first	
Pulsewidth (ms)	***mean I (µA)***	***std (µA)***	***mean I (µA)***	***std (µA)***	***Pulsewidth (ms)***	***mean I (µA)***	***std (µA)***	***mean I (µA)***	***std (µA)***
0.1	71.9	10.4	62.1	11.1	*0.1*	149.9	44.8	179.9	85.6
0.5	19.2	7.9	14.9	2.1	*0.5*	49.5	17.5	44.4	20.9
0.8	13.1	5.3	10.2	1.9	*0.8*	35.0	13.5	28.9	11.9
1	10.9	4.2	8.5	1.8	*1*	28.3	10.8	23.7	9.4
2	6.4	2.6	4.7	0.9	*2*	16.2	6.6	13.1	4.2
3	4.4	1.6	3.4	0.6	*3*	11.5	4.7	9.6	2.9
4	3.6	1.3	2.7	0.4	*4*	8.9	3.8	7.6	2.3
5	3.0	1.2	2.3	0.3	*5*	7.2	2.9	6.4	1.9
10	1.8	0.6	1.4	0.1	*10*	4.1	1.6	3.8	1.1

Table B.1.: Maximum current values of KiRi and PiRi electrodes before reaching the maximum cathodic E_{mc} or anodic E_{ma} potential limits during voltage transient measurements depending on the pulsewidth and pulse type (anodic or cathodic first biphasic pulses)

KiRi	Anodic first		Cathodic first		**PiRi**	Anodic first		Cathodic first	
Pulsewidth (ms)	***mean CIC***	***std CIC***	***mean CIC***	***std CIC***	***Pulsewidth (ms)***	***mean CIC***	***std CIC***	***mean CIC***	***std CIC***
0.1	1.5	0.2	1.3	0.2	*0.1*	1.7	0.9	1.7	0.7
0.5	2.0	0.9	1.5	0.2	*0.5*	2.5	1.1	2.1	0.7
0.8	2.1	0.9	1.7	0.3	*0.8*	2.8	1.1	2.2	0.7
1	2.2	0.9	1.7	0.4	*1*	2.8	1.1	2.3	0.7
2	2.6	1.1	1.9	0.4	*2*	3.3	1.2	2.6	0.9
3	2.7	1.1	2.1	0.4	*3*	3.5	1.3	2.9	0.9
4	2.9	1.2	2.2	0.4	*4*	3.6	1.4	3.1	1.1
5	3.1	1.2	2.3	0.3	*5*	3.7	1.4	3.2	1.2
10	3.7	1.2	2.9	0.2	*10*	4.2	1.6	3.8	1.4

Table B.2.: CIC of KiRi and PiRi electrodes depending on the pulsewidth and pulse type (anodic or cathodic first)

Device	Components	Main Material	Young's modulus (GPa)	Pillar Length (µm)	Diameter (at the base) (µm)	E · I (Nµm^2)	cross-section at centroid (µm^2)	Reference
This work: PiRi	Hollow IPL pillars filled with Au	IPL	4.73	Up to 500	straight pillars: 12 cone-shaped pillars: 35 multisite pillars: 36 x 12	3.9 50.7 11.6	110 541 250	This work [41]
This work: KiRi	Flat Shanks	PaC	1.7	up to 1000	50 x 10 (thickness x width)	7.1	500	This work [177]
Silicon microneedle array	Needle electrodes	Si	160	100	10	78.5	78.5	Lee et al. 2022 [116]
Sea of electrodes	Needle electrodes	Si	160	500	20	398	177	Zardini et al., 2021 [115]
Inkjet-Printed and electroplated electrodes	Solid pillar electrodes	AgNP ink	82	560	32	4220	804	Grob et al. 2021 [114]
3D printed electrodes	Cone-shaped pillar electrodes	ormocomp	1	350	50	97	1105	Brown et al. 2022 [117]
Utah Array	Cone-shaped needle electrodes	Si	160	1500	90	163040	3579	Campbell et al., 1991 [24]
(Stacked) stiff Michigan array	Flat shanks	Si	160		10 x 50 (thickness x width)	16667	500	Wise at al., 1970 [25]
Flexible 3D stacks (Michigan-style)	Flat shank	Pi	2.5		14 x 80 (thickness x width)	45.73	1120	Chung et al., 2019 [118]
***in vivo* kirigami**	Flat shanks	Pi	2.5	1500	20 x 200 (thickness x width)	333.3	4000	Lee et al., 2022 [37]
***in vitro* kirigami**	Flat shanks	Pi	2.5	1100	15 x 90 (thickness x width)	63.3	1350	Soscia et al., 2020 [36]
Neural threads	Thin flexible threads with single electrodes	SU-8	2		0.94 x 1 (thickness x width)	0.00017	≈ 1	Yang et al., 2019 [32]

Table B.3.: Bending stiffness comparison of probes used in this work with examples from the literature.

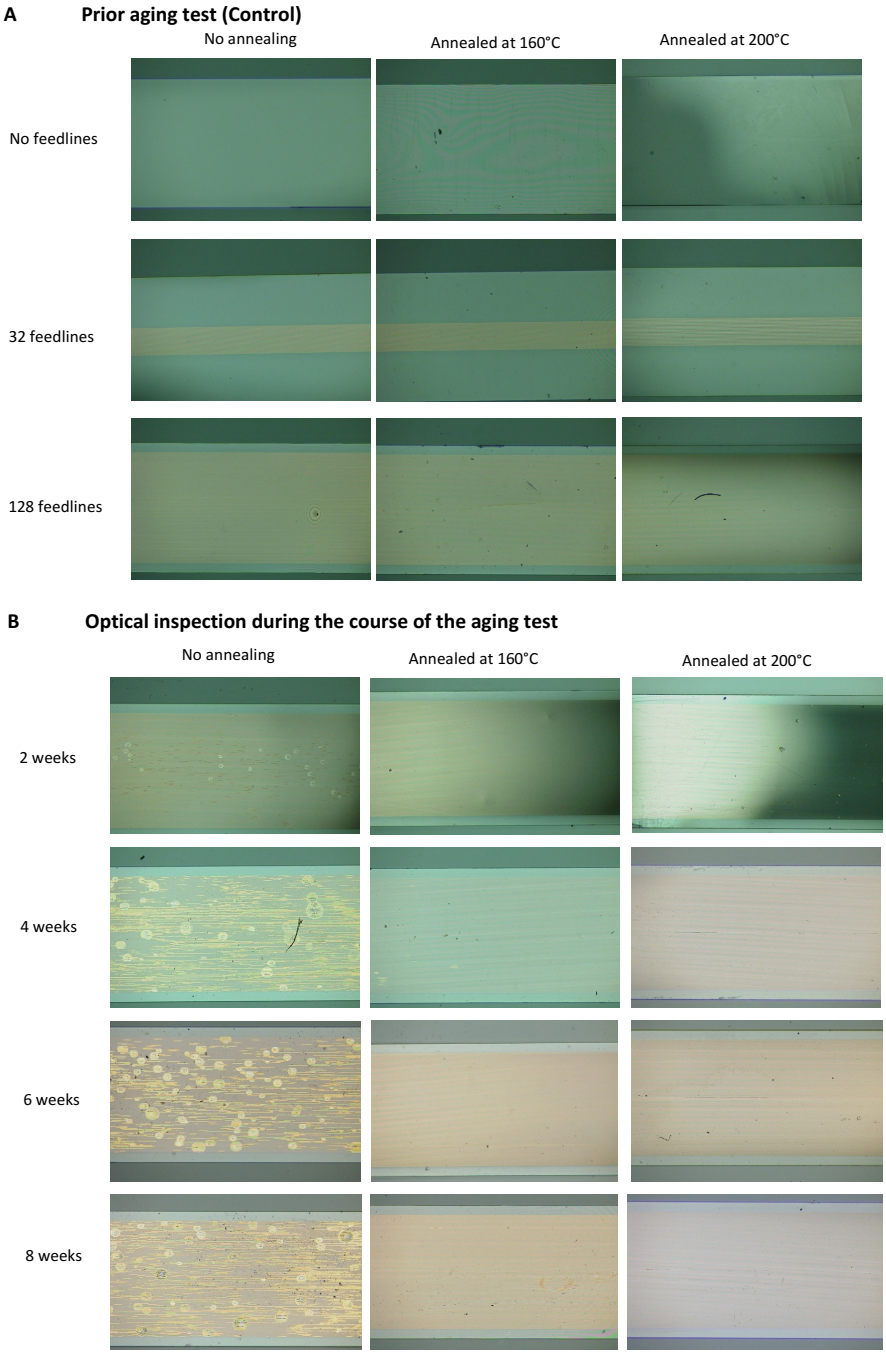

Figure B.1.: Microscopic inspection prior and during the aging test. A) Microscopic inspection of samples prior to the start of the aging test, which have either no, 32 or 128 feedlines, and B) pictures taken during the course of the aging test (after 2, 4, 6 and 8 weeks). The columns are the annealing groups (unannealed, annealed at 160 ℃ and annealed at 200 ℃.

C. Appendix: Applications

C.1. Medium preparations

C.1.1. Ames' medium

For the preparation of 1 l, a bottle(8.8 g/l) of Ames' medium (A1420, Sigma Aldrich) was used and dissolved in 1 l of distilled water. 1.7 g/l of sodium bicarbonate ($NaHCO_3$) (S5761, Sigma Aldrich) were added. Then, the solution was oxygenated with carbogen gas containing 95% O2 and 5% CO2 (The Linde Group, Germany) for at least 30 mins. The pH was adjusted to 7.4 using sodium bicarbonate ($NaHCO_3$).

C.1.2. Artifical cerebrospinal fluid (aCSF) and modified aCSF

For the preparation of 1 l aCSF, (in mM) 124 NaCl, 24 NaHC03, 3 KCl, 1.25 NaH2P04, 1.25 MgCl2, 2 CaCl2, and 10 glucoses were dissolved in 1 l distilled water according to [277]. Then, the solution was oxygenated with carbogen gas containing 95% O2 and 5% CO2 (The Linde Group, Germany) for at least 30 mins. The pH was adjusted to 7.4 using sodium bicarbonate ($NaHCO_3$).

C.2. Retina applications

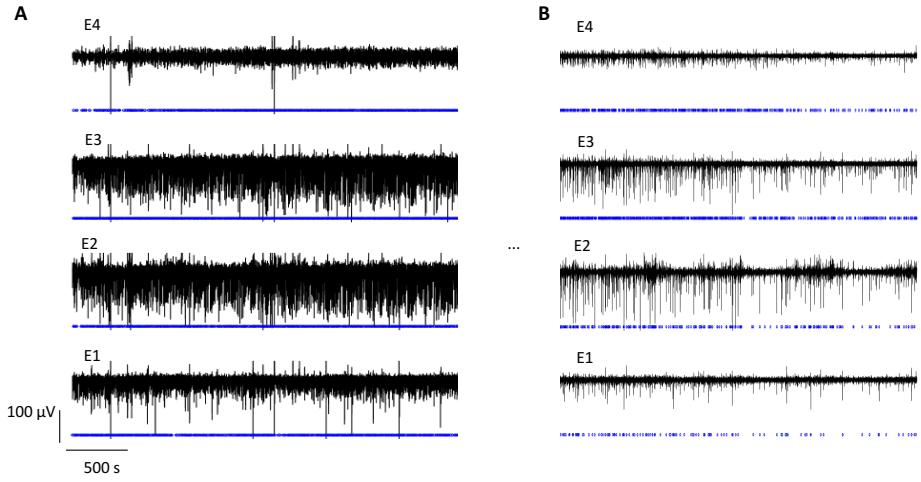

Figure C.1.: Application of GABA to abolish oscillations Recording of a retina from a 19-month old RCS rat, where the oscillations were abolished using GABA. The effect of GABA took around 60 min until a decrease of deflections was evident and no oscillatory activity was anymore observed.

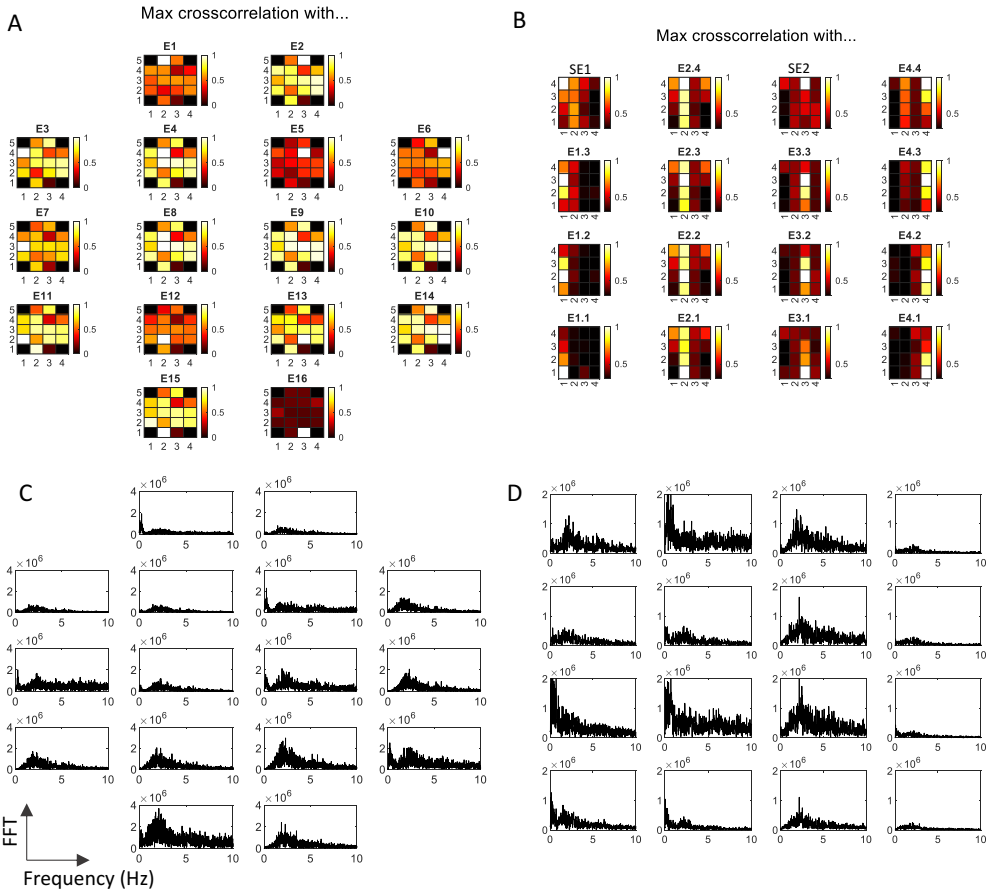

Figure C.2.: Cross-correlations and FFT in RCS retina Maximum value of the cross-correlations of each electrode with all other electrodes for a KiRi (A) and PiRi (B) electrode using the LFP data recorded in a RCS rat. FFTs of each electrode (raw data) during a period of oscillations recorded with KiRi (C) and PiRi (D) electrodes (modified from [197]).

C.3. Cortical applications

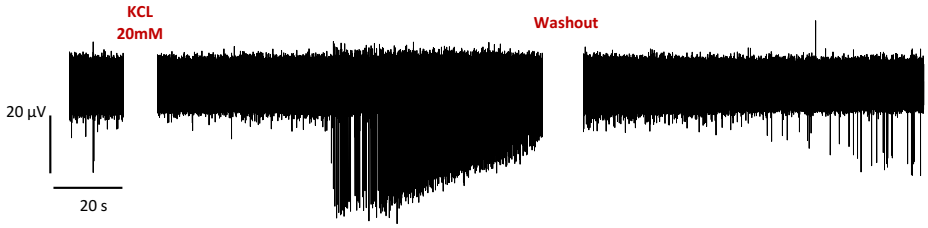

Figure C.3.: Inducing a depolarization block with modified aCSF and recording the activity with a PiRi electrode.

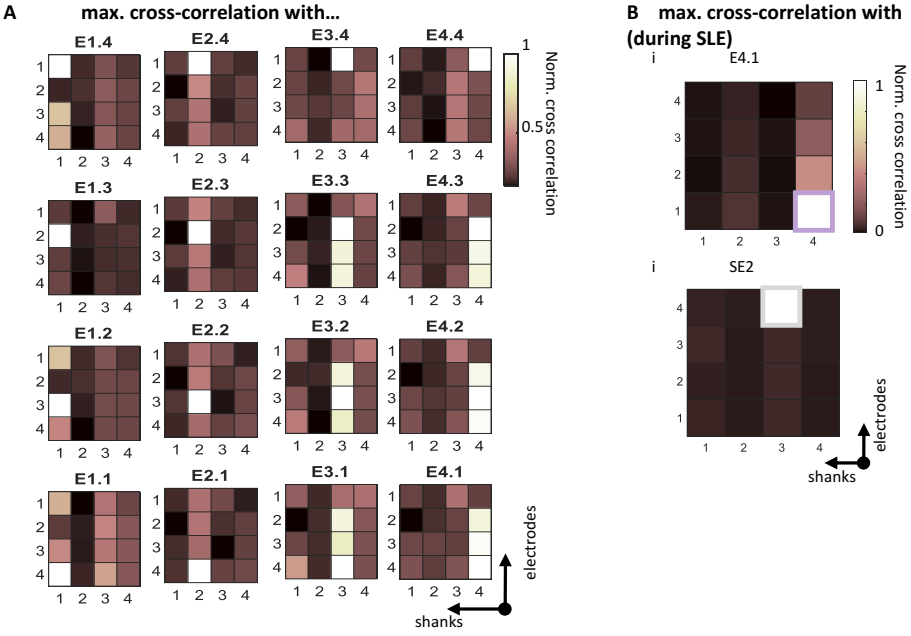

Figure C.4.: Analysis of the correlation of activity recorded with KiRi electrodes during SLEs A) Map of the maximum value of the cross-correlation of the raw data trace of all electrodes with all other electrodes. B) Maximal value of the cross-correlation for electrode E4.1 and SE2 with all the other electrodes during the SLEs in those electrodes (modified from [177]).

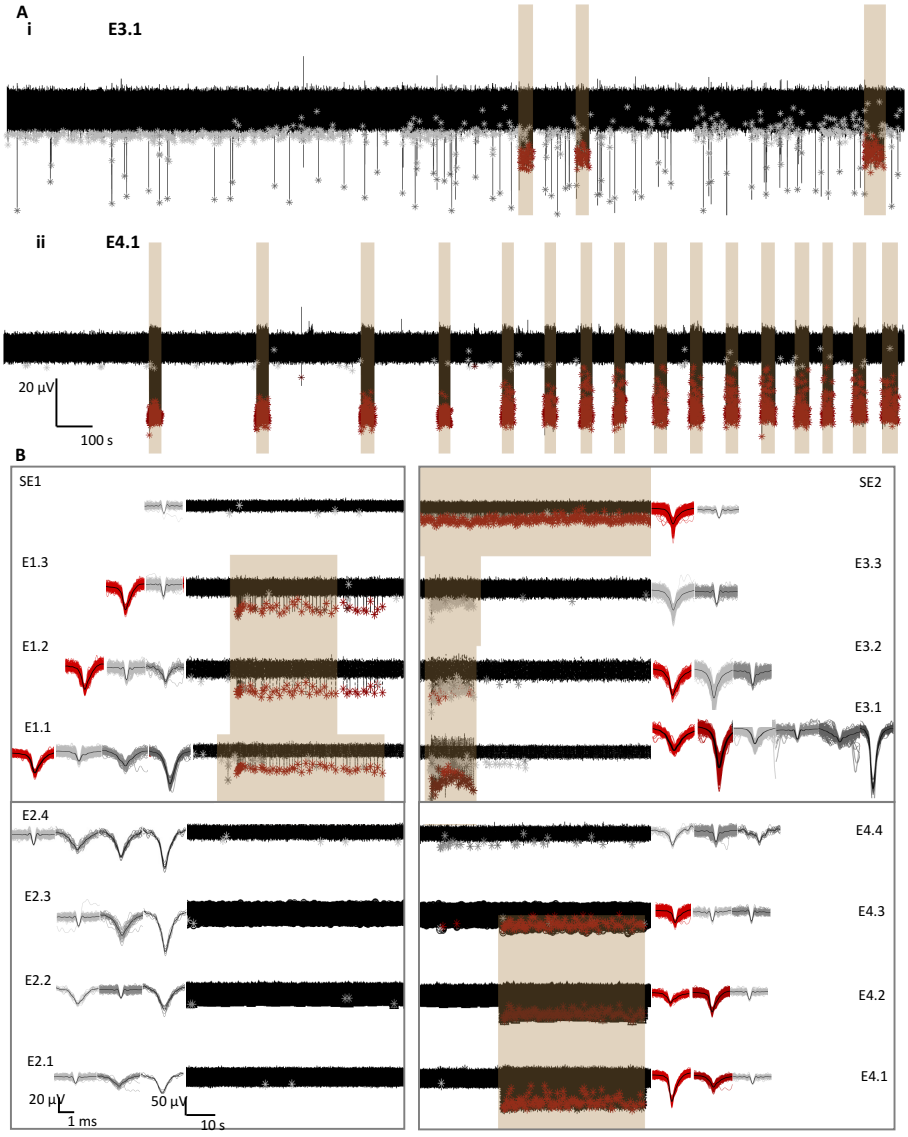

Figure C.5.: Spiking activity of human brain slices in modified aCSF A) The complete recording of two example electrodes (E3.1 and E4.1) is displayed (bandpass-filtered data).B) A snapshot of all electrodes is presented, showing SLEs in Shank 1, 2, 3, and 4, as well as in the surface electrodes SE1 and SE2. The sorted spiking units are displayed alongside the bandpass-filtered data. Spikes that occur during the SLEs are red, while spikes outside of the SLEs are displayed in gray [177].

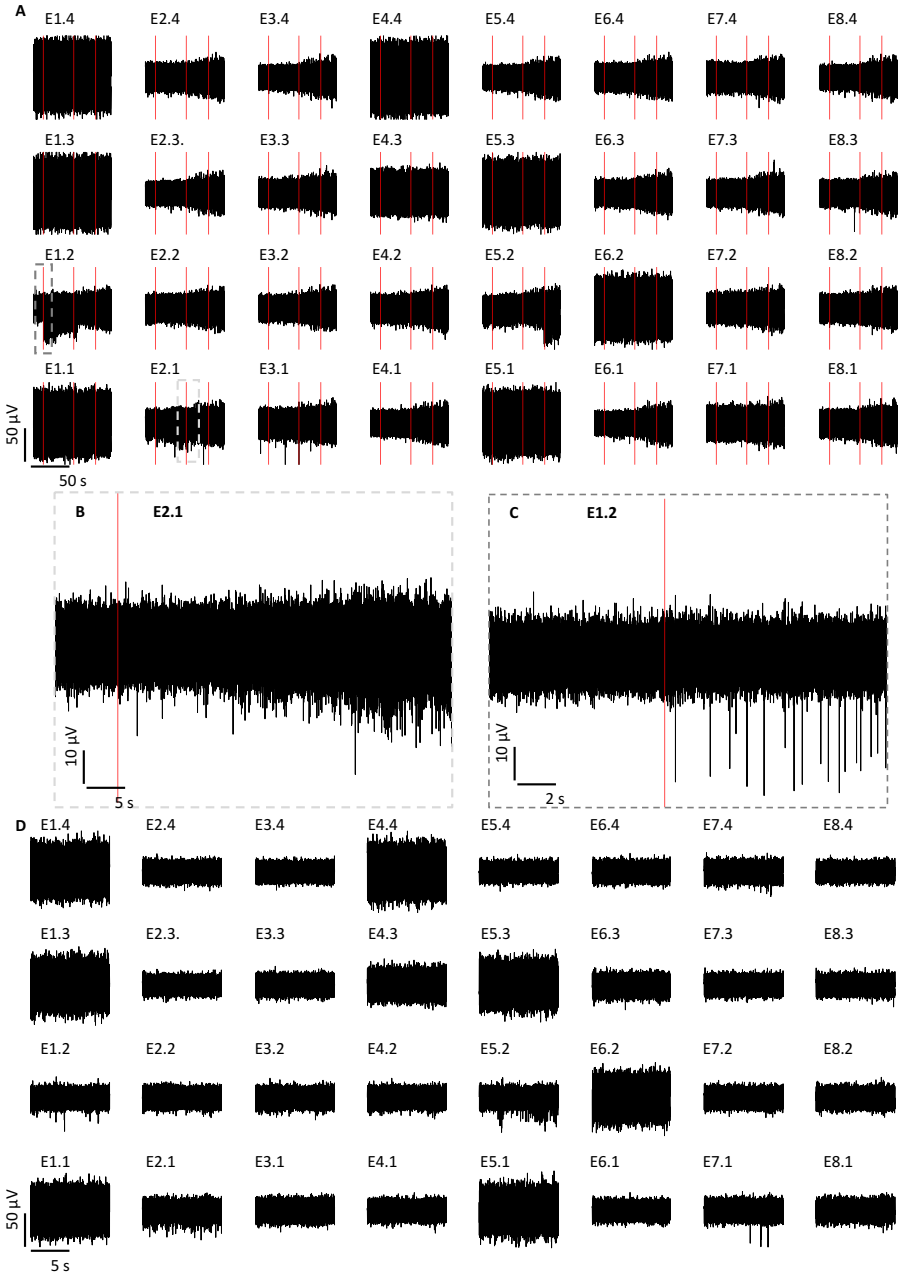

Figure C.6.: Spiking activity during the insertion of a KiRiCor implant with 8 shanks containing four electrodes into the cortex A) Exemplary band-pass filtered (100 Hz – 3 kHz) electrophysiological data. The insertion was carried out in a stepwise manner, with the timing of each step indicated by vertical red lines. The insertion process resulted in the observation of various spiking activity patterns across shanks. While some electrodes recorded an increase in spiking activity over the subsequent seconds following insertion (as illustrated in E2.1, B), other electrodes exhibited an abrupt elevation in spiking activity (as seen in E1.2, C). Following a brief period of rest, which lasted for approximately two minutes in this example, the activity returned to its baseline state (D). This was characterized by the presence of regular spontaneous spiking activity across the majority of the electrodes (as depicted in the band-pass filtered data) [177].

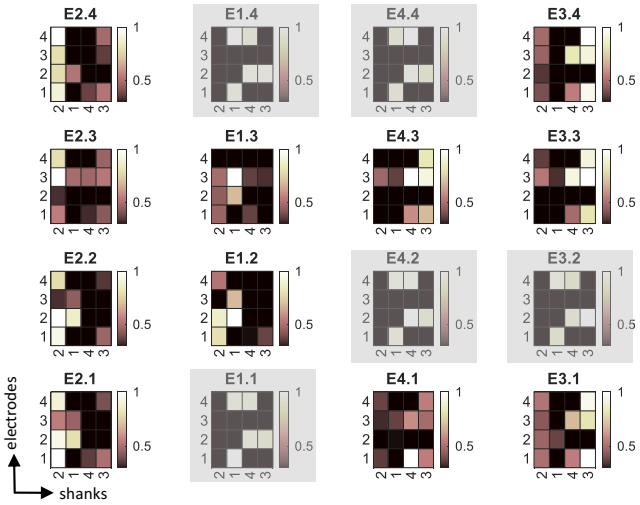

Figure C.7.: Cross-correlation analysis of the LFPs of each electrode with all the other electrodes during acute *in vivo* recordings in the mouse somatosensory cortex and stimulating the hind paw. The cross-correlation plots of non-working electrodes are represented in gray and as black boxes in the other heatmaps [177].

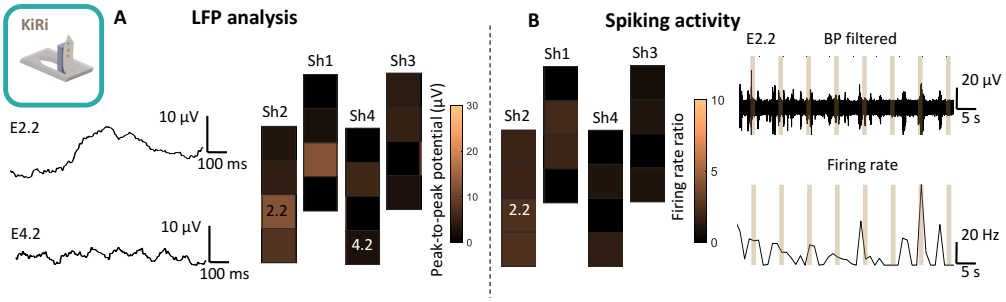

Figure C.8.: Recording from S1 using KiRis during tactile stimulation of the fore limb A) Averaged LFPs during the initial second of tactile stimulation, exemplary data of E2.2 and E4.2. The peak-to-peak potentials were derived from the averaged LFPs over 50 trials. B) The spiking activity demonstrates a corresponding increase in response to the stimulation (brown bars). The mean changes (firing rate ratio during versus before stimulation) in spiking activity are also dependent on the position of the electrodes. The band-pass filtered data and firing rate trace of E2.2 are visualized as an example.

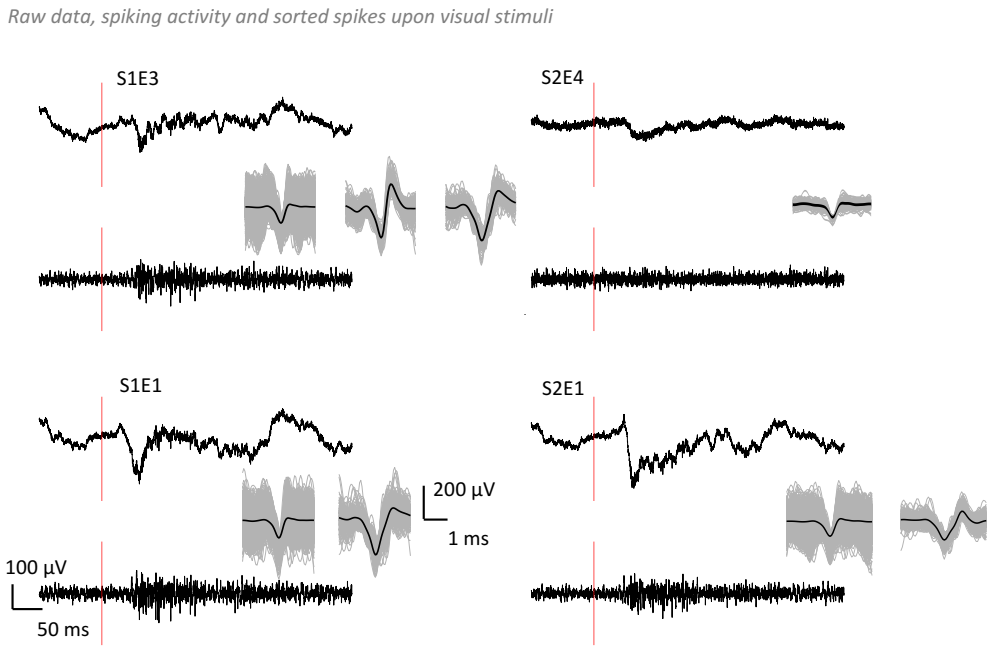

Figure C.9.: Spiking activity measured in the visual cortex with a KiRi implant This Figure illustrates the raw, filtered data as well as the sorted spikes of one trial in response to the simple grating visual stimulus. The red bar denotes the onset of the stimulus [177].

Band / Volume 286
***Ab initio* investigation of intrinsic antiferromagnetic solitons**
Amal Jawdat Nayef Aldarawsheh (2024), xv, 164 pp
ISBN: 978-3-95806-785-1

Band / Volume 287
Understanding the dynamics of Plant-Bacteria-Bacteriophage interactions as a means to improve plant performance
S. H. Erdrich (2024), ix, 176 pp
ISBN: 978-3-95806-791-2

Band / Volume 288
Prediction of Magnetic Materials for Energy and Information Combining Data-Analytics and First-Principles Theory
R. Hilgers (2024), xv, 215 pp
ISBN: 978-3-95806-795-0

Band / Volume 289
Biodegradation and microbial upcycling of plastics
J. de Witt (2025), XVI, 259 pp
ISBN: 978-3-95806-804-9

Band / Volume 290
Practical Methods for Efficient Analytical Control in Superconducting Qubits
B. Li (2025), 202 pp
ISBN: 978-3-95806-807-0

Band / Volume 291
Ab initio investigation of topological magnetism in two-dimensional van der Waals heterostructures
N. Abuawwad (2025), xviii, 135 pp
ISBN: 978-3-95806-808-7

Band / Volume 292
Tolerance engineering of Pseudomonas for the efficient conversion and production of aldehydes
T. Lechtenberg (2025), XVI, 185 pp
ISBN: 978-3-95806-817-9

Band / Volume 293
Exploring the process window for production of itaconic, 2-hydroxyparaconic, and itatartaric acid with engineered *Ustilago* strains
P. Ernst (2025), x, 145 pp
ISBN: 978-3-95806-825-4

Band / Volume 294
Surface Plasmon Resonance Microscopy for the Characterization of Cell-Substrate Distances
J. Bednar (2025), xxiii, 187 pp
ISBN: 978-3-95806-830-8

Band / Volume 295
Microfluidic-MEA hybrid systems for electrophysiological recordings of neuronal co-cultures
J. Stevanović (2025), ix, 186 pp
ISBN: 978-3-95806-831-5

Band / Volume 296
Structural and Magnetic Properties of Biocompatible Iron Oxide Nanoparticles for Medical Applications
A. Nasser (2025), xii, 140 pp
ISBN: 978-3-95806-837-7

Band / Volume 297
Metabolic engineering of *Pseudomonas taiwanensis* for the improved production of styrene
J. Rönitz (2025), XII, 147 pp
ISBN: 978-3-95806-841-4

Band / Volume 298
Elucidation of anti-viral strategies in *Streptomyces*
B. U. Rackow (2025), xii, 148 pp
ISBN: 978-3-95806-842-1

Band / Volume 299
Ab initio investigations of spin-orbit functionalized graphene
D. Mazhjoo (2025), 163 pp
ISBN: 978-3-95806-847-6

Band / Volume 300
3D neural implants for* in vivo *applications
M. Jung (2025), xvi, 215 pp
ISBN: 978-3-95806-852-0

Schlüsseltechnologien / Key Technologies
Band / Volume 300
ISBN 978-3-95806-852-0

Mitglied der Helmholtz-Gemeinschaft

JÜLICH
Forschungszentrum